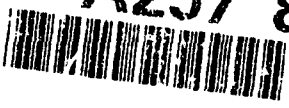


2

AD-A257 894  


RL-TR-91-385  
Final Technical Report  
December 1991



# NEW TECHNIQUES IN OPTICAL COMMUNICATIONS AND SIGNAL PROCESSING

DTIC  
ELECTE  
NOV 24 1992  
S C D

Rensselaer Polytechnic Institute

Dr. Pankaj K. Das, Dr. Henry Stark, Dr. Nickolas P. Vlannes

*APPROVED FOR PUBLIC RELEASE; DISTRIBUTION UNLIMITED.*

  
92-30080

Rome Laboratory  
Air Force Systems Command  
Griffiss Air Force Base, NY 13441-5700

92 1

This report has been reviewed by the Rome Laboratory Public Affairs Office (PA) and is releasable to the National Technical Information Service (NTIS). At NTIS it will be releasable to the general public, including foreign nations.

RL-TR-91-385 has been reviewed and is approved for publication.

APPROVED:



NORMAN P. BERNSTEIN  
Project Engineer

FOR THE COMMANDER:



JOHN A. GRANIERO  
Chief Scientist for C3

If your address has changed or if you wish to be removed from the Rome Laboratory mailing list, or if the addressee is no longer employed by your organization, please notify RL( C3DB ) Griffiss AFB, NY 13441-5700. This will assist us in maintaining a current mailing list.

Do not return copies of this report unless contractual obligations or notices on a specific document require that it be returned.

# REPORT DOCUMENTATION PAGE

Form Approved  
OMB No. 0704-0188

Public reporting burden for this collection of information is estimated to average 1 hour per response, including the time for reviewing instructions, searching existing data sources, gathering and maintaining the data needed, and completing and reviewing the collection of information. Send comments regarding this burden estimate or any other aspect of this collection of information, including suggestions for reducing this burden, to Washington Headquarters Services, Directorate for Information Operations and Reports, 1215 Jefferson Davis Highway, Suite 1204, Arlington, VA 22202-4302, and to the Office of Management and Budget, Paperwork Reduction Project (0704-0188), Washington, DC 20503.

1. AGENCY USE ONLY (Leave Blank)		2. REPORT DATE December 1991		3. REPORT TYPE AND DATES COVERED Final Aug 88 - Apr 90	
4. TITLE AND SUBTITLE NEW TECHNIQUES IN OPTICAL COMMUNICATIONS AND SIGNAL PROCESSING				5. FUNDING NUMBERS C - F30602-88-D-0025 PE - 63726F PR - 2863 TA - 92 WU - PE	
6. AUTHOR(S) Dr. Pankaj K. Das, Dr. Henry Stark, Dr. Nickolas P. Vlannes					
7. PERFORMING ORGANIZATION NAME(S) AND ADDRESS(ES) Rensselaer Polytechnic Institute Troy NY 12180-3590				8. PERFORMING ORGANIZATION REPORT NUMBER N/A	
9. SPONSORING/MONITORING AGENCY NAME(S) AND ADDRESS(ES) Rome Laboratory (C3DB) Griffiss AFB NY 13441-5700				10. SPONSORING/MONITORING AGENCY REPORT NUMBER RL-TR-91-385	
11. SUPPLEMENTARY NOTES Rome Laboratory Project Engineer: Norman P. Bernstein/C3DB/(315) 330-4092 This effort is an Expert Science program under subcontract to Georgia Institute of Technology.					
12a. DISTRIBUTION/AVAILABILITY STATEMENT Approved for public release; distribution unlimited.				12b. DISTRIBUTION CODE	
13. ABSTRACT (Maximum 200 words)  This report provides a synopsis of research in several areas of optical communications and signal processing.  The report is divided into sections on "Spread Spectrum Techniques in Optical Communications; Optical Controller for Phased Array Radar Using Neural Network Architectures; Two Dimensional Phased-Array Optic; Hybrid Optical/Electronic Nonlinear Optical Devices; and Image Recovery From Image Plane Arrays.  Each subject area is treated individually with its own authors, synopsis, and conclusion. A summarization of papers and presentations which resulted from the research effort is provided at the end of the report.					
14. SUBJECT TERMS Optics, Computing, Neural Networks, Phased Arrays, Image Processing, E-O Materials				15. NUMBER OF PAGES 228	
				16. PRICE CODE	
17. SECURITY CLASSIFICATION OF REPORT UNCLASSIFIED	18. SECURITY CLASSIFICATION OF THIS PAGE UNCLASSIFIED	19. SECURITY CLASSIFICATION OF ABSTRACT UNCLASSIFIED	20. LIMITATION OF ABSTRACT UL		

## TABLE of CONTENTS

	<u>PAGE:</u>
ABSTRACT .....	1
I. INTRODUCTION .....	2
1.1 Research Topics and Objectives .....	2
1.2 Report Organization .....	5
II. SPREAD SPECTRUM TECHNIQUES IN OPTICAL COMMUNICATIONS .....	6
2.1 Introduction .....	6
2.2 Transform Domain Processing in the Optical Domain .....	8
2.3 Optical Pulse Compression and Spectral Modulation .....	11
2.4 Spread Spectrum Techniques in Optical Communication .....	20
2.5 Applications .....	28
2.6 Conclusions .....	32
2.7 Acknowledgements .....	34
Chapter II - References .....	35
III. OPTICAL CONTROLLER FOR ADAPTIVE PHASED ARRAY ANTENNAS USING NEURAL NETWORK ARCHITECTURE .....	37
3.1 Introduction .....	37
3.2 Optical Architectures and Technology .....	40
3.3 Perceptron Implementation .....	43
3.4 Optical Architectures for the Perceptron .....	56
3.5 Conclusions .....	62
3.6 Acknowledgements .....	63
Chapter III - References .....	64
IV. TWO-DIMENSIONAL PHASED-ARRAY OPTICS .....	65
4.1 Introduction .....	65
4.2 Phased-Array Theory .....	66
4.3 Phased-Array Modulator Background .....	82
4.4 Phased-Array Optics – Electro-Optical Materials .....	88
4.5 Phased-Array Optics – Device Designs .....	95
4.6 Device Fabrication .....	124
4.7 Applications .....	136



	<u>PAGE:</u>
4.8 Concluding Discussion .....	137
Chapter IV - References .....	138
<b>V. HYBRID OPTICAL/ELECTRONIC NONLINEAR OPTICAL DEVICES .....</b>	<b>145</b>
5.1 Introduction .....	145
5.2 Acousto-Optic Bistable Optical Experiment .....	152
5.3 Experimental Results .....	162
5.4 Conceptual Electro-Optic Hybrid Optical/Electronic Nonlinear Device .....	168
5.5 HO/E Nonlinear Optical Arrays .....	179
5.6 Concluding Discussion .....	182
5.7 Acknowledgements .....	183
Chapter V - References .....	184
<b>VI. HIGH RESOLUTION IMAGE RECOVERY FROM IMAGE PLANE ARRAYS USING CONVEX PROJECTIONS .....</b>	<b>189</b>
6.1 Introduction .....	189
6.2 The Method of Convex Projections .....	190
6.3 The Method of POCS Applied to the Problem at Hand .....	190
6.4 Experimental Results .....	195
Chapter VI - References .....	215
APPENDIX A .....	216
APPENDIX B - Papers and Presentations .....	218

## ABSTRACT

Research into optical communications and signal processing has yielded novel conceptual and experimental results. The research fields include systems architecture, device technology, and processing algorithms.

a) Spread Spectrum Techniques in Optical Communications:

The interference suppression capability of spread spectrum techniques is enhanced by optical transform domain processing and a design for spectral coding at optical frequencies is presented. The encoding system is formulated on optical pulse compression and shaping.

b) Optical Controller for Phased Array Radar Using Neural Network Architectures:

The control of adaptive phased-array antennas using the least mean squares algorithm is shown to be analogous to the implementation of a two-layer perceptron. From the two-level perceptron architecture, an optical processor for the control of adaptive antennas is proposed.

c) Two-Dimensional Phased-Array Optics:

Device concepts for phased-array optics applicable to two-dimensional beam scanning, wavefront shaping, and dynamic lenses are formulated. The proposed devices employ element and array scanning for control of an optical beam. Dielectric waveguide optics and electro-optic organic materials can be used to form multiple layers of electro-optically controlled channel waveguides and artificial prisms. These techniques permit the fabrication of monolithic and integrated devices.

d) Hybrid Optical/Electronic Nonlinear Optical Devices:

Nonlinear optical devices that are based on linear optical modulators and nonlinear electronic feedback can be fabricated that are electronically tuneable and detector limited sensitive. A proof-of-concept experiment using an acousto-optic modulator and a nonlinear electronic Schmitt trigger has been performed. An electro-optic hybrid optical/electronic nonlinear optical device that can be integrated with conventional semiconductor electronics is examined in concept and fabrication techniques.

e) Image Recovery from Image Plane Arrays:

High-resolution reconstruction of remotely obtained images from image-plane detector arrays with individual detectors smaller than the blur spot of optics can be acquired by scanning or rotating the image with respect to the detector. The method of convex projections is developed as an alternative to matrix inversion and least-squares estimation. With readily obtained prior knowledge, good quality imagery can be produced with reduced data.

DTIC QUALITY INSPECTED 4

Accession For	
NTIS	<input checked="checked" type="checkbox"/>
DTIC TAB	<input type="checkbox"/>
Unannounced	<input type="checkbox"/>
Justification	
By	
Distribution/	
Availability Codes	
Aval and/or	
Dist	Special
A-1	

## *Chapter I*

### **Introduction**

#### **1.1 RESEARCH TOPICS and OBJECTIVES**

The properties of light in the infrared to visible wavelengths offer improved and novel means for communications and signal processing. Communication by light promises enormous bandwidth, security, and economy in comparison to present techniques. Optical signal processing and computing have the advantage of tremendous throughput due to light-speed computation and massive parallelism.

With the advantages offered by the application of optical techniques, five research areas were explored in order to investigate systems architecture, device technology, and processing algorithms to exploit light. The research was conducted to develop and evaluate concepts and experimentally demonstrate proof-of-concept. These topic areas are:

- 1) Spread Spectrum Techniques in Optical Communications;
- 2) Optical Controller for Adaptive Phased Array Antennas Using Neural Network Architecture;
- 3) Two-Dimensional Phased-Array Optics;
- 4) Hybrid Optical/Electronic Nonlinear Optical Devices; and,
- 5) High Resolution Image Recovery from Image Plane Arrays Using Convex Projection.

A brief description of the research topics and discussion of the objectives of this research follows.

#### **1) Spread Spectrum Techniques in Optical Communications:**

The objective of the study of spread spectrum techniques is the evaluation of spread spectrum techniques as applied to light communications. Spread spec-

trum methods are resistant to jamming and interference which are advantages over narrow band communication techniques. Despite the improvements in using spread spectrum, this approach has not been utilized in optical communications due to lack of effective modulation and coding methods available at optical frequencies. The research in this area explores coding schemes and modulators to incorporate spread spectrum into optical communications. A conceptual design for spectral coding at optical frequencies has been developed, and applications of this system to fiber optics, laser radar, and free space optical communications are examined.

## 2) Optical Controller for Adaptive Phased Array Antennas Using Neural Network Architecture

Processing of signals from adaptive phased-array antennas has received attention as a means of detection of broadband information in the presence of multiple interference sources and Gaussian noise. An investigation into the use of a neural network for an optical controller for adaptive phased-array antennas was conducted with the objective of evaluating perceptron architecture, and the associated technology to implement the optical controller. The control of adaptive phased array antennas using the least mean squares (LMS) algorithm is shown to be analogous to the implementation of a two-layer perceptron neural network. The adaptive weights may be calculated using the back propagation algorithm, which is a generalized version of LMS. By using a full perceptron model, we introduce additional adaptive weights at the receiver; this is expected to improve performance over existing systems. An optical processor for the control of adaptive antennas is proposed, based on a two-level perceptron. It is shown that currently available technology is capable of realizing this receiver; the optical architecture may also be applied to the demands of future wideband interference suppression systems.

### 3) Two-Dimensional Phased-Array Optics

Phased-Array optics is the optical analog of phased-array radar. The objective of this research is the concept design of optical systems that permit optical beam forming and scanning in two dimensions that are electronically tuneable, and avoid mechanical rotation and translation mechanisms. While devices have been developed that yield one dimensional scanning, no extant technique can provide two-dimensional beam-steering and shaping that is a monolithic structure and can be integrated with other technology. This investigation has led to conceptual designs that utilize waveguide optics and artificial prisms that can be stacked in multiple layers. These designs use electro-optic organic materials and embedded electrodes to form the elements of the arrays. Combining element scanning, array scanning, and nonuniform spacing of elements yield devices with increased resolution and reduced side-lobes.

### 4) Hybrid Optical/Electronic Nonlinear Optical Devices

Nonlinear optics has been pursued as a method of generating bistable and hysteresis for light signals. Current research and development has concentrated on the use of nonlinear optical materials or nonlinear optical structures to achieve this result. These approaches suffer drawbacks in the limitations imposed by the inherent properties of nonlinear materials and nonlinear optical structures. In contrast, hybrid devices in which nonlinear electronics with feedback control of linear optical modulators can presently permit the development of nonlinear optics without the drawbacks of the other techniques. Because the nonlinearity is contained entirely in the feedback electronics, the nonlinearity is electronically and optically tuneable. Hybrid optical/electronic nonlinear optical devices are only limited in sensitivity to the detectors used to sample the optical signals, and can be manufactured with conventional semiconductor electronics. The

objectives of the research into this area were device architectures, applications, fabrication methods, and proof-of-concept.

#### **5) High Resolution Image Recovery from Image Plane Arrays Using Convex Projection**

The purpose of this research topic is the study of reconstructing remotely obtained images from image-plane detector arrays with large blur spots of the optics, reduce data, and noise affecting the reconstruction. While the individual detectors may be larger than the blur spot of the imaging optics, high-resolution reconstructions can be obtained by scanning or rotating the image with respect to the detector. As an alternative to matrix inversion or least-squares estimation, the method of convex projections is proposed. The research shows that readily obtained prior knowledge can be used to obtain good quality imagery with reduced data.

### **1.2 REPORT ORGANIZATION**

Because of the diverse nature of the research pursued, the technical discussion is divided into each of the five areas presented above. Each area has an independent and self-contained chapter with the authors of the chapter identified under the title. A given chapter contains its own concluding discussion, acknowledgement, and reference sections. There are two appendices. Appendix A relates to Chapter 6, and Appendix B is a list of papers and presentations derived from this research contract.

## *Chapter II*

# **Spread Spectrum Techniques in Optical Communication Using Transform Domain Processing**

*Casimer DeCusatis and Pankaj Das*

### **2.1 INTRODUCTION**

Spread spectrum communication consists of transmitting a given signal by modulating the information with a large bandwidth, coded waveform such as a PN sequence [1-4]. The transmitted signal occupies a bandwidth much larger than the information bandwidth. Such systems possess a number of special properties which distinguish them from narrowband communication techniques. A primary advantage of such systems is resistance to jamming and interference. A broad spectral signal bandwidth is more difficult to distinguish from ambient noise, which adds to the security of the channel.

Spread spectrum techniques have not been utilized in optical communication systems, despite their increasing popularity and inherently wide bandwidths, due to a lack of effective modulation and coding methods available at optical frequencies. We propose several methods for incorporating spread spectrum techniques into optical communications.

A typical direct sequence spread spectrum communications system is shown in Figure 2.1. An information sequence,  $S(t)$ , is modulated by a PN code sequence,  $c(t)$ . The modulated signal is corrupted in the communications channel by interference,  $I(t)$ , and additive, almost white Gaussian noise,  $n(t)$ . The corrupted signal is recovered by a matched filter containing the code sequence.

The ability of a spread spectrum system to resist jamming is determined by the processing gain, which in turn is given by the ratio of transmission bandwidth to data bandwidth. Large processing gains provide a high degree of jamming immunity. Since processing gain cannot be increased indefinitely, it is desirable

FIGURE 2.1

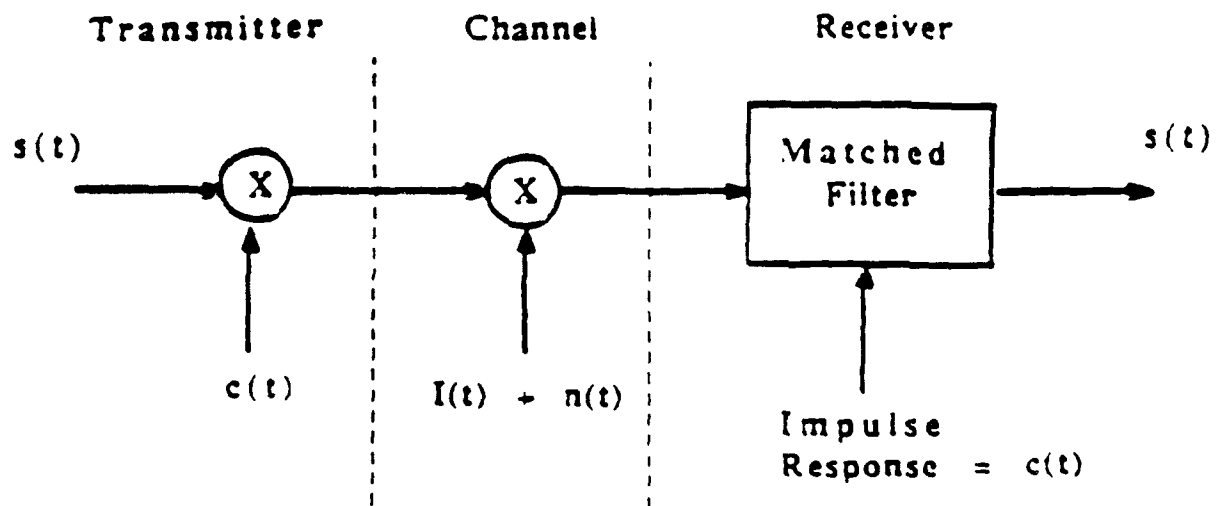


Figure 2.1. Block diagram of a typical direct sequence spread spectrum communications system.



to supplement the jamming resistance. This has led to the use of transform domain processing techniques [4-10].

A transform domain receiver is shown in Figure 2.2. The received signal is  $x(t) = S(t) c(t)$ , plus channel interference and noise. Filtering by the transfer function  $H(\omega)$  is performed by multiplication followed by inverse transformation. This real time frequency domain multiplication has been demonstrated both theoretically and experimentally [1,2]. An alternate receiver implementation replaces the matched filter by multiplication with the complex conjugate of the signal spectra in the transform domain. Taking the inverse Fourier transform produces a result equivalent to Figure 2.2.

Transform domain processing techniques effectively suppress narrow band jammers in a spread spectrum system. The jammer may be removed by the system illustrated in Figure 2.3. Input consists of the code and jammer on an RF carrier; a high power, narrow band jammer appears as an impulse in the transform domain. A gating function removes the portion of the spectrum containing the jammer. The gate output is the PN code; since the code has a large bandwidth, the notch filter has not seriously degraded the signal spectrum. Correlation is performed by multiplication in the transform domain, followed by an inverse Fourier transform.

## 2.2 TRANSFORM DOMAIN PROCESSING in the OPTICAL DOMAIN

Optical signal processing techniques are suited to applications in transform domain processing. We shall consider the Chirp transform, which can be used to implement a real-time Fourier transform.

The Chirp transform is illustrated by Figure 2.4(a). An arbitrary signal  $f(t)$  is multiplied by a down-chirp, then passes through a linear system whose impulse response is an up-chirp. The result is multiplied by a down-chirp; the

FIGURE 2.2

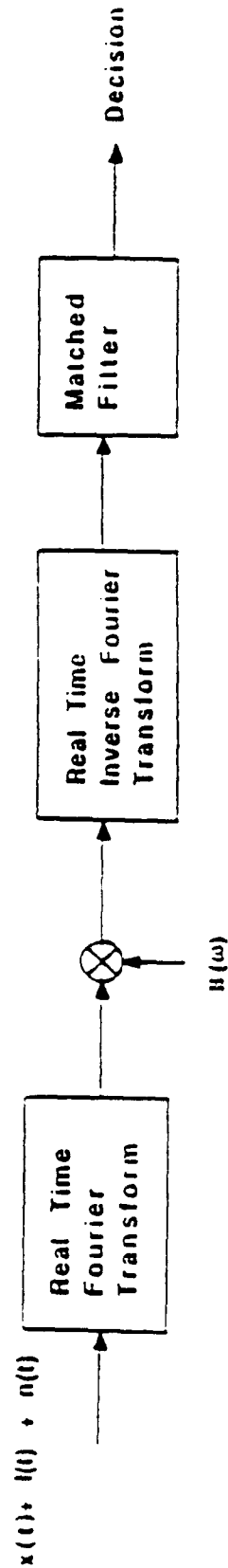


Figure 2.2. General form of a transform domain receiver.  $x(t)$  = signal.  $n(t)$  = noise.  $I(t)$  = interference.  $I(\omega)$  = excision function in the Fourier domain.

FIGURE 2.3

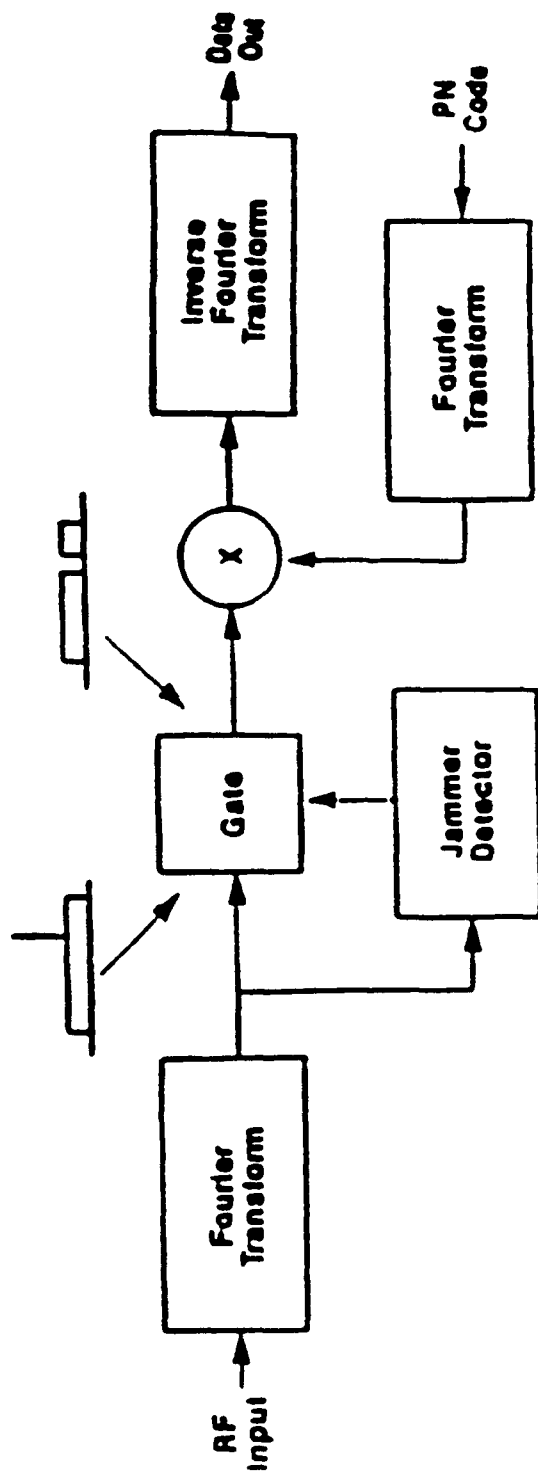


Figure 2.3. System to remove narrowband jammer in the transform domain.

output is the Fourier transform of the input. This is also known as the multiply-convolve-multiply (MCM) algorithm; the system of Figure 2.4(b) performs the same operation by a dual process called the convolve-multiply-convolve (CMC) algorithm. In both cases, the same result holds if the impulse responses are down-chirps and we multiply by the up-chirps. If the input is  $F(w)$ , the algorithms invert the Fourier transform to yield  $f(-t)$ .

Either algorithm can be used in optics to perform spatial Fourier transforms of optical signals. The MCM algorithm may also be applied to optical pulse compression systems. This process can be realized in the time domain, which forms the basis for the use of spread spectrum systems at optical frequencies.

### 2.3 OPTICAL PULSE COMPRESSION and SPECTRAL MODULATION

The basic configuration for optical pulse compression and shaping is shown in Figure 2.5, after the treatment of references [11] and [12]. Note that Figure 2.5 is an optical implementation of Figure 2.4(a), where  $f(t)$  is the pulse to be compressed. This pulse compression is achieved by inducing a chirp, or linear frequency sweep, on an optical pulse and subsequently rephasing the chirped frequency components. Although there are several means of obtaining chirped optical pulses, a single mode optical fiber induces uniform frequency modulation across the entire pulse profile. The frequency chirp is generated by self-phase modulation, which arises from the interaction of the propagating light and the intensity dependent portion of the fiber's refractive index [13]. It is then necessary to re-phase the spectral components to compress the pulse in time. The system in Figure 2.5 uses a diffraction grating pair as a dispersive delay line [14]. This system can be modified to encode an optical pulse in the frequency domain.

FIGURE 2.4

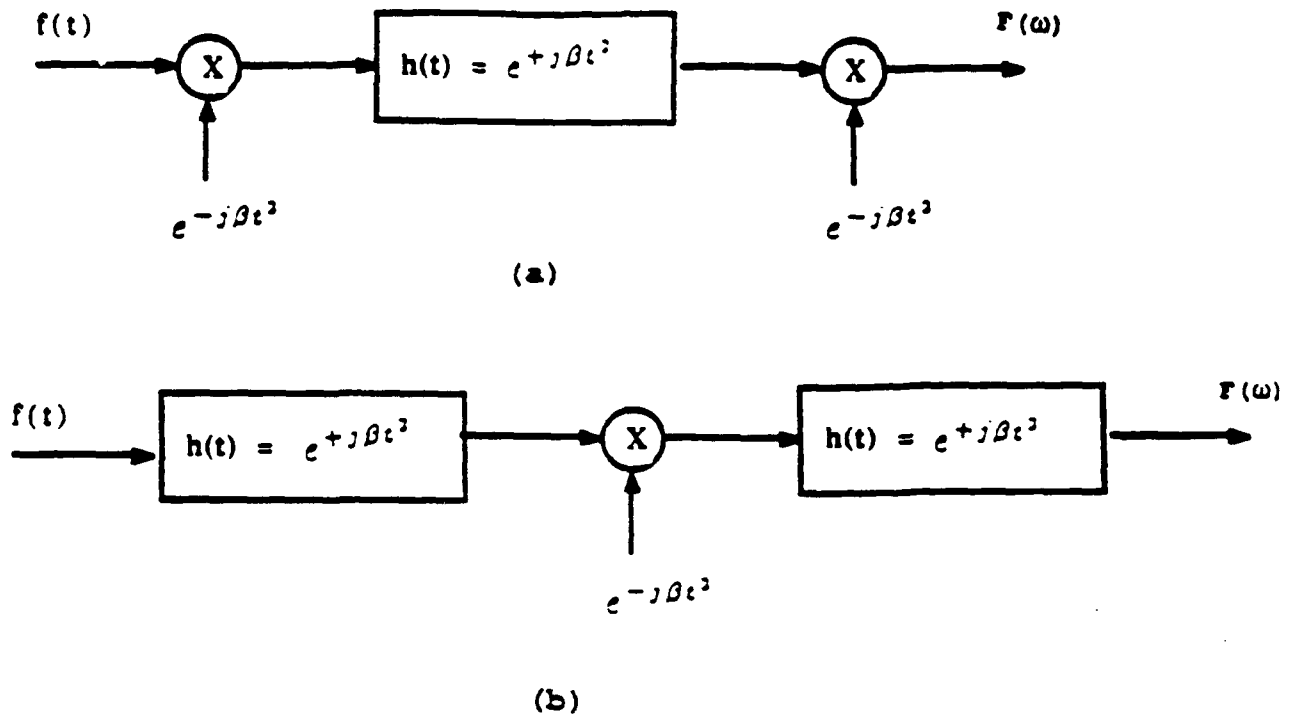


Figure 2.4. Block diagram of a chirp transform system. (a) MCM algorithm. (b) CMC algorithm.

FIGURE 2.5

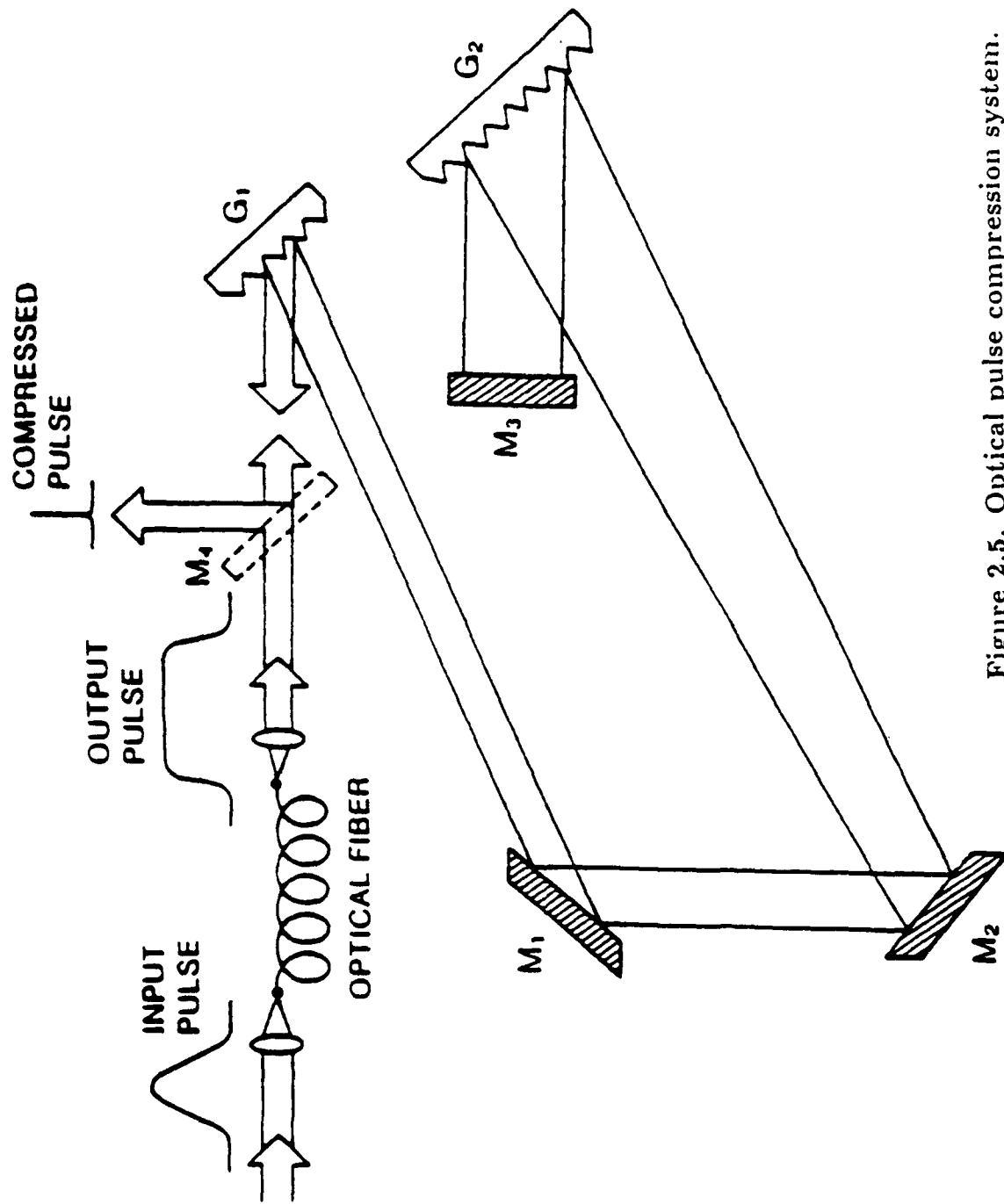


Figure 2.5. Optical pulse compression system.

A chirped optical pulse can be produced by the nonlinear process of self-phase modulation (SPM). The fiber's refractive index is given by:

$$n(t) = n_0 + n_2 I(t) \quad (2.1)$$

where  $I(t)$  is the intensity profile of the light, and  $n_2$  is a positive material constant [13]. The propagation constant is given by:

$$k = \frac{\omega}{c} n(t) = \frac{\omega n_0}{c} + A I(t) \quad (2.2)$$

where  $c$  is the speed of light and the constant  $A$  represents a collection of terms. The phase of the optical pulse becomes:

$$\theta = \omega_0 t - \frac{\omega n_0 z}{c} - A I(t) \quad (2.3)$$

where  $z$  is the propagation distance. The instantaneous frequency is thus proportional to the negative time derivative of the intensity profile,

$$\omega_i = \frac{d\theta}{dt} = \omega_0 - A \frac{d}{dt}[I(t)] \quad (2.4)$$

and the properties of the resulting chirp depend on the time-varying intensity.

However, the chirp produced by SPM alone is not linear over the full intensity profile. The linearity of the chirp can be improved by the effect of positive group velocity dispersion (GVD) in the fiber. This effect is calculated by expanding the propagation constant,  $k(\omega)$ , about the center frequency  $\omega_0$ ; the relevant term is:

$$\beta = \left( \frac{\partial^2 k}{\partial \omega^2} \right) \ell = k_2 \ell \quad (2.5)$$

where  $\ell$  is the length of the fiber. The combined effect of SPM and GVD is called dispersive self-phase modulation (DSPM); it produces an approximate square, linearly up-chirped pulse from a single frequency input of nonuniform intensity.

As mentioned before, the system of Figure 2.5 implements the following relation:

$$(f(t)e^{+j\beta t^2}) * e^{-j\beta t^2} = F(\omega)e^{-j\beta t^2} \quad (2.6)$$

where  $F(\omega)$  is its Fourier transform of  $f(t)$ ,  $\omega = 2\pi f$  is the angular frequency, and  $\beta$  is a chirping factor to be determined.

The chirp parameter for a grating pair is given by [14]:

$$\beta = \pi(\Delta f)^2 d / bT \quad (2.7)$$

where  $d$  is the grating constant  $\equiv 1/\text{number of lines per mm}$ ,  $b$  is the grating separation, and  $T$  is a constant determined by the angle of incidence. Thus, the system of Figure 2.5 realizes equation (2.6); the analogous functions for each component are shown in Figure 2.6.

The time-bandwidth product of a grating pair delay line may also be expressed in terms of the grating's physical properties as:

$$(\Delta\tau)(\Delta f) = \frac{mbT}{d} \left(\frac{\Delta f}{f}\right)^2 \quad (2.8)$$

where  $m$  is the diffracted order. Note that the time-bandwidth product may be increased by using higher diffracted orders; this could be realized with blazed diffraction gratings, designed to diffract most of the optical power into higher orders. After one pass through the grating pair the optical signal,  $g_1(t)$ , is given by:

$$g_1(t) = F(\beta t / \pi) e^{-j\beta t^2} \quad (2.9)$$

The first pass through the gratings has taken the Fourier transform of the original input signal, because the grating pair input had the opposite chirp as the impulse response,  $h(t)$ , of the grating pair. The signal of equation (2.6) now possesses a chirp of the same sign as  $h(t)$ ; if this signal reflects from the mirror and traverses the grating pair a second time, no further Fourier transformation can occur.



FIGURE 2.6

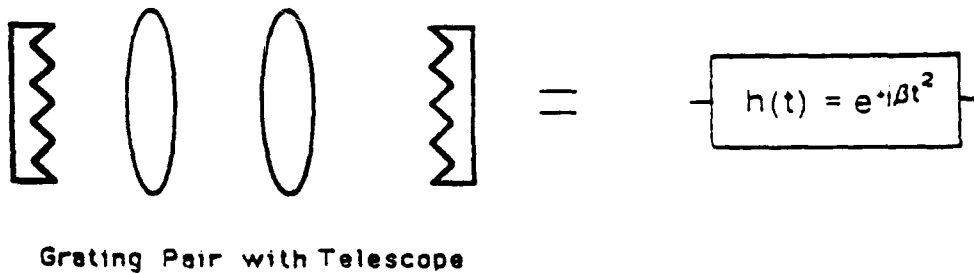
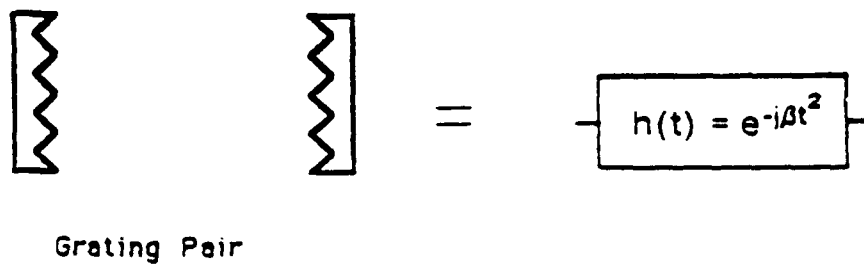
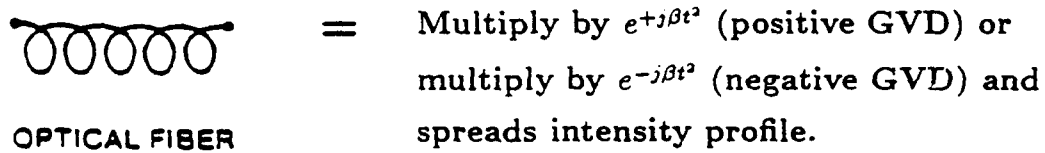
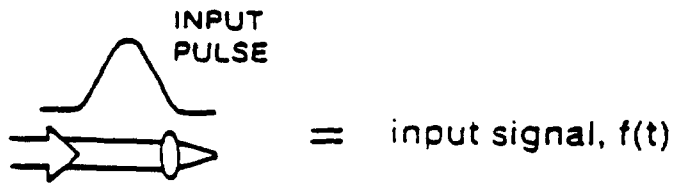


Figure 2.6. Block diagram of analogous pulse compression.

This second pass through the gratings doubles the chirp factor; the final output of the system,  $g_2(t)$ , is:

$$g_2(t) = F(\beta t/\pi) e^{-j2\beta t^2} \quad (2.10)$$

The system has performed pulse compression as an MCM system. After one pass through the gratings, the Fourier spectra of the signal is spatially separated in a plane. By placing some form of transmission mask in this plane, it is possible to modulate the frequency components of the optical signal. If a transmission mask function  $M(f)$  is placed in this plane as indicated by Figure 2.7, then the final output will be:

$$g_2(t) = F(\beta t/\pi) M(\beta t/\pi) e^{-j2\beta t^2} \quad (2.11)$$

Heritage et. al. [15] have experimented with simple two-dimensional amplitude and phase masks, as well as spectral windows to eliminate nonlinear behavior at the edges of the pulse [16]. We propose to use this principle to achieve spread spectrum coding of the optical signals.

Note that in place of a grating pair, a fiber optic delay line with negative GVD could be used if only pulse compression was desired. However, the grating pair is more suitable for our purposes, as it provides a means to modify the spectral components.

In the preceding discussion, we noted that the impulse response of a grating pair is given by a downchirp, which compresses the output of a fiber with positive GVD. However, GVD in an optical fiber is positive only for wavelengths below  $1.3 \mu\text{m}$  [13]; the region of lowest loss is  $1.3\text{-}1.6 \mu\text{m}$ , which is also a region of negative GVD. In order to utilize our system in this region, the grating pair impulse response must be an upchirp. This may be realized by using a telescope between the gratings, as first derived by Martinez et. al. [17]. The concept is illustrated in Figure 2.8; two lenses of focal length  $f_1$  and  $f_2$  are placed between

FIGURE 2.7

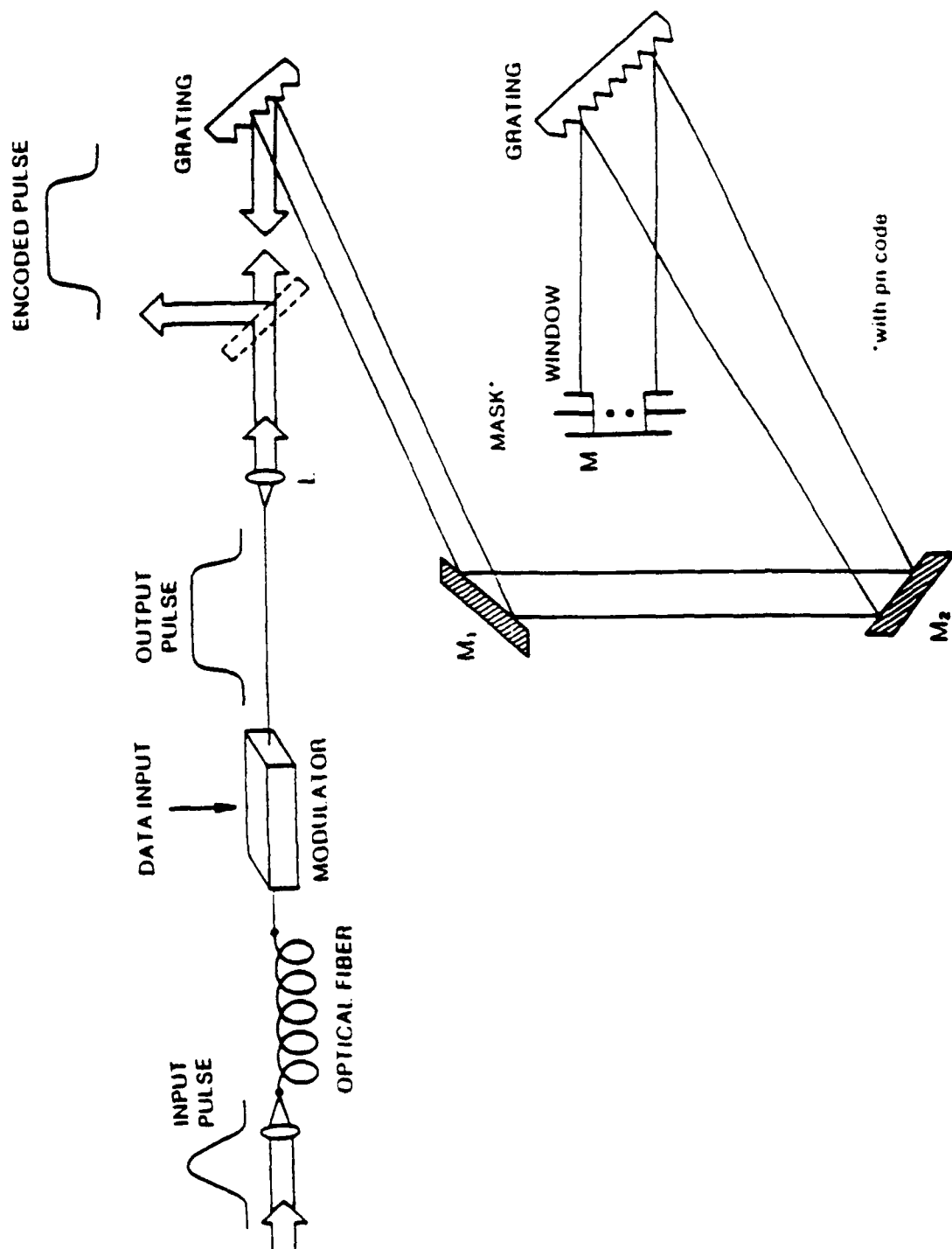


Figure 2.7. Transform domain spread spectrum optical encoder.

FIGURE 2.8

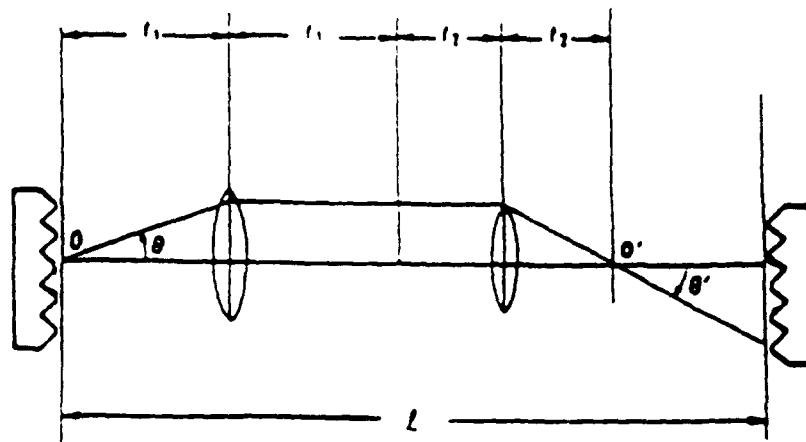


Figure 2.8. Grating pair delay line with up-chirp impulse response.

a grating pair separated by a distance  $\ell$ . The lenses are assumed to induce no aberrations, so that the optical path between their focal planes does not depend on the angle  $\theta$ . In other words, the telescope only magnifies the angular dispersion of the grating pair. To obtain the effective dispersion length (i.e., grating spacing) the distance between  $0$  and  $0'$  must be subtracted from  $\ell$ ; accounting for angular magnification, the effective grating spacing becomes:

$$b_{eff} = [\ell - 2(f_1 + f_2)](f_1/f_2)^2 \quad (2.12)$$

Note that  $b_{eff}$  may not take on negative values, reversing the sign of the chirp given by equation (2.7). This allows our system to accommodate optical signals in the realm of negative fiber GVD. The value of  $b_{eff}$  may also be increased by the angular magnification of the telescope optics. This increases the time-bandwidth product of the system, as given by equation (2.8). A pulse compression system using this design has been implemented experimentally by Martinez [18] using standard off the shelf laser optics. A theoretical analysis including limitations of the telescope pupils and lateral spectral walkoff was also developed. Maine and Strickland et. al. [19] have demonstrated compression schemes using grating pairs with both positive and negative GVD.

The grating pair delay lines may be replaced by a pair of refractive prisms, as illustrated in Figure 2.9. It has been shown [17] that the angular dispersion of a prism delay line realizes a chirp impulse response equivalent to a grating pair; prism systems have been successfully demonstrated in optical pulse compressors [20].

## 2.4 SPREAD SPECTRUM TECHNIQUES in OPTICAL COMMUNICATION

There are many possible designs for an optical spread spectrum communication system based on the pulse compression architecture described previously. Figure 2.7 illustrates how the chirped light may be modulated with binary data:

FIGURE 2.9

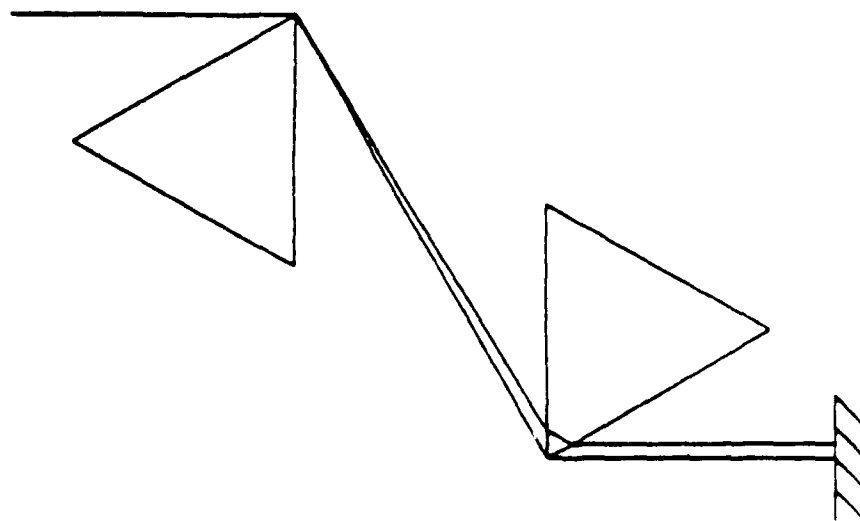


Figure 2.9. Prism pair delay line with down-chirp impulse response.

an optical signal with positive GVD is assumed, although negative GVD may also be realized as discussed earlier. The appropriate pn code must now be impressed upon this data. One implementation involves placing a transmission-type mask between the grating pair and the feedback mirror, as shown in Figure 2.7. Since the frequency components are spatially distributed in this plane, it is possible to perform both amplitude and phase modulation on the optical signal. The optical signal passes through the transmission mask twice; the second pass can only be neglected if a binary amplitude mask is used (consisting of either opaque or transparent pixels). If more complicated masks are required, then the square root of the desired amplitude function must be implemented on the mask. Any types of phase coding must account for the double phase delay incurred by a second pass through the mask. The optical signal at the encoding plane is the Fourier transform of the input pulse; thus, the encoding mask must be the Fourier transform of the desired code. The output of the system is then given by equation (2.14).

The encoded optical pulse is transmitted along a fiber optical link. We assume that any further chirping due to this transmission may be accounted for. An optical receiver and decoding scheme for this signal is shown in Figure 2.10. The optical signal is passed through a grating pair, which spatially separates the frequency components without affecting the encoded signal. The grating pair is now separated by twice the distance provided at the encoder, to account for the double chirp rate. This spatially dispersed signal is then passed through the complex conjugate of the encoding mask,  $M^*(f)$ . Multiplication in the transform domain is equivalent to correlation in the time domain. If the decoding mask matches the signal modulation, a correlation peak will be observed. Otherwise, the output will resemble random noise, since the cross-correlation of two different codes is near zero. The optical signal passes through another grating

FIGURE 2.10

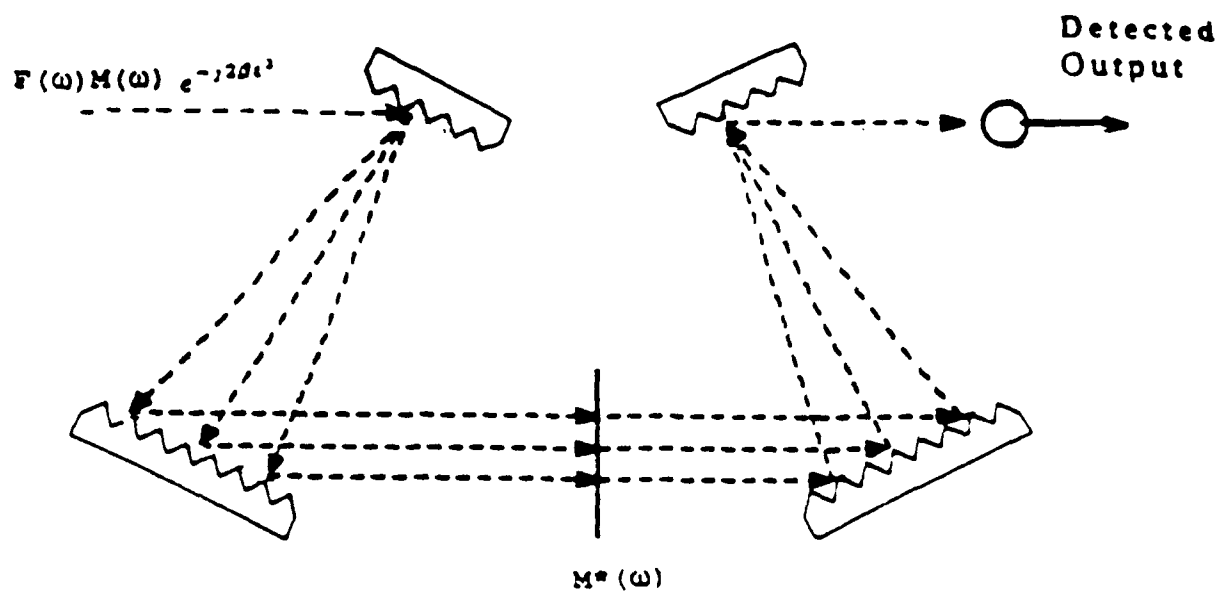


Figure 2.10. Receiver for optical frequency coding system.



pair to compress the spectra before detection. The correlation receiver design is greatly simplified in the transform domain. Spread spectrum coding techniques at optical frequencies can be implemented in this way.

An alternative approach eliminates the second pass through the grating pair at both the transmitter and receiver. This second pass serves to recompress the optical spectra spatially prior to transmission, and also doubles the chirp rate. In the system of Figure 2.11, a lens is placed between the transmission mask to spatially recombine the spectra. The transmitted signal retains its original chirp rate, so that the grating spacing at both the transmitter and receiver may be the same. The receiver design is similar to Figure 2.10; a grating pair spatially disperses the optical pulse, which passes through a decoding mask. A lens replaces the second grating pair to compress the spatially distributed pulse for optical detection. This system would require a nearly "ideal" lens at both the transmitter and receiver - a lens possessing a large field of view and practically no chromatic dispersion. Compound lenses of this type are available, although they are much more expensive than high quality diffraction gratings.

If optical signals in the realm of negative GVD are used, a telescope is inserted between the transmitter grating pair as discussed earlier. This system implements the dual form of equation (2.6), namely

$$(f(t)e^{-j\beta t^2}) * e^{j\beta t^2} = F(\omega)e^{j\beta t^2} \quad (2.13)$$

and the transmitter output will be of the form of equation (2.11), with an up-chirp. A transform domain receiver similar to those described earlier may be used for this signal.

These systems transmit coded optical pulses in the transform domain, and decode them in the same manner. For some applications, we may transmit the temporal form of the coded pulses. For example, Bar-David and Salz [21] have

FIGURE 2.11

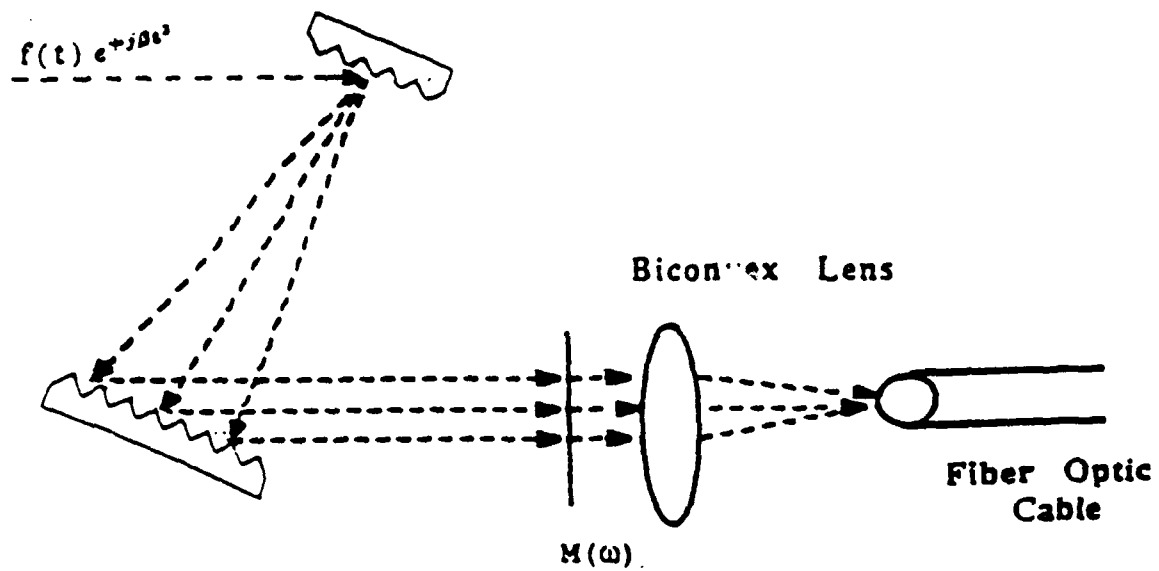


Figure 2.11. Optical coding system using a lens.

described a balanced dual heterodyne detection scheme for phase modulated signals in the time domain; phase noise is reduced at the expense of amplitude noise, which is more easily controlled. A time domain transmitter must perform an inverse Fourier transform of the encoded signal; this may be done using two grating pairs whose impulse responses are chirps of opposite sign.

A time domain transmitter is illustrated in Figure 2.12, assuming an optical signal with positive GVD. After passing through the encoding mask, the signal is passed through a second grating pair whose impulse response is the upchirp; this inverts the Fourier transform of the coded signal. The system output is given by:

$$f(t) m(t) e^{-j\beta t^2}. \quad (2.14)$$

If the original optical signal is in the realm of negative GVD, the telescope system must be placed inside the first grating pair rather than the second. The system output would be the same as given by equation (2.14) with the sign of the chirp reversed. In this manner, grating pairs with suitable impulse responses may be used to easily convert between the time and frequency domains.

The received signal is passed through a grating pair whose impulse response is a down-chirp; this takes the Fourier transform of the received signal. An appropriate decoding mask is used as before in the transform domain, and the decoded signal may be spatially compressed (using either a lens or another grating pair) for detection. A receiver for negative GVD signals uses the same design, with a telescope system between the receiver grating pair. In other words, the receiver impulse response must now become an upchirp in order to Fourier transform the received signal. There are other possible designs for time domain transmitters and receivers which do not require the upchirp grating pair, although they are generally more complicated [22].

FIGURE 2.12

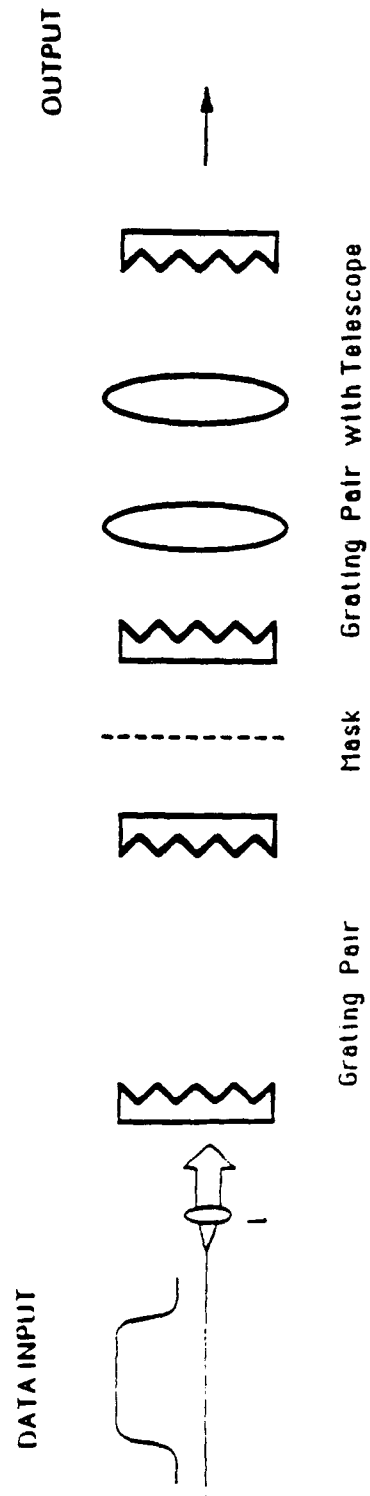


Figure 2.12. Time domain spread spectrum transmitter.

There exists another method for generating optical pulses of arbitrary shape which is different from the preceding systems [23], illustrated in Figure 2.13. The pulse shape is controlled by a programmable electro-optic modulator at the system input. The optical pulse is modulated and amplified prior to passing through the spectral rephasing process; a translating mirror is used to control the phase of the signal. Modulating the pulse before it enters the pulse compression stage controls the resulting pulse shape and spectral content [23]. The analysis of this system is similar to our earlier discussion; this method represents an alternative way to achieve coding of the optical pulses. The electro-optic modulator must be clocked at a rate equal to the fiber optic cable's data rate may approach several gigabits/second, the processing speed would be limited by the electro-optic modulator (a few hundred megabits/second). This is a disadvantage compared to systems which achieve real-time encoding using transform domain techniques.

## 2.5 APPLICATIONS

There are many applications for transform domain processing in the optical regime. One possibility is a fiber optic communication system using spread spectrum techniques. Fiber optics represents a secure method of communication because of its resistance to electromagnetic interference. The high bandwidth of an optical fiber system may be fully exploited to provide maximum security by employing optical encoding techniques. The concept of a free space laser communication system has been proposed; laser signals suffer from degradation caused by pulse spreading or scattering in the atmosphere. In order to transmit information reliably under these conditions, some form of coding is highly desirable.

Another application is laser radar systems. A fundamental problem in conventional radar systems is the decrease in returning signal amplitude with range. Although the problem can be overcome by the use of larger antenna and higher

FIGURE 2.13

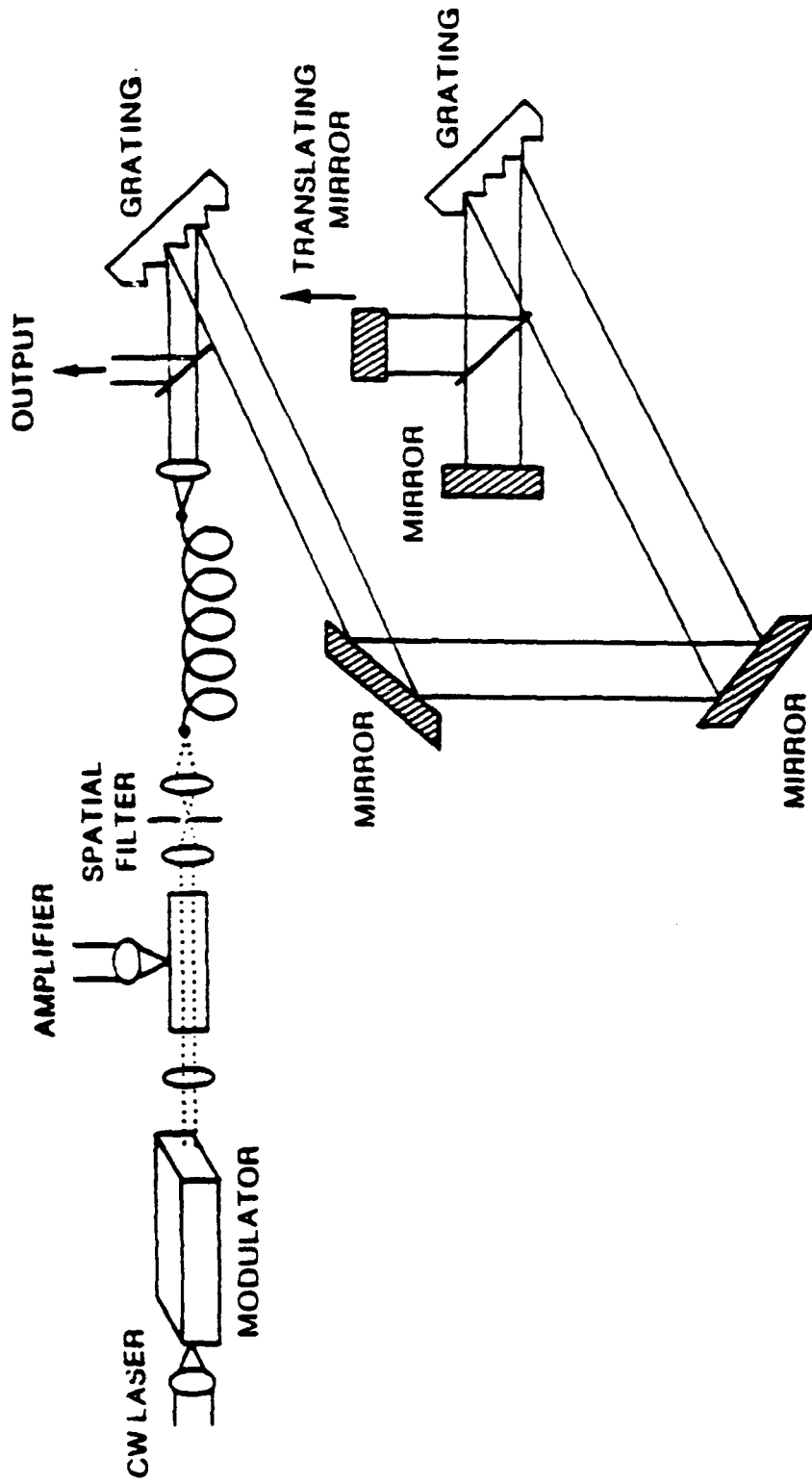


Figure 2.13. Optical coding and pulse shaping system using electro-optic modulator input.

transmission power levels, there are practical limits to this approach [13]. Pulse compression techniques combined with spectral weighting has been used in microwave radar systems to overcome this problem. By transmitting a chirped pulse, it is possible to use compression techniques to concentrate the energy of the returning echo into a detectable signal. Similar techniques would be effective in laser radar systems, provided the optical pulse spectra is encoded.

A closely related problem is satellite laser range finding (SLR), which involves high accuracy measurements of the range between a ground station and an orbiting satellite. Such measurements not only provide accurate position location, but also supply data on areas such as tectonic plate motion and variations in Earth's rotation rate. A global network of both fixed and mobile SLR ground stations is currently in use, most notably NASA's Laser Geodynamics Satellite [24]. A technique using pseudonoise coded laser pulses to improve the accuracy of SLR has recently been proposed [24], and it has been shown that a maximum-likelihood receiver for estimating target range is a correlation receiver. A theoretical analysis, including noise effects for rough and smooth targets, indicates that a 1023 bit pn code yields range accuracies on the order of 1 cm [24]; this represents another application for our system, since improved accuracy should result from using longer pn codes.

The coding of optical pulses also has applications in fiber optic code division multiple access systems [25]. The scheme uses the excess bandwidth of fiber optics to map low information rate electrical or optical signals into high data rate optical pulse sequences. Single-mode fibers are well suited to this application. The sequences can be used to achieve random, asynchronous access to a communication system, free of network control among many users. Each user of a multiple-access system is provided a unique code, whose cross-correlation with other system codes is nearly zero. A set of Optical Orthogonal Codes has

been developed for this purpose [25]. A coding system which operates at optical frequencies is essential to such a system.

Because optical transform domain processing is suited to optical transmission over long distances, it possesses several applications to outer space systems. The Strategic Defense Initiative Organization has expressed a need for the transmission of high intensity, short duration laser pulses. This problem is analogous to a long-range radar system; a similar solution involves generating lower intensity laser pulses encoded with a frequency chirp. Such pulses could be directed to a target by reflection from a pulse compression system, producing laser pulses of shorter duration and higher intensity. Optical transform domain encoding would be necessary to reduce the sidelobes of the compressed pulse. Smaller scale pulse compression systems have provided compression factors of 3000 or more [18]. Systems of this type would be effective if ground based lasers were used to supply orbital satellites equipped with large mirrors and diffraction grating compressors. The problems of high energy beam propagation through the atmosphere could be minimized by the use of optical transform domain coding. gigawatt optical pulses of a few hundred microseconds duration.

Another space application involves a proposal by NASA to develop a laser powered single stage-to-orbit space vehicle by the twenty-first century [26,27]. This vehicle, the Apollo Lightcraft, would receive its power from a remote laser source and requires gigawatt optical pulses of a few hundred microseconds duration. To realize efficient transmission of the optical power beam, transform domain encoding could be used.

We may implement the optical coding system in a compact format for telecommunications or optical computing applications. The entire system could be realized in an integrated optics configuration as illustrated in Figure 2.14. A



surface waveguide could generate the same type of frequency chirps as an optical fiber; the same amount of chirping might be achieved by a short segment of properly doped surface waveguide. The use of surface waveguides is pulse compression has already been investigated [18]. The waveguide can also be designed as the delay line media between the two diffraction gratings. Gratings could be realized using acousto-optic or electro-optic methods. Both effects can exist simultaneously in a piezoelectric crystal resulting in an acousto-electro-optic diffraction grating, which has advantages over applying either effect separately [29]. Since all of these methods modulate the diffracted light, they could be used to generate masks for transform domain encoding. Electro-optic modulators have been used [23] to modulate optical signals before performing pulse compression, and the design of prism delay lines for semiconductor lasers has been proposed [17]. As the technology of optical pulse shaping continues to develop, the use of integrated optics will become increasingly important.

## 2.6 CONCLUSIONS

We have described a system for implementing spread spectrum communication techniques at optical frequencies. The frequency encoding is achieved by a modified optical pulse compression system using transform domain processing techniques. This system is available to exploit the high bandwidth of optical communication systems; different optical implementations may be realized. Applications include improved fiber optic code division multiple access, free space optical communications systems, laser radar, integrated optical systems, and space applications such as NASA's Apollo Lightcraft project.

FIGURE 2.14

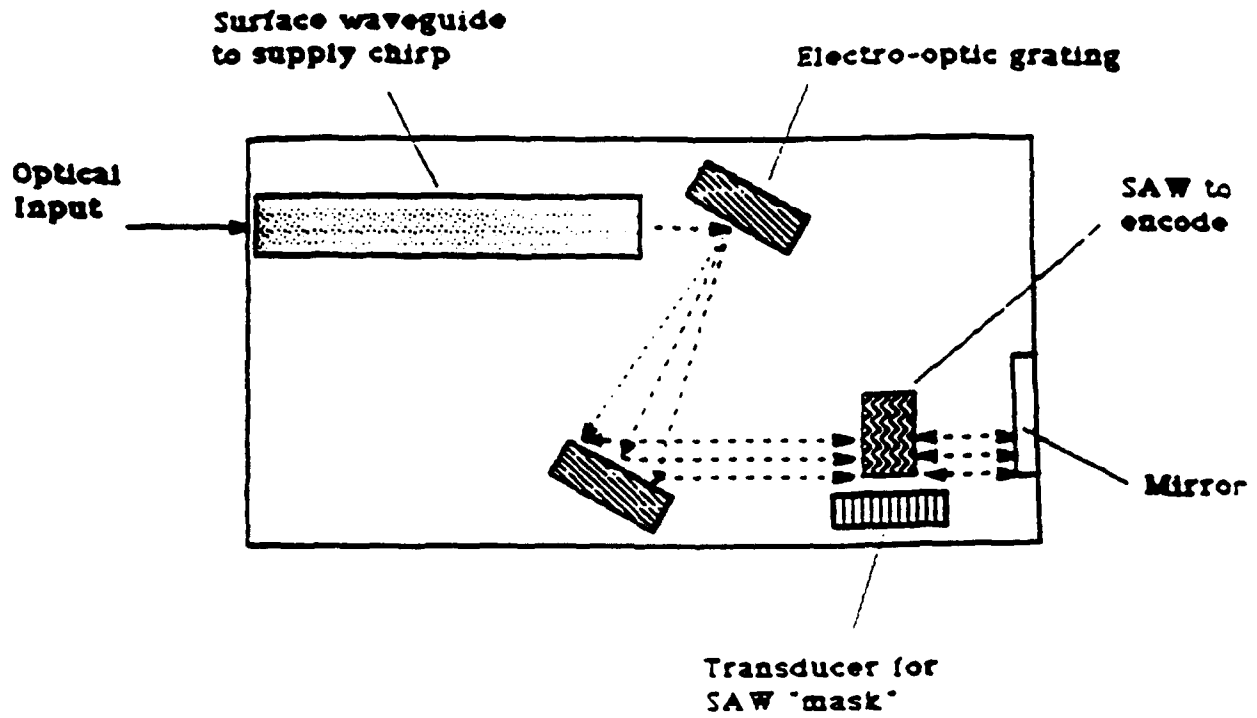


Figure 2.14. Conceptual design of an integrated optics device for transform domain coding.

## **2.7 ACKNOWLEDGEMENTS**

It is a pleasure to thank Col. Dan Litynski of the United States Military Academy, West Point, Mr. Brian Hendrickson of RADC and Dr. L. B. Milstein of UCSD for valuable technical discussions regarding this work.

## Chapter II - REFERENCES

- [1] Holmes, *Coherent Spread Spectrum Systems*, New York, NY: John Wiley and Sons, Inc., 1982.
- [2] P. Das, *Optical Signal Processing*, Springer-Verlag, to be published.
- [3] L. B. Milstein and P. Das, *IEEE Trans. Commun.*, vol. COM-28, no. 6, pp. 816-824, 1980.
- [4] L. B. Milstein, P. Das and J. Gevargiz, *MILCOM '82*, pp. 21.2.1-21.2.4.
- [5] D. Shklarsky, P. Das and L. B. Milstein, *National Telecommunications Conference*, November 1979, pp. 15.2.1-15.2.4.
- [6] M. Rosenmann, J. Gevargiz, P. Das and L. B. Milstein, *MILCOM '83*, pp. 636-640.
- [7] John Gevargiz, P. Das, L. B. Milstein, John Moran and Oscar McKee, *Proc. MILCOM '86*, IEEE Pub. No. CH2323-4/86, pp. 20.1.1-20.1.5, 1986.
- [8] T. W. Bristol, *Case Studies in Advanced Signal Processing*, Sept. 1979, pp. 226-231.
- [9] J. H. Collins and P. M. Grant, *IEEE Trans. Sonics and Ultrasonics*, vol. SU-28, May, pp. 117-125, 1981.
- [10] J. Gevargiz, M. Rosenmann, P. Das and L. B. Milstein, *MILCOM '84*, pp. 32.3.1-32.3.4.
- [11] D. Grischkowsky and A. C. Balant, *App. Phys. Lett.*, vol. 41, pp. 1-3, 1982.
- [12] A. M. Johnson, R. H. Stolen, and W. M. Simpson, *App. Phys. Lett.*, vol. 44, pp. 729-731, 1984.
- [13] H. A. Haus, *Waves and Fields in Optoelectronics*, Englewood Cliffs, N. J.: Prentice-Hall, 1984.
- [14] E. B. Treacy, *Phys. Lett.*, vol. 28A, no. 1, pp. 34-35, 1968.
- [15] J. P. Heritage, R. N. Thurston, W. J. Tomlinson, A. M. Weiner, and R. H. Stolen, *App. Phys. Lett.*, vol. 47, pp. 87-89, 1985.
- [16] J. P. Heritage, A. M. Weiner, and R. N. Thurston, *Opt. Lett.*, vol. 10, pp. 609-611, 1985.
- [17] O. E. Martinez, J. P. Gordon, and R. L. Fork, *Journ. Opt. Soc. Am. A*, vol. 1, no. 10, pp. 1003-1006, 1984.
- [18] O. E. Martinez, *IEEE Journ. Quant. Elec.*, vol QE-23, pp. 59-64, 1987.
- [19] P. Maine, D. Strickland, P. Bado, M. Pessot and G. Mourou, *IEEE Journ. Quant. Elec.*, vol QE-24, pp. 401-403, 1987.
- [20] J. D. Kafka and T. Baer, *Opt. Lett.*, vol. 12, pp. 401-403, 1987.
- [21] I. Bar-David and J. Saly, *IEEE Trans. on Commun.*, vol. COM-36, pp. 1309-1315, 1988.
- [22] P. Das, C. DeCusatis and D. M. Litynski, *MILCOM '88*, pp. 203-213.

- [23] M. Haner and W. S. Warren, *Opt. Lett.*, vol. 12, pp. 398-400, 1987.
- [24] D. M. Norman and C. S. Gardner, *Opt. Opt.*, vol. 27, pp. 3650-3655, 1988.
- [25] J. A. Salehi and C. A. Brackett, *Proc. IEEE International Conference on Communications '87*, vol. 3, pp. 1601-1609, 1987.
- [26] L. N. Myrabo et.al., *Apollo Lightcraft Project Annual Report*, NASA/USRA Advanced Design Program 4th annual summer conference, Kennedy Space Flight Center, Florida, June 1988.
- [27] D. H. Douglas-Hamilton, A. R. Kantrowitz, D. A. Reily, "Laser assisted propulsion research" in *Radiation Energy Conversion in Space*, ed. by K. W. Billman, Washington, D. C.: AIAA, 1978, pp. 271-278.
- [28] N. Okamoto and S. Ito, *IEEE Journ. Quant. Elec.*, vol QE-24, pp. 1966-1969, 1988.
- [29] P. Das et.al., *App. Phys. Lett.*, vol. 49, no. 16, pp. 1016-1018, 1986.

*Chapter III*  
**Optical Controller for Adaptive Phased Array Antennas  
Using Neural Network Architecture**

*Casimer M. DeCusatis and Pankaj K. Das*

### **3.1 INTRODUCTION**

Adaptive phased array antennas have received considerable attention as a means for the detection of a broadband signal in the presence of multiple interference sources and additive white Gaussian noise [1,2]. If the signal and noise statistics were completely known, an optimal receiver such as the Wiener filter could be implemented. When insufficient a priori information is available, an adaptive processor is required to estimate the required signal and noise characteristics. In order to null an antenna pattern in the directions of narrowband jammers, the antenna outputs are multiplied by complex-valued weights which are computed adaptively. A block diagram of a typical broadband adaptive antenna steering system is shown in Figure 3.1, consisting of  $M$  antenna elements, each with an  $N$ -tap delay line. We assume that the antenna elements are equally spaced.

The iterative calculation of these weights is the underlying problem for an adaptive phased array receiver, and various algorithms have been suggested for calculating the optimal weights. The simplest of these algorithms is the gradient steepest descent (GSD) procedure, in which the receiver perturbs each weight by a small amount and calculates the gradient of the output with respect to the perturbation [1]. Although this procedure is very robust and simple to implement, its performance is generally inadequate for most practical broadband nulling applications. A more useful approach involves iterative adjustment of the weights to minimize the mean squared error at the system output. This least mean squares (LMS) algorithm provides improved performance over GSD, and

FIGURE 3.1

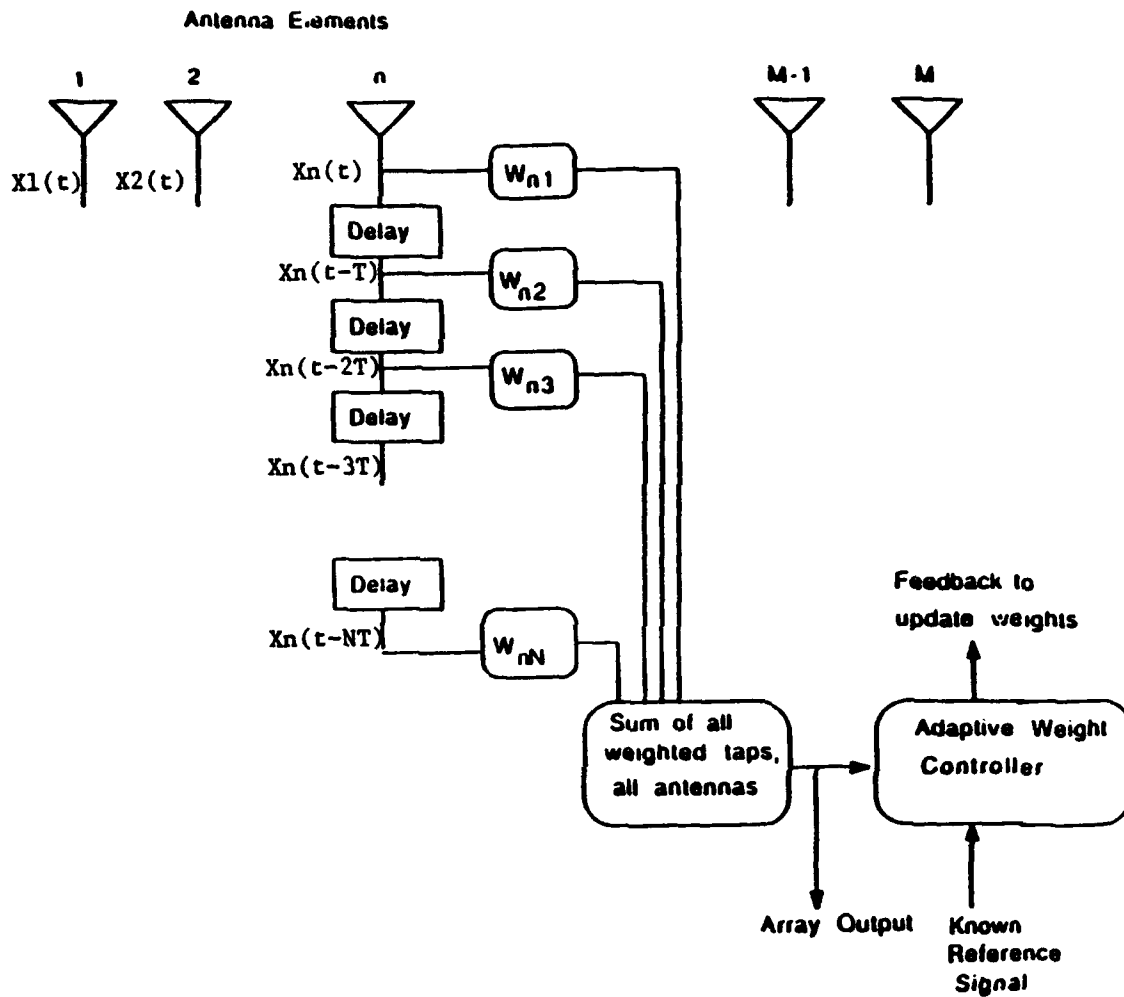


Figure 3.1. Block diagram of a general adaptive array processor

has been widely implemented in practical adaptive antenna systems [1,2]. The block diagram of Figure 3.1 could be used to implement the LMS algorithm; the received signal at each antenna element is given by:

$$x(t) = s(t) + I(t) + n(t) \quad (3.1)$$

where  $s(t)$  is the desired signal,  $I(t)$  is the interference, and  $n(t)$  is additive white Gaussian noise. In general, both the received signal and the weights will be complex values. Delayed versions of the signal are multiplied by the antenna weights, then summed to yield an estimate of the signal:

$$\hat{s}(t) = \sum_M \sum_N w_{mn} x_m(t - nT) \quad (3.2)$$

where the variable  $t$  represents discrete time. The processor forms an error signal which represents the difference between this estimate and a reference signal,  $r(t)$ , which is an approximation of the desired array output,

$$e(t) = \hat{s}(t) - r(t) \quad (3.3)$$

The weights are then updated by the algorithm:

$$w_{mn}(t) = w_{mn}(t-1) + \eta e(t) x_m(t - nT) \quad (3.4)$$

where the constant  $\eta$  represents a fixed gain factor, chosen to insure convergence of the procedure; it is also known as an "acceleration parameter" because it affects the rate of convergence [1,2]. Iterative processing continues until the error signal is minimized, at which point the weights are nearly optimal and the receiver output represents the best possible estimate of the desired signal.

Even more powerful techniques may be employed, including recursive least squares (RLS) processing which estimates the correlation matrix and its inverse for the received signal plus noise and interference at each antenna element [3].



Implementations of RLS tend to be extremely computation intensive, however; LMS thus represents an adequate compromise between algorithm complexity and performance for most applications.

In the following paper, we show that the LMS algorithm implemented with the receiver of Figure 3.1 may be viewed as a special case of the perceptron neural network model. By including more adaptive weights in this system, the antenna controller can be realized as a two-level perceptron; this is expected to improve adaptive nulling performance, particularly for broadband interference. The perceptron weights are updated by the back propagation algorithm, which is a generalized form of LMS [4,5]. We will develop the neural network analogy and suggest an optical implementation for the two-level perceptron. First, however, we must address the question of whether optical control systems are practical for adaptive antenna systems. This will be done in the following section, where we briefly review various adaptive controllers which have been implemented using existing technology.

### 3.2 OPTICAL ARCHITECTURES and TECHNOLOGY

Because calculation of the receiver weights requires high speed and parallel processing of wideband signals, several optical architectures have been proposed to implement adaptive null steering. The optimal weights for an adaptive receiver may be found as the solution to a matrix-vector calculation, which requires the inverse of the covariance matrix for the received signal plus interference. This is known as direct matrix inversion (DMI); it can be realized by implementing the Richardson algorithm on an optical matrix-vector processor with electronic output feedback [6]. The basic optical system design is well known; a programmable mask such as a liquid crystal television may be used, as well as a linear array of laser diode sources and photodiode detectors. Various schemes for optical manipulation of the complex weight values have been proposed; if a

sufficiently coherent laser source is used, both amplitude and phase information of the optical signal can be preserved, and complex values may be represented directly. Otherwise, some form of coding or pre-processing of the data is required, since the optical intensities are restricted to real, positive values.

However, forming the covariance matrix may be a significant computational problem, and the DMI routine functions poorly if this matrix is ill-conditioned or singular. An alternative is the correlation cancellation loop (CCL), which performs the equivalent function of DMI. This process requires a programmable finite impulse response (FIR) filter capable of changing its transfer function in response to prevailing conditions at the receiver. Typically, the filter must adapt in order to minimize the correlation between the input and a residual error signal, which represents the difference between the received signal and the filter output. A particular realization of the CCL uses a transversal filter architecture with feedback to form an adaptive linear predictor; this design has been investigated by Vander Lugt [7] using an acousto-optic cell as an optically tapped delay line. Psaltis and Hong have also realized the CCL [8] for two-dimensional signals as an adaptive matched filter using bulk acousto-optic convolvers and correlators. This implementation requires a desired reference signal to be available at the receiver. If this is not practical, the system may transmit a known pilot signal to calibrate the receiver weights. Casasent et. al. have implemented a similar design [9] based on an adaptive acousto-optic FIR filter with a separate system for optical feedback. For many optical null steering systems, heterodyne detection of the optical signals is required to achieve the necessary degree of accuracy; this realization used a Mach-Zehnder interferometer to derive the optical reference beam.

The preceding systems illustrate the feasibility of optical processors for adaptive null steering applications. Their high processing rates, broad bandwidth,

and inherent potential for two-dimensional processing make optical systems well suited for this application. In addition, it has been shown that practical adaptive processors may be realized with existing optical technology. For example, recall that in order to null wideband interference a transversal filter is required at each antenna output. This may be realized by using the antenna output to drive an acousto-optic (AO) cell, illuminated by a coherent laser source. The AO device acts as an optically tapped delay line, with the modulated output light representing delayed versions of the input signal. The use of AO tapped delay lines has been reported previously [7] for adaptive receiver implementations. This approach yields a continuously tapped delay line, which is an advantage over discrete electronic implementations where the tap spacing is inversely proportional to the bandwidth of the interference [1]. This makes it very difficult to realize discrete tapped delay lines to null broadband interference.

By contrast, multi-channel AO Bragg cells have been demonstrated with center frequencies near 1 GHz, several hundred MHz bandwidth, and linear dynamic ranges approaching 60-70 dB [9]. This eliminates the need for frequency down-conversion circuitry at each antenna tap, and simplifies the optical architecture. Up to 64 channels have been demonstrated in GaP multi-channel AO devices, with up to 128 channels in TeO<sub>2</sub>. [10]. Other types of optical modulators such as electro-optic devices may be incorporated into many of these systems, and hybrid optical/electronic processors using heterodyne detection have demonstrated the equivalent of 10-bit digital accuracy [9]. Thus, it is feasible to construct optical processors for practical adaptive antenna systems using currently available technology. Most of the systems proposed to date have employed some variation of the LMS algorithm; in the following section, we propose a new approach based on the perceptron neural network.

### 3.3 PERCEPTRON IMPLEMENTATION

Perceptron neural nets have been investigated by Rumulhart et. al. [5] as a robust means of recovering signals embedded in high levels of noise and interference. It was first shown by Widrow [11] that a tapped delay line with adaptive weights could be realized as a single perceptron neural network. The basic structure of a perceptron is illustrated in Figure 3.2. Each neuron is a simple processing unit which is interconnected with every other neuron in the network. An individual neuron receives weighted inputs from other neurons, as shown; these values are summed and applied to a thresholding function. An additional input with a preset, constant value may be used to bias individual neurons, as shown; this bias value may also be computed adaptively, in the same manner as the connection weights. The simplest possible threshold is a step function, for which the neuron generates an output signal only if the weighted sum of the inputs exceeds a preset level. Other types of thresholds, such as linear relations or sigmoid functions, are also possible. The perceptron "learns" to recognize a corrupted input signal by adaptively updating the interconnection weights based on the error between the network output and a desired reference signal. Weights are updated by the back propagation algorithm, to be discussed shortly. Perceptrons may be constructed as a layered, feed-forward network as illustrated by Figure 3.4; each layer receives input only from the immediately preceding layer. Although more complex networks may realize a larger number of associations, it has been shown [4] that using more than two to three layers does not significantly improve the noise suppression characteristics of the network.

A signal flow diagram for the typical LMS adaptive antenna receiver is shown in Figure 3.3, along with the diagram of a two-level perceptron network. By comparison of the two, it is apparent that the current receiver design is equivalent

**FIGURE 3.2**

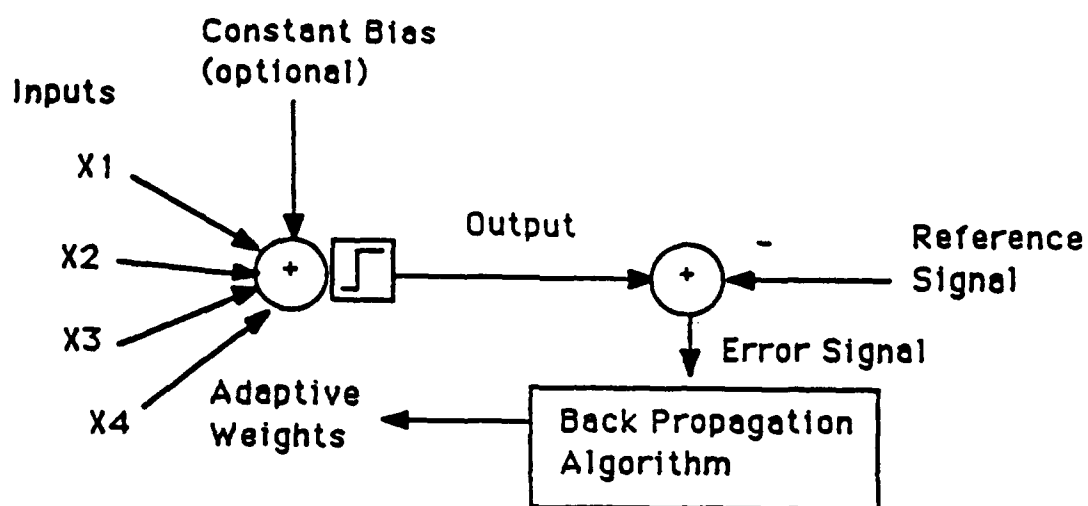


**Figure 3.2. Basic perceptron architecture.**

to a perceptron with the following limitations. First, the inputs are not connected to every summing junction in the second layer, while the perceptron is fully interconnected. Second, the weights between the first and second layers have been held fixed at one, while the perceptron adapts these weights as well. Finally, the perceptron uses some type of thresholding function to operate on the summed weights, which is not present in the antenna receiver. By removing these restrictions, it is possible to realize an adaptive phased array antenna controller using a two-level perceptron neural network.

In conventional antenna systems, both the signals and weights are in general complex valued. For simplicity, we assume a quadrature phase shifter at each antenna output to separate the real and imaginary parts of the incoming signal, as illustrated by Figure 3.4. In this manner, the perceptron can function with strictly real weights, which may be either positive or negative depending on whether they excite or inhibit a given interconnection in the network. We may also use a sigmoid thresholding function in the network, to allow for continuous-valued rather than binary outputs. This threshold takes the general form [4]:

$$f(x) = \frac{1}{1 + e^{-(x-\beta)}} \quad (3.5)$$

where  $\beta$  is a constant. The sigmoid is also continuously differentiable, a necessary condition for the back propagation algorithm which updates the interconnection weights; the following review of this algorithm follows the development of reference [4].

Back-propagation is an iterative gradient algorithm designed to minimize the mean square error between the actual and desired perceptron outputs. In a multi-layer network the weights are updated recursively, starting at the output layer and working backward through the hidden layer to the input. For simplicity, we consider only the case of a two-layer network, as illustrated by Figure

FIGURE 3.3

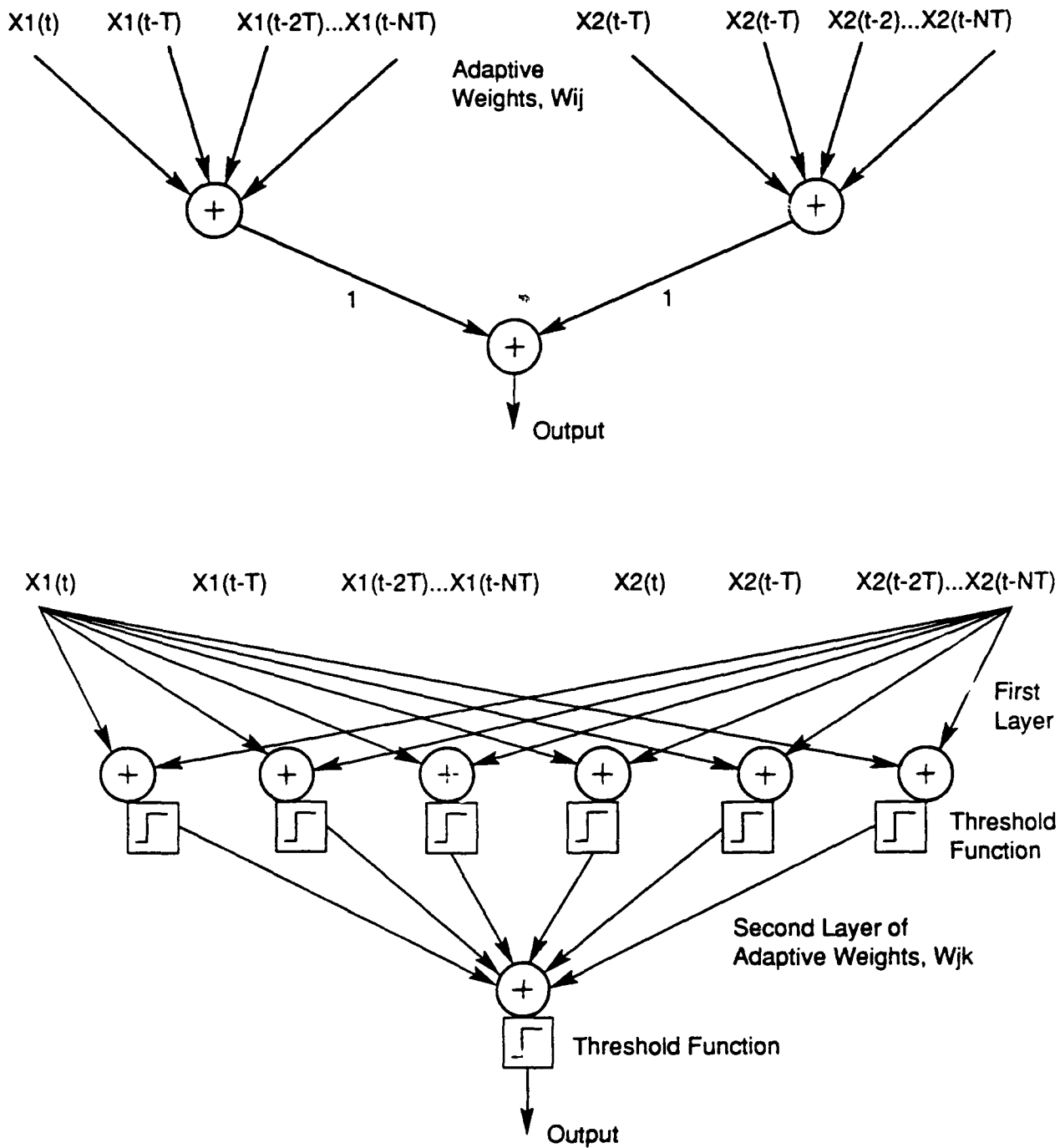


Figure 3.3. Architecture for 2 antenna, N-tap LMS receiver and typical LMS controller and two-layer perceptron.

FIGURE 3.4

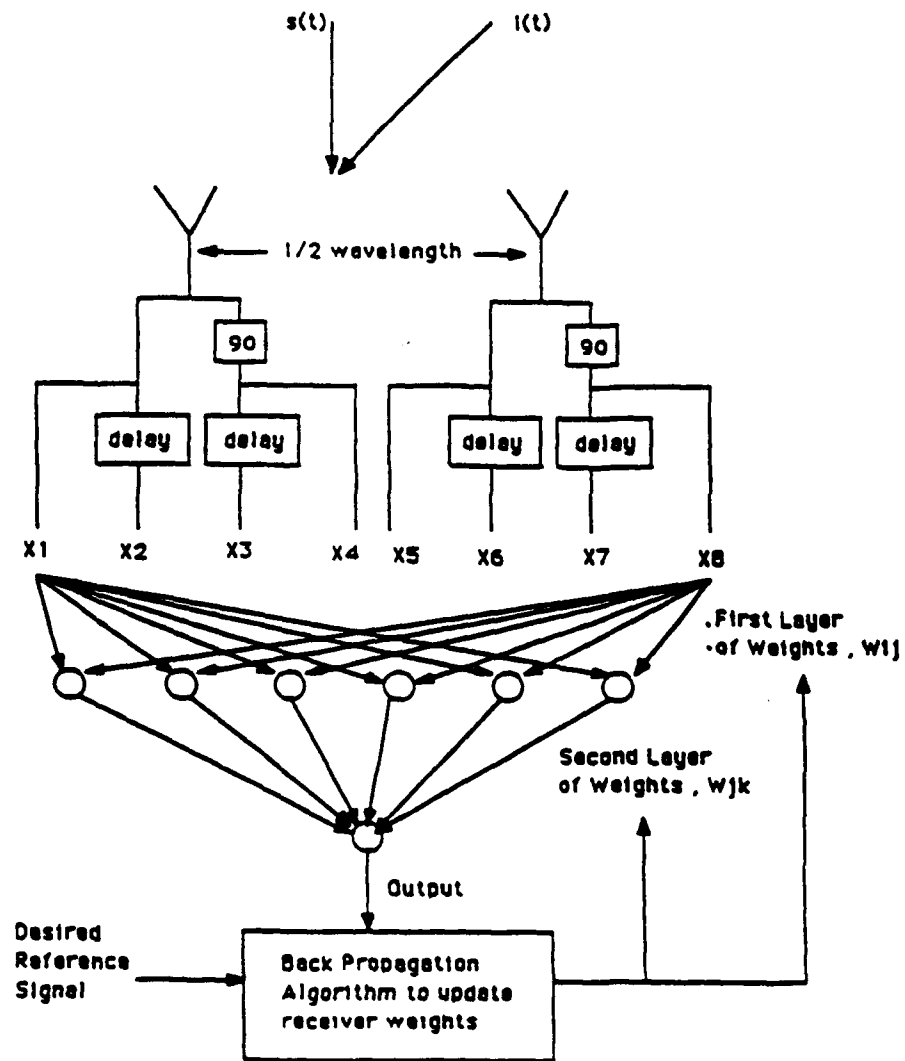


Figure 3.4. Receiver model for 2 antenna, 2 tap system, using only real weights.



3.4. The weights are updated according to:

$$\begin{aligned}w_{ij}(t+1) &= w_{ij}(t) + \eta \Delta_j x_i \\w_{jk}(t+1) &= w_{jk}(t) + \eta \Delta_k x_j\end{aligned}\tag{3.6}$$

where  $w_{ij}$  is the weight from node  $i$  to node  $j$ ,  $w_{jk}$  is the weight from node  $j$  to node  $k$ ,  $\eta$  is a convergence parameter as presented earlier for the LMS algorithm,  $x_i$  is an input to the network, and  $x_j$  is the output of node  $j$  (the hidden layer). The error term at the network output,  $\Delta_k$ , is given by:

$$\Delta_k = y_k(1 - y_k)(r_k - y_k)\tag{3.7}$$

where  $r_k$  is the desired reference signal for the  $k^{th}$  output neuron, and  $y_k$  is the actual output of the  $k^{th}$  neuron. For the system shown in Figure 3.4, there is only a single output ( $k = 1$ ). After the weights to the output layer have been updated according to equation (3.7), the new weights are used to calculate the error term for the previous layer according to:

$$\Delta_j = x_j(1 - x_j) \sum_k \Delta_k w_{jk}\tag{3.8}$$

where the sum is taken over all nodes in the layer above the output. In this manner, the algorithm works back to the first set of input weights until all the network weights have been adjusted. Iterative processing continues in this manner until the weights converge to their optimal values and the error term has been minimized. A more detailed treatment of the algorithm has been given in reference [4]; it has been shown that faster convergence of the network may be obtained if a "momentum term" is added to the weight update equation; this may be written in general as:

$$w_{ij}(t+1) = w_{ij}(t) + \eta \Delta_j x_i + \alpha(w_{ij}(t) - w_{ij}(t-1)) \quad \text{for } 0 < \alpha < 1\tag{3.9}$$

We have used a two-level perceptron with eight inputs, six neurons in a hidden layer, and one output neuron to simulate an adaptive antenna as shown in Figure 3.4. This perceptron must compute 54 adaptive weights, versus only 8 for the conventional adaptive processor. Although the perceptron receiver requires more weights to be computed, it should provide improved performance over the LMS algorithm because of the additional degrees of freedom in the adaptation process. This is especially important in the case of wideband interference cancellation. By using an optical architecture to realize this system, the additional weight calculations may be performed in parallel so that overall processing time is expected to be at least comparable to existing systems. Total processing time depends on both the time required to update the weights and the number of iterations until convergence; thus, if back propagation converges in few iterations than LMS (because of the additional weights), the complexity of the weight updating may be offset.

In order to demonstrate proof of concept, we have simulated the response of a two-element adaptive antenna as illustrated by Figure 3.4. Each element has a two-tap delay line, and we separate the received signal into its real and imaginary components as shown. This provides a total of eight input signals for the neural network adaptive processor; we have chosen six neurons for the hidden layer, followed by a single output neuron. We have simulated the behavior of the perceptron shown using the software package Brainmaker version 3.02 from California Scientific Software [12], running on an IBM PC-XT. This program implements the back propagation algorithm with smoothing as given by eq. (9) with  $\alpha = 0.9$  and  $\eta = 1.0$ . We used a sigmoid thresholding function to train the network as given by eq. (5) with  $\beta = 0$ . These are default values set by the program, and may be adjusted in future simulations. The output of the

perceptron network,  $y(t)$ , is given by:

$$y(t) = f\left(\sum_j w_j(t) f\left(\sum_i w_{ij}(t) x_i(t) e^{j\phi_i} - c_i\right) - c_j\right) \quad (3.10)$$

where the thresholding function  $f(x)$  is a sigmoid,  $j$  is the square root of -1, and the constants  $c_i$  and  $c_j$  represent a fixed bias applied to each neuron. The neuron bias terms are also computed adaptively; they are treated as connection weights from auxiliary constant-valued inputs [4]. We assume antenna spacing of one-half wavelength (at the signal center frequency) so that a signal or interference incident at some angle with respect to the antenna normal will experience a phase shift given in equation (3.10) by:

$$e^{j\phi_i} \quad \text{where} \quad \phi_i = \pm \pi i \sin \theta \quad (3.11)$$

Neglecting the sigmoid function, the array factor for this network is given by:

$$A(\theta) = \sum_j w_j \left( \sum_i w_{ij} e^{j\phi_i} - c_i \right) - c_j \quad (3.12)$$

and the gain pattern,  $G(\theta)$ , may be calculated from:

$$G(\theta) = 10 \log(|A(\theta)|^2/M) \quad (3.13)$$

where  $M$  is the number of antenna elements (for our case,  $M = 2$ ). This result is valid when the system operates within the linear region of the sigmoid function, near the origin, or when a linear threshold is used with a trained network.

We have considered the test case of a sinusoidal input signal at frequency  $\omega_1$  incident normal to the array, and a sinusoidal jammer at a different frequency  $\omega_2$  incident at an angle of 30 degrees with respect to the array normal. Thus, both the signal and interference are narrowband for this case; while this is sufficient to demonstrate the concept, we expect the true advantage of perceptrons to be in the case of broadband interference and multiple jammers. Both the signal

and jammer powers were normalized to one for these simulations. The signal amplitude is assumed to be digital (either 1 or 0 in amplitude) while the jammer amplitude remains constant. Under these circumstances, our system must satisfy the condition [13]:

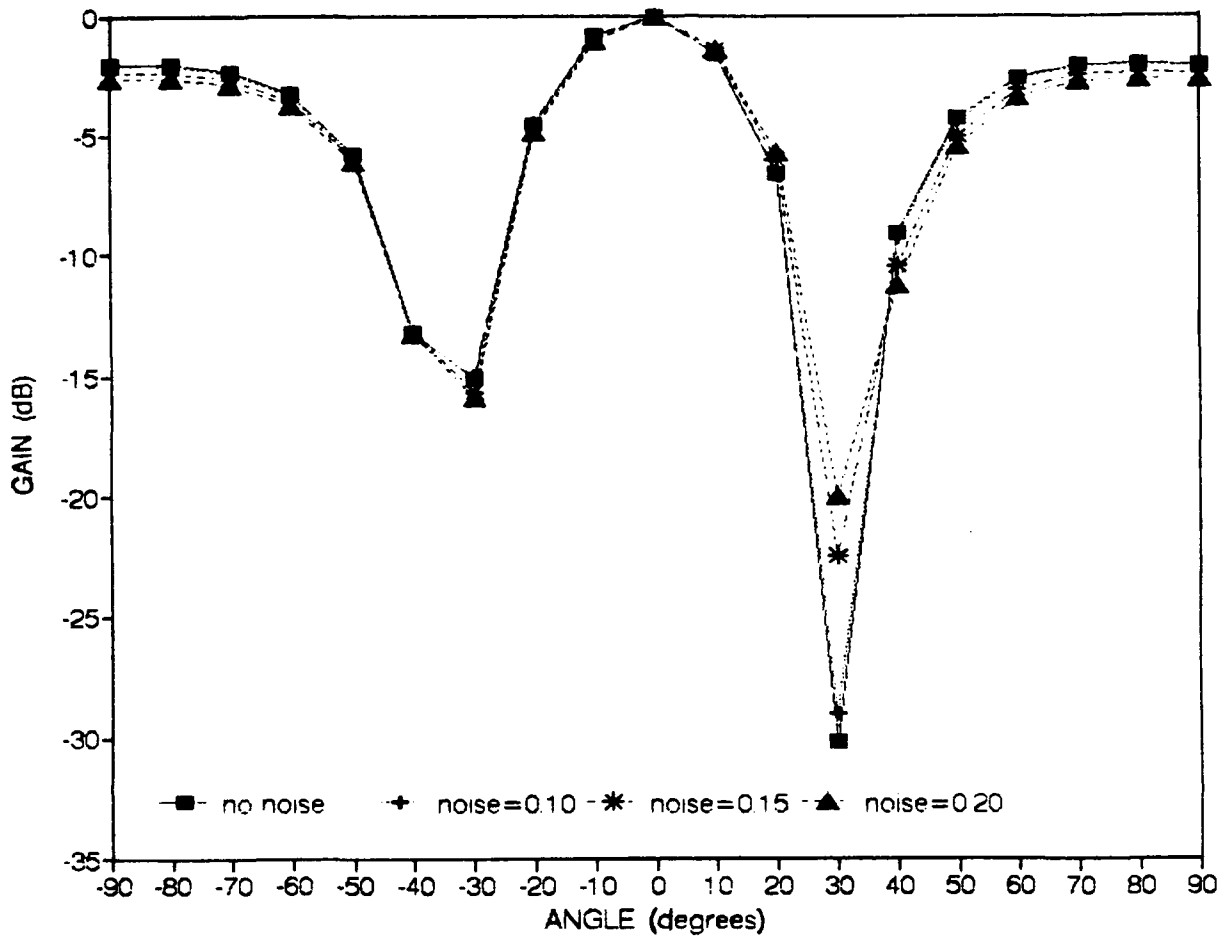
$$(\omega_2 - \omega_1)T = \frac{\pi}{6} \quad (3.14)$$

where  $T$  is the delay as defined in Figure 3.4, although the values of  $\omega_1$ ,  $\omega_2$  and  $T$  are not otherwise restricted. A complete theoretical treatment of this adaptive antenna problem is given by Milstein [13].

The Brainmaker program allows for the addition of white Gaussian noise with zero mean and adjustable variance. Initially, we trained the network in the absence of noise to null the antenna pattern in the direction of the jammer; results are shown in Figure 3.5. The null is just over 33 dB down from the normal look direction; this compares favorably with the conventional adaptive solution for a two-element, two-tap antenna [6,14]. The weights were allowed to adapt until the network output had converged to the desired reference signal with a tolerance of 0.1; by allowing the network to iterate further, we obtained convergence to within a tolerance of 0.025, although the antenna pattern of Figure 3.5 remained virtually unchanged. While maintaining a tolerance of 0.1, we then supplied noise of variance 0.10, 0.15, and 0.20 while allowing the weights to adapt. We attempted to prevent the perceptron from becoming "stuck" in a local minima during optimization by training the network several times; the final weights were acceptable only if the network converged to the same result on three successive trials. The resulting antenna patterns are given in Figure 3.5, and illustrate how the notch depth is degraded by the presence of increasing amounts of noise.

Although neural networks have been the subject of active research, many aspects of their performance have yet to be investigated. For example, the

FIGURE 3.5



ANGLE (degrees)	GAIN(dB) no noise	GAIN(dB) noise= 0.10	GAIN(dB) noise=0.15	GAIN(dB) noise=0.20
-90	-2.0177491	-2.0963797	-2.3979059	-2.6264483
-80	-2.0670346	-2.1454887	-2.4340744	-2.6550779
-70	-2.3496065	-2.4282111	-2.6797893	-2.8798647
-60	-3.288629	-3.3699914	-3.5620492	-3.7307799
-50	-5.8043403	-5.8978266	-5.9946703	-6.1200177
-40	-13.165019	-13.330072	-13.146745	-13.17523
-30	-15.076854	-14.955628	-15.612757	-15.880148
-20	-4.5194847	-4.5062178	-4.7461414	-4.865774
-10	-0.8423717	-0.8428455	-0.9561933	-1.0173872
0	0.0	0.0	0.0	0.0
10	-1.5952437	-1.5839122	-1.4222345	-1.3291339
20	-6.6206543	-6.5680695	-6.0255676	-5.7141472
30	-30.162635	-28.945993	-22.437758	-19.977746
40	-9.105833	-9.2585061	-10.417554	-11.249533
50	-4.2935315	-4.3931444	-5.005699	-5.4355812
60	-2.5668645	-2.6522484	-3.0926454	-3.4073305
70	-2.0436965	-2.124141	-2.4812262	-2.7432172
80	-1.9910199	-2.0699307	-2.38475	-2.6211433
90	-2.0177448	-2.0963755	-2.3979031	-2.6264464

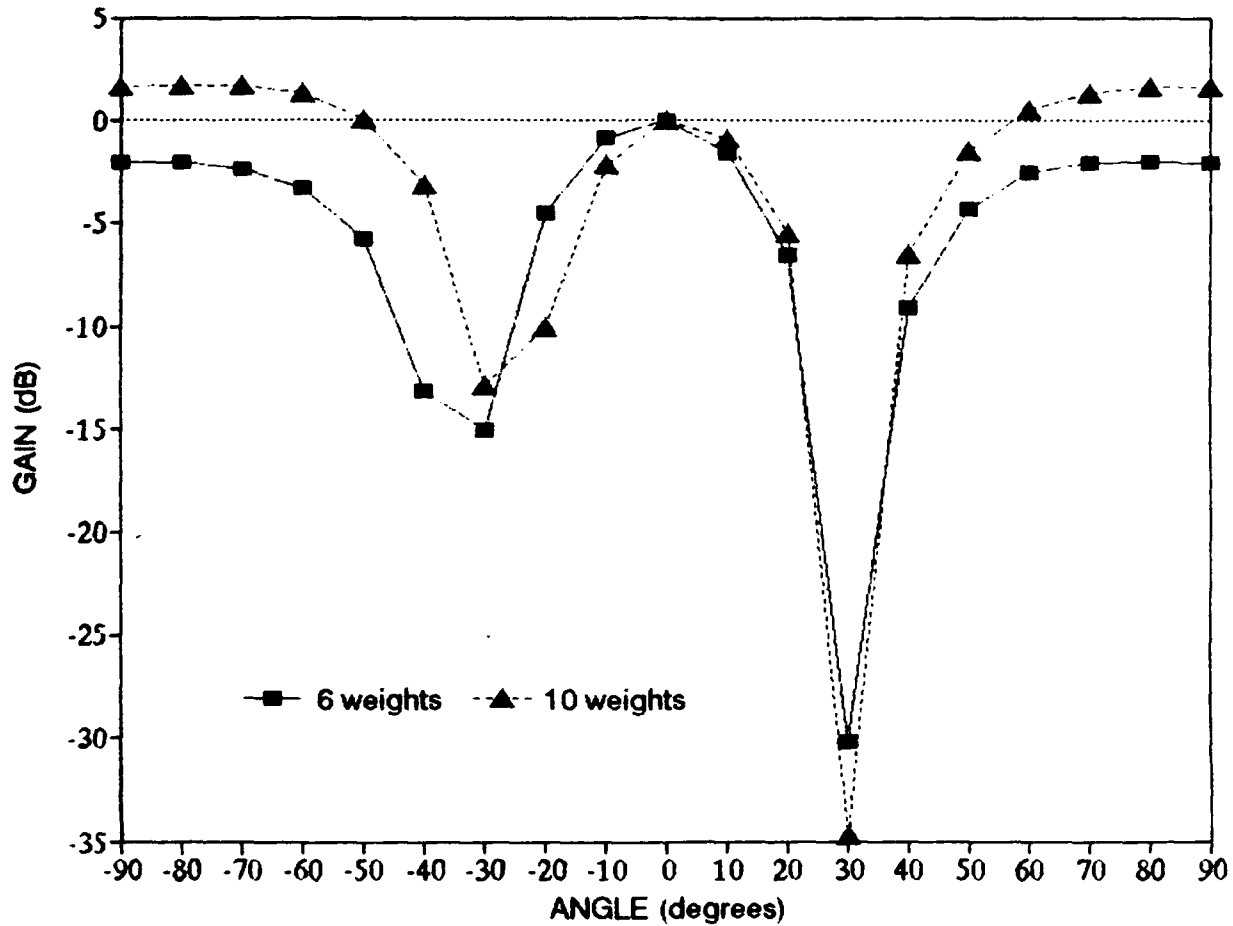
Figure 3.5. Perceptron receiver antenna pattern for different input noise levels. Gain-versus-angle graph and data table. Threshold = 0.10.

choice of the number of neurons for the hidden layer is somewhat arbitrary, and must be optimized for any given problem [4]. As a first effort in this area, we have considered the effect of including ten neurons in the hidden layer, rather than six. Note that this system uses more hidden neurons than there are input signals; a comparison of the six and ten neuron systems without noise is shown in Figure 3.6. Including more hidden neurons improves the notch depth by only a few dB; it may be possible to reduce the number of hidden neurons below six and still maintain satisfactory performance. However, these results are for a two-element, two-tap system with narrowband interference; inclusion of more antennas and taps will increase the number of weights, and enable the system to suppress wideband noise as well. This is a subject of continuing research.

All of the weights used in these simulations were computed to three decimal places; we have also investigated the effect of reduced accuracy in the weights. As shown in Figure 3.7, there is essentially no change in the array pattern when the accuracy of the weights is reduced from 3 decimal places to 2 and finally to 1. Conventional adaptive algorithms exhibit this same robustness to weight accuracy for the two-element case we are considering [14]; however, these results demonstrate that the perceptron model could be realized with low accuracy optical processors and still yield adequate performance. Eventually, it may be possible to realize a more complicated neural net whose weights need only be either 1 or 0; such a processor would be extremely well suited to optical implementation, and would offer distinct advantages over the analog systems currently in use. The Brainmaker program also provides the capacity to introduce noise in the weight values themselves to simulate inaccuracies in the system; this will be an area of future research.

Note that a conventional adaptive antenna using the LMS algorithm is essentially equivalent to a single layer perceptron with one output neuron [11].

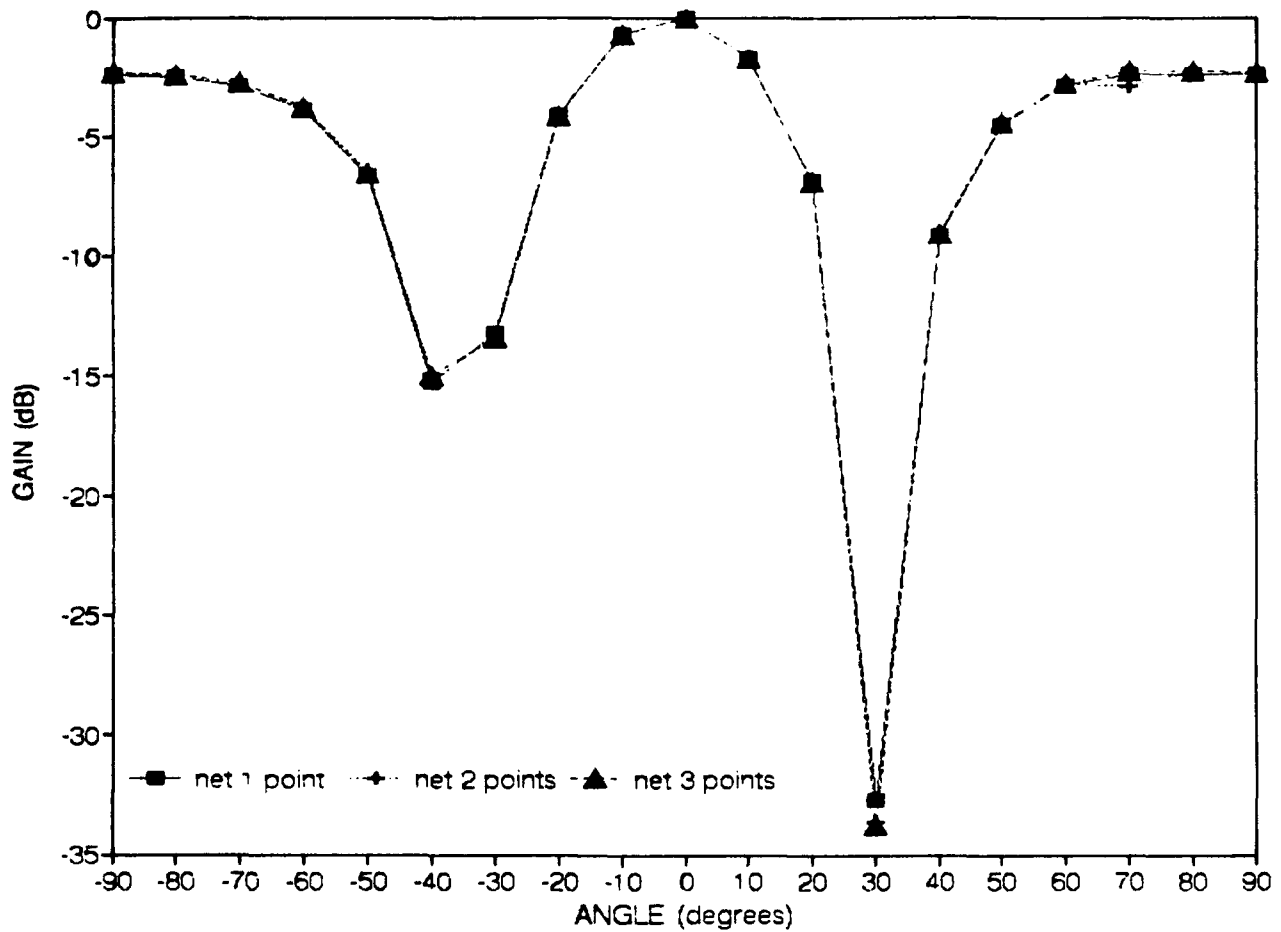
FIGURE 3.6



ANGLE (degrees)	GAIN(dB) 6 weights	GAIN(dB) 10 weights
-90	-2.0177491	1.64381393
-80	-2.0670346	1.67673106
-70	-2.3496065	1.66761438
-60	-3.288629	1.30438076
-50	-5.8043403	0.04715944
-40	-13.165019	-3.1799032
-30	-15.076854	-12.891331
-20	-4.5194847	-10.064767
-10	-0.8423717	-2.2009899
0	0.0	0.0
10	-1.5952437	-0.8833168
20	-6.6206543	-5.5250464
30	-30.162635	-34.72625
40	-9.105833	-6.5094988
50	-4.2935315	-1.5028169
60	-2.5668645	0.52179579
70	-2.0436965	1.33032115
80	-1.9910119	1.59259973
90	-2.0177448	1.64380926

Figure 3.6. Comparison of antenna patterns for six and ten hidden neuron systems. Gain-versus-angle graph and data table.

FIGURE 3.7



ANGLE (degrees)	GAIN(dB) net 1 point	GAIN(dB) net 2 points	GAIN(dB) net 3 points
-90	-2.4018979	-2.3144468	-2.322328
-80	-2.4670113	-2.378065	-2.3864325
-70	-2.8019572	-2.7075692	-2.7175166
-60	-3.8527334	-3.7450297	-3.7582571
-50	-6.6342788	-6.4904396	-6.5113197
-40	-15.267177	-14.922831	-14.981762
-30	-13.209868	-13.430101	-13.383708
-20	-4.0768739	-4.1248776	-4.1125988
-10	-0.6950709	-0.7082993	-0.7039446
0	0.0	0.0	0.0
10	-1.706001	-1.7029269	-1.7067464
20	-6.8681078	-6.879092	-6.8889903
30	-32.741079	-33.613135	-33.800944
40	-9.1542939	-9.054471	-9.0491258
50	-4.4809871	-4.4000592	-4.4011103
60	-2.8339674	-2.7540279	-2.7580864
70	-2.3713372	-2.884455	-2.2945418
80	-2.3600591	-2.2739553	-2.2813675
90	-2.401892	-2.314441	-2.3223221

Figure 3.7. Perceptron performance for different weight accuracies. Gain-versus-angle graph and data table.

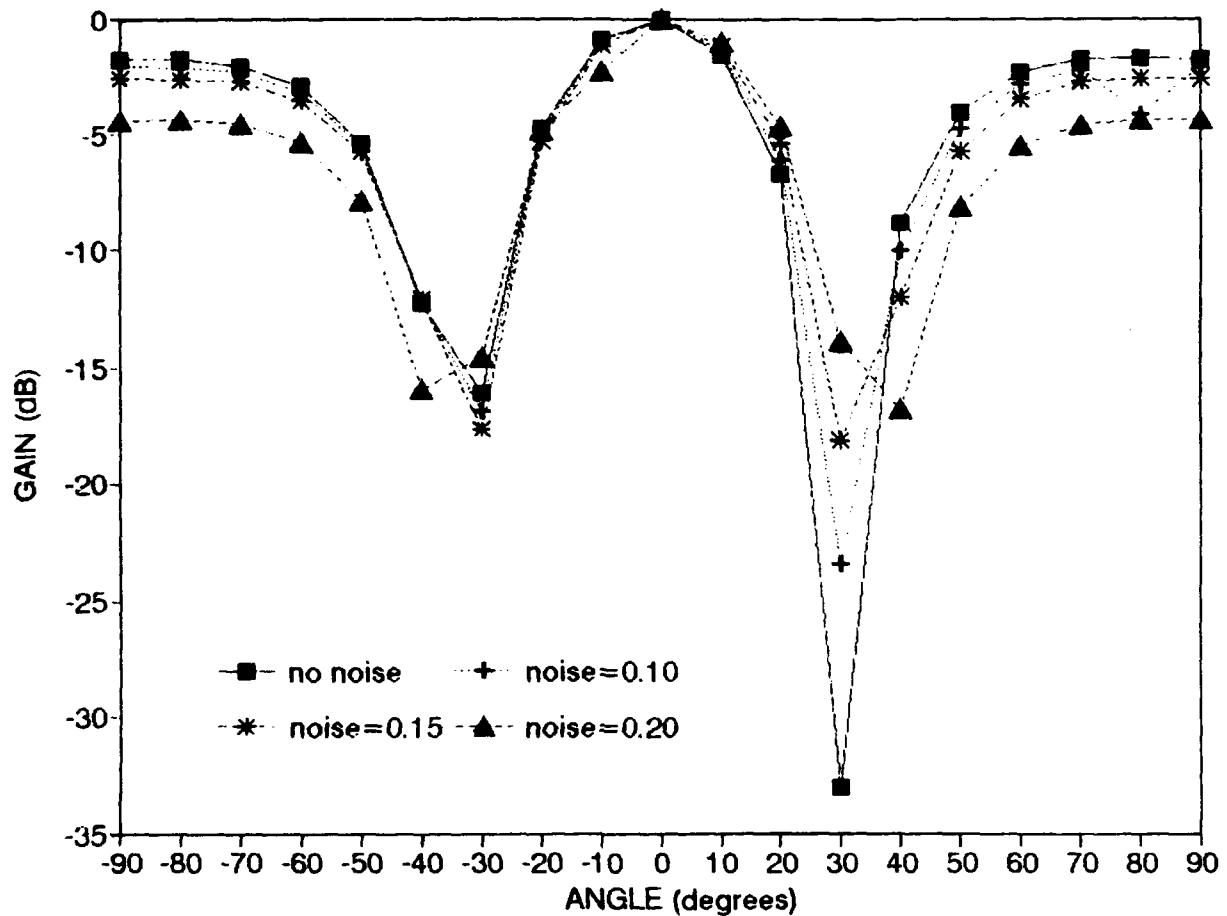


Thus, we may use Brainmaker to simulate the Widrow-Hoff solution with such a network. Figure 3.8 illustrates the results for this case when the Widrow-Hoff network is trained with various levels of Gaussian noise. Note that a single layer perceptron is a particularly straight forward way to generate the Widrow-Hoff solution, without directly inverting the signal correlation matrix. For comparison, the performance of our multi-layer perceptron for different noise levels was shown in Figure 3.5; for this test case, the results are always equal to or slightly better than the Widrow-Hoff solution network, as expected [14].

### 3.4 OPTICAL ARCHITECTURES for the PERCEPTRON

There has recently been a revival of interest in the optical realization of neural networks. Adaptive optical processors which realize the Widrow-Hoff algorithm have been implemented [15]; in addition, the first optical realization of a single perceptron was performed by Psaltis et. al. [16]. A volume hologram stored in SBN:6OCe was used to store the interconnection weights; two-dimensional optical input patterns were presented to the system using a liquid crystal television as a spatial light modulator. The optical output was summed by a lens and monitored by a photodetector; the weight updates were calculated by a digital computer using the photodetector signal. This paper also defined a means to update the weights by using the photorefractive response of the material; the required updates were written directly over the stored volume holographic weights. This concept has recently been used by Paek et. al. to realize an optical perceptron with multiple output states [17]; such a device has potential applications as a multi-level classifier. Multi-layer perceptrons using phase conjugate mirrors for optical error feedback have been proposed by Psaltis et. al. [18]. Additionally, the use of photorefractive volume holograms in conjunction with adaptive acousto-optic filters has been investigated by several authors [19,20,21].

FIGURE 3.8



ANGLE (degrees)	GAIN(dB) <u>no noise</u>	GAIN(dB) <u>noise=0.10</u>	GAIN(dB) <u>noise=0.15</u>	GAIN(dB) <u>noise=0.20</u>
-90	-1.7220188	-2.0619498	-2.5645149	-4.3620632
-80	-1.7672785	-2.0934312	-2.577768	-4.3284003
-70	-2.0349235	-2.3218177	-2.7552384	-4.5071459
-60	-2.9369312	-3.161368	-3.5173268	-5.3343712
-50	-5.3542852	-5.4816802	-5.7270057	-7.8348927
-40	-12.257864	-12.126691	-12.110341	-15.929526
-30	-16.052273	-16.825681	-17.668091	-14.509873
-20	-4.6904479	-4.9537091	-5.2601116	-4.852622
-10	-0.8863611	-1.0108134	-1.1603837	-1.1178104
0	0.0	0.0	0.0	0.0
10	-1.5889854	-1.4092305	-1.1909994	-1.0381533
20	-6.6728795	-6.060419	-5.3435467	-4.6466079
30	-33.031893	-23.452081	-18.071314	-13.817506
40	-8.7376207	-9.9827844	-11.934401	-16.73002
50	-4.0055955	-4.6779609	-5.6604419	-8.0619466
60	-2.2887224	-2.7772008	-3.4858163	-5.4373706
70	-1.7597083	-2.1589798	-2.7419199	-4.5501615
80	-1.698858	-2.0529633	-2.5744602	-4.3390562
90	-1.722015	-2.0619476	-2.5645147	-4.3206368

Figure 3.8. Widrow-Hoff simulation at different noise levels. Gain-versus-angle graph and data table.

One possible implementation of our system is based on an extension of this technology, as illustrated in Figure 3.9. Interconnection weights for each layer of the perceptron are stored in volume holograms by the photorefractive effect. The corrupted antenna signals are used to modulate an array of AO cells, which are addressed by a laser diode array (diodes with a 60-70 dB dynamic range are available which operate at high modulation frequencies [9]). This generates the necessary delayed versions of the signal; these delayed signals are spread by a cylindrical lens over a photorefractive volume hologram, which contains the interconnection weights. The modulated light from the first hologram is summed by a lens system and focussed to a photodetector; the detector signal may be processed electronically to provide the necessary thresholding operations. The thresholded signals are used to drive a second laser diode array, which addresses the second hologram. The modulated light output is summed, thresholded and detected as before to yield the network output. At this point, we introduce the electronic reference signal to calculate the error term. The calculation of the error terms may be performed either electronically, or optically as described by Psaltis et. al. [8,18]. The hologram weights are updated using the photorefractive effect; a separate laser array writes the weight corrections directly over the second volume hologram. These updated weights, in turn, are used to calculate an update for the previous layer, as discussed earlier; this hologram is overwritten in a similar manner. The processor iterates in this manner until the weights converge; although back propagation introduces some delay in the updating procedure, this effect should be minimal if dedicated electronic hardware or optics is used. The most computation-intensive portion of the algorithm is performed by the optical system. In addition, optics is used to realize the large number of

interconnections required by a true perceptron model; because of these two reasons, it would be difficult to implement this algorithm efficiently without using an optical processor.

Another possible implementation involves using acousto-optic (AO) or electro-optic (EO) devices to represent the weights; suitable devices are available, as discussed in a previous section. The proposed architecture is illustrated in Figure 3.10; the operating principle is similar to the volume holographic implementation, except that the weights are presented on an array of AO or EO cells. The updating procedure no longer requires a separate laser array to overwrite the volume holograms; instead, the AO or EO devices can be modulated directly by the feedback electronics. This could improve the update time, which was limited in the previous case by the write time of the volume holograms.

Both architectures may require heterodyne optical detection to obtain the required accuracy of the weights; it has been shown [22] that such detection can improve performance by 15-20 dB. This is particularly convenient to realize with the second design using EO devices to represent the weights; by applying an AO signal simultaneously to the EO device, we may generate a second diffracted beam with a frequency shift. This type of acousto-electro-optic (AEO) interaction has been reported [23] as a means for internal generation of reference beams for heterodyning, eliminating the need for an external optical path as required by some other architectures [9]. The use of internally generated reference beams provides for a more rugged device, which is less sensitive to misalignment and vibrations.

In the future, optical adaptive processors could represent an important alternative for broad bandwidth communication systems subjected to multiple interference sources or a single source with multipath echoes. For example, current research efforts are considering a long range, line of sight spread spectrum

FIGURE 3.9

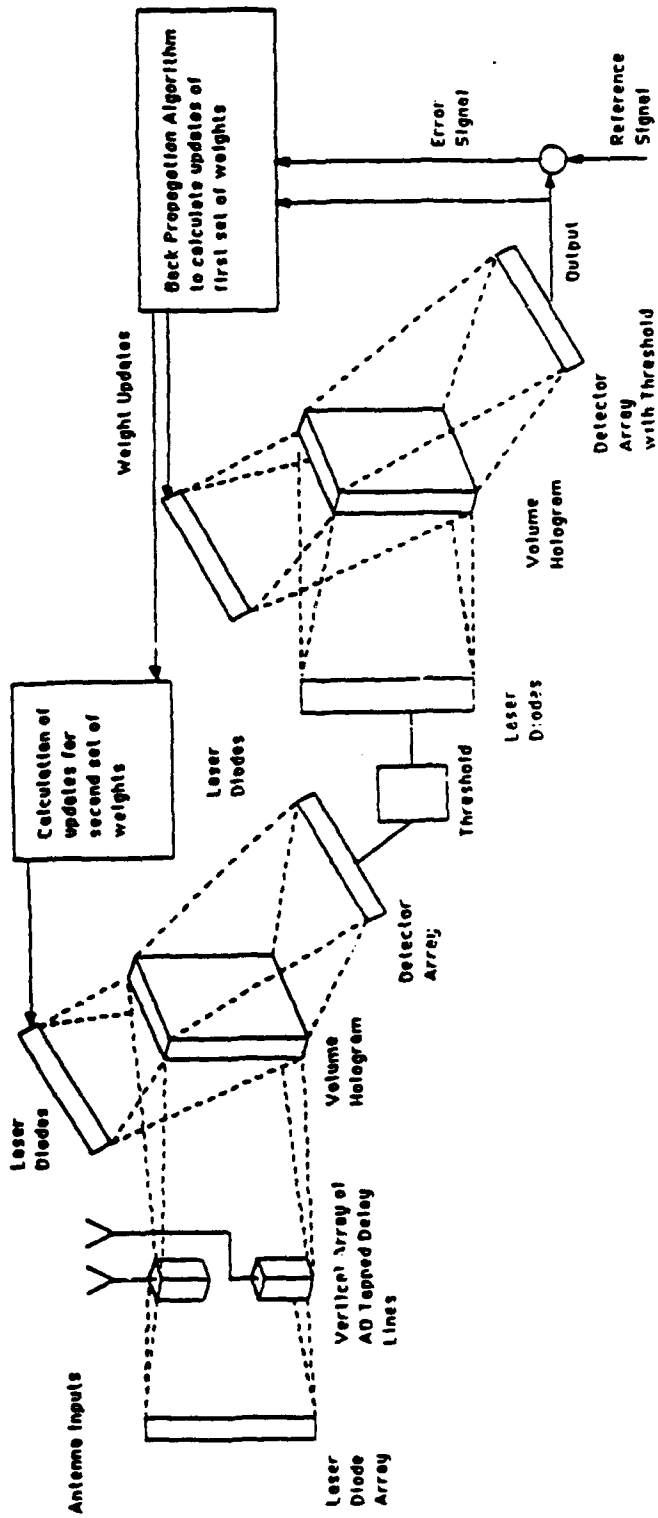


Figure 3.9. Optical implementation of a two-level perceptron using volume holograms; optical path shown by dotted lines, imaging lenses omitted for clarity.

FIGURE 3.10

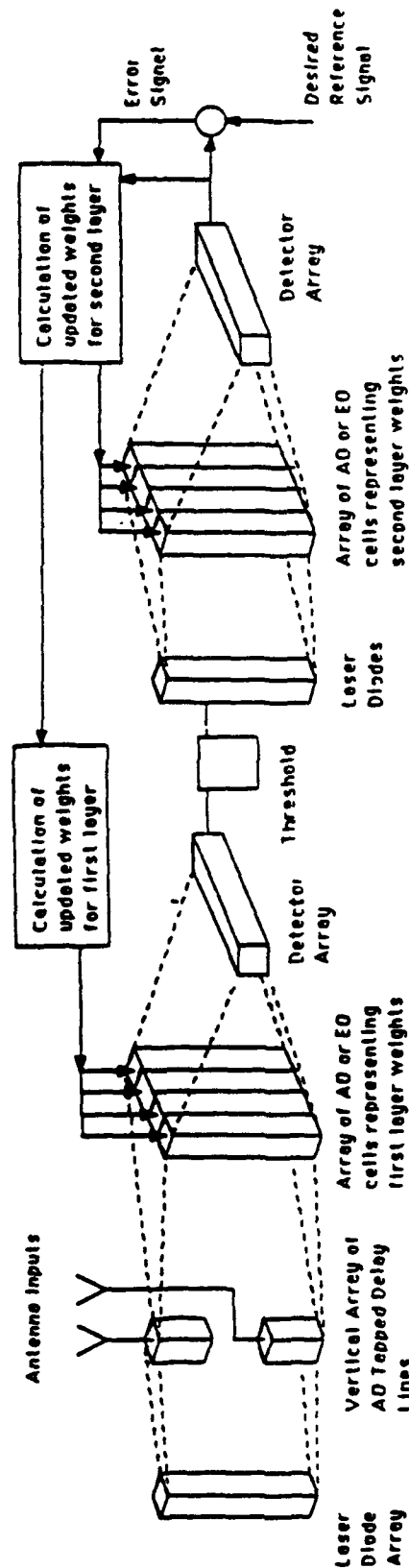


Figure 3.10. Optical implementation of a two-level perceptron using acousto-optic (AO) and electro-optic (EO) devices; optical path shown by dotted lines, imaging optics and angles of diffracted beams not shown and separation between AO tapped delay lines elements exaggerated for clarity.

system covering approximately 300 MHz bandwidth centered around 1 GHz. An electronic adaptive processor would require a discrete tapped delay line with tap spacing of less than 4 ns; the taps would probably be required to an accuracy of less than 1 ns. An adaptive receiver would not only have to protect the entire bandwidth, but is required to adapt within about 1 ms to accommodate high signaling rates. Additionally, the long range communication requires a dynamic range approaching 70 dB; the presence of multipath interference or multiple interference sources requires high resolution in the antenna gain pattern (deep, narrow nulls in the angular steering response). These requirements for a typical future communication system can best be realized using optical processing; continuous tapped delay lines meet the resolution requirements, while high speed, parallel processing is required to maintain effective communication rates. Given these requirements, optical components are expected to play an important role in the adaptive control of future wideband communication systems.

### 3.5 CONCLUSIONS

There is a strong analogy between conventional adaptive phased array antenna controllers based on the least mean squares algorithm and the two-level perceptron neural network. We have proposed an adaptive antenna controller based on a perceptron; antenna weights are updated using the back propagation algorithm, which is a generalized form of least mean squares. By introducing additional adaptive weights at the receiver, improved performance is expected for a broadband interference suppression system. A proposed system design is given which could be realized using conventional optical technology; existing optical devices not only meet the requirements of this system, but may be applied to future wideband communication systems as well.

### **3.6 ACKNOWLEDGEMENTS**

We gratefully acknowledge contributions to this research by Mr. Richard Bijjani of Rensselaer Polytechnic Institute, as well as Mr. Matt Sherman and Dr. Eugene Skurnick of Plessey Electronic Systems Corporation.



### Chapter III - REFERENCES

- [1] R. A. Monzingo and T. W. Miller, *Introduction to Adaptive Arrays*, New York, NY: Wiley and Sons, 1980.
- [2] B. Widrow, P.E. Mantey, L. J. Griffiths, and B. B. Goode, "Adaptive antenna systems", *Proc. IEEE*, vol. 55, no. 12, pp. 2143-2159, 1967.
- [3] E. J. Baranoski and D. P. Casasent, "Optical processing of covariance matrices for adaptive processors," *Proc. SPIE*, vol. 886, pp. 140-150, 1988.
- [4] R. P. Lippmann, "An introduction to computing with neural nets," *IEEE ASSP Magazine*, pp. 4-22, April, 1987.
- [5] D. E. Rumelhart, G. E. Hinton, and R. J. Williams, "Learning internal representations by error propagation", from D. E. Rumelhart and J. L. McClelland, (editors) *Parallel Distributed Processing: Explorations in the Microstructure of Cognition, Volume 1, Foundations*; Cambridge, MA: MIT Press, 1986.
- [6] D. Casasent and M. Carlotto, "Multidimensional adaptive radar array processing using an iterative optical matrix-vector processor", *Opt. Eng.*, vol. 21, no. 5, pp. 814-821, 1982.
- [7] A. Vander Lugt, "Adaptive optical processor", *Appl. Opt.*, vol. 21, no. 22, pp. 4005-4011, 1982.
- [8] D. Psaltis and J. Hong, "Adaptive acoustooptic processor", *Proc. SPIE*, vol. 519, pp. 62-68, 1984.
- [9] E. Pochapsky and D. Casasent, "Optical linear heterodyne matrix-vector processor", *Proc. SPIE*, vol. 886, pp. 158-170, 1988.
- [10] W. Beaudet, M. Popek and D. Pape, "Advances in multi-channel Bragg cell technology", *Proc. SPIE*, vol. 639, pp. 28-33, 1986.
- [11] B. Widrow and M. E. Hoff, "Adaptive switching circuits," *1960 IRE WESCON Convention Record, part 4*, pp. 96-104, August, 1960.
- [12] J. Stanley, *Introduction to Neural Networks, 2nd Edition*, ed. by S. Luedeking, Sierra Madre, CA: California Scientific Software, 1989.
- [13] L. B. Milstein, "Interference rejection techniques in spread spectrum communications," *Proc. IEEE*, vol. 76, no. 6, pp. 657-671, 1988.
- [14] B. Widrow (study director), *DARPA Neural Network Study*, Fairfax, VA: AFCEA Int. Press, 1988.
- [15] A. D. Fisher, W. L. Lippincott, and J. N. Lee, "Optical implementations of associative networks with versatile adaptive learning capabilities," *Appl. Opt.*, vol. 26, no. 23, pp. 5039-5054, 1987.
- [16] D. Brady, X. G. Gu, and D. Psaltis, "Photorefractive crystals in optical neural computers," *Proc. SPIE*, vol. 882, pp. 132-136, 1988.
- [17] E. G. Paek, J. W. Wullert II, and J. S. Patel, "Optical learning machine for multi-category classification," *Optics News*, vol. 15, no. 12, p. 28, 1989.
- [18] K. Wagner and D. Psaltis, "Multilayer optical learning networks," *Appl. Opt.*, vol. 26, no. 23, pp. 5061-5076, 1987.
- [19] R. M. Montgomery, "Acousto-optic/photorefractive processor for adaptive antenna arrays," *SPIE Proc. 1217, OE/LASE '90*, to be published, 1990.
- [20] J. Hong, S. Hudson, Y. Yu, and D. Psaltis, "Photorefractive crystals as adaptive elements in acousto-optic processors," *SPIE Proc. 789*, pp. 136-144, 1987.
- [21] J. G. Von Saders and V. H. Syed, "An optical adaptive processor for null steering in phased array antennas," *SI SPIE Proc. 789*, pp. 80-87, 1987.
- [22] G. Borsuk, G. Anderson, and F. Kub, "Photodetectors for acousto-optic signal processing," *Proc. SPIE*, vol. 639, pp. 2-10, 1986.
- [23] D. M. Litynski, P. Das, and A. J. Urillo, "Signal processing using an integrated surface acoustic wave (SAW) acousto-electro-optic (AEO) device," *Proc. SPIE*, vol. 700, pp. 221-229, 1986.

## *Chapter IV*

# Two-Dimensional Phased-Array Optics

*Nickolas P. Vlannes*

### 4.1 INTRODUCTION

Selective control of the phase across the wavefront of light permits modulation of light in its phase wavefront pattern, and consequently the spatial intensity distribution. With active control of the elements that give selective phase modulation to an optical wavefront, dynamic phase-only spatial-light-modulators can be developed that can act to modify only the phase properties of the light without changing intensity patterns, or function as an optical analog of phased-array radar providing high speed and agile beam control for light. With the development of new organic electro-optical materials, new opportunities exist for the production of phase spatial-light-modulators as controlled phased-arrays.

Light beam modulation by varying the phase properties of light across its wavefront has been pursued for light beam deflection and modulation using bulk devices, phase gratings, and controlled arrays. Bulk device techniques were reviewed by Fowler and Schlafer [1] discussing techniques that included variable reflectors [2-5] and refractors [6-17] and birefringent [18-27] and interference [28-31] deflectors. Phase grating deflectors and modulators are primarily represented by acousto-optic modulators based on travelling acoustic waves [30-33], or electro-optic modulators formed using interdigital electrodes [34]. These phase grating techniques primarily rely on Brillouin scattering usually in the form of Bragg, Raman-Nath or Debye-Sears interference interactions. The basic concepts and applications of these devices are discussed in references [30] through [35], and presently form the basis of most nonmechanical deflection and modulation schemes. The third approach is the development of arrays of controllable

elements. Each element controls the phase of light that propagates through that element. Light that leaves the element then forms an interference pattern in the far field with the light from other elements. It is to the development of phased-arrays that this paper is addressed.

## 4.2 PHASED-ARRAY THEORY

Phased-array systems are based on the interference effect of radiating elements as light emerges from the elements and subsequently diffracts. For this discussion, two planes are specified in Figure 4.1 which also defines two coordinate systems. One of the planes and coordinate systems specifies the geometry of the array  $(x_a, y_a, z)$ , and the other plane is a parallel plane and coordinate system that specifies the location of an observer  $(x_o, y_o, z)$ . The origin of  $z$  is in the  $(x_a, y_a)$  plane. Individual elements are not shown in Figure 4.1, and it is assumed that the elements are coplanar. The light that emerges from the radiating elements is assumed to be monochromatic and have the same polarization. The electromagnetic field distribution of the light, in amplitude and phase, is specified by the function  $\Psi$ . The field distribution at the array plane is given as  $\Psi_a$ , and at the observation plane as  $\Psi_o$ . The relation between  $\Psi_a$  and  $\Psi_o$  is given by the Rayleigh-Sommerfeld theory [36] as:

$$\Psi_o(x_o, y_o) = \iint h(x_o, y_o; x_a, y_a) \Psi_a(x_a, y_a) dx_a dy_a; \quad (4.1)$$

where,

$$h(x_o, y_o; x_a, y_a) = \frac{i}{\lambda} \frac{\exp(-ikr_{oa})}{r_{oa}} \cos(\hat{n}, \bar{r}_{oa}); \quad (4.2)$$

$\lambda$  is the light wavelength,  $k$  is the magnitude of the propagation vector ( $k = 2\pi/\lambda$ );  $r_{oa}$  is given by:

$$r_{oa} = \sqrt{z^2 + (x_o - x_a)^2 + (y_o - y_a)^2}. \quad (4.3)$$

FIGURE 4.1

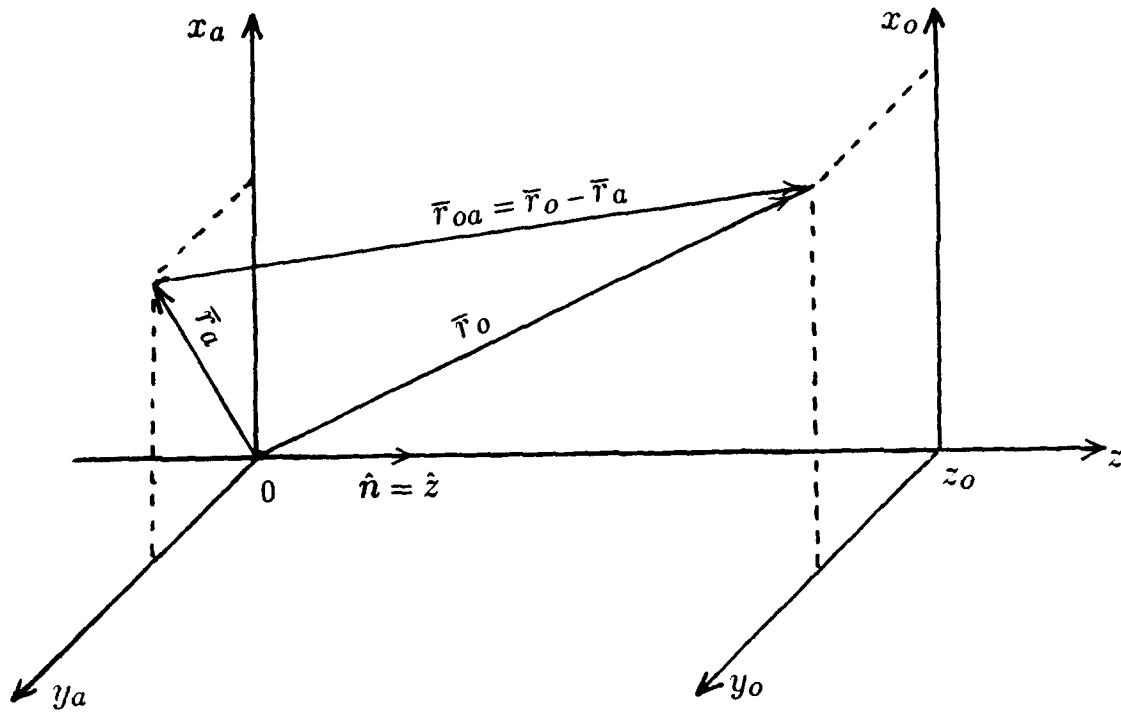


Figure 4.1. Array plane and observation plane. Array plane Cartesian coordinate system  $(x_a, y_a, z = 0)$ . Observation plane Cartesian coordinate system  $(x_o, y_o, z = z_o)$ .

and is the distance between the observer and a point in the array plane; and the term:

$$\cos(\hat{n}, \bar{r}_{oa}) = \frac{\hat{n} \cdot (\bar{r}_o - \bar{r}_a)}{|\bar{r}_o - \bar{r}_a|}. \quad (4.4)$$

The vector  $\bar{r}_a$  is the position vector of a point in the array plane with respect to the origin of the array plane coordinate system, and  $\bar{r}_o$  is the position vector of a point in the observation plane referenced to the origin of the array plane (Figure 4.1).  $\hat{n}$  is the unit vector normal to the array plane and oriented as shown in Figure 4.1.

Equation (4.1) is applicable to near-field and far-field calculations. Generally, equation (4.1) is approximated in the Fraunhofer diffraction regime which relates  $\Psi_o$  to  $\Psi_a$  via the Fourier transform of  $\Psi_a$ ,  $\mathcal{F}[\Psi_a]$ :

$$\Psi_o(x_o, y_o) = \frac{i}{\lambda z} \exp(-ikz) \exp\left[-i\frac{k}{2z}(x_o^2 + y_o^2)\right] \mathcal{F}[\Psi_a(x_a, y_a)] \quad (4.5)$$

with,

$$\mathcal{F}[\Psi_a(x_a, y_a)] = \int \int \Psi_a(x_a, y_a) \exp\left[i\frac{2\pi}{\lambda z}(x_o x_a + y_o y_a)\right] dx_a dy_a \quad (4.6)$$

let

$$f_x = \frac{x_o}{\lambda z}; \quad f_y = \frac{y_o}{\lambda z}; \quad (4.7)$$

and equation (4.6) can be rewritten as:

$$\mathcal{F}[\Psi_a(x_a, y_a)] = \int \int \Psi_a(x_a, y_a) \exp[i2\pi(f_x x_a + f_y y_a)] dx_a dy_a \quad (4.8)$$

$\Psi_o$  represents the field distribution at  $(x_o, y_o, z)$ ; however, the measureable quantity is the intensity distribution,  $I$ , which is related to  $\Psi$ . In this discussion,  $\Psi$  is normalized so that:

$$I = |\Psi|^2 \quad (4.9)$$

and thus,

$$I_o = |\Psi_o|^2 = |\mathcal{F}[\Psi_a]|^2 / \lambda^2 z^2 \quad (4.10)$$

$\Psi_a$  is composed of the contributions of each of the radiating elements. Each element adds a field distribution function  $\psi_{an}(x_a, y_a)$  to  $\Psi_a$ . The subscript  $n$  of  $\psi_n$  indicates the field distribution of the  $n^{th}$  element.  $\Psi_{an}$  and the  $\psi_{an}$  are related by:

$$\Psi_a = \sum_n \psi_{an}. \quad (4.11)$$

Consequently,  $\Psi_o$  can be represented as:

$$\Psi_o(x_o, y_o) = \frac{i}{\lambda z} \exp(-ikz) \exp\left[-i\frac{k}{2z}(x_o^2 + y_o^2)\right] \sum_n \mathcal{F}[\psi_{an}(x_a, y_a)]; \quad (4.12)$$

and the intensity  $I_o$  can be expressed as:

$$I_o = \frac{1}{\lambda^2 z^2} \left| \sum_n \mathcal{F}[\psi_{an}] \right|^2 \quad (4.13)$$

Each  $\psi_{an}$  consist of a magnitude,  $A_n(x_a, y_a)$ , and phase,  $\phi_n(x_a, y_a)$  which are functions of  $x_a$  and  $y_a$ . The relation among these terms is:

$$\psi_{an} = A_n(x_a, y_a) \exp[i\phi_n(x_a, y_a)], \quad (4.14)$$

Equations (4.1) through (4.14) provide the theoretical basis for phased-array optics. A discussion of several elementary examples of phased arrays ensues. The arrays are restricted to vary in one dimension,  $x_a$ , and uniform in  $y_a$ . Figure 4.2 shows the one dimensional relation between the array plane and the observer plane. These simple examples provide basic models for the design of phased array optical devices that are discussed section 4.5.

The simplest array consists of a single element with uniform magnitude and phase. Figure 4.3 illustrates this one dimensional case. This element has a uniform magnitude,  $a$ , and phase,  $\varphi$ .  $\psi_{a1}$  is then represented as:

$$\psi_{a1} = ae^{i\varphi} \text{rect}\left[\frac{x_a - \Delta}{\delta}\right] \quad (4.15)$$

FIGURE 4.2

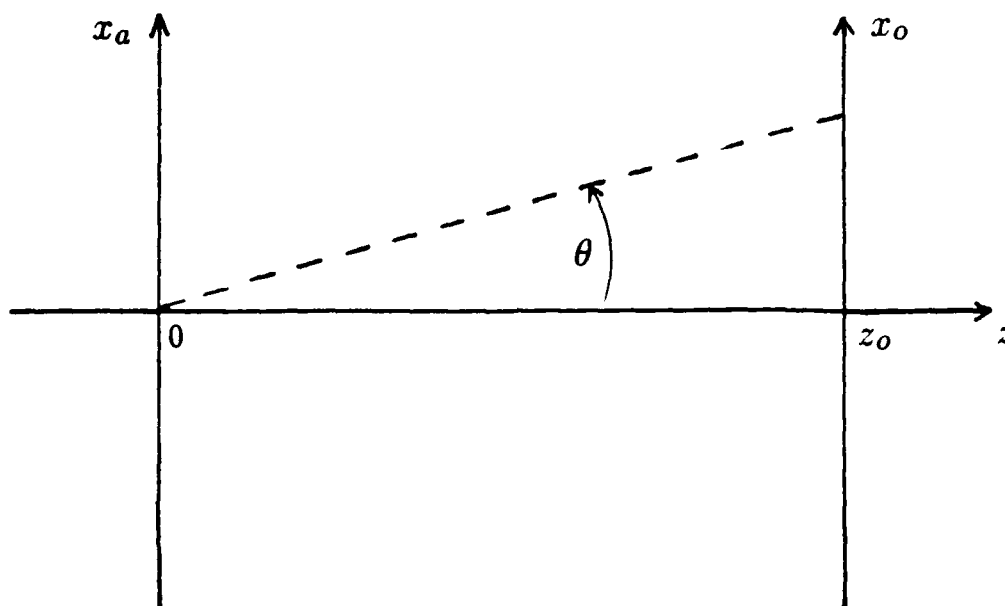


Figure 4.2.  $x_a$  and  $x_o$  coordinate axes.

FIGURE 4.3

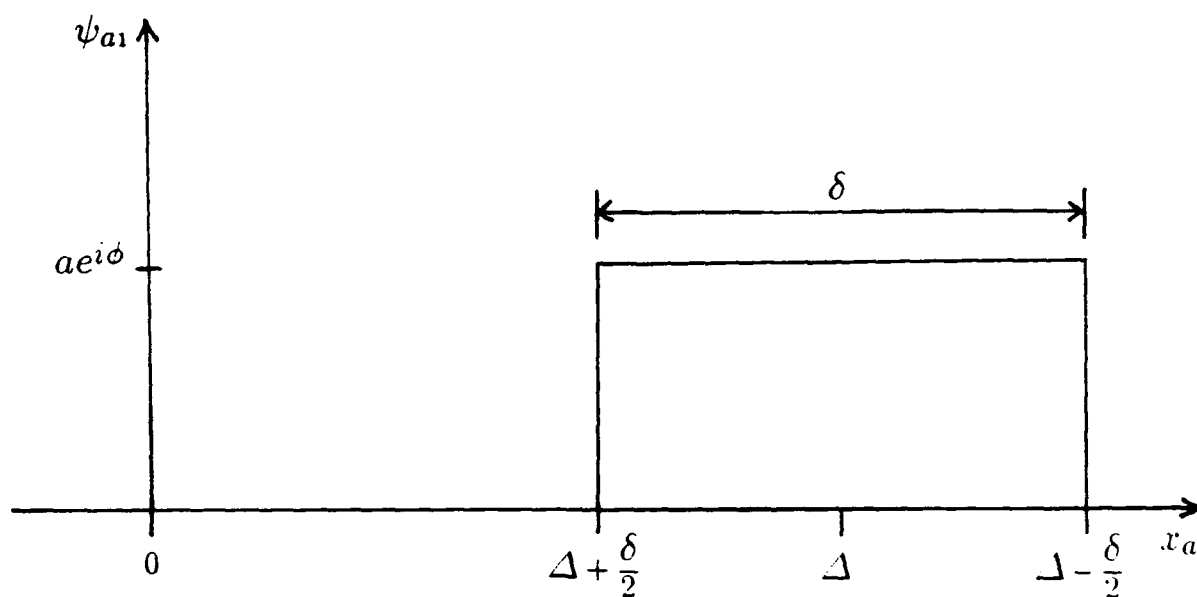


Figure 4.3. Single element field distribution at array plane,  $\psi_{a1}$ .



the *rect* function is specified as:

$$\text{rect}(x) = \begin{cases} 1, & \text{if } |x| \leq 1/2; \\ 0, & \text{otherwise;} \end{cases}$$

$\Delta$  is the position of the center of the element, and  $\delta$  is the width of the element. Substituting (4.15) into equation (4.5) yields a single element far-field distribution pattern,  $\psi_{o1}$  of:

$$\psi_{o1} = \frac{i}{\lambda z} \exp(-ikz) \exp\left[-i\frac{k}{2z}(x_o^2)\right] a\delta \exp[i(\varphi + 2\pi f_x \Delta)] \left[\frac{\sin(\pi f_x \delta)}{\pi f_x \delta}\right] \quad (4.16)$$

The intensity distribution of the single element,  $I_{o1}$ ,

$$I_{o1} = |\psi_{o1}|^2 = \frac{a^2 \delta^2}{z^2 \lambda^2} \left[\frac{\sin(\pi f_x \delta)}{\pi f_x \delta}\right]^2 \quad (4.17)$$

The term  $f_x = x_o/\lambda z$  permits equation (4.17) to be rewritten in terms of the normalized variables;  $\hat{\delta} = \delta/\lambda$ ,  $\hat{a} = a/z$ , and  $\hat{x}_o = x_o/z$ ; as:

$$I_{o1} = |\psi_{o1}|^2 = \hat{a}^2 \hat{\delta}^2 \left[\frac{\sin(\pi \hat{\delta} \hat{x}_o)}{\pi \hat{\delta} \hat{x}_o}\right]^2 \quad (4.18)$$

Alternatively, equation (4.18) can be expressed in terms of the relation:

$$\tan(\theta) = \frac{x_o}{z} = \hat{x}_o \quad (4.19)$$

where  $\theta$  is specified in Figure 4.2. Equation (4.18) then becomes:

$$I_{o1} = |\psi_{o1}|^2 = \hat{a}^2 \hat{\delta}^2 \left[\frac{\sin(\pi \hat{\delta} \tan(\theta))}{\pi \hat{\delta} \tan(\theta)}\right]^2 \quad (4.20)$$

As can be seen from equations (4.17) - (4.20), the intensity distribution is dependent on the distance the observer is from the array plane,  $z$  and the position in the observer plane,  $x_o$ , or equivalently the angle  $\theta$ ; the width of the element,  $\delta$ ; and the magnitude,  $a$ . The uniform phase  $\varphi$  does not contribute to the intensity distribution for the single element; however, as seen below,  $\varphi$  affects the intensity distribution of multiple element arrays.

The second example to be discussed is an array of  $N$  elements with equal and constant magnitude,  $a$ ; with element width  $\delta$ ; uniformly spaced with periodicity,  $\Lambda$ ; but with different phases  $\varphi_n$ , where the subscript  $n$  indicates the  $n^{\text{th}}$  element. Figure 4.4 illustrates this geometry. If the  $x_o$  coordinate system is placed at the center of the array, then the field distribution pattern,  $\Psi_a$  can be expressed as:

$$\Psi_a = \sum_{n=1}^N a \text{rect} \left[ \frac{x_o - \Lambda[n - (N+1)/2]}{\delta} \right] \exp(i\varphi_n) \quad (4.21)$$

Applying equation (4.5) gives:

$$\begin{aligned} \Psi_o = \frac{i}{\lambda z} \exp(-ikz) \exp \left[ -i \frac{k}{2z} (x_o^2) \right] \exp[-i(2\pi f_x \Lambda((N+1)/2))] \\ \left[ \frac{\sin(\pi f_x \delta)}{\pi f_x \delta} \right] \sum_{n=1}^N \exp[i(\varphi_n + 2\pi f_x \Lambda n)] \end{aligned} \quad (4.22)$$

If the difference in phase between nearest neighbor elements is a constant,

$$\varphi_n = n\varphi_o; \text{ and } \varphi_n - \varphi_{n-1} = \varphi_o \quad (4.23)$$

then equation (4.22) can be rewritten as:

$$\Psi_o = \frac{i}{\lambda z} \exp(-ikz) \exp \left[ -i \frac{k}{2z} (x_o^2) \right] a\delta \left[ \frac{\sin(\pi f_x \delta)}{\pi f_x \delta} \right] \left[ \frac{\sin[N(2\pi f_x \Lambda + \varphi_o)/2]}{\sin[(2\pi f_x \Lambda + \varphi_o)/2]} \right] \quad (4.24)$$

The intensity  $I_o = |\Psi_o|^2$  yields:

$$I_o = \frac{a^2 \delta^2}{\lambda^2 z^2} \left[ \frac{\sin(\pi f_x \delta)}{\pi f_x \delta} \right]^2 \left[ \frac{\sin[N(2\pi f_x \Lambda + \varphi_o)/2]}{\sin[(2\pi f_x \Lambda + \varphi_o)/2]} \right]^2 \quad (4.25)$$

or,

$$I_o = I_{o1} \left[ \frac{\sin[N(2\pi f_x \Lambda + \varphi_o)/2]}{\sin[(2\pi f_x \Lambda + \varphi_o)/2]} \right]^2 \quad (4.26)$$

The intensity  $I_o$  contains terms that are characteristic of the array and the elements. As seen in equation (4.26),  $I_o$  has the intensity distribution pattern of a single element modified by a term that contains properties of the array. The expressions:

$$\left[ \frac{\sin(\pi f_x \delta)}{\pi f_x \delta} \right]^2; \text{ and } \left[ \frac{\sin[N(2\pi f_x \Lambda + \varphi_o)/2]}{\sin[(2\pi f_x \Lambda + \varphi_o)/2]} \right]^2;$$

FIGURE 4.4

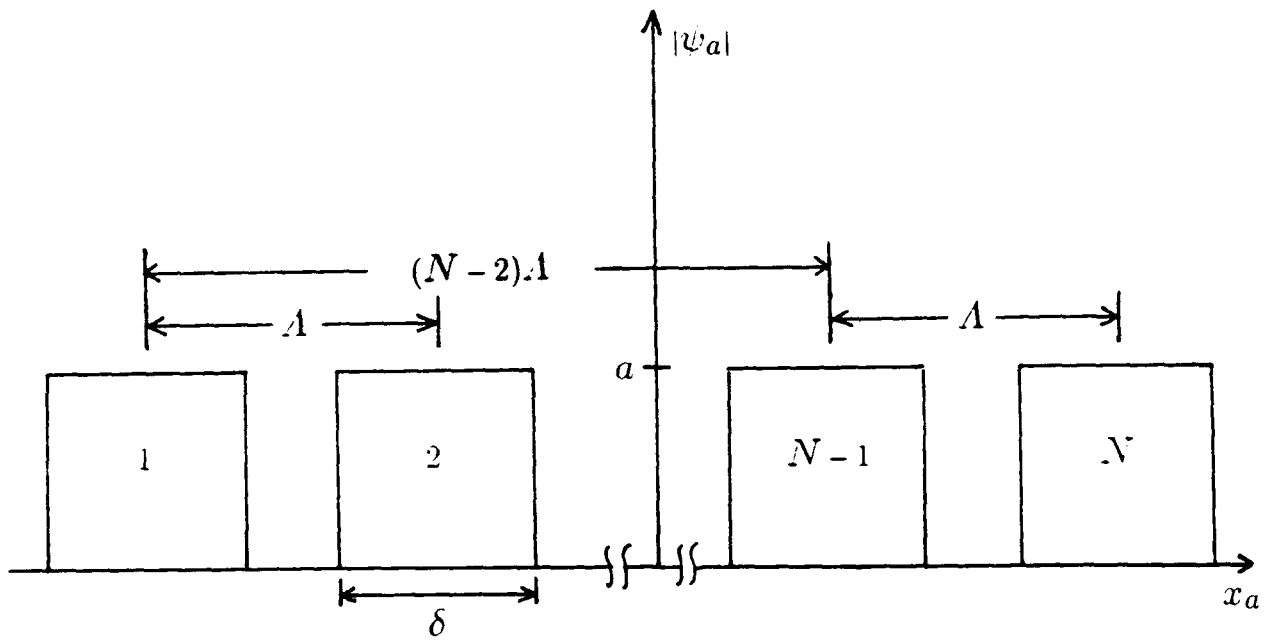


Figure 4.4. Array of  $N$  elements of equal spatial distribution. Field magnitude of each element is identical,  $a$ . Phase of each element,  $\varphi_n$  is different.

specify the spatial distribution of the intensity in the  $x_o$  coordinate direction in the observer plane. The first of these two expressions is identified as the element-factor  $E_f$ :

$$E_f = \left[ \frac{\sin(\pi f_x \delta)}{\pi f_x \delta} \right]^2; \quad (4.27)$$

and the other term is the array-factor,  $A_f$ :

$$A_f = \left[ \frac{\sin[N(2\pi f_x \Lambda + \varphi_o)/2]}{\sin[(2\pi f_x \Lambda + \varphi_o)/2]} \right]^2 \quad (4.28)$$

Equation (4.27) is plotted in Figure 4.5(a), and equation (4.28) is shown in Figure 4.5(b) with  $\varphi_o = 0$ . The product of  $A_f$  and  $E_f$ :

$$\hat{I} = A_f \cdot E_f = I_o \left[ \frac{a^2 \delta^2}{\lambda^2 z^2} \right]^{-1} \quad (4.29)$$

is given in Figure 4.5(c). The normalized intensity  $\hat{I}$  has a main central lobe, with symmetric side-lobes.

If the relative phase term  $\varphi_o$  is not zero, then  $A_f$  is shifted along the horizontal axis as shown in Figure 4.6(b). Figure 4.6(a) is identical to Figure 4.5(a) and is reproduced to show the relative shape between  $E_f$  and  $A_f$  when  $\varphi_o \neq 0$ . Figure 4.6(c) shows  $\hat{I}$ . In this case, the central lobe of  $\hat{I}$  has shifted along  $x_o$  and decreased in value, while one of the side-lobes has increased. By controlling  $\varphi_o$ , the intensity pattern can be shifted in space; however, as the magnitude of  $\varphi_o$  increases, the side-lobe continues to increase in value until it is of the same magnitude as the former central lobe, and then becomes the central lobe. If a single beam is intended with minimum of side-lobes, then the range of  $\varphi_o$  is limited and the resolution of the intensity pattern is reduced. The growth of the side-lobe is due to the stationary element factor. As the array-factor moves as a function of  $\varphi_o$ , the multiple lobes of the array-factor are then multiplied by the stationary element-factor, and the side-lobes increase until a new central lobe is formed. However, if the element-factor can also be made to move simultaneously

FIGURE 4.5

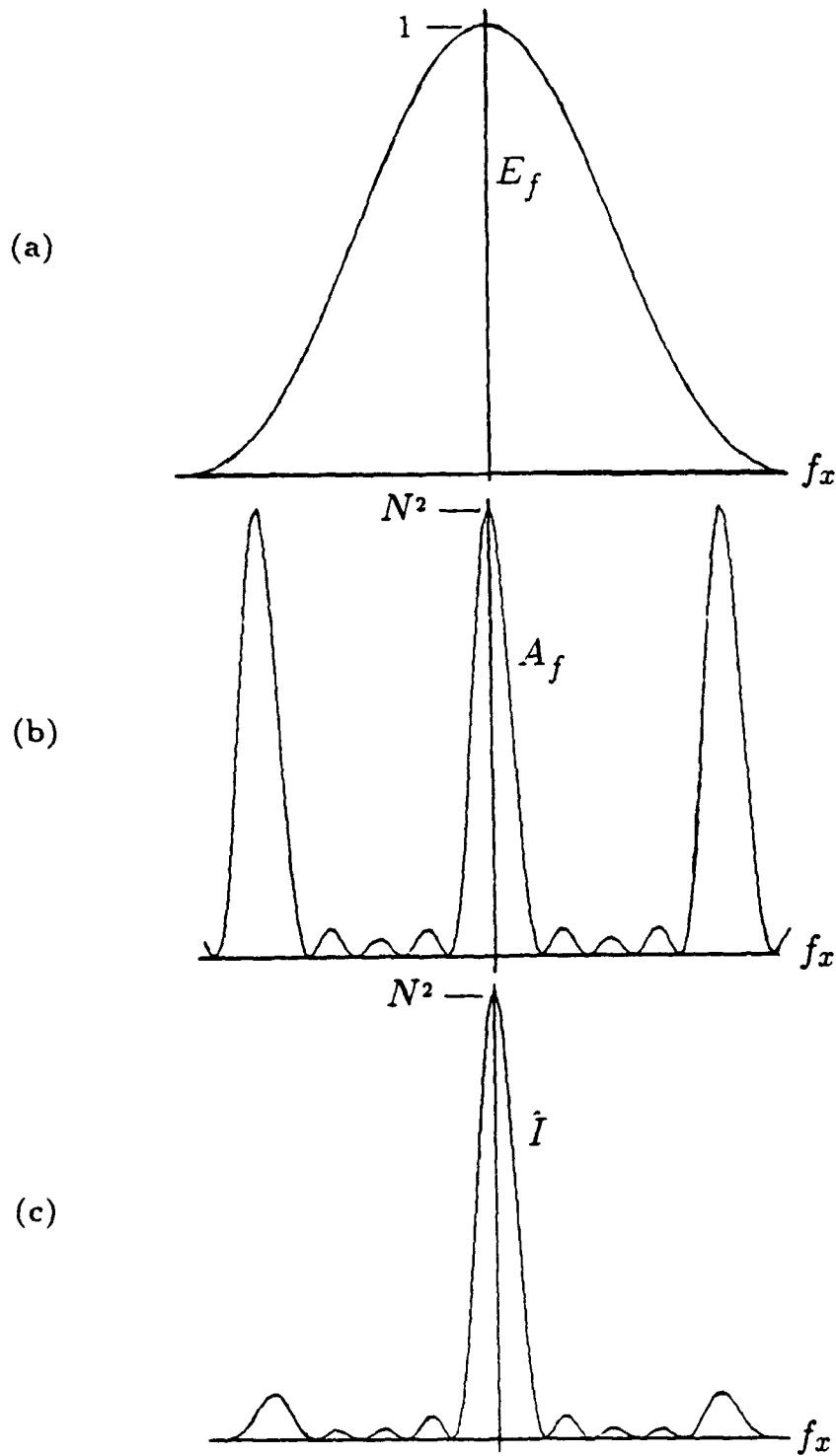


Figure 4.5. Spatial Patterns,  $\varphi_0 = 0$ . (a) Element-factor,  $E_f$ . (b) Array-factor,  $A_f$ . (c) Normalized intensity distribution,  $\hat{I}$ .

with the array-factor, so that the relative spatial patterns of  $A_f$  and  $E_f$  remain the same, then  $\hat{I}$  can be made to retain its shape and be moved along  $x_o$ .

To accomplish movement of the element-factor in  $x_o$ , the phase terms  $\phi_n$  must have a spatial function in  $x_a$  that is identical for each element. A simple linear function  $x_a$  for  $\phi_n$  will introduce a uniform variable for changing the position of the element factor. The functional form of  $\phi_n$  becomes:

$$\phi_n = \left[ n\varphi_o + \frac{2\varphi_e}{\delta}(x_a - \Lambda[n - (N + 1)]/2) \right] \text{rect} \left[ \frac{x_a - \Lambda[n - (N + 1)]/2}{\delta} \right] \quad (4.30)$$

Figure 4.7 shows this functional form for  $\phi_n$ . Using this expression in calculating  $\hat{I}$ , the element-factor becomes:

$$E_f(\varphi_e) = \left[ \frac{\sin(\pi f_x \delta + \varphi_e)}{\pi f_x \delta + \varphi_e} \right]^2 \quad (4.31)$$

$\hat{I}$  can be written as:

$$\hat{I} = \left[ \frac{\sin(\pi f_x \delta + \varphi_e)}{\pi f_x \delta + \varphi_e} \right]^2 \left[ \frac{\sin[N(2\pi f_x \Lambda + \varphi_o)/2]}{\sin[(2\pi f_x \Lambda + \varphi_o)/2]} \right]^2 \quad (4.32)$$

Rewriting equation (4.32):

$$\hat{I} = \left[ \frac{\sin(\pi \delta [f_x + \varphi_e/\pi \delta])}{\pi \delta [f_x + \varphi_e/\pi \delta]} \right]^2 \left[ \frac{\sin(N\pi \Lambda [f_x + \varphi_o/2\pi \Lambda])}{\sin(\pi \Lambda [f_x + \varphi_o/2\pi \Lambda])} \right]^2 \quad (4.33)$$

With  $\Lambda > \delta$ , a smaller change in  $\varphi_e$  will shift the element-factor by the same amount for a given  $\varphi_o$ . Thus a mechanism exists for shifting both the element and array-factor, and hence moving the intensity pattern  $\hat{I}$  in space and retaining the shape of  $\hat{I}$ . Figure 4.8 shows both a shift in  $A_f$  and  $E_f$  that preserves the shape of  $\hat{I}$ .

Regardless of how the element-factor or array-factor is moved, side-lobes will remain in the intensity pattern due to the periodicity of the array-factor which has multiple lobes (Figures 4.5(b) and 4.6(b)). However, for application, side-lobes are an unwanted characteristic. Side-lobes impede directing optical

FIGURE 4.6

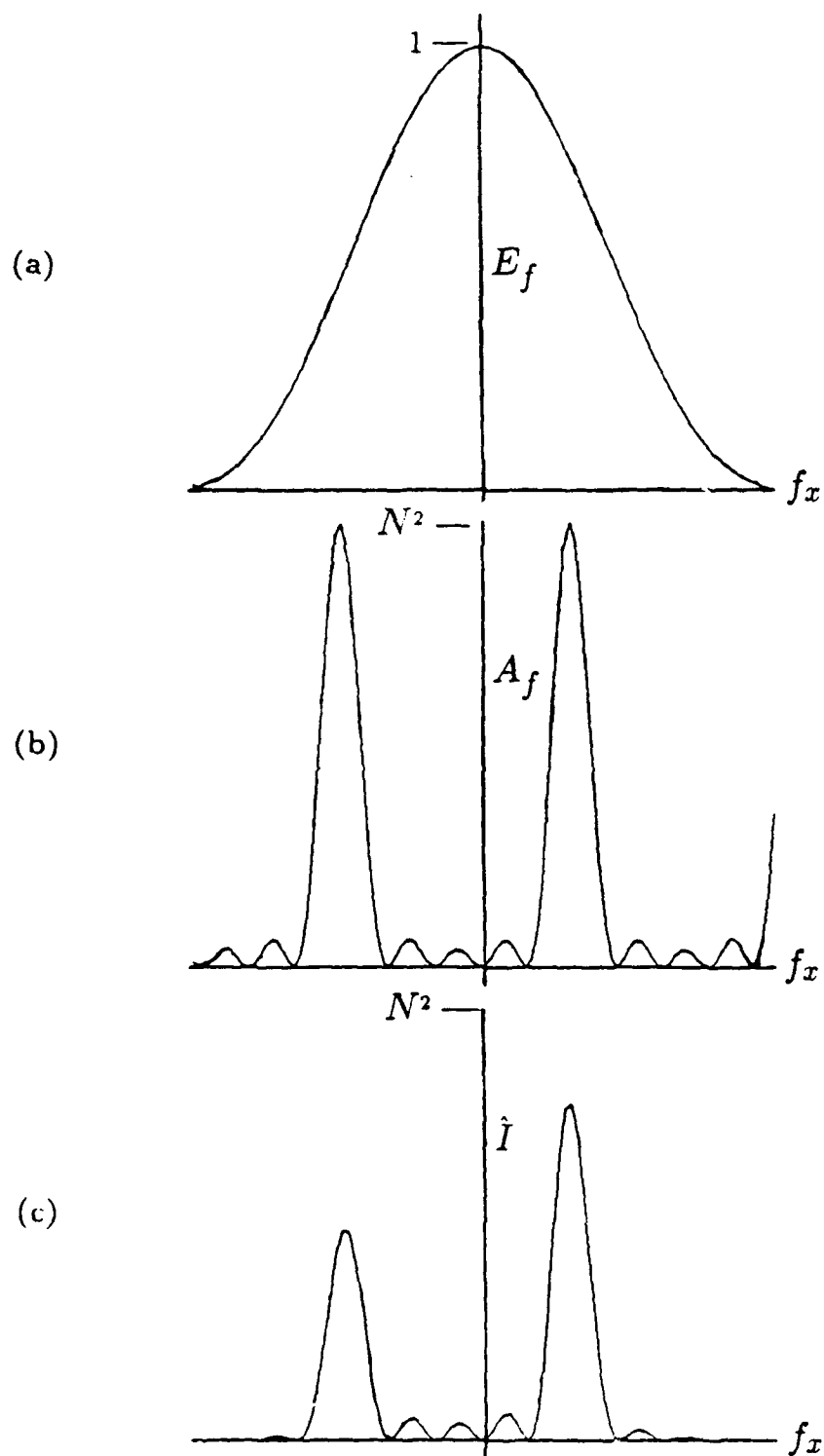


Figure 4.6. Spatial Patterns,  $\varphi_0 \neq 0$ . (a) Element-factor,  $E_f$ . (b) Array-factor,  $A_f$ . (c) Normalized intensity distribution,  $\hat{I}$ .

FIGURE 4.7

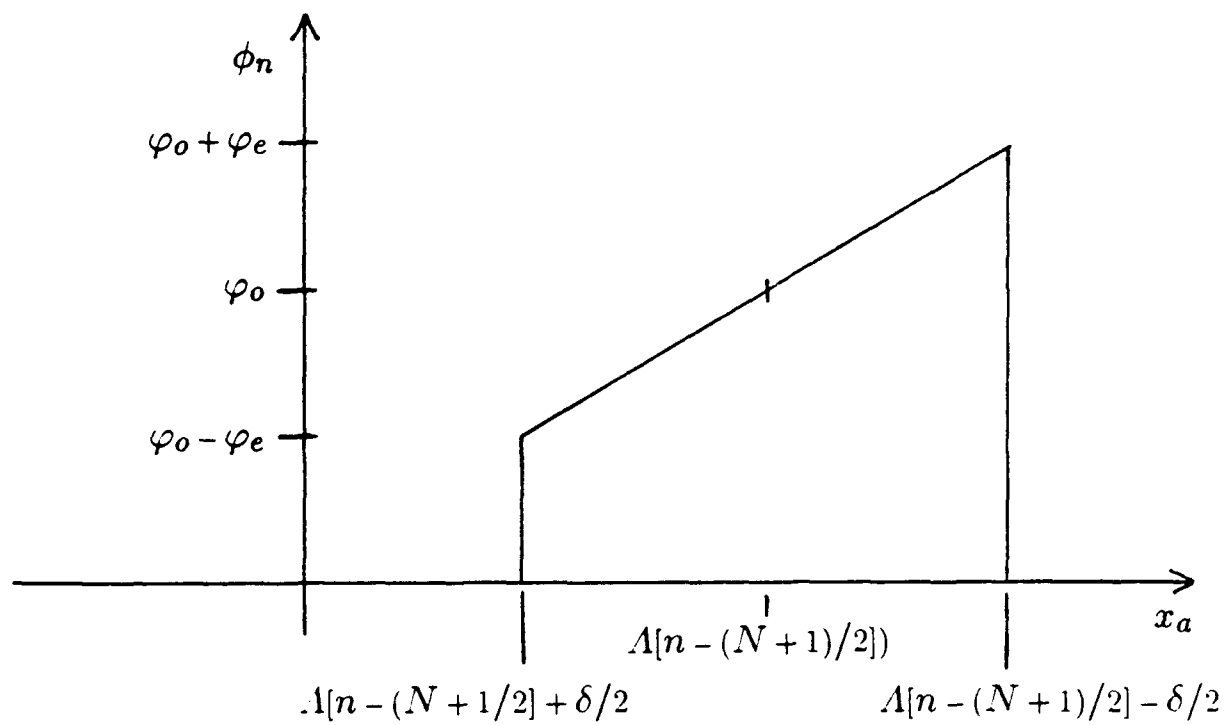


Figure 4.7. Element spatial phase distribution,  $\phi_n$ , as a function of position,  $x_a$ .



FIGURE 4.8

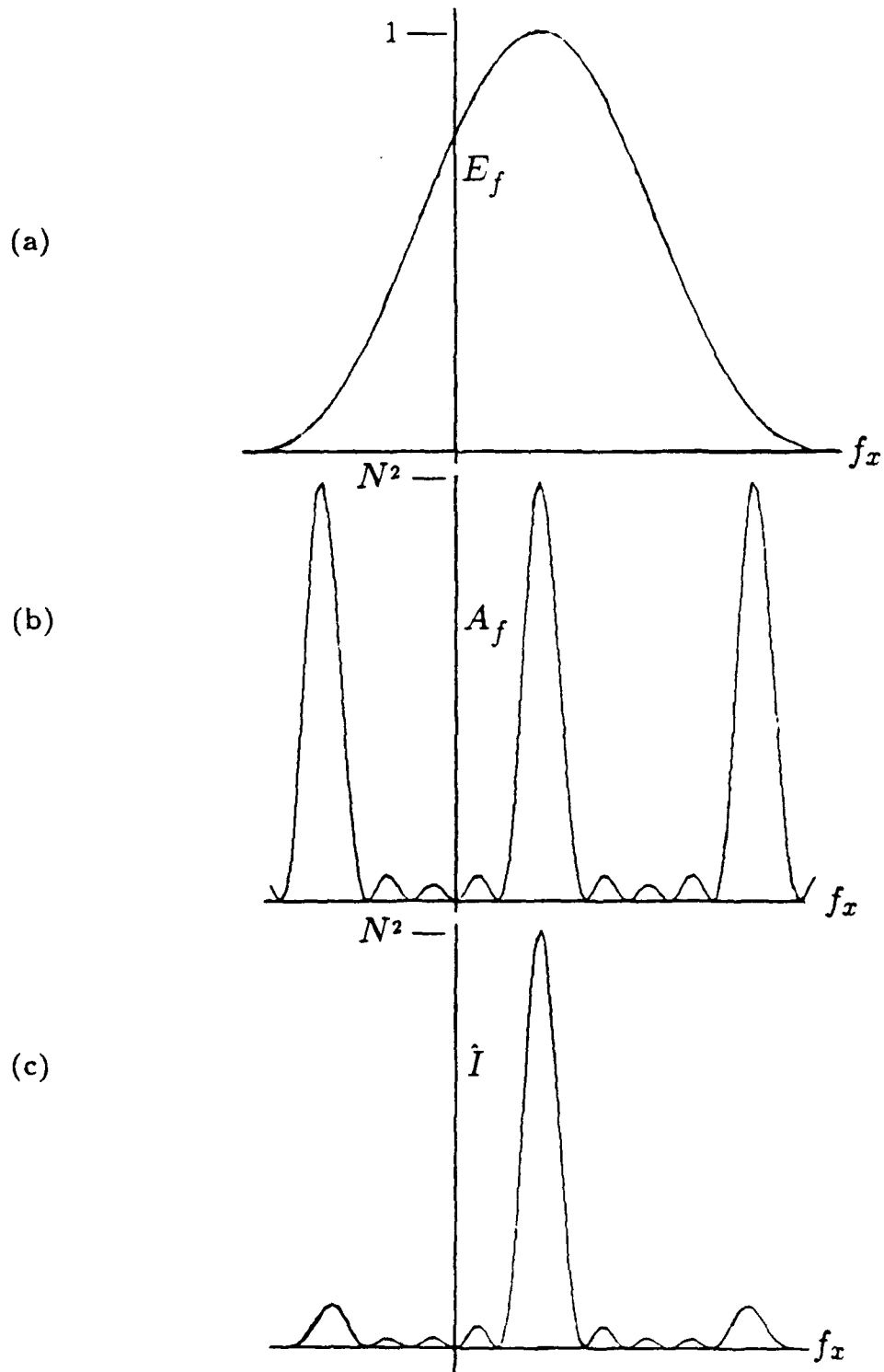


Figure 4.8. Spatial Patterns,  $\varphi_o \neq 0, \varphi_e = \varphi_o \delta / 2\Lambda$ . (a) Element-factor,  $E_f$ . (b) Array-factor,  $A_f$ . (c) Normalized intensity distribution,  $\hat{I}$ .

energy at a single target, reduce the angular range, and decrease the number of resolvable spots. One method of reducing the side-lobes in the intensity pattern,  $\hat{I}$  is to increase the spacing between adjacent lobes of the array-factor. This requires decreasing the spacing between emitters at the array plane. This approach is hindered by the current inability to fabricate center-to-center spacing between the emitters less than optical wavelengths. The minimum  $\Lambda$  between the centers of each element of the array is  $\delta$ , which yield a minimum of side-lobe amplitude. Therefore side-lobes can be designed to be a minimum, but will remain part of the intensity distribution at the observer plane for the emitter geometry discussed. An alternative approach for side-lobe reduction, proposed by Abeles and Deri [37], is to “chirp” the spacing between identical emitters which changes the array factor. By eliminating the periodicity of the array, the constructive interference that creates the periodicity of the array-factor is removed, while the main lobe remains intact. The interelement spacing,  $\Delta_{j+1,j}$  between the  $j$  and  $j + 1$  ( $j \geq 1$ ) adjacent elements is given as:

$$\Delta_{j+1,j} = d_a + c_o(j - 1) \quad (4.34)$$

with  $d_a$  the minimum spacing between elements and  $c_o$  the chirp factor. With this spacing side lobes have been reduced to 2.9% of the main lobe [37].

Therefore it is conceivable that arrays with chirped spacing that have an array-factor with reduced side-lobes, and is scannable in space due to a variable phase relation (equation (4.23)), can be formed. This array pattern can be coupled with elements that have the element-factor that is scannable due to phase variation across each element (equation (4.30)), and thus produce a scannable intensity distribution that has a predominant main lobe that is preserved during scanning and which can be directed.

As indicated, the above discussion is intended as a reference and background to the design of phased-array devices discussed in the following sections. This discussion presents concepts that have been considered for one dimensional scanning devices, and reference [38] presents an evaluation of several of these devices. With this theoretical basis, a discussion of previous research into optical phased arrays follows in the next section.

### 4.3 PHASED-ARRAY MODULATOR BACKGROUND

Phased array modulators that have been fabricated are one dimensional modulators in that light is spatially varied in only one direction. These devices were initially implemented in electro-optical crystalline ceramic materials, such as lithium tantalate [39] and lithium niobate [40-43], as platelet and in diffused thin film devices. More recently, electro-optic semiconductor devices using GaAs/AlGaAs have been fabricated [44-50, 53]. The electro-optic ceramic material devices were formed with two primary approaches to device design. These are the channel devices (Figure 4.9) [39,40] and prism type devices (Figure 4.10) [42-43,52]. The semiconductor devices have been a multilayer stack in which each layer contains a planar electro-optical waveguide (Figure 4.11) [44]; a modification of the prism concept as a tuneable lens for a laser diode [45-47]; tuneable twin-stripe channel diode lasers [48,49]; and surface gratings [50,51]. A brief discussion of these devices ensues.

Channel devices were developed as channel-electrode devices (Figure 4.9a) [39], and channel-waveguide structures (Figure 4.9b) [40]. The channel-electrode device uses an array of electrodes deposited on one surface of a platelet with a common plane deposited on the underlying surface [39] (Figure 4.9a). Each electrode acts as a separate channel to modulate the phase across the wavefront. In contrast, the channel-waveguide device utilizes channel dielectric waveguides

FIGURE 4.9

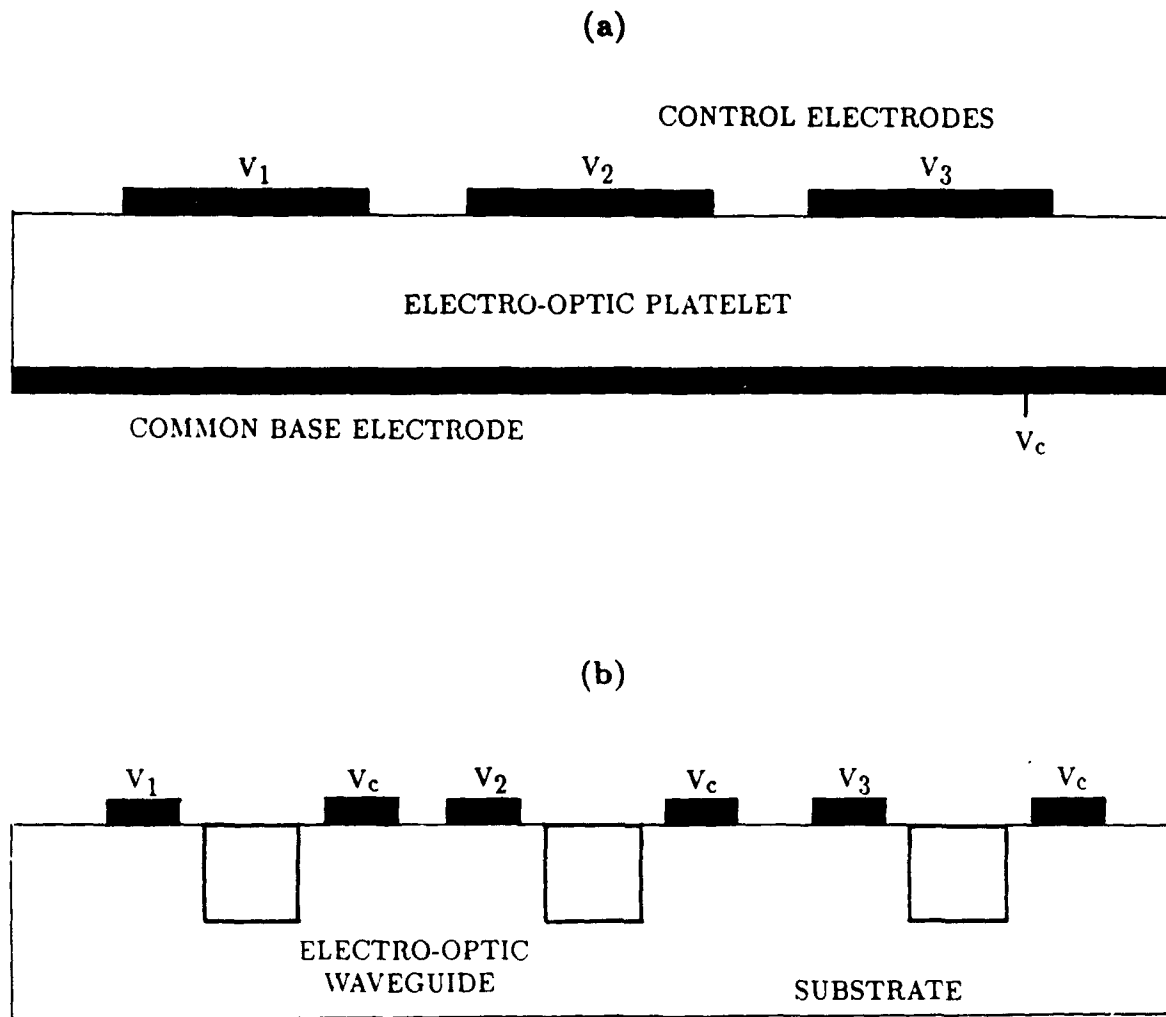


Figure 4.9. Channel array devices as viewed in cross-section. (a) Platelet channel-electrode structure. (b) Channel waveguides with surface control electrode geometry.

FIGURE 4.10

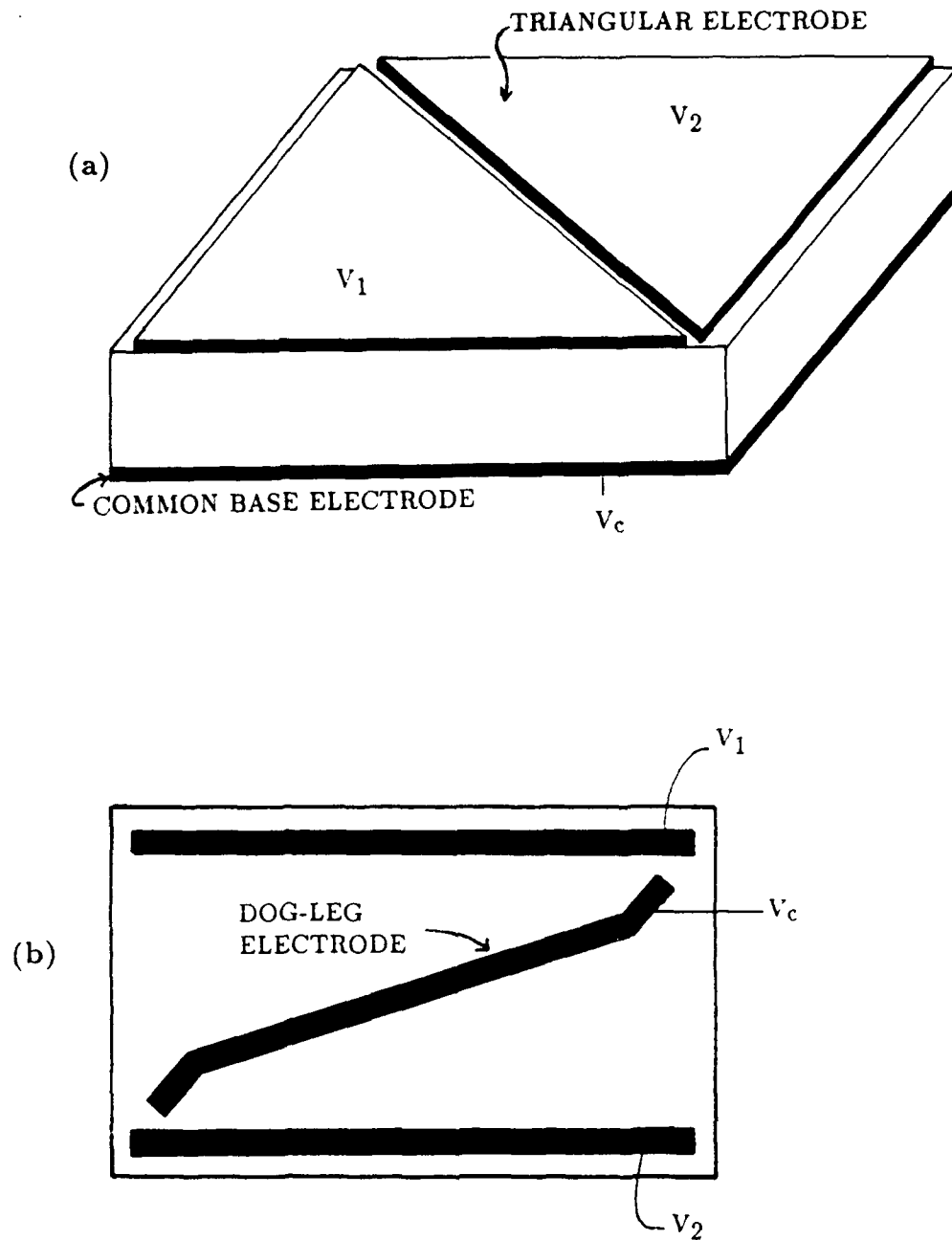


Figure 4.10. Artificial prism devices. (a) Perspective view of platelet with triangular parallel plate electrode structure. (b) Top view of surface electrode geometry with dog-leg electrode.

formed into the substrate, and an electrode pair for each waveguide deposited on the surface of the substrate controls the phase of the light in each waveguide.

The prism device is an evolution of the bulk prism devices [9,22,23,49]; however, instead of an actual prism, the electrodes of the device induce index of refraction change that simulate prisms. The artificial prism devices were developed with two different electrode configurations. One of these is the parallel plate electrode structure shown in Figure 4.10a [41], and Figure 4.10b illustrates the surface electrode geometry [42,43]. The geometry of Figure 4.10(a) utilizes a platelet with the electrode deposited on the top and bottom surfaces. Figure 4.10(b) has a planar waveguide embedded in the surface of an electro-optic substrate, such as titanium diffused in  $\text{LiNbO}_3$  [42,43], and the controlling electrodes are then deposited on the surface over the waveguide. These prism electrode-structures use three electrodes in which two electrodes act with a common electrode. Typically, electric potentials of opposite polarity are applied to the control electrodes ( $V_1$  and  $V_2$ ) against a common electrode ( $V_c$ ). With the electrodes applying an electric field in opposite directions for each half of the structure an increase and decrease in index of refraction occurs inducing a double prism. A single artificial prism device can act as a light deflector; however, the number of resolvable spots for a given deflection angle is enhanced with an array of prisms [39,52]. Recently a hybrid design consisting of electro-optic gratings and artificial prisms has been developed, in which both techniques are used simultaneously in beam scanning. These hybrid devices are based on AlGaAs as the electro-optic material [53].

Both the channel and prism devices were developed with all the elements of the devices parallel to the surface of the platelets or substrates on which guiding layers were formed. This permits scanning of light in only one dimension, and

for freely propagating light the scan is parallel to the surface of the platelet or substrate.

Figure 4.11 illustrates the geometry of the planar multilayer stack. Electro-optical material is sandwiched between electrodes. In the case of the multilayer semiconductor devices [44] the electrodes are alternately n-type and p-type AlGaAs, and the electro-optical material is intrinsic AlGaAs or GaAs. The intrinsic layer acts as a planar dielectric waveguide in which the index of refraction can be modified by a potential difference between the two neighboring electrodes. This geometry permits scanning of light perpendicular to the planar layers.

The twin stripe injection beam steering concept [48,49] utilizes two diode lasers in close proximity. The phase and intensity of the light in each laser is modified by the injection current. This type of device is conceivably applicable to more than two diode lasers in an array pattern, and is an extension of the channel array.

Grating devices for scanning [50,51] have been developed to scan light in one dimension. These devices use a fixed grating periodicity, and then vary the wavelength of light that encounters the grating. The angle at which the beam emerges from interaction with the grating is wavelength dependent, and as the wavelength is changed, the beam angle changes to scan the light. These devices have scan angles of at most a few degrees, and require a variable wavelength light source.

Figures 4.9, 4.10, and 4.11 represent different methods of light modulation and structure geometry. Figure 4.9 and Figure 4.11 employ array modulation, that is  $\varphi_o$  is changed and  $\varphi_e = 0$  (equation (4.33)). Alternatively, the artificial prism method of Figure 4.10 uses element modulation,  $\varphi_e \neq 0$  and  $\varphi_o$  is unchanged. Figures 4.9 and 4.10 are single layer coplanar structures which permit

FIGURE 4.11

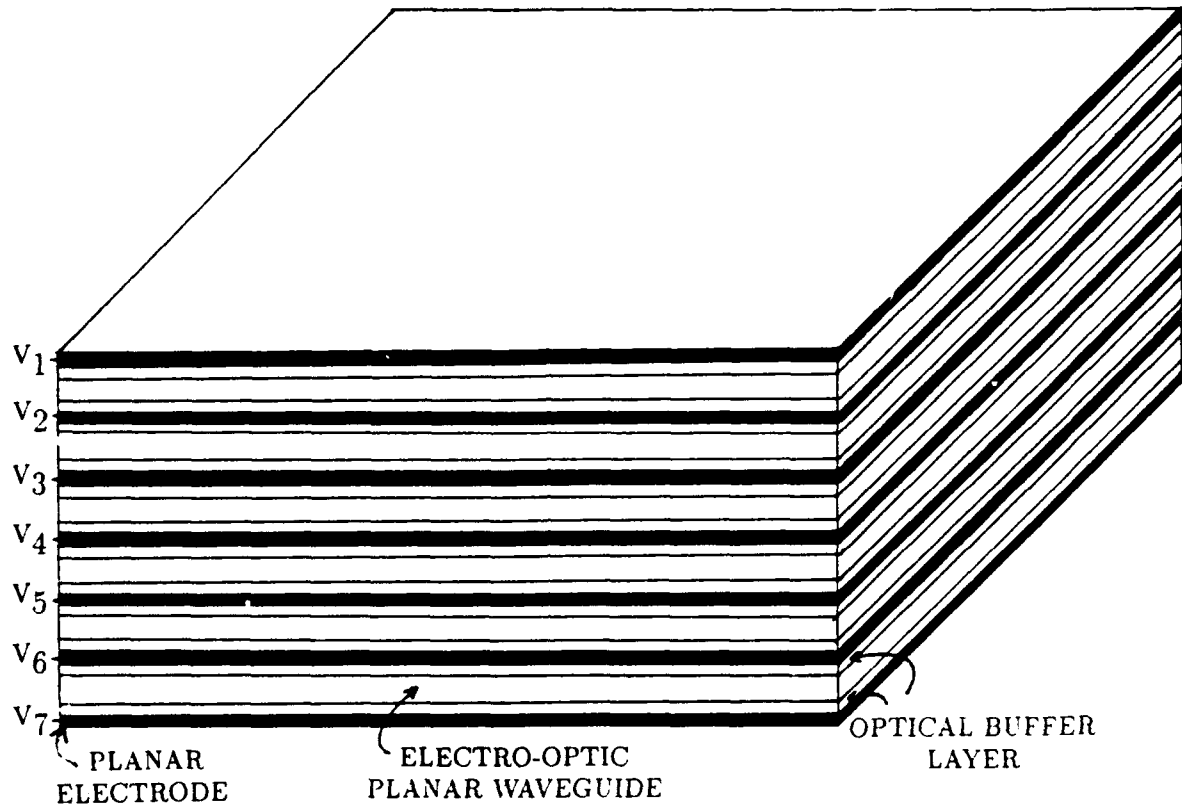


Figure 4.11. Planar multilayer stack.  $V_i, i = 1, \dots, 8$  are control electric potentials.



scanning parallel to the plane of the structures. In contrast, Figure 4.11 is a multilayer structure with each layer uniform, and the scan direction is perpendicular to the layers. All of these devices only permit modulation in one dimension, and none utilize simultaneous element and array modulation. Combining multiple layers of coplanar structures would permit phased-array control in two dimensions. It is to the development of devices with two-dimensional modulation, that combines element and array modification, that research has been conducted and the following sections are addressed.

#### 4.4 PHASED-ARRAY OPTICS – ELECTRO-OPTICAL MATERIALS

Because of the control provided by electric fields, phased-array optics has been explored with electro-optic materials, and devices have been fabricated with semiconductors and the crystalline ceramics. Recently electro-optic organic materials [54-70] have been synthesized that may be applied to phased-array optics, and be the most versatile in fabricating phased-array devices. This versatility is based on the low fabrication temperature of electro-optic organic material ( $< 200^{\circ}\text{C}$ ) in comparison to semiconductor and ceramic materials, on the comparative ability of these materials to adhere to other materials such as metals, and on the ability to specify electro-optic axes after the material is deposited.

The magnitude of the electro-optic effect in presently known electro-optic materials limits the device design of phased-array optics, and subsequently presents drawbacks for application of semiconductor and crystalline ceramic materials. Currently, the strongest electro-optic materials are the crystalline ceramics followed by the electro-optic organics. The primary crystalline ceramic that has found technological application is lithium niobate,  $\text{LiNbO}_3$ . Barium titanate has a larger electro-optic effect [101]; however, bulk single crystal and thin films of this material do not have the crystalline quality of lithium niobate.  $\text{LiNbO}_3$  has an  $n^3r$  value of 328 pm/V (picometers/Volt). One of the strongest electro-optic

organic material is HC-1232 with  $n^3r = 195 \text{ pm/V}$  [68,75].  $n$  is the unperturbed index of refraction of the material and  $r$  is the electro-optic coefficient.  $n^3r$  is the figure of merit since it represents the quantity that is multiplied by electric field to calculate changes in index of refraction with an electric field applied, and thus light phase shift as the light propagates through the material. For both  $\text{LiNbO}_3$  and HC-1232, in order to induce electro-optic phase shifts of  $\pi$  with voltages as high as 20 volts over 5 microns requires a propagation path of several millimeters to 2.5 cm [71-76]. In order to effect the far field interference pattern of the array for such applications as beam steering, each element of the array must be on the order of, or less than, 50 to 200 optical wavelengths of each other, hence on the order of 50 to 200 microns or less. Thus each array element is an optical waveguide, and not a planar pixel such as found in liquid crystal displays. Except for applications in which light is to be confined to a single plane within the electro-optic material, or is end-emitted from a single plane and diffracts spatially (Figure 4.9), a three-dimensional stack must be formed with each layer containing emitting elements. The simplest type of stack is the generic planar structure as shown in Figure 4.11, and has been implemented in a semiconductor structure [44]. However, the implementation of this geometry illustrates the difficulties of working with semiconductor materials and correspondingly ceramic materials.

In order to fabricate the simple planar stack shown in Figure 4.11, multiple layers of materials must be deposited to form the electro-optic waveguide layers and the electrodes. Fabrication of crystalline semiconductor or ceramic layers can require high temperatures (greater than  $500^\circ\text{C}$ ), high vacuum ( $10^{-10}$  torr to  $10^{-6}$  torr), low growth rates (one micron per several hours), or combination of these factors [77,78]. High temperatures and low-growth rates are exhibited by liquid-phase-epitaxy (LPE), molecular-beam-epitaxy (MBE), and

organo-metallic chemical vapor deposition (OMCVD). The high temperatures associated with these processes preclude formation of stacks of materials that do not have similar chemistry. As an example, if materials, such as metals, are deposited to form electrode-structures for electro-optic control, additional layers of the electro-optic materials cannot be deposited over the metal without the risk of destroying the metal patterns due to the high temperature of deposition, or the electro-optic materials may not grow over the additional materials and retain their properties. This particular problem was addressed for GaAs/AlGaAs semiconductor stacks grown by OMCVD [44] by forming electrodes from heavily doped AlGaAs; however, growth rates are slow. High initial vacuum conditions and continued vacuum integrity of the growth chamber required by MBE or OMCVD add to the technical complexity of the fabrication process. In the case of layered ceramic materials, grown by liquid-phase-epitaxy (LPE), the growth temperatures would destroy any metal electrode patterns, and the electro-optic ceramics are insulators precluding the electrode technique used with semiconductors. As a result of these drawbacks, the development of phased-array optics based on electro-optic semiconductors or ceramics is sufficiently uncertain to warrant consideration of materials that are not limited in the same manner, in particular the application of organic electro-optic materials.

Organic materials that have been explored and are presently being investigated include crystalline materials such as 2-methyl 4-nitroaniline (MNA) [58,59], and amorphous materials that have electro-optic properties induced with an electric field [60-70]. Though the crystalline organics have exhibited electro-optic effects that are applicable to devices, single-crystal thin-films and bulk crystals, on the scale of  $\text{LiNbO}_3$  wafers have been elusive. Without crystalline uniformity throughout a sample, scattering loss prevents device applications that

are competitive with  $\text{LiNbO}_3$ . Fabrication of single crystal MNA remains a research area. In contrast, electro-optic materials that are formed by electrically inducing an anisotropy in polarizable molecules (poling), that are embedded in a uniform amorphous host to form electro-optic regions, do not require the precision of crystallinity. Among these types of materials are guest-host [63-66] and backbone pendant [66-70] polymers. Representative of the guest-host materials are azo dye Disperse Red I in poly(methyl methacrylate) (DR1/PMMA) [63], and MNA/PMMA, p-NA/PMMA, PONS/MMA, DCV/MMA. The backbone pendant type include such materials as PC6S, HC-1238, and HC-1232 [67,68] and rigid nonlinear materials such as cumulenes [69,70]. None of these materials have the  $n^3r$  of  $\text{LiNbO}_3$ , though HC-1232 approaches the  $\text{LiNbO}_3$  value, and materials are being explored to equal and surpass the  $\text{LiNbO}_3$  value. An electromagnetic material property that the electro-optic organics have as an advantage over the crystalline ceramics is the low-frequency (non-optical) electro-quasistatic (*eqs*) dielectric constant ( $\epsilon_{eqs}$ ). Typically, the organic materials have an  $\epsilon_{eqs}$  on the order of 4 while the crystalline ceramics have  $\epsilon_{eqs}$  values on the order of 40 [63]. Thus modulation rates are increased because of the lower capacitance effects of the organic materials. A summary of a comparison between  $\text{Ti:LiNbO}_3$  and electro-optic organics is given in Table I. However, further research into the electro-optic organic materials with improved optical properties of electro-optic effect, and reduced scattering loss, is required to make these compounds competitive with ceramics purely on an optical material property basis. As discussed below, devices have been fabricated using the organic materials, and HC-1232 appears immediately applicable to phased arrays.

There is one significant drawback, at this time, to practical device application of the electro-optic organic materials in all environments. This is the problem of the electro-optic molecules randomly orienting again due to thermal agitation

**TABLE I**  
**COMPARISON OF Ti-LiNbO<sub>3</sub> and**  
**ELECTRO-OPTICAL ORGANICS**

<b><u>PROPERTIES</u></b>	<b><u>Ti-LiNbO<sub>3</sub></u></b>	<b><u>Organics</u></b>
Electro-Optical Coefficient, $r_{jk}$ [pm/V]	32	10 - 100
Index of Refraction, n	2.28	1.5 - 1.7
$n^3r$ [pm/V]	380	34 - 490
Low Frequency Dielectric Constant ( $\epsilon_{eqs}$ )	40	4
Loss [dB/cm] (0.85 -1.3 $\mu\text{m}$ )	0.1	0.2 - 1.0
Material Processing Temperature	1000°C	150-250 °C
Patterning	Difficult	Easy (O <sub>2</sub> RIE)
Materials Integration		
Heterogenous Deposition:	NO	YES
Multilayers:	NO	YES
Direct Integration with Semiconductor Electronics (Si, GaAs)	NO	YES

or mechanical relaxation. If the environment that the electro-optically poled materials are in has a temperature range that includes the glass transition, then the electro-optic dipoles will randomly orient again. Military specifications (Mil. Spec. 883c Level 2) require operation temperatures of 125°C and storage of up to 200°C. These temperatures are in the range of the glass transition temperature of current guest-host and backbone-pendant polymer materials. Hence the low temperature of deposition is a boon for fabrication, but a bane for stability. Also during the fabrication of devices, temperatures of 100°C to 320°C can be encountered in such processes as fiber attachment, wire bond, hermetic packaging, die attach, and subassembly [76]. Further, particularly in the case of the guest-host materials, relaxation of mechanical stress caused during the orientation of the guest electro-optic molecules will also yield disordering electro-optic dipoles, and hence reduction of the electro-optic effect. Thus for general use, limitations exist for current organic materials. However, research is continuing into the synthesis of materials that have rigid nonlinear optical molecules either inherent to the structure [69] or which can be induced [71] and meet the temperature and stability requirements. Further, careful planning of fabrication can lead to reduced temperature extremes suffered by the materials during manufacture as suggested in section 4.6. Lastly, devices can have self-test and monitoring built into the package that can compensate for reduction in material effects by increasing applied electric fields during operations, and maintaining a poling field during storage or operation.

At this time the primary advantage that the organics have is the ease of fabrication, that permits multilayered devices. Unlike the crystalline ceramics, the organic materials can be deposited at low temperatures, less than 200°C, and in the case of the poled polymers room temperature deposition by spin coating

is available [60-70]. These materials can be applied directly to previously fabricated structures without damaging these structures either due to the deposition process or chemical interaction. Also, if deposited on metals, the organics will adhere to metals, and metals can overcoat the organics and remain in place.

Electro-optic properties of poled polymers are created by inducing the alignment of electro-optically polarizable molecules that are embedded in a host material. The material is deposited on a substrate and allowed to solidify. Initially the material is amorphous and isotropic optically, and electro-optically neutral. To attain an alignment of the electro-optic molecules, the material is heated above its glass transition which permits movement of the dopant molecules of guest-host materials or side-chains of the backbone-pendant variety. Concurrently an electric field is applied by either electrodes [63-72] or corona poling [73], to attain an average alignment of the molecules. As the temperature is reduced, a preferred orientation of the electro-optic molecules is achieved until the molecules are again mechanically rigid. This average alignment creates a uniaxial electro-optic region with direction of the extraordinary axis along the direction of the poling field. Hence, it is possible to shape the optical characteristics of the electro-optic region, in terms of the magnitude and direction of the electro-optic effect, and its spatial distribution, by the applied poling electric field [63-72]. Further, the index of refraction of the extraordinary axis is higher for the material after poling even without an applied electric field. Thus, if only a portion of the unpoled polymer is subject to the poling electric field, a polarization specific waveguide can be formed by selectively poling the material in those regions that the waveguide is to exist [71,72,74,76].

Organic electro-optic materials have been applied to the development of integrated optic waveguide devices [71-76]. Devices such as phase modulators,

“Mach-Zehnder” switches, directional coupler switches/modulators, and waveguide modulators have been developed. These devices have analogs first made in ceramics and semiconductors. Thus a proof-of-concept base exists for development of the two-dimensional phased-array devices using electro-optic organic materials.

#### 4.5 PHASED-ARRAY OPTICS – DEVICE DESIGNS

Because of the electro-optic properties, flexibility, and processing simplicity and versatility, of organic electro-optical materials as a fabrication foundation, designs for two-dimensional phased-arrays can be considered which can be developed. These properties of the materials permit the multi-element and multi-layer structures that ensue in this presentation. Devices that can be formed from single element dielectric waveguides, artificial prisms, and combinations are described. Fabrication of these devices are discussed in the section 4.6.

##### 4.5.1 PLANAR MULTILAYER STACK:

The simplest design and fabricatable structure is the multiple layer stack of Figure 4.11. This figure illustrates the multiple levels of control electrode, buffer region, electro-optic material, buffer region and control electrode in a continual integrated device. Each sandwich of this combination forms an electro-optically controlled planar waveguide. The electro-optic material is an organic material inserted between two buffer layers. The buffer layers can be organic materials, such as siloxane [71,72], polyimide [79], or parylene [80,81], and must have an index of refraction less than that of the electro-optical material. If the electrodes are metal, and hence possess a conductivity, the buffer layers serve the purpose of isolating the electro-optical waveguide from the metal electrodes to reduce propagation loss [82-90]. In this configuration, and assuming an electric field poled electro-optic organic material for the waveguides, the electro-optic dipole



orientation is perpendicular to the plane of the structure. In order for the light to be affected by the electro-optic effect, the electric-field polarization of the light must be parallel to the electro-optic dipoles, and thus perpendicular to the metal plane and the sides of the planar waveguide. This results in a TM like mode for this direction of the dielectric waveguide. Metal walls directly in contact with the electro-optic waveguide can create optical losses on the order of 30 dB/cm for the lowest order TM mode and higher losses for higher order modes. This loss is unacceptable for the phased-array devices because of the need for excessive optical power at the input of the device. The buffer layer acts to separate the metal from the waveguide. With a buffer layer on the order of 1  $\mu\text{m}$  to 2  $\mu\text{m}$ , losses can be reduced to 0.5 dB/cm to 0.2 dB/cm [82-90]. The difference in the index of refractions between the buffer layer and the electro-optic waveguide, the greater the confinement of the light to the waveguide, and the lower loss from metal wall interactions. Besides metal, conducting polymers can be used for the electrode material [91,92], and polymers that are conducting and transparent exist [92]. Transparent conducting polymers could alleviate the need for buffer layers if the index of refraction of these materials are less than the electro-optic waveguide. This would improve packing density and simplify fabrication. Dimensions perpendicular to the plane are on the order of 1  $\mu\text{m}$  to 10  $\mu\text{m}$  for the thickness of the waveguide ( $d_w$ ), 1  $\mu\text{m}$  to 2  $\mu\text{m}$  for the buffer layer ( $d_b$ ), and 0.1  $\mu\text{m}$  to 1  $\mu\text{m}$  for the electrode layers ( $d_e$ ). These dimensions are compatible with the formation of waveguides for near infrared and visible light. As presented before, the length,  $L$ , of the device is the propagation length, and would fall in the range of several millimeters to 2.5 cm.

As discussed previously, the planar multilayer structure will only permit wavefront modulation in one-dimension. To have two-dimensional modulation, an array of channel waveguides needs to be introduced to each layer, thereby

forming a two-dimensional matrix of emitting elements. Each waveguide is controlled to produce changes in light phase. Phase change may be introduced as a uniform modification across the channel waveguide as shown in Figure 4.9, with artificial prisms as represented in Figure 4.10, and combinations of these two approaches. The ensuing discussion examines designs that incorporate these various techniques. Figures 4.12, 4.13, 4.14, and 4.15 present channel waveguides with uniform phase control across each element of the array. Figure 4.16 and Figure 4.17 present artificial prisms. Figures 4.18 through 4.21 illustrate combinations of channel and artificial prism control that enhances phase modification. It should be noted that Figures 4.12 through 4.21 are not drawn to relative or absolute scale.

The uniform channel waveguide method can be approached from two different strategies as illustrated in Figures 4.12 - 4.15. Each electro-optic channel waveguide is individually controlled to create a matrix of waveguides that produces a flexible phased array. For simplicity of illustration, each figure represents one horizontal row of dielectric waveguides and control electrodes of a multilayer stack that is generic to each layer of the device. Figures 4.12 and 4.13 utilize planar electrode geometry, while Figure 4.15 applies embedded electrodes.

#### 4.5.2 WAVEGUIDE MATRIX ARRAY - PLANAR ELECTRODES:

Illustrated in Figure 4.12, is a geometry for individual waveguide control with planar electrodes that control each waveguide. The term planar refers to all of the control electrodes lying in the same plane. Starting from the bottom, Figure 4.12 shows the cross-sectional structure of the design for each layer with thickness dimension ( $a_i$ ,  $i$  = layer number) as:

- (1) common planar electrode ( $a_1$ );
- (2) optical buffer layer between planar electrode and dielectric waveguides ( $a_2$ );

FIGURE 4.12

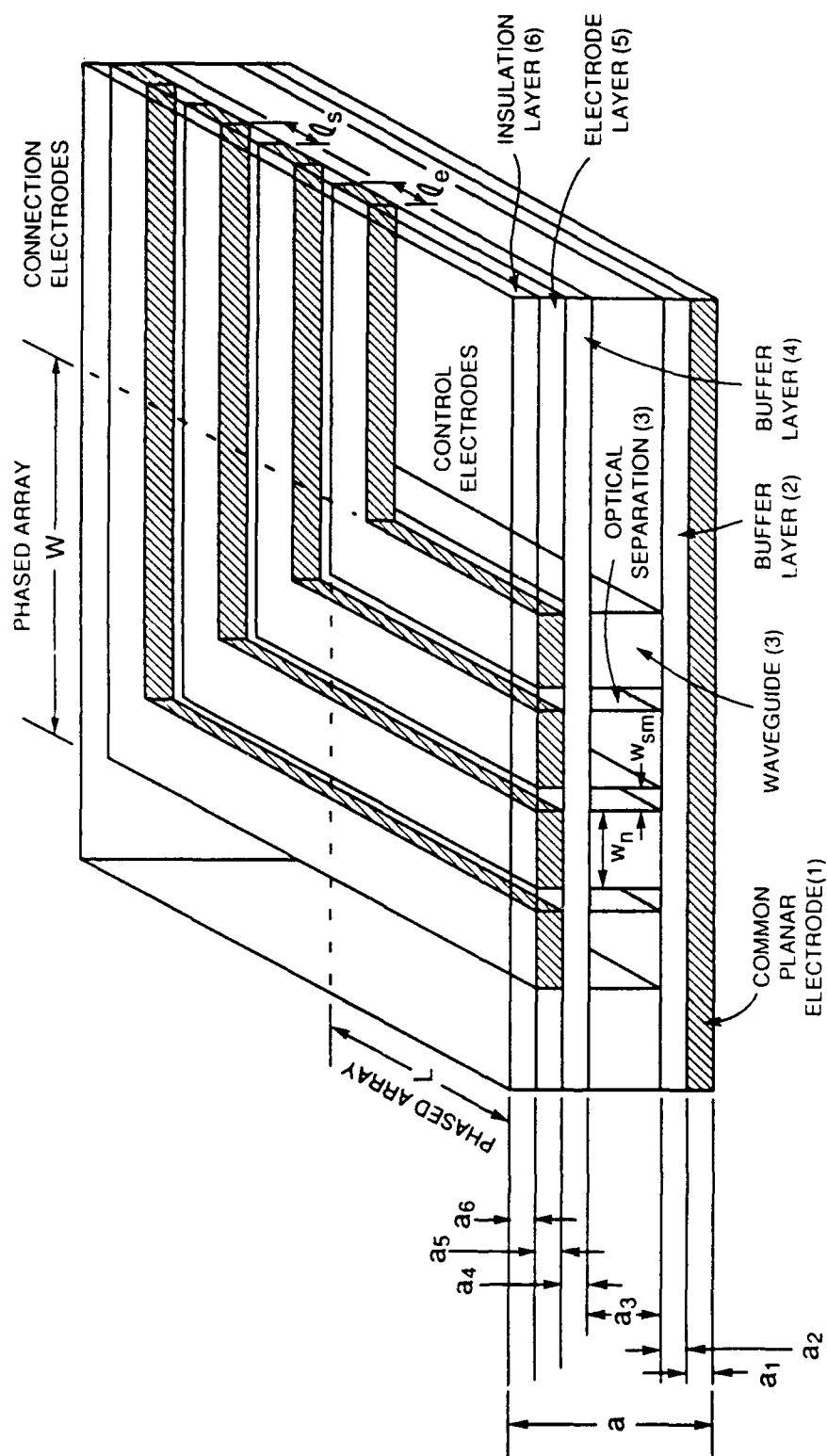
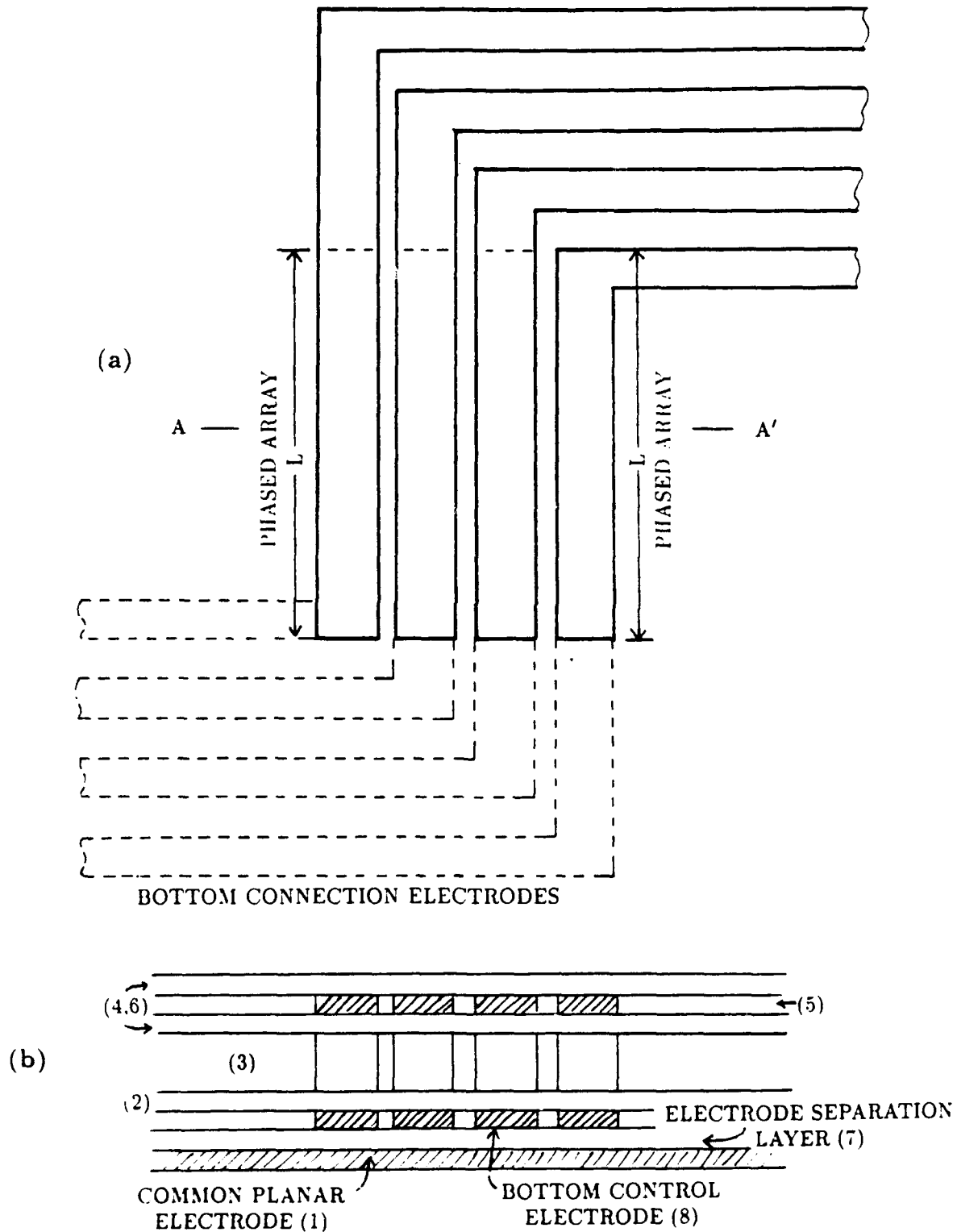


Figure 4.12. Coplanar electrode geometry. Control electrodes and connection electrodes in the same plane. Common planar electrode geometry for control and connection electrode, and layer electrical isolation.

**FIGURE 4.13**

TOP CONNECTION ELECTRODES



**Figure 4.13. Coplanar paired electrode geometry. Control electrodes and connection electrodes in same plane. (a) Top view of paired control electrode geometry. (b) Cross-section view along A-A'.**

FIGURE 4.14

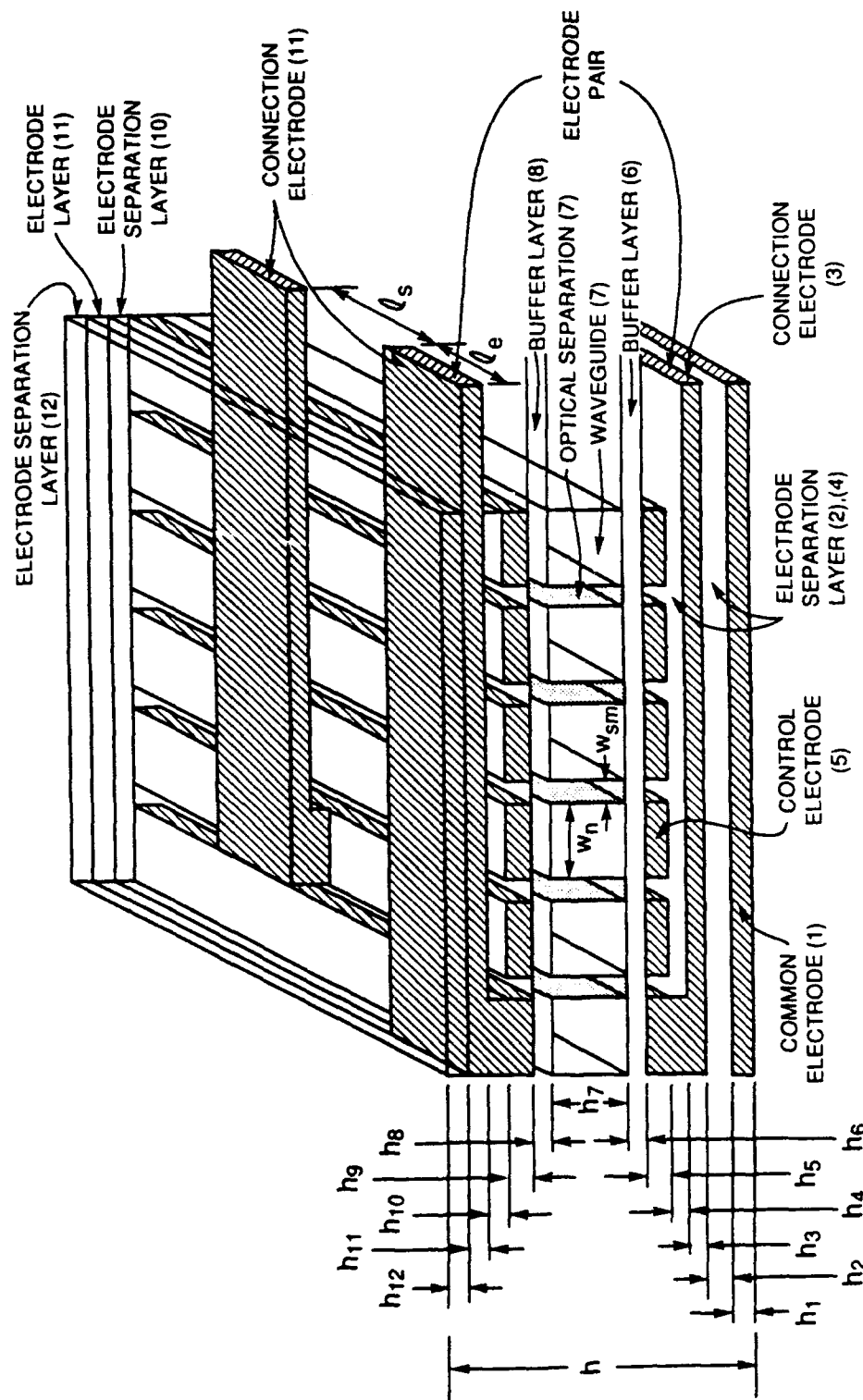


Figure 4.14. Waveguide matrix array with two-layer planar control and connection electrode geometry.

- (3) dielectric waveguide layer ( $a_3$ );
- (4) optical buffer layer between dielectric waveguides and control electrodes ( $a_4$ );
- (5) control electrode layer ( $a_5$ ); and
- (6) insulation layer between control electrodes and common planar electrode of the following row ( $a_6$ ).

The common planar electrode layer (1) is identical for each row and all are held at a common electrical potential. This is done to prevent electrical cross-talk between each row. The optical buffer layers, (2) and (4), exist to reduce optical loss due to light interaction in the waveguides (3) with the common planar electrode and the control electrodes (4). The waveguides have a width  $w_n$  and is removed from its neighbors by  $w_{sm}$ . The subscripts  $n$  and  $m$  indicate the  $n^{th}$  waveguide (equation (4.11)), and  $m^{th}$  separation region, respectively. The electrodes have a width  $\ell_e$  and separated by a distance  $\ell_s$ . The insulation layer (6) is an electrical insulation between the control electrodes and the common planar electrode that would be the bottom of the surmounting row.

Dimensions for this coplanar control and connection electrodes design are:

TABLE II  
COPLANAR ELECTRODE DEVICE DIMENSIONS

$a_1 \sim 0.2 \mu m \rightarrow 1.0 \mu m$	$a_2, a_4 \sim 0.2 \mu m \rightarrow 1.0 \mu m$	$a_3 \sim 1.0 \mu m \rightarrow 10.0 \mu m$
$a_5 \sim 0.1 \mu m \rightarrow 1.0 \mu m$	$a_6 \geq (0.2 \mu m \rightarrow 1.0 \mu m)$	
$\ell_e \sim 5 \mu m \rightarrow 10 \mu m$	$\ell_s \geq 5 \mu m$	
$w_n \sim 1 \mu m \rightarrow 10 \mu m$	$w_{sm} \sim 1 \mu m \rightarrow 10 \mu m$	

The total thickness of a row,  $a$  is given by:

$$a = \sum_i a_i \sim 3 \mu m \rightarrow 20 \mu m, \quad (4.35)$$

where the subscript  $i$  represents the layer number previously specified. The dimensions  $L$  and  $W$  are the total length and width, respectively, of the array, and are dependent on the electro-optic materials, and function of the device. Thus no particular numbers are specified. A range of values for  $L$  was discussed previously for the multilayer stack, and would apply to this case.

Figure 4.12 shows a uniform geometry in waveguide separation and size, and is presented for ease of display. The waveguide widths,  $w_n$  do not have to be identical, and the separation between waveguides,  $w_{sm}$  can also be variable. Order of magnitude dimensions of  $1\ \mu m$  to  $10\ \mu m$  for  $w_n$  are expected, with minimum separation between waveguides,  $w_{ms}$ , from  $1\ \mu m$  to  $10\ \mu m$ . For a chirp spacing between waveguides, as discussed in section 4.2,  $w_{ms}$  is variable, and depending on the intensity pattern intended in the far-field,  $w_n$  can also be variable in a row.

Optically, this structure does not present a uniform environment for light propagating into it. As can be seen from Figure 4.12, the connection electrodes extend over the entrance, or equivalently the exit, to the waveguide array. The light entering in the extreme left waveguide propagates through the device under different conditions than the extreme right waveguide. The light entering the array and propagating into the left waveguide experiences a uniform electrode with uniform electrical properties, while the light entering the array and proceeding into the right waveguide experiences an array of electrodes with varying electrical conditions. Scattering of light is enhanced by this multiple electrode environment, as well as nonuniform electro-optic conditions unless the electro-optic material is confined only to the region identified as the array region. One technique to compensate for this is illustrated in Figure 4.13. This shows a top view of the structure. Instead of a common planar electrode as part of the

control electrodes, the common electrode is replaced by an array of control electrodes. Each waveguide is controlled by its own pair of electrodes. As seen in Figure 4.13, the light entering each waveguide has a more uniform propagation environment. This uniformity is at the cost of additional layers for each row as shown in Figure 4.13b. Layers (7) and (8) are added to accommodate the extra electrodes. Layer (7) separates the common planar electrode from the lower set of control electrodes, and layer (8) is the control electrode layer. The dimensions  $a_7 = a_6$  and  $a_8 = a_5$ . Besides the uniformity issue, this geometry adds to the length of the device. As seen in Figure 4.12, the connection electrodes extend beyond the end of the control electrodes and hence the phased array. This length is doubled for the structure of Figure 4.13a. Hence, additional propagation loss can be expected for this type of device due to increased length. Therefore, the simplicity of the structure of Figures 4.12 and 4.13 can introduce adverse propagation conditions for the light. Figure 4.14 illustrates a more uniform and shorter device design at the expense of layer complexity.

Figure 4.14 shows a technique in which each channel waveguide has its own independent pair of control electrodes. To change the phase of a particular waveguide, only the two electrodes for that waveguide are addressed. The planar electrode structure refers to the paired control electrodes lying in planes parallel to the direction of the row of waveguides. Starting from the bottom of the figure, this geometry and layer thickness ( $h_i$ ) consists of :

- (1) common planar electrode ( $h_1$ );
- (2) an electrical insulation layer for electrode separation ( $h_2$ );
- (3) an electrical connection layer for external electrical contact ( $h_3$ );
- (4) another insulating electrode separation layer to isolate the connection layer from the following control electrodes ( $h_4$ );
- (5) a plane of control electrodes ( $h_5$ );



- (6) a buffer layer between the electrode layer and the optical waveguides ( $h_6$ );
- (7) optical waveguide layer ( $h_7$ );
- (8) another buffer layer between the waveguide layer and the next electrode layer ( $h_8$ );
- (9) the second plane of control electrodes ( $h_9$ );
- (10) an insulating separation layer between the electrodes and the external electrical connection layer ( $h_{10}$ );
- (11) external connection electrodes ( $h_{11}$ ); and
- (12) an insulating separation layer on the top that would be in contact with the common electrode of the next row of dielectric waveguides ( $h_{12}$ ).

The common electrode layer (1) for each row of waveguides is held at a common potential to prevent electric field interference between each row of emitting elements. The insulating layer above the common electrode (2) is to electrically isolate the external connection lines to each of the lower controlling electrodes (3) from the common electrode. The width of the external connection lines is  $\ell_e$ , and the lines are separated from each other by a distance  $\ell_s$ . The external connection to each electrode must be isolated from the other electrodes in the vertical direction, and thus another insulating layer (4) is added to accomplish this. A via is formed in this insulating layer to attach an external connection to its respective electrode. The first control electrode layer (5) has all of the electrodes existing in a plane, hence the name planar electrode geometry, in contrast to the embedded electrodes of Figure 4.15. Each plane electrode acts as one terminal of a parallel plate capacitor with the other terminal the electrode immediately above it. The electrodes are then separated from the waveguides by a buffer layer (6) to reduce optical loss from contact with the metal of the electrodes. This buffer layer is transparent and at a lower index of refraction than the electro-optic waveguides. The waveguide layer (7) consists of channel

dielectric waveguides. Each waveguide has a width  $w_n$ , and is isolated from its nearest neighbors by an optical separation (width  $w_{sm}$ ). With the light uniformly distributed in the waveguides, cross-talk between the waveguides will not occur, and if an electric field is applied to the waveguides to change the index of refraction, cross-talk will be further discouraged since any two neighboring guides will be different. Surmounting the waveguide layer is another buffer region (8) between the waveguides and the partner electrodes on the following layer (9). The top electrodes are also electrically isolated from the external connections for these electrodes by way of an electrode separation layer (10). In this separation layer, vias are again formed to connect the appropriate external connection to its electrode. The ensuing layer is the external control connection layer (11) followed by the electrode separation layer (12) that is in contact with the common electrode for the next row of waveguides.

Realizable dimensions for such a structure are summarized in the following table of range of values:

TABLE III

*TWO - LAYER PLANAR ELECTRODE DEVICE DIMENSIONS*

$h_1 \sim 0.1 \mu m \rightarrow 0.5 \mu m$	$h_2 \sim 0.2 \mu m \rightarrow 1.0 \mu m$	$h_3, h_{11} \sim 0.1 \mu m \rightarrow 0.5 \mu m$
$h_4, h_{10} \sim 0.2 \mu m \rightarrow 1.0 \mu m$	$h_5, h_9 \sim 0.1 \mu m \rightarrow 0.5 \mu m$	$h_6, h_8 \sim 0.2 \mu m \sim 1.0 \mu m$
$h_7 \sim 1.0 \mu m \sim 10.0 \mu m$	$h_{12} \geq 0.2 \mu m$	
$\ell_e \sim 5 \mu m \rightarrow 10 \mu m$	$\ell_s \geq 5 \mu m$	
$w_n \sim 1 \mu m \rightarrow 10 \mu m$	$w_{sm} \sim 1 \mu m \rightarrow 10 \mu m$	

The dimensions  $w_n$  and  $w_{sm}$  are the same as those discussed for Figures 4.12 and 4.13. The total thickness of a row,  $h$ , is determined by substituting  $h$  for  $a$ , and  $h_i$  for  $a_i$  in equation (4.35):

$$h \sim 3 \mu m - 20 \mu m$$

The coplanar geometry of Figures 4.12, 4.13, and Figure 4.14 permits each waveguide to be addressed individually, and thus control electronics are required for each waveguide. However, because of the small dimensions of  $w_n$  and  $w_{sm}$ , the electrode pairs do not form perfect parallel plate capacitors. The electric field from one electrode-pair can fringe to neighboring waveguides thereby interfering with nearest neighbors. This is worse for Figure 4.12 with the control electrode being a common electrode. The degree of fringing is dependent on  $w_n$  and  $w_{sm}$ , and imposes limitations on this design. Detailed electric field studies that would characterize the extent of the fringing would need to be done to determine the extent of the fringing and its interference. However, the fringing can be eliminated, and also optical isolation for each channel waveguide from its neighbors can be achieved by the use of embedded microstructures.

#### 4.5.3 WAVEGUIDE MATRIX ARRAY - EMBEDDED ELECTRODES:

Figure 4.15 illustrates a single row of the design of the waveguide matrix array utilizing embedded electrodes. Again, starting from the bottom of the figure the geometry and layer thickness ( $t_i$ ) are:

- (1) separation layer between this waveguide layer and common planar electrode of its lower neighbor ( $t_1$ );
- (2) dielectric waveguide and embedded electrode layer ( $t_2$ );
- (3) optical buffer and separation layer between external connection electrodes and embedded control electrodes ( $t_3$ );
- (4) electrical connection layer for external electrical contact for control electrodes ( $t_4$ );
- (5) insulation layer between the control electrodes and common planar electrode ( $t_5$ ); and,
- (6) planar electrode common electrode ( $t_6$ ).

FIGURE 4.15

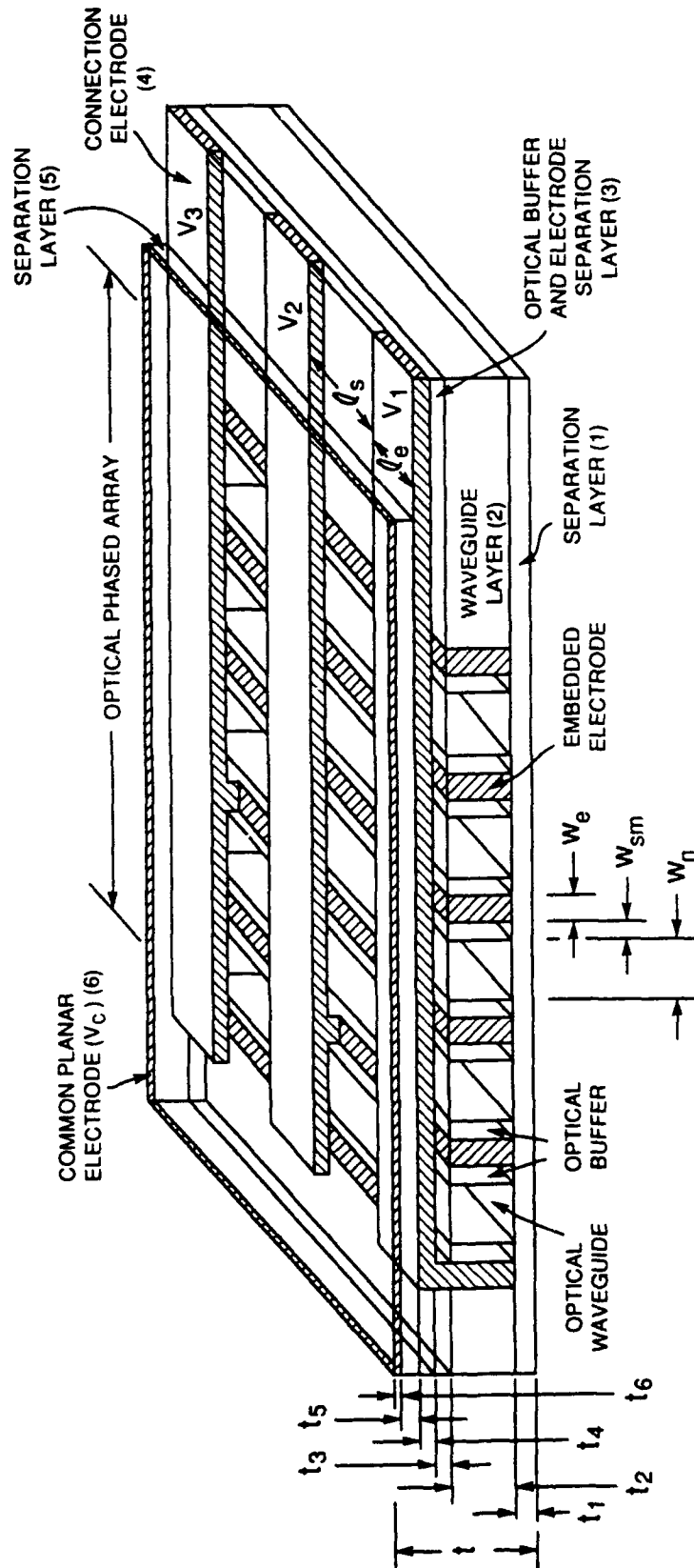


Figure 4.15. Waveguide matrix array with embedded electrode geometry.

The first layer shown in Figure 4.15 is a separation layer (1) that would isolate this row of dielectric waveguides and embedded electrodes from the common planar electrode of a lower row. On this separation layer is the waveguide and embedded electrode layer (2). The embedded electrode geometry has the controlling electrodes of each waveguide embedded in the same layer as the waveguide. This configuration serves several purposes. First, the embedded electrodes controlling a given waveguide will have a reduced fringing field than could the planar electrodes, and thus interference will be reduced between nearest neighbor waveguides. Second, the reduced fringing will enhance the local electric field of that waveguide in uniformity and intensity [93-95]. Third, the embedded electrodes act to optically isolate each waveguide from its neighbors, and this would increase the waveguide packing density of the device [93]. Fourth, the embedded electrode geometry reduces the number of layers for a row of waveguides, and hence increase the packing density of waveguide rows in the vertical direction. In this case there are only six layers compared to the twelve layers of the planar electrode geometry. To reduce light loss due to interaction with the metal electrodes, an optical buffer is placed between the waveguides and the embedded electrodes. Each waveguide can be addressed independently with this geometry even though two waveguides share the same electrode. Consider that the center waveguide shown in Figure 4.15 is to be addressed only. A positive potential is applied to the left electrode and a negative potential is applied to the right electrode. As long as all of the electrodes to the left of the center waveguide maintain the same potential difference with the respect to the positively activated electrode, and all of the electrodes to the right of the center waveguide maintain the same potential difference with respect to the negatively activated electrode, then the index of refraction of the other waveguides will be not be changed. Thus a potential difference balance must be electronically enforced

as individual waveguides are selectively addressed. Surmounting the waveguide layer, a buffer region (3), followed by an electrical connection layer (4) for external connection of the embedded electrodes, exists. The buffer layer (3) serves to optically isolate the waveguides and electrically isolate the embedded electrodes from the external connections (4). Vias are fabricated in the buffer layer in order to connect the embedded electrodes with the control electrode. Another separation layer (5) divides the control electrode connections from the top common planar electrode (6). The top common planar electrode is maintained at the same potential as the common planar electrode of other waveguide layers, and thus electrically isolates this row of waveguides from its neighbors. The next layer above the common planar electrode would be the first separation layer of the next waveguide row.

Dimensions for the embedded geometry are not unlike those of the planar geometry. The following table summarizes these dimensions:

TABLE IV

*EMBEDDED ELECTRODE DEVICE DIMENSIONS*

$t_1 \geq (0.2 \mu m \rightarrow 1.0 \mu m)$	$t_2 \sim 1.0 \mu m \rightarrow 10.0 \mu m$	$t_3 \sim 0.2 \mu m \rightarrow 1.0 \mu m$
$t_4 \sim 0.1 \mu m \rightarrow 0.5 \mu m$	$t_5 \sim 0.2 \mu m \rightarrow 1.0 \mu m$	$t_6 \sim 0.1 \mu m \rightarrow 0.5 \mu m$
$w_n \sim 1 \mu m \rightarrow 10 \mu m$	$w_e \sim 0.5 \mu m \rightarrow 1.0 \mu m$	$w_{bm} \sim 0.2 \mu m \rightarrow 1.0 \mu m$
$\ell_e \sim 5 \mu m \rightarrow 10 \mu m$	$\ell_s \geq 5 \mu m$	

Replacing  $a$ , and  $a_i$ , with  $t$ , and  $t_i$ , respectively, in equation (4.35) gives the total thickness for a row of this geometry. In this case, the total thickness  $t$  is:

$$t \sim 1.8 \mu m \rightarrow 14 \mu m$$

The width of the waveguides,  $w_n$ , embedded electrodes,  $w_e$ , and the optical buffer,  $w_{bm}$ , can be variable, and the above values in the chart represent typical values

for uniform spacing of the waveguides. If a non-uniform spacing is intended, such as a chirp spacing, then  $w_{bm}$  is the primary spacing factor.

As seen in Figure 4.15, each connection electrode extends across the waveguide array. This is done to insure that light propagating through any waveguide experiences the same optical factors introduced by the presence of metal for the electrodes, otherwise light propagating through the extreme left waveguide will not have the same propagation environment as the extreme right waveguide because the extreme right waveguide would have more metal lines running over it than does the extreme left waveguide. Regardless of the metal losses, and geometries to present a uniform metal environment, electric field nonuniformities also arise to distort the waveguides's optical character. This is due to the connection electrodes interacting to establish electric fields between themselves and the embedded control electrodes that are underneath. These electric fields would vary locally, and hence introduce electro-optical changes to the waveguides that the connection electrodes pass over. This would create nonuniform optical propagation conditions for each waveguide and its relative propagation condition to the other waveguides. Two possible solutions are the use of very thin connection lines and large separation distances between each other, or introducing another common planar layer. In the first case, minimizing  $\ell_c$  of the each connection line will reduce the spatial extent of the intensity distribution of the electric fields formed between the connection electrodes and the control electrodes, and maximizing  $\ell_s$  will reduce the electric fields between the connection lines. Alternatively, a second common planar layer can be placed between the connection electrodes and the control electrodes. The common planar electrode would be placed on top of the insulation layer (5) and an additional insulation layer would be placed on top of this to separate the connection electrodes from this common electrode. Vias, with insulation, would be formed in the common

planar electrode so that each connection electrode could be attached its respective control electrode. Hence, nonuniform effects, due to electric fields formed among connection electrodes, and between connection electrodes and embedded electrodes, can be reduced or eliminated as a perturbing factor.

The embedded electrode geometry has advantages over that of the planar electrode structure. As discussed these include fewer layers and thus increased vertical packing density, larger horizontal packing density, and greater optical isolation of each waveguide from its neighbors. Both of these geometries permit addressing of individual waveguides. However, in both the planar and embedded electrode case, only array modulation ( $\varphi_o$ ) occurs and not element modulation ( $\varphi_e$ ) since there is no control of phase across the cross-section of each waveguide. This requires the artificial prism.

#### 4.5.4 ARTIFICIAL PRISM GEOMETRIES:

Figures 4.16 and 4.17 show artificial prism designs for phased-array optics. Figure 4.16 illustrates a single prism element which is then vertically stacked to create a two dimensional array. Figure 4.17 presents an array of prisms for a given level of the phased array.

The single prism represents an alternative to array modulation to cause a beam to scan in the horizontal direction. Figure 4.16 is the same geometrical form as the parallel plate prisms of Figure 4.10a. This geometry permits a more uniform and intense electric field than that available from the structure of Figure 4.10b. Starting from the bottom layer, this configuration of a single level of the array is comprised of:

- (1) a bottom common planar electrode ( $d_1$ );
- (2) a buffer layer ( $d_2$ );
- (3) the electro-optic waveguide region ( $d_3$ );
- (4) a second buffer layer ( $d_4$ );



FIGURE 4.16

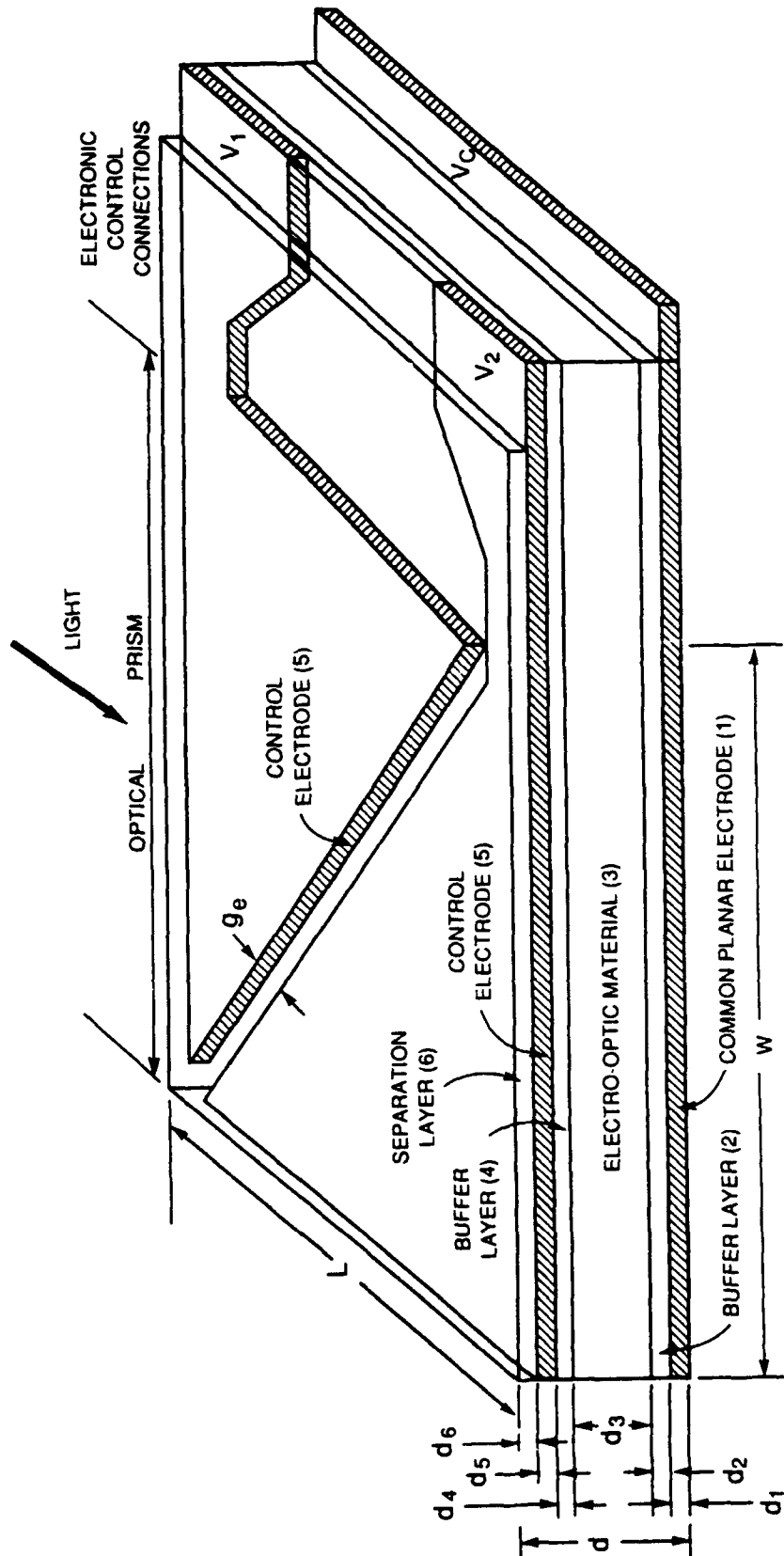


Figure 4.16. Single artificial prism

(5) the control electrodes ( $d_5$ ); and,

(6) a separation layer between the control electrodes and the common planar electrode of the next higher level of the array ( $d_6$ ).

In this case, the common electrode (1) not only provides electrical isolation of the waveguide levels of the device, but also forms the base electrode of the artificial prism. The two buffer layers, (2) and (4), separate the electro-optic waveguide from the electrodes. For this single prism device, the electro-optic waveguide (3) is a planar waveguide, and extends across the width of the array. The control electrodes (5) are triangular to provide independent phase control of the electro-optic waveguide, and to act in a push-pull manner to double the phase change across the waveguide for the same magnitude of electric field. The electric potentials  $V_1$  and  $V_2$  provide the control potentials against  $V_c$ , and as  $V_1$  is made positive,  $V_2$  can be made negative to enhance  $\varphi_c$ . The top separation layer (6) divides this row from the surmounting row, and electrically isolates the control electrodes from the common planar electrode of the next level of the array. Each of the common planar electrodes are maintained at the same potential to isolate the electric fields of each layer.

The dimensions of this structure in the vertical direction are comparable to those of embedded electrode geometry. Given below is a table that presents these dimensions.

TABLE V

*ARTIFICIAL PRISM DEVICE DIMENSIONS*

$d_1 \sim 0.2 \mu m \rightarrow 1.0 \mu m$	$d_2, d_4 \sim 0.2 \mu m \rightarrow 1.0 \mu m$	$d_3 \sim 1.0 \mu m \rightarrow 10.0 \mu m$
$d_5 \sim 0.1 \mu m \rightarrow 1.0 \mu m$	$d_6 \geq (0.2 \mu m \rightarrow 1.0 \mu m)$	

The dimensions  $L$  and  $W$  are the overall length and width of the artificial prism respectively. For variable vertical spacing, the depth factor  $d_6$  would be used to modify the spacing between levels, and would be the dimension varied for

chirp spacing. The gap between the two control electrodes is given by  $g_e$ , and would have a representative spacing from  $5\ \mu m$  to  $10\ \mu m$ . As in the case of the embedded electrodes, there are six layers to the prism electrode. With the dimensions given above, the vertical thickness of a layer, excluding chirping conditions, would fall in the range from  $1.8\ \mu m$  to  $14\ \mu m$ . These dimensions are achievable with electro-optic organic materials, and are not attainable with platelets of a ceramic material. Thus the parallel plate geometry (Figure 4.10a) can be revived with its accompanying advantages over the surface electrode configuration (Figure 4.10b). Further the organic materials allow closely space vertical stacking that is not obtainable with the ceramics.

The resolution of the single artificial prism is dependent on the width  $W$ . The larger  $W$  is, the smaller the number of resolvable spots for a given  $\varphi_e$ . To increase the scanning resolution, additional artificial prisms of smaller width contained in the same space  $W$  will increase the number of resolvable spots. For every additional artificial prism, an additional resolvable spot is added [38]. Thus an array of prisms as illustrated in Figure 4.17 is considered.

The prism array geometry of Figure 4.17 shows how the control electrodes can be modified to permit the formation of an array of artificial prisms. The vertical dimensions ( $d$ 's) of the prism array are identical to those of the single prism as well as the electrode-gap,  $g_e$ , and the length  $L$ . The width of each prism element is represented by  $W_a$ . Though shown as uniformly distributed, the prism elements can be variably spaced in width  $W_a$  and interelement spacing. Previously, artificial prisms have been fabricated with dimensions for  $W_a$  of  $100\ \mu m$  to  $150\ \mu m$ ; and electrode gap,  $g_e$ , of  $5\ \mu m$  to  $10\ \mu m$  [38,42,43]. Previous devices have operated with adjacent electrode potentials of 15 V over  $5\ \mu m$  electrode gaps. This would correspond to the small gap between the dog-leg electrode

FIGURE 4.17

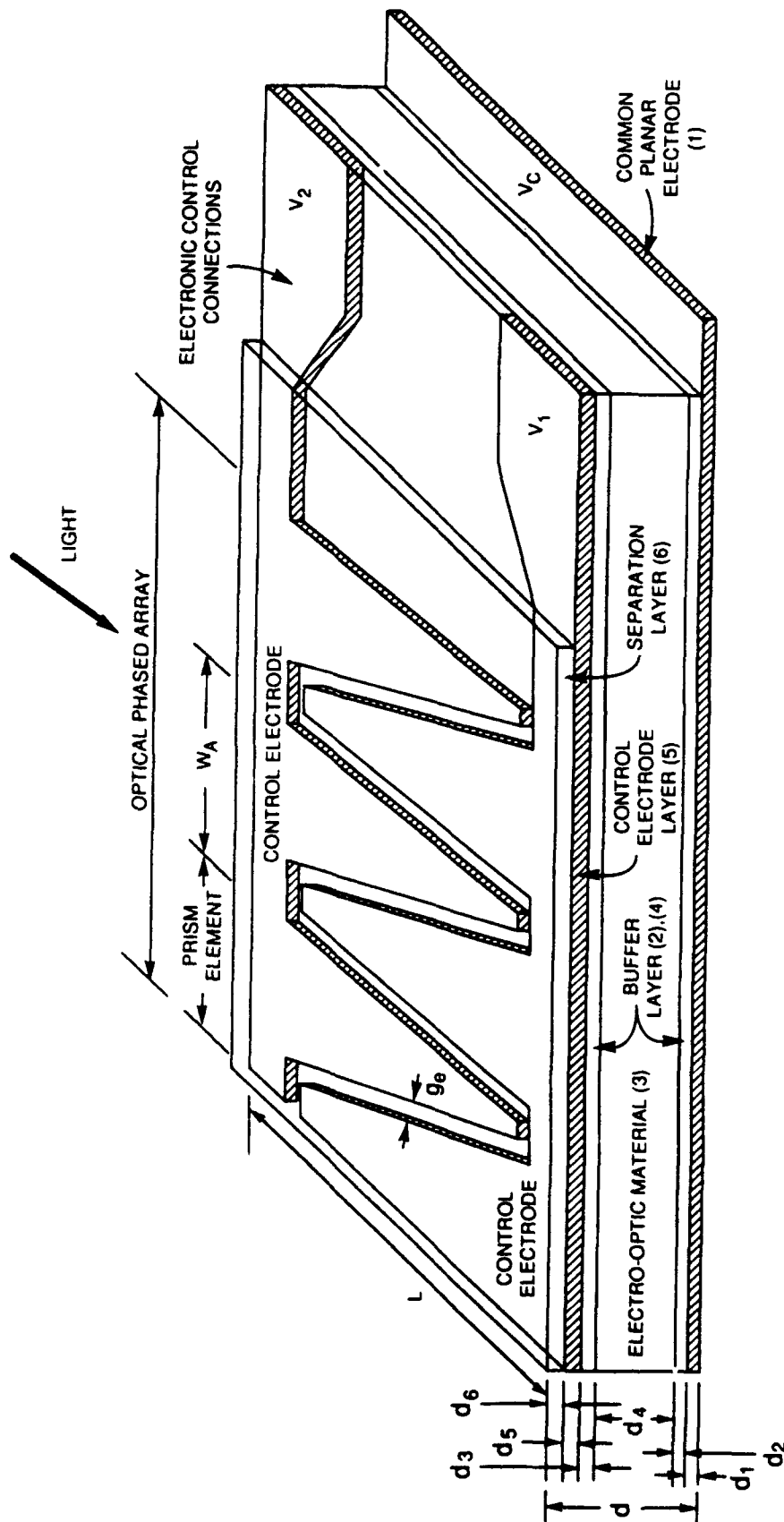


Figure 4.17. Artificial prism array.

and an adjacent electrode of Figure 4.10b [38]. Limitations on the width of the prisms is dependent on lithography capability in the fabrication of the device.

The geometry Figure 4.17 has introduced element modulation,  $\varphi_e$ , to an array. However, with the control electrodes given in this figure, each prism element has the same phase relation between each prism. There is no array modulation,  $\varphi_a$ . Therefore in order to maintain the resolution capability of array and element modulation, the two techniques must be combined.

#### 4.5.5 COMBINED ARRAY and ELEMENT MODULATION:

Two basic approaches exist to simultaneously having the capability of array and element modulation. One approach is to have a series of individually addressed channel waveguides that are also artificial prisms. This method is illustrated in Figure 4.18 and Figure 4.19. The second technique is to have an array of artificial prisms as given in Figure 4.17, coupled with a mechanism to modify the phase of the light as it enters the artificial prism array. This is illustrated in Figures 4.20 and 4.21.

The method illustrated in Figure 4.18 and 4.19 is a modification of the planar electrode structure of Figure 4.13. Figure 4.18 is identical in the vertical dimensions as Figure 4.13. Figure 4.19 differs from Figure 4.18 in that the lower artificial prism control electrodes are replaced with a common electrode. The geometry of Figure 4.18 reduces fringing fields since each electrode is directly paired with an electrode directly above or below it respectively. This is balanced against the increased vertical packing density and greater ease of fabrication of the structure of Figure 4.19. In Figure 4.19, the different layers represent:

- (1) common planar electrode ( $p_1 = h_5$ );
- (2) optical buffer layer ( $p_2 = h_6$ );
- (3) artificial prism waveguide layer ( $p_3 = h_7$ );
- (4) optical buffer layer ( $p_4 = h_6$ );

117

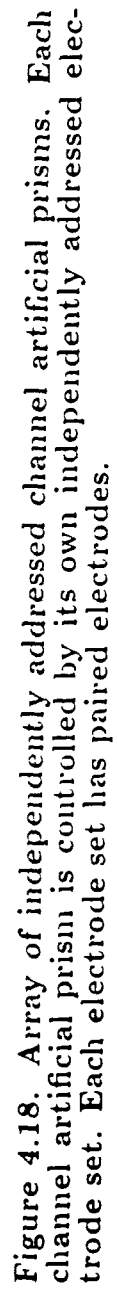


FIGURE 4.19

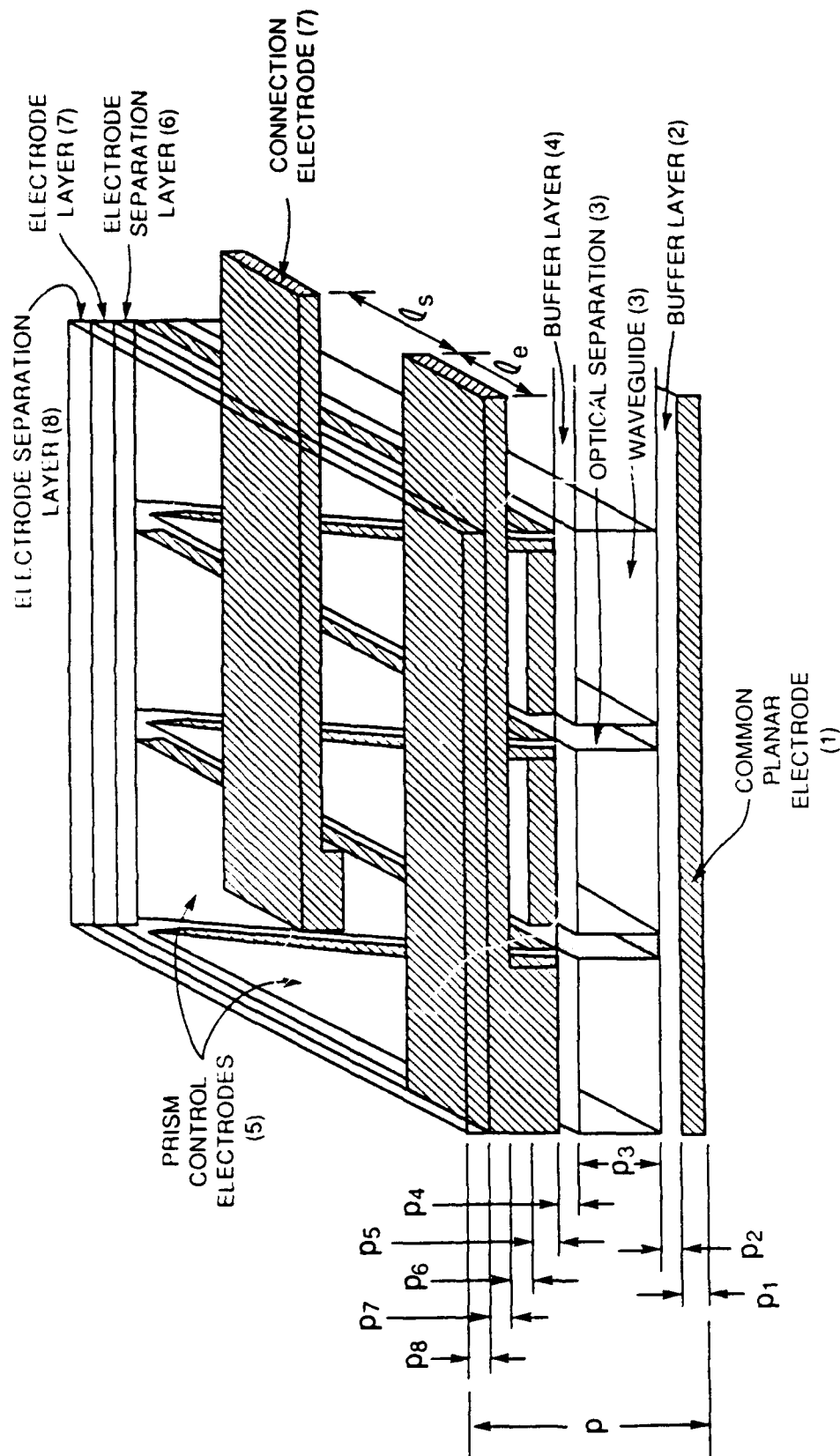


Figure 4.19. Array of independently addressed channel artificial prisms. Each channel artificial prism is controlled by its own independently addressed electrode set with common planar electrode for all electrodes.

- (5) artificial prism control electrodes ( $p_5 = h_9$ );
- (6) electrode separation layer ( $p_6 = h_{10}$ );
- (7) external electrode connection layer ( $p_7 = h_{11}$ ); and,
- (8) separation layers between rows ( $p_8 = h_{12}$ ).

With the geometries of Figures 4.18 and 4.19 each artificial prism can be individually addressed, and thus the element and array modulation can be accomplished for general conditions. The ability to individually address each prism, is at the expense of extra layers for the control electrodes external connections. If simultaneous array and element modulation is intended for beam scanning only, then Figures 4.20 and 4.21 offer alternatives that are easier to fabricate.

Figures 4.20 and 4.21 utilize the prism array of Figure 4.17 for element modulation. Array phase-modulation is introduced in Figure 4.20 by an artificial phase control prism that precedes the prism array in the direction of light propagation. The phase control prism changes the phase of the light across the full width of the light as it proceeds through this large prism. Thus the light has different phase at each of the prism elements of the prism array, and hence array modulation has occurred. The phase control prism may introduce a shift in the intensity of light towards the side of the prism with the largest index of refraction of the electro-optic material. This may have an adverse effect during light propagation by introducing non-uniform intensities and phase shift to the prism array. This needs to be studied in more detail by theoretically examining light propagation in this type structure. An alternative technique to the phase control prism, is the phase control waveguide array of Figure 4.21. In essence the phase control prism of Figure 4.20 has been divided into dielectric waveguides that confine the light to a region that is equal in width to the following prism element. The phase control is introduced by electrodes that control the index of refraction of the dielectric waveguides. By dividing the electrodes in



FIGURE 4.20

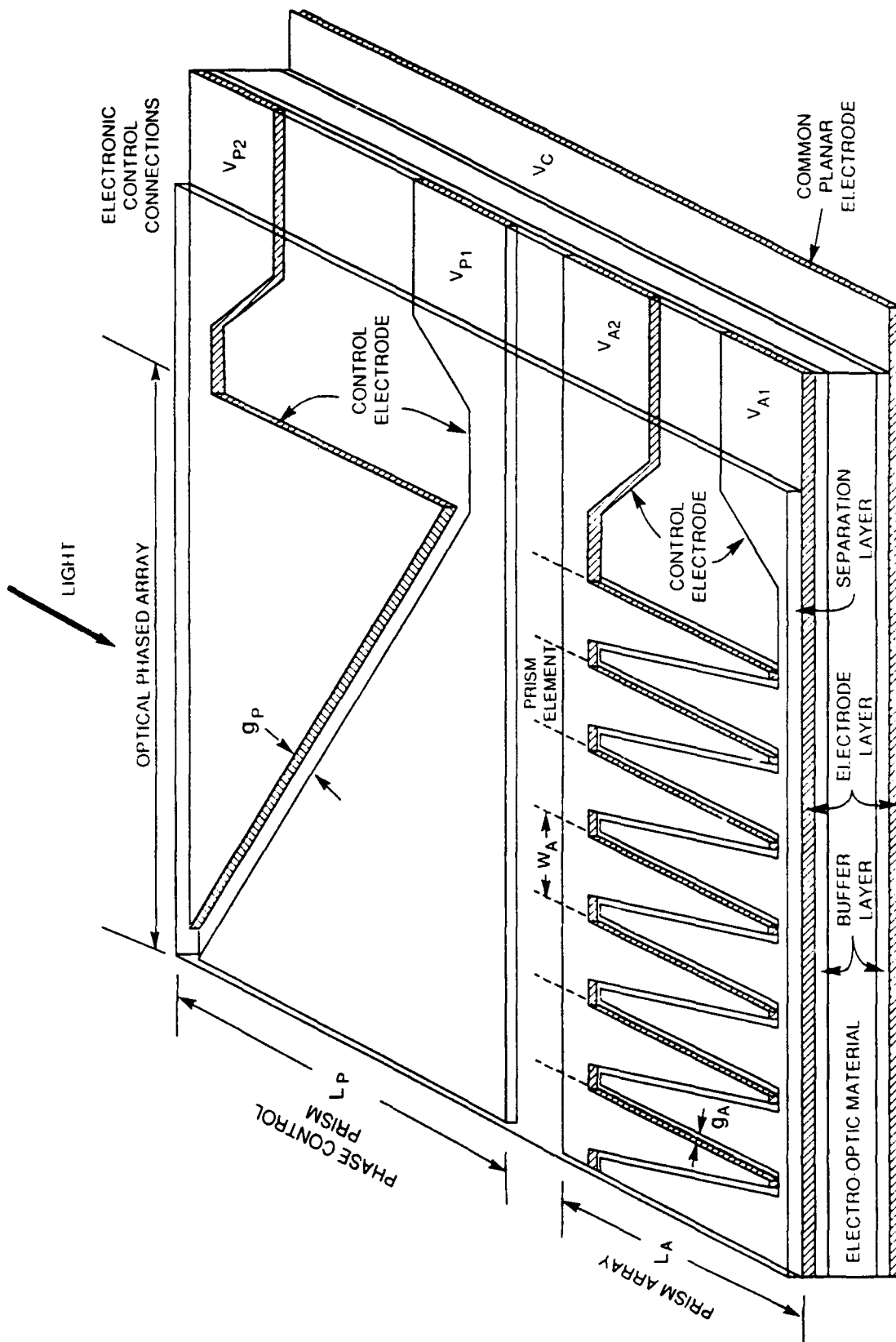


Figure 4.20. Element modulation prism array with array modulation phase control prism.

121

a geometry that approximates the triangular shape of the phase control prism control electrodes of Figure 4.20, a uniform phase difference ( $\varphi_o$ ) can then be introduced between the waveguides, and thus impose an array modulation on the light that enters the prism array. In both Figure 4.20 and Figure 4.21, the array modulation is controlled with electric potential  $V_{P1}$  and  $V_{P2}$ , or  $V_{W1}$  and  $V_{W2}$ , respectively, while the element modulation is controlled by  $V_{A1}$  and  $V_{A2}$ .

The vertical geometry and dimensions of Figures 4.20 and 4.21 are identical to Figure 4.17. The dimension  $g_A$ ,  $g_P$ , and  $g_W$  are on the order of  $g_e$  of Figure 4.17.  $L_P = L_W$ , and of the same size range as discussed above for  $L$ .

#### 4.5.6 VERTICAL GEOMETRY:

Figure 4.12 through Figure 4.21, illustrate various designs for phased-array optical devices. These figure show the geometry for a single row of the array. A two-dimensional device is developed by stacking rows on top of each other. These rows can incorporate element and array modulation simultaneously for the horizontal direction. However, the vertical direction is limited to array modulation. Tentatively, element modulation cannot be incorporated into a row for the vertical direction. This limitation is presently imposed by the directional nature of the applied electro-optic organic materials and difficulty in fabricating a prism with electrodes oriented vertically. Consequently, array modulation is only available for the vertical direction, and thus the resolution in this direction will not be as great as in the horizontal direction. To partly overcome the side-lobe limitations of uniform vertical spacing of the rows, the spacing can be nonuniformly done in a chirped manner as discussed previously. Also, nonuniform thickness of the waveguides can be considered, but at this stage need to be explored further in detail.

#### 4.5.7 DIMENSIONS – MODULATION and SIDE-LOBES:

The dimensions of the two-dimensional phased-array optics present design criteria on the speed of modulation of the arrays and the light pattern formed. These criteria are contained in the length ( $L$ ) dimensions, and the dimensions of the individual elements and spacing between elements. If one considers each element of the array (waveguide and distance to nearest neighbors) to be at an extreme of  $100\ \mu m$ , with 100 elements in each row, and 100 rows, then the cross-sectional dimensions of the device are 1 cm. With a worse case length of 2.5 cm for the length of the device, the overall dimensions of the device are 1 cm x 1 cm x 2.5 cm.

In considering these structural dimensions as criteria for modulating the device, an electromagnetic view of the modulation must be examined. This structure can be considered as a lumped element for wavelengths greater than 10 cm which corresponds to frequencies up to 3 GHz. Thus the physical dimensions of the device permit rapid modulation and scan rates that are not attainable with mechanical systems. The limitations of modulation are primarily associated with the control electronics in the time necessary to calculate the correct phase of each element and required applied modulation electric fields for a specific light pattern that is to be projected. With 30 MHz and higher clock rates for personal computers, random scan patterning of 1 MHz or greater is attainable, and for a fixed raster scan, dedicated electronics can exceed 30 MHz for scan speed.

The dimensions of the waveguides, and spacing between each waveguide, introduce side-lobes which must be controlled to minimize or eliminate the effects on the far-field light patterns. This can be accomplished by judicious design of the device, such as chirping the interelement spacing, and employing nonuniform waveguides. Alternatively, electronically tuneable external optics can also be used that block side-lobes. Consider a moveable window in a transparent screen

that is of the proper aperture size to permit the central-lobe (main-lobe) of the far-field light pattern to propagate through, while the side-lobes are blocked. This screen and window can be developed from liquid-crystal display technology. The liquid-crystal screen can be formed in a pixel pattern that corresponds to resolvable spots of the phased array. As the array is scanned to a particular location, the window is opened so that the central-lobe of that spot can be transmitted, while the side-lobes encounter opaque regions and are blocked. This type of a device is electronically controllable and agile, and can be formed from current liquid-crystal technology. Thus external optics exist that can be added to a phased array to enhance device resolution.

#### 4.5.8 DESIGNS and FABRICATION

The designs for the devices discussed above were considered in both an optical context and fabrication context. These device designs were explored with realizable manufacturing as part of the design criteria, and represent designs that are deemed makeable with current technology. The fabrication techniques and options for making devices are discussed in section 4.6.

### 4.6 DEVICE FABRICATION

The devices discussed in section 4.5 can be manufactured using current microelectronic fabrication technology [77]. Vertical dimensions that were presented pose no hindrance to device fabrication, and the smallest horizontal dimension is on the order of one half micron which was the width of the embedded electrodes or optical buffer regions between dielectric waveguides. Half micron linewidths are attainable with electron-beam lithography or from masks generated from electron-beam systems and ultraviolet lithography [77,97]. For smaller sub-micron microstructures, fabrication techniques exist such as electron-beam

lithography with increased resolution to  $0.25\ \mu\text{m}$  linewidths and smaller, and x-ray lithography. However, these finer dimensions are not inherently needed for the device designs discussed above, even though vertical and horizontal geometries must be delineated for the various parts of a device structure and fabricated. To illustrate the techniques available for material deposition to form the various layers, the simple one-dimensional vertical stack will be used as a basis for discussion. From this planar stack, the division of each row into an array of waveguides is then presented accompanied by the formation of the electrodes.

The planar structure of Figure 4.11 can be fabricated in a relatively straightforward manner by layering one type of material on top of another. However, several techniques exist for forming this stack. A flat substrate material is used to form the base of the stack. Metal can be deposited on this substrate, if the substrate is insulating, to act as the first electrode, and on top of this an optical buffer layer made of materials such as parylene [80,81], polyimide [79] or siloxane [71,72,74]. Over the first buffer layer is deposited the first layer of organic electro-active material, after which another layer of optical buffer is added. Surmounting the optical buffer, another layer of metal is placed to form the top electrode and the planar waveguide and bottom electrode of the next level. This process continues until the stack, as shown in Figure 4.11, is complete.

This formation of the multilayer stack requires multiple deposition of metal and organic materials. Generally, metal electrodes would be deposited under vacuum conditions by electron beam evaporation. The organic layers (optical buffer and electro-optic waveguide) can be deposited by an atmospheric process such as spin coating [62-70], and this necessitates moving the sample from vacuum conditions to atmospheric pressure, and back again. If the organic material can be deposited from a vapor phase as is possible with parylene, then low pressure conditions can be maintained continuously, for deposition of metal and the

organics. This then raises the possibility that all of the material deposition processes can be conducted in a low pressure and clean environment, whether the device is fabricated in a single chamber or shuttled between chambers through vacuum interlocks. Typically metal is considered as the material for the electrode; however, an alternative to metal as an electrode are conductive polymers [91,92] that are chemically compatible with the electro-optic organic, and hence only an atmospheric fabrication method may be needed; however, connection to external controlling electronics would still require a metallization of the conducting polymer at a contact junction. Further, if the conductive polymer is also transparent [92], then the optical loss problem associated with metals is eliminated. If the transparent conductive polymer also has an index of refraction less than that of the electro-optic organic, then the optical buffer region can be removed between the electrodes and the waveguides, and this increases vertical packing density.

With the formation of the stack, external contact means must be fabricated as shown in Figure 4.22. A directional gaseous etching technique such as reactive-ion-etching (RIE) or reactive-ion-beam-etching (RIBE) [96] can be applied to the connection electrode segment of the stack, with the directional etch oriented at an angle with respect to the stack as shown in Figure 4.22a. This would then form a slanted edge on one side of the stack. A second chemical etch, either gaseous or liquid, that is selective for the non-conductive materials will then expose the electrode layers to form bonding pads for contact with external electronics. A directional gaseous etch selective for the organic materials (Figure 4.22b), aimed perpendicular to the plane of the stack, would be preferred for this step since undercutting of the electrode would be minimized, and is particularly applicable to metal electrodes. With attachment of connection wires, a method now ensues for orienting organic materials that attain the electro-optic state from

poling. The complete unit of Figure 4.22c can be heated, and with appropriate voltage differences between each electrode, the organic electro-optic material can be poled, and the complete unit then cooled to attain preferential orientation of the dipole moments. Thus the controlling electrodes act in the capacity of poling electrodes to form the electro-optic medium and as the controlling electrodes for the phased array. If numerous devices are fabricated on the same substrate, the substrate and devices can be separated from one another by directional gaseous etching, sawing, or other methods. If damage occurs to the optical ends, then polishing can restore optical quality.

The above description of forming the multilayer stack illustrates the formation of layers of each row of an array, and indicates methods applicable to two-dimensional arrays. Figures 4.13 and 4.15 show a row of an array with well defined waveguides and electrodes as part of the multiple layers. Deposition of each layer of metal or organic material would use the same techniques as that described for the one-dimensional planar device. The formation of the individual elements of the array require microelectronic lithography and etching techniques.

Consider the fabrication of the structure of Figure 4.13. Layers (1) and (2), are planar levels. Level (3) contains control electrodes that attach to external control electronics. These control electrodes can be formed by lift-off or etching methods using standard photolithography [77,96-98]. In the case of etching, the electrode material is deposited as a plane, and then lithography and etching are used to define the electrode and remove unwanted material respectively. Etching can be liquid or gaseous depending on the materials involved. The lift-off process would first use lithography to define those regions for metal to be deposited as part of the device, the electrode material is then deposited, and as the resists used in the lithography are removed, the unwanted metal is also removed. Either



FIGURE 4.22

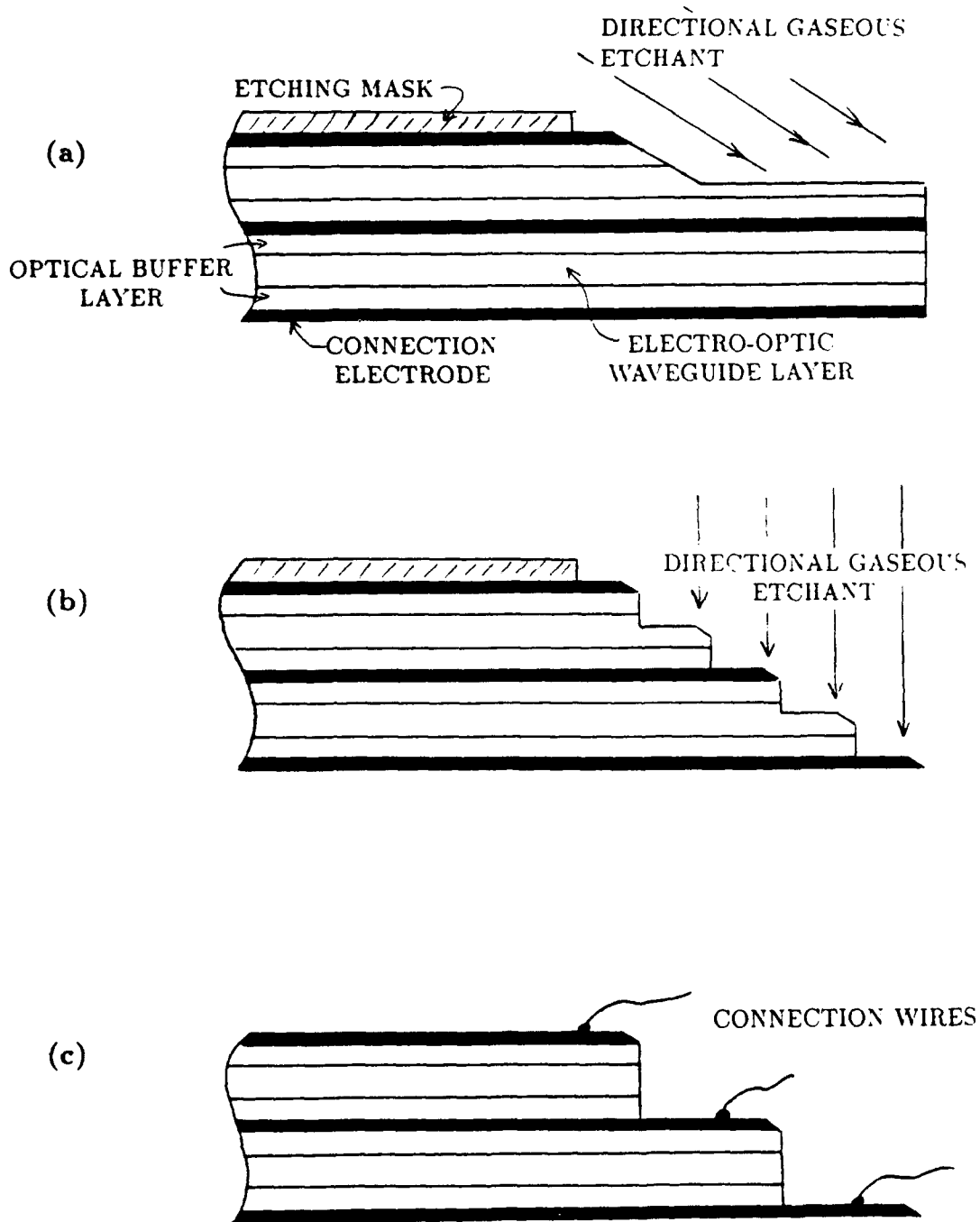


**Figure 4.22.** Formation of connection junctions for connection electrodes. (a) Angular directional gaseous etching to form connection levels. (b) Perpendicular directional gaseous etching to form connection junction steps. (c) Device with connection junction steps with connection wires.

technique is applicable. The next layer (4) is an insulating separation layer that can be deposited as a plane. Vias through this layer, to connect the waveguide electrodes and external connection electrodes, are formed by etching through the separation layer, and then forming the vias by lift-off or etching. The electrode layer (5) is made using the same techniques as the connection electrodes. The buffer layer (6), waveguide array (7), and buffer layer (8) can be fabricated by several approaches and are discussed in following paragraphs. Layers (9) through (12), the top four layers of electrodes and electrode separation layers are formed in the same manner as layers (2) through (5), but in reverse order.

Several techniques exist for the formation of the waveguide array and associated buffer layers. One approach is to deposit the lower electrode layer (5), buffer layer (6), electro-optic waveguide material (7), and the next buffer layer (8) as planar layers. On top of layer (8) fabricate the planar electrodes as metal electrodes in the manner indicated above. The planar electrodes then form a mask for oxygen reactive-ion-etching or reactive-ion-beam-etching [60] of the top buffer layer, the waveguide layer, the lower buffer layer, and the lower set of electrodes. RIBE and RIE can achieve height to width ratios of ten to one or greater, and form vertical sidewalls. This forms channels that delineate each waveguide and the lower electrodes. The following separation layer (10) can then be added to cover the top electrode of each electrode pair and also fill in the channels. Excess material composing the separation layer can be removed by mechanical polishing or shallow angle ion milling. This procedure is viable provided the deposition of the material for the separation layer uniformly fills the channel to create an uniform optical environment. This is dependent on the insulating material, method of deposition, and the dimensions  $w_{sm}$  and sum of  $h_5$  through  $h_9$ . The more narrow  $w_{sm}$  is and the thicker these layers, the more difficult it is for the material to uniformly fill the channels. Hence this approach is heavily

dependent on device design and materials. A variation on this procedure is to only deposit the buffer layer (6) and the waveguide layer, and then use a mask on top of the waveguide layer and reactive-ion-etching to form channels only in the waveguide material. However, since  $h_7$  is the largest vertical dimension, this has the same limitations as just described. In both of these cases, the electro-optic effect is induced in the waveguides by using the electrodes as poling electrodes.

An alternative to etching channels that form empty regions between waveguides, is to deposit a thick layer ( $h_6 + h_7$ ) of buffer material and then etch channels of width  $w_n$  and height  $h_7$ . This leaves mesas of buffer material of width  $w_{sn}$  and height  $h_7$ . The empty channels between the mesas are then filled with the electro-optic material to form the waveguides, and excess material is then removed. Depending on the design,  $w_n$  can be larger than  $w_{sn}$ , and hence a channel width  $w_n$  can be more easily filled. The top buffer layer (8) can be then deposited, and following layers formed.

The two methods described above rely on the physical removal of material and insertion of additional material to define a waveguide. However, it is not necessary to completely remove material to form the electro-optic waveguide. Ridge guiding [90] and the poling induced waveguiding are alternatives. In the case of ridge guiding, a ridge of material is left over the region to define the waveguide (Figure 4.23). Thin ridges are part of electro-optic material region. The electro-optic material is deposited as a layer, and then ridges are formed by masking the areas for the waveguide, and removing material by reactive-ion-etching. The buffer layer and electrodes are placed over the ridged waveguide layer with the electrodes directly over the ridges. Alternatively, one can deposit the electro-optic waveguide material as discussed in references [71,72,74-76], and then a waveguide can be defined from electric field poling. The buffer layers and the electro-optic waveguide layer can be deposited as planes, and the succeeding

FIGURE 4.23

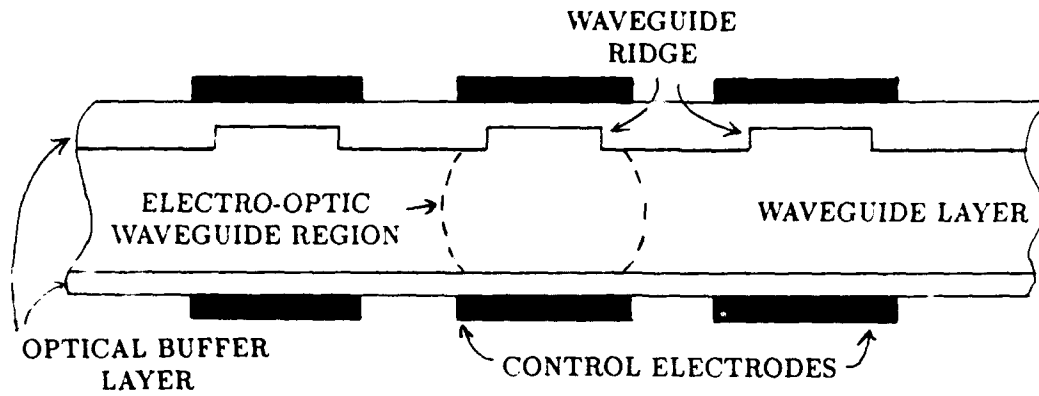


Figure 4.23. Cross-sectional view of ridge waveguides with planar electrodes.

layers and electrodes fabricated as discussed before. The electrodes induce the electro-optic effect from poling of the electro-optic material, and because the electrodes are separated, the electric fields of the electrodes also induce regions of higher index of refraction between each pair of electrodes. This can be reinforced by alternating the polarity of the electrodes in each electrode plane. The effect would be that the electric field between neighboring pairs of electrodes is reduced, and hence enhance the index of refraction between a specific electrode pair, and reduce the index of refraction between neighboring electrode pairs along the width dimension. Hence, the physical delineation steps are not necessarily required to form an electro-optic waveguide for the planar electrode geometry, but it is necessary for the embedded electrode geometry.

The embedded electrode geometry of Figure 4.15 requires the formation of electrodes that are inserted into the waveguide layer. These embedded electrodes require a different approach to formation than that of planar electrodes; however, the remaining layers can be fabricated from techniques already discussed. Again, several strategies can be considered for fabricating the embedded layer. These different methods are based on which materials are to be deposited and then have channels etched to form the waveguide array. One method forms the separation layer as a base layer of thickness ( $t_1$ ) followed by deposition of the electro-optic waveguide material. The embedded electrodes and optical buffer are then inserted into the waveguide layer by successive application of reactive-ion-etching methods to form channels into which the electrode metal material and optical buffer materials are deposited. Initially, mesas of electro-optical material are formed. The second approach is to fabricate a layer of separation material of thickness  $t_1 + t_2$ . This layer is then successively etched to form channels of depth  $t_2$  for deposition of electro-optic waveguide materials and electrode materials. In this case, the first etching forms initial mesas of the optical buffer

material. Lastly, The separation layer is again formed to a depth of  $t_1$  onto which a layer of electrode material is deposited to a depth of  $t_2$ . The electrode material is then etched to form the channels for the deposition of the electro-optic waveguides and optical buffers, and correspondingly mesas of the electrode material. All of the organic materials that would comprise the buffer or waveguides can be etched with reactive ions of oxygen [60], and various metals can also be etched by RIE and RIBE. Which of the processes described above is used is dependent on the choice of materials, and methods of depositing materials into deep channels with height to width aspect ratios of 10 to 1. Formation of well defined embedded microstructures, whether waveguides or electrodes, is not a mature technology particularly for the organic materials. Uniformity of deposition in narrow channels, or etching to controlled depths, are not well characterized processes for organic materials. In contrast directional reactive gaseous etching of metals [96], and narrow channel deposition of metals by the partially-ionized-beam (PIB) technique [99], or electron beam evaporation [77,98], is a better understood and currently available technology. PIB is particularly effective in filling narrow channels [99]. Though microelectronic techniques exist for forming embedded microstructures for phased arrays, the choice of fabrication strategy is not clearly apparent. Again, the electro-optic effect is induced after the phased array has been fabricated by using the embedded electrodes as poling electrodes.

Unlike the fabrication of the geometry of Figure 4.15, and the physically delineated waveguide approach to Figure 4.13 and Figure 4.18, the prism structures of Figures 4.16, 4.17, 4.20 and 4.21 are all planar, and do not require an embedding process except for the vias. All of the deposition of material for these prism devices can be done as successive layers. Relatively deep and narrow channels do not need to be formed for defining waveguides or electrodes. This simplifies fabrication and reduces the lithography to defining the electrodes. The

electro-optic effect is induced in the waveguide material by using the controlling electrodes as poling electrodes. The planar prism geometries thus become attractive from a fabrication as well as from the array and element modulation point of view.

Throughout this discussion, the waveguide material becomes electro-optically active following poling of the material using the control electrodes. This part of the fabrication process imposes limitations on the dimensions of the device in order to prevent dielectric breakdown. Electric fields of 200 MV/m [68,75] have been sustained by the electro-optic organics, and can be used as a figure of merit. This would correspond to a potential difference of 1000 V for electrode spacing of 5  $\mu\text{m}$ . If 200 MV/m is the electric field magnitude between the poling electrodes, then those regions between electrodes that are closer than the width of the waveguides and have an electric potential difference on the order of the potential difference between the poling electrodes, or have sharp edges, could experience electric fields that would lead to dielectric breakdown of the electrically insulating materials. Regions where breakdown could occur are between:

- a) closely spaced planar electrodes of the planar electrode geometry and artificial prisms;
- b) control electrodes and connection electrodes as found in the planar electrode and embedded electrode geometries; and,
- c) common planar electrodes and control or connection electrodes.

To overcome this potential problem, device geometry and electric potential application to the various electrodes must be examined. Once dielectric breakdown fields are established for a given insulator material, device geometries can be evaluated using standard computer programs to determine regions that could experience electric fields that exceed breakdown for a given scheme of applying

electric potentials to the control electrodes. The device geometries and electric potentials can then be modified accordingly to avoid dielectric breakdown. An alternative approach is to use geometries and apply electric potentials that avoid forming regions of high electric field except between controlling electrodes. These types of geometries are represented by the planar electrodes of Figures 4.12, 4.13, and Figures 4.16 through Figure 4.21.

The planar electrode geometry permits each electrode in a given layer to be maintained at the same electric potential during poling. This then eliminates high intensity electric fields between electrodes in the same layer. For the connection electrodes of Figures 4.13 and 4.18, these are at the same electric potential as the layer of control electrodes to which the connection electrodes are attached, and hence no electric field between these closely spaced electrodes. To prevent breakdown between the common planar electrodes and other electrodes, the common planar electrodes can be given variable potentials during the poling process, and then following poling placed at a common potential. With each common planar electrode not fixed at the same electrode, the common planar electrode between rows can be held at the potential of the two sets of electrodes of the two adjacent rows to which it is in closest proximity. Thus, there are no electric fields between the common planar electrodes and nearest neighbor electrodes, and hence no dielectric breakdown. However, this would cause neighboring rows to be poled in opposite directions, but if necessary this can be compensated by the control electrode polarity during electro-optic operation. Thus the planar electrode geometry offers a fabrication advantage if poling electric fields are required at the control electrodes that could lead to dielectric breakdown elsewhere.

The discussion of this section has presented the major issues of fabricating two-dimensional phased-array optics. As discussed current microelectronics



manufacturing technology and materials are available to make the devices that were discussed in section 4.5. Hence, with the materials, design, and fabrication capability existing, potential applications of these devices can be explored.

#### 4.7 APPLICATIONS

Phased-array optics have potential application in optical systems that require dynamic control of the wavefront of light. Selective pointing and shaping of light for free space propagation is applicable to optical communications, computing, signal processing, sensors, and xerography. Free space optical communications is represented by communications between moving platforms such as satellites and aircraft. Mechanical systems with moving mirrors or prisms introduce mechanical jitter, and have eventual mechanical wear. Such mechanical limitations reduce the effectiveness of optical communications for satellite communications. The phased-array devices have no moving parts, and can be scanned in position at megahertz rates which is not attainable by mechanics. The same phased-array optics used with communications systems is also available for lidar systems for pointing and tracking, and as scanners for inventory control such as used in supermarket check-out counters and xerographic laser printers. As components of detection and sensor systems, phased-arrays have application as tuneable lenses for selective sighting of a scene which is analogous to the directionality of phased-array radar receivers. Applications to optical computing and signal processing for phased arrays are based on the capability to dynamically create multiple beams from a single beam which enhances parallel optical computation, and change the optical system function of computation based on Fourier optics. Also, the techniques of fabrication and organic electro-optic materials discussed previously, can be used to fabricate two-dimensional optical wavefront sensors as proposed in reference [100]. These sensors can be used for beam evaluation and correction, and as means of communication coding

by wavefront modulation. This discussion represents only a few of the potential uses of two-dimensional phased-array optics. Applications that essentially need dynamic modulation of optical beam shape or position can find solutions in two-dimensional phased-array optics.

#### 4.8 CONCLUDING DISCUSSION

New capabilities in manufacturing and electro-optics brought by organic electro-optic materials permit the development of phase control optics that yield two-dimensional modulation of the wavefront of light. Implemented as arrays, the optical analog of phased-array radar can be developed. Employing element and array modulation, increased scan range with reduced side-lobes can be attained thereby increasing resolution. Because the control of light beams is electronic, increased modulation speeds, beam agility, and dynamic modulation are available that are not possible with mechanical systems. Microelectronic fabrication techniques can be employed that make the manufacturing of the devices feasible with current technology. An extensive range of application of light beam steering and shaping, including optical computing, communications, sensors, and printers can make immediate use of the capabilities of two-dimensional phased array optics.

This study has examined the conceptual basis, designs, and manufacturing feasibility of phased-array optics. Research into the actual construction of these devices, testing, and application to various uses is the next required step in the development of this technology.

## Chapter 4 - REFERENCES

- [1] V. J. Fowler and J. Schlafer, "A Survey of Laser Beam Deflection Techniques," *Proc. IEEE*, vol. 54, no. 10, pp. 1437-1444, 1966.
- [2] F. Dostal, "The fork as a scanner: a new twist," *Electronic Communicator*, vol. 1, pp. 4-5, 1966.
- [3] C. M. Alsabrook, "A multicolor laser display," *18<sup>th</sup> Annual National Aerospace Electronics Conference*, pp. 325-331, May 1966.
- [4] C. E. Baker and A. D. Rugari, "The laser display," *31965 Proc. Society for Information Display, 6th National Symposium on Information Display*, p. 85.
- [5] J. Schlafer and V. J. Fowler, "A precision, high speed, optical beam steerer," presented at the 1965 International Electron Devices Meeting.
- [6] F. S. Chen, J. E. Geusic, S. K. Kurtz, J. G. Skinner, and S. H. Wemple, "Light modulation and beam deflection with potassium tantalate-niobate crystals," *J. Appl. Phys.*, vol. 37, no. 1, pp. 388-398, 1966.
- [7] V. J. Fowler, C. F. Buhrer, and L. R. Bloom, "Electro-optic light beam deflector," *Proc. IEEE*, vol. 52, no. 2, pp. 193-194, 1964.
- [8] F. S. Chen, J. E. Greusic, S. K. Kurtz, J. G. Skinner, and S. H. Wemple, "The use of Perovskite paraelectrics in beam deflectors and light modulators," *Proc. IEEE*, vol. 52, no. 10, pp. 1258-1259, 1964.
- [9] W. Haas, R. Johannes, and P. Cholet, "Light beam deflection using the Kerr effect in single crystal prisms of BaTiO<sub>3</sub>," *Appl. Optics*, vol. 3, no. 8, pp. 988-989, 1964.
- [10] I. P. Kaminow, "Microwave modulation of the electro-optic effect in KHPO<sub>3</sub>," *Phys. Rev. Lett.*, vol. 6, no. 10, pp. 528-530, 1961.
- [11] R. Kalibjian, T. Huen, C. Maninger, and J. Yee, "Laser deflection modulation in a CdS prism," *Proc. IEEE*, vol. 53, no. 5, p. 539, 1965.
- [12] S. G. Liu and W. L. Walters, "Optical beam deflection by pulsed temperature gradients in bulk GaAs," *Proc. IEEE*, vol. 53, no. 5, p. 522, 1965.
- [13] K. W. Boer, "Franz-Keldysh effect for appreciable deflection of light beams," *Phys. Stat. Solidi B*, vol. 8, no. 3, pp. K179-K180, 1965.
- [14] U. J. Schmidt, "Problems of light beam deflection at high frequencies," in *Proc. Symp on Optical Processing of Information*, ed. by K. Pollack et. al., Baltimore, MD: Spartan, 1963, pp. 98-103.
- [15] A. J. Giarola and T. R. Billeter, "Electroacoustic deflection of a coherent light beam," *Proc. IEEE*, vol. 51, no. 8, pp. 1150-1151, 1963.
- [16] R. Lipnick, A. Reich, and G. A. Schoen, "Nonmechanical scanning of light in one and two dimensions," *Proc. IEEE*, vol. 53, no. 3, p. 321, 1965.
- [17] H. G. Aas and R. K. Erf, "Application of ultrasonic standing waves to the generation of optical beam scanning," *J. Acous. Soc. Am.*, vol. 36, no. 10, pp. 1906-1913, 1964.

- [18] W. Kulcke, T. J. Harris, K. Kosanke, and E. Max, "A fast digital-indexed light deflector," *IBM Jour.*, vol. 8, no. 1, pp. 64-67, 1964.
- [19] W. Kulcke, K. Kosanke, E. Max, H. Fleischer, and T. J. Harris, "Convergent beam digital light deflector," Chapter 23, *Optical and Electrooptical Information Processing*, ed. by J. T. Tippet et. al., (Cambridge: MIT Press, 1965).
- [20] T. J. Nelson, "Digital light deflection," *Bell Sys. Tech. J.*, vol. 43, no. 3, pp. 821-845, 1964.
- [21] U. J. Schmidt, "A high speed digital light beam deflector," *Phys. Lett.*, vol. 12, no. 3, pp. 205-206, 1964.
- [22] W. J. Tabor, "The use of Wollaston prisms for a high capacity digital light deflector," *Bell. Sys. Tech. J.*, vol. 43, no. 3, pp. 1153-1154, 1964.
- [23] R. A. Soref and D. H. McMahon, "Optical design of Wollaston-prism digital light deflectors," *Appl. Optics*, vol. 5, no. 3, pp. 425-434, 1966.
- [24] R. K. Lee, Jr and F. Moskowitz, "Transmission and self-generated characteristics of polarization scanned digital optical systems," *Appl. Optics*, vol. 3, no. 11, pp. 1305-1310, 1964.
- [25] A. Bromley, "High-power light flux resulting from bunching of light wave packets," *Appl. Phys. Lett.*, vol. 5, no. 10, pp. 210-212, 1964.
- [26] R. Burns, "On the possibility of using conical refraction phenomena for laser beam steering," *Appl. Optics*, vol. 3, no. 12, pp. 1505-1506, 1964.
- [27] W. Haas and R. Johannes, "Light beam scanning using conical refraction and optical activity," *Appl. Optics*, vol. 5, no. 6, pp. 1088-1089, 1966.
- [28] W. E. Buck and T. E. Holland, "Optical beam deflector," *Appl. Phys. Letts.*, vol. 8, no. 8, pp. 198-199, 1966.
- [29] A. Korpel, "Phased array type scanning of a laser beam," *Proc. IEEE*, vol. 53, no. 10, pp. 1666-1667, 1965.
- [30] A. Korpel, R. Adler, P. Desmares, and T. M. Smith, "An ultrasonic light deflection system," *IEEE J. Quantum Elec.*, vol. QE-1, no. 1, pp. 60-61, 1965.
- [31] I. C. Chang, "Acoustooptic Devices and Applications," *IEEE Trans. Sonics and Ultrason.*, vol. SU-23, no. 1, pp. 2-21, 1976.
- [32] A. Korpel, "Acousto-Optics - A Review of Fundamentals," *Proc. IEEE*, vol. 69, no. 1, pp. 48-53, 1981.
- [33] E. H. Young, Jr. and S.-K. Yao, "Design Considerations for Acousto-Optic Devices," *Proc. IEEE*, vol. 69, no. 1, pp. 54-64, 1981.
- [34] M. G. Cohen and E. I. Gordon, "Electro-optic [ $\text{KTa}_{2-x}\text{Nb}_{1-x}\text{O}$  (KTN)] grating for light beam modulation and deflection," *Appl. Phys. Lett.*, vol. 5, no. 9, pp. 181-182, 1964.
- [35] A. Yariv and P. Yeh, *Optical Waves in Crystals*, New York, NY: John Wiley & Sons, 1984, pp. 220-404.
- [36] J. W. Goodman, *Introduction to Fourier Optics*, New York, NY: McGraw-Hill, Inc., 1968, pp. 30-74.

- [37] J. H. Abeles and R. J. Deri, "Suppression of sidelobes in the far-field radiation patterns of optical waveguide arrays," *Appl. Phys. Lett.*, vol. 53, no. 15, pp. 1375-1377, 1988.
- [38] C. W. Bulmer, W. K. Burns, and T. G. Giallorenzi, "Performance criteria and limitations of electrooptic waveguide array deflectors," *Appl. Optics*, vol. 18, no. 19, pp. 3282-3295, 1979.
- [39] R. A. Meyer, "Optical Beam Steering Using a Multichannel Lithium Tantalate Crystal," *Appl. Optics*, vol. 11, no. 3, pp. 613-616, 1972.
- [40] H. Sasaki and R. M. De La Rue, "ELECTRO-OPTIC MULTICHANNEL WAVEGUIDE DEFLECTOR," *Electronic Lett.* vol. 13, no. 10, pp. 295-296, 1977.
- [41] Y. Ninomiya, "Ultrahigh Resolving Electrooptic Prism Array Light Deflectors," *IEEE J. Quantum Elec.*, vol. QE-9, no. 8, pp. 791-795, 1973.
- [42] I. P. Kaminow and L. W. Stulz, "A Planar Electrooptic-Prism Switch," *IEEE J. Quantum Elec.*, vol. QE-11, no. 8, pp. 633-635, 1975.
- [43] C. S. Tsai and P. Saunier, "Ultrafast guided-light beam deflection/switching and modulation using simulated electro-optic prism structures in  $\text{LiNbO}_3$  waveguides," *Appl. Phys. Lett.*, vol. 27, no. 4, pp. 248-250, 1975.
- [44] R. H. Hobbs, A. J. Cantor, D. H. Grantham, A. J. Shuskus, J. M. Berak, M. E. Cowher, J. D. Farina, N. N. Hoffman, J. F. Black, G. W. Drake, R. T. Brown, C. E. Holton, B. B. Silverman, F. J. Leonberger, and A. J. De-Maria, "Laser Electro-Optic Phased Array Devices (LEOPARD)," *LEOS '88 Conference Proceedings*, Nov. 2-4, 1988, Santa Clara, CA. (IEEE Catalog Number: 88CH 2683-1), pp. 94-95.
- [45] J. Katz, "Electronic beam steering of semiconductor injection lasers: a theoretical analysis," *Appl. Optics*, vol. 22, no. 2, pp. 313-317, 1983.
- [46] S. Mukai, M. Watanabe, H. Itoh. and H. Yajima, "Analysis of a Double-Heterostructure Spatial-Phase Controller for Diode-Laser Beam Steering," *IEEE J. Quantum Electron.*, vol. QE-24, no. 12, pp. 2415-2422, 1988.
- [47] S. Mukai, M. Watanabe, H. Itoh, H. Yajima, "Integration of a diode laser and an electronic lens for controlling the beam focus position," *Appl. Phys. Lett.*, vol. 54, no. 4, pp. 315-316, 1989.
- [48] D. R. Scifres, W. Streifer, and R. D. Burnham, "Beam scanning with twin stripe injection lasers," *Appl. Phys. Lett.*, vol. 33, no. 8, pp. 702-704, 1978.
- [49] S. Mukai, M. Watanabe, H. Itoh, H. Yajima, Y. Hosoi, S Uekusa, "Beam scanning and switching characteristics of twin striped lasers with reduced stripe spacing," *Opt. Quantum Electron.*, vol. 17, pp. 431-434, 1985.
- [50] K. Kojima and K. Kyuma, "Fast beam switching in surface emitting distributed Bragg reflector laser," *Appl. Phys. Lett.*, vol. 53, no. 15, pp. 1357-1359, 1988.
- [51] N. W. Carlson, G. A. Evans, R. Amantea, S. L. Palfrey, J. M. Hammer, M. Lurie, L. A. Carr, F. Z. Hawrylo, E. A. James, C. J. Kaiser, J. B. Kirk, and W. F. Reichart, "Electronic beam steering in monolithic grating-surface-emitting diode laser," *Appl. Phys. Lett.*, vol. 53, no. 23, pp. 2275-2277, 1988.

- [52] T. C. Lee and J. D. Zook, "Light Beam Deflection with Electrooptic Prisms," *IEEE J. Quantum Electron.*, vol. QE-4, no. 7, pp. 442-454, 1968.
- [53] W. T. Boord, *Integrated Optic Device for Laser Beam Scanning, Final Report*, National Aeronautics and Space R& E Systems Procurement Office, Administration, Lyndon B. Johnson Space Center, Contract Number NAS 9-17813.
- [54] *Nonlinear Optical and Electroactive Polymers*, ed. by P. N. Prasad and D. R. Ulrich, New York, NY: Plenum Press, 1988.
- [55] *Organic Materials For Non-Linear Optics*, ed. by R. A. Hann and D. Bloor, London: Royal Society of Chemistry, Burlington House, 1989.
- [56] *Non-Linear Optical Properties of Organic and Polymeric Materials*, ed. by D. J. Williams, Washington, D. C.: American Chemical Society, 1985.
- [57] *Non-linear Optical Properties of Organic Molecules and Crystals*, ed. by D. S. Chemla and J. Zyss, New York, NY: Academic Press, 1987.
- [58] B. F. Levine, C. G. Bethea, C. D. Thurmand, R. T. Lynch, and J. L. Bernstein, "An organic crystal with an exceptionally large optical second harmonic coefficient: 2-methyl-4-nitroaniline," *J. Appl. Phys.*, vol. 50, no. 4, pp. 2523-2527, 1979.
- [59] G. F. Lipscomb, A. F. Garito, and R. S. Narang, "An exceptionally large linear electro-optic effect in the organic solid MNA," *J. Chem. Phys.*, vol. 75, no. 3, pp. 1509-1516, 1981.
- [60] D. Williams, "Polymers in Non-linear Optics," in *Electronic and Photonic Application of Polymers*, ed. by M. J. Bowden and S. J. Turner, Washington D. C.: American Chemical Society, 1988, pp. 297-330.
- [61] "Nonlinear Optical Properties of Materials," ed. by C. M. Bowden and J. W. Haus in *J. Opt. Soc. Amer. B*, vol. 6, no. 4, pp. 778-823, 1989.
- [62] K. D. Singer, J. E. Sohn, and S. J. Lalama, "Second harmonic generation in poled polymer films," *Appl. Phys. Lett.*, vol. 49, no. 5, pp. 248-250, 1986.
- [63] K. D. Singer, S. L. Lalama, J. E. Sohn, and R. D. Small, "Electro-Optic Organic Materials," in *Nonlinear Optical Properties of Organic Molecules and Crystals*, vol. 1, ed. by D. S. Chemla and J. Zyss, New York, NY: Academic Press, 1988, pp. 437-468.
- [64] C. S. Willand, S. E. Feth, M. Scozzafava, D. J. Williams, G. D. Green, J. I. Weinschenk, III, H. K. Hall, Jr., and J. E. Mulvaney, "Electric-Field Poling of Nonlinear Optical Polymers," in *Nonlinear Optical and Electroactive Polymers*, ed. by P. N. Prasad and D. R. Ulrich, New York, NY: Plenum Press, 1988, pp. 107-120.
- [65] K. D. Singer, M. G. Kuzuk, and J. S. Sohn, "Orientationally Ordered Electro-Optical Materials," in *Non-linear Optical and Electroactive Polymers*, ed. by P. N. Prasad and D. R. Ulrich, New York, NY: Plenum Press, 1988, pp. 189-204.
- [66] D. R. Ulrich, "Overview: Non-linear Optical Organics and Devices," in *Organic Materials for Non-linear Optics*, ed. by R. A. Hann and D. Bloor, Burlington House, London: Royal Chemical Society, 1989, pp. 241-263.
- [67] R. N. Demartino, E. W. Choe, G. Khamarian, D. Hass, T. Leslie, G. Nelson, J. Stamatoff, D. Stuetz, C. C. Tang, and H. Yoon, "Development of Polymeric

- Non-linear Optical Materials", in *Non-linear Optical and Electroactive Polymers*, ed. by P. N. Prasad and D. A. Ulrich, New York, NY: Plenum Press, 1988, pp. 169-188.
- [68] R. N. DeMartino, G. Khanarian, T. M. Leslie, M. J. Sansone, J. B. Stamatoff, and H. N. Yoon, "ORGANIC AND POLYMERIC MATERIALS FOR NON LINEAR DEVICES," in *SPIE vol. 1105 - Materials for Optical Switches, Isolators, and Limiters*, Bellingham, WA: Society of Photo-Optical Instrumentation Engineers, pp. 2-13, 1989.
  - [69] S. Ermer, S. Lovejoy, D. Leung, J. Altman, K. Aron, R. Spitzer, and G. Hansen, "Synthesis and Evaluation of Cumulenes: Novel Rigid Nonlinear Optical Materials," *SPIE-1990*, vol. 1337, pp. 11- , 1990.
  - [70] M. A. Hubbard, T. J. Marks, J. Yang, G. K. Wong, "Poled Polymeric Non-linear Optical Materials, Enhanced Second Harmonic Generation Stability of Cross-Linkable Matrix/Chromophore Ensemble," *Chemistry of Materials*, vol. 1, no. 2, pp. 167-169, 1989.
  - [71] J. I. Thackara, G. F. Lipscomb, M. A. Stilley, A. J. Ticknor, and R. S. Lytel, "Poled electro-optic waveguide formation in thin-film organic media," *Appl. Phys. Lett.*, vol. 52, no. 13, pp. 1031-1033, 1986.
  - [72] J. I. Thackara, G. F. Lipscomb, R. S. Lytel, and J. Ticknor, "Advances in Organic Electro-Optic Devices", *Non-linear Optical Properties of Polymers*, ed. by A. J. Heeger, J. Orenstein, and D. R. Ulrich, Boston, MA: Materials Research Society, 1987, pp. 10-27.
  - [73] W. R. Holland, "Electro-Optic Polymer Waveguides," *LEOS '88 Conference Proceedings*, Nov. 2-4, 1988, Santa Clara, CA. (IEEE Catalog Number: 88CH 2683-1), pp. 164-165.
  - [74] R. Lytel, G. F. Lipscomb, J. Thackara, J. Altman, P. Elizordo, Stiller and B. Sullivan, "Non-linear and Electro-Optic Devices," in *Non-linear Optical and Electroactive Polymers*, ed. by P. N. Prasad and D. R. Ulrich, New York: Plenum Press, 1988, pp. 241-263.
  - [75] D. Haas, H. Yoon, H.-T. Man, G. Cross, S. Mann, N. Parsons, "Polymeric electro-optic modulator; materials and fabrication," in *SPIE Vol. 1147 Nonlinear Optical Properties of Organic Materials II*, ed. by G. Khanarian, Bellingham, WA: Society of Photo-Optical Instrumentation Engineers, pp. 222-232, 1989.
  - [76] G. F. Lipscomb, R. S. Lytel, A. J. Ticknor, T. E. Van Eck, S. L. Kwiakowski, and D. G. Girton, "Developments in Organic Electro-Optic Devices at Lockheed," *SPIE-1337*, pp. 1-12, 1990.
  - [77] S. K. Ghandhi, *VLSI Fabrication Principles*, New York, NY: John Wiley & Sons, 1983, pp. 213-297.
  - [78] C. W. Pierce, "Epitaxy," in *VLSI Technology*, ed. by S. M. Sze, New York, NY: McGraw-Hill Book Company, 1988, pp. 55-97.
  - [79] R. Selvaraj, H. T. Lin, and J. F. McDonald, "Integrated Optical Waveguides in Polyimide for Wafer Scale Integration," *J. of Lightwave Tech.*, vol. LT-6, no. 6, pp. 1034-1044, 1988.

- [80] N. Mario, S. Dabral, and J. F. McDonald, "The Parylene-Aluminum Multilayer Interconnection System for Wafer Scale Integration and Wafer Scale Hybrid Packaging," *J. Electronic Mat.*, vol. 18, no. 8, pp. 301-311, 1989.
- [81] O. I. Szentesi and E. A. Noga, "Parylene C Films for Optical Waveguides," *Appl. Optics*, vol. 13, no. 11, pp. 2458-2459, 1974.
- [82] A. Otto and W. Sohler, "Modification of the Total Reflection Modes in a Dielectric Film by One Metal Boundary," *Optics Commun.*, vol. 3, no. 4, pp. 254-258, 1971.
- [83] Y. Suematsu and K. Furuya, "Propagation Mode and Scattering Loss of a Two-Dimensional Dielectric Waveguide with Gradual Distribution of Refractive Index," *IEEE Trans. Microwave Theory and Tech.*, vol. MTT-20, no. 8, pp. 524-531, 1972.
- [84] Y. Suematsu, M. Hakuta, K. Furuya, K. Chiba, and R. Hasumi, "Fundamental Transverse Electric Field (TE) Mode selection for thin film asymmetric light guides," *Appl. Phys. Lett.*, vol. 21, no. 6, pp. 291-293, 1972.
- [85] A. Reisinger, "Characteristics of Optical Guided Modes in Lossy Waveguides," *Appl. Optics*, vol. 12, no. 5, pp. 1015-1025, 1973.
- [86] I. P. Kaminow, W. L. Mammel, and H. P. Weber, "Metal-Clad Optical Waveguides: Analytical and Experimental Study," *Appl. Optics*, vol. 13, no. 2, pp. 396-405, 1974.
- [87] P. K. Tien, R. J. Martin, and S. Riva-Sanseverina, "Novel metal-clad optical components and methods of isolating high-index substrates for forming integrated optical circuits," *Appl. Phys.*, vol. 27, no. 4, pp. 251-253, 1974.
- [88] M. Masuda, A. Tanji, Y. Ando, and J. Koyana, "Propagation losses of Guided Modes in an Optical Graded Index Slab Waveguide with Metal Cladding," *IEEE Trans. Microwave Theory Tech.*, vol. MTT-25, no. 9, pp. 773-776, 1977.
- [89] Z. H. Wang and S. R. Seshadri, "Metal-clad planar four-layer optical waveguide," *J. Opt. Soc. Am. A*, vol. 6, no. 1, pp. 142-144, 1989.
- [90] H. Nishihara, M. Haruna, and T. Suhara, *Optical Integrated Circuits*, New York, NY: McGraw-Hill Book Company, 1989, pp. 16-21.
- [91] M. Kobayashi, N. Colaneri, M. Boysel, F. Wudl, A. J. Heeger, "The electronic and electrochemical properties of poly(isothianophene)," *J. Chem. Phys.*, vol. 82, no. 12, pp. 5717-5723, 1985.
- [92] A. Bolognesi, M. Catallani, S. Destri, R. Zamboni, and C. Taliani, "Poly(dithieno [3,4-b: 3', 4'-d] thiophene): A New Transparent Conducting Polymer," *J. Chemical Soc., Chem. Commun.*, vol. 1988, no. 4, pp. 246-247, 1988.
- [93] N. P. Vlannes, *Embedded Microstructures for High-Density-Integrated and Phased-Array Optics*, Concept paper, Rensselaer Polytechnic Institute, 1987.
- [94] K. P. Nelson and N. P. Vlannes, "Analysis of Electro-Optic Waveguides with Embedded Electrode Structures," presented 1990 LEOS Annual Meeting, Nov. 5-9, 1990, Boston, MA.



- [95] M. A. Title and S. H. Lee, "Modeling and characterization of embedded electrode performance in transverse electro-optic modulators," *Appl. Optics*, vol. 29, no. 1, pp. 85-98, 1990.
- [96] R. J. Schultz, "Reactive Plasma Etching," in *VLSI Technology, Second Edition*, ed. by S. M. Sze, New York, NY: McGraw-Hill Book Company, 1988, pp. 184-232.
- [97] R. K. Watts, "Lithography," in *VLSI Technology, Second Edition*, ed. by S. M. Sze, New York, NY: McGraw-Hill Book Company, 1988, pp. 141-183.
- [98] S. P. Murarka, "Metallization," in *VLSI Technology, Second Edition*, ed. by S. M. Sze, New York, NY: McGraw-Hill Book Company, 1988, pp. 375-421.
- [99] S.-N. Mei, T.-M. Lu, S. Roberts, "Non-conformal Al Via Filling and Planarization by Partially Ionized Beam Deposition for Multilevel Interconnections," *IEEE Electron Device Lett.*, vol. EDL-8, no. 10, pp. 503-505, 1987.
- [100] R. H. Rediker, T. A. Lund, B. E. Burke, "Optical Wavefront Measurement and/or Modification Using Integrated Optics," *J. of Lightwave Tech.*, vol. LT-6, no. 6, pp. 916-932, 1988.
- [101] A. Yariv and P. Yeh, *Optical Waves in Crystals*, New York, NY: John Wiley & Sons, 1984, pp. 230-234.

## *CHAPTER V*

### **Hybrid Optical/Electronic Nonlinear Optical Devices**

*Nickolas P. Vlannes, Casimer M. DeCusatis, and Pankaj K. Das*

#### **5.1 INTRODUCTION**

Nonlinear photonics that exhibit bistability and hysteresis can be developed from three basic methods that provide the nonlinear-optical behavior of a device. These three approaches are based on:

1. Nonlinear Optical Materials,
2. Nonlinear Optical Structures, and
4. Nonlinear Electronic Feedback.

Nonlinear optical materials provide an optical nonlinearity that is characteristic of the material. Nonlinear optical structures are founded on the nonlinear response of light to the geometry of a device rather than the materials from which it is made. In contrast to nonlinear-optical materials and structures, which have inherent optical nonlinearity, nonlinear electronic feedback is an active and external control mechanism that creates an optical nonlinearity. To illustrate and contrast these three techniques for forming nonlinear photonics that have bistable and hysteresis properties, a brief description of these three techniques ensues. This discussion is illustrative of these methods and not exhaustive.

##### **5.1.1 NONLINEAR OPTICAL MATERIALS:**

Optical material nonlinearities, arising from nonlinear optical susceptibilities ( $\chi^{(2)}$ ,  $\chi^{(3)}$ ) [1] in semiconductors, crystalline ceramics [2], organic compounds [3-7], and composites [8]. The nonlinear effects are usually restricted to relatively high optical intensities ( $10^6$  to  $10^9$  W/m<sup>2</sup>) in which the refractive index is a function of optical intensity,  $I$ :

$$n(\bar{r}, t) = n_0(\bar{r}) + n_2(\bar{r})I(\bar{r}, t), \quad (5.1)$$

where  $\bar{r}$  and  $t$  are respectively position and time.  $n_0$  and  $n_2$  are terms whose values depend on the specific material. At sufficiently low  $I$ ,  $n$  is approximated as the unperturbed  $n_0$ . Devices developed from nonlinear materials exhibit properties such as optical bistability, hysteresis, limiting effects and switching, without resorting to nonlinear structures [9-13] to produce these effects. In addition to purely intrinsic nonlinear optical interactions, nonlinear optical devices using the nonlinear properties of materials with electronic connection between devices have been developed such as self-electro-optic effect devices [14-16].

### 5.1.2 NONLINEAR OPTICAL STRUCTURES:

Another approach to development of nonlinear optical devices is to use nonlinear optical structures. The optical properties of the structure provide the nonlinearity. One example of such a nonlinear structure is the Fabry-Perot interferometer. This device has a relationship between transmitted ( $I_t$ ) and incident ( $I_i$ ) light intensity given by:

$$I_t = \frac{(1 - R)^2}{(1 - R)^2 + 4R \sin^2(\Theta)} I_i \quad (5.2)$$

where  $R$  is the reflectivity of the mirrors of the Fabry-Perot etalon, and  $\Theta$  is a controllable phase term. Other examples of nonlinear structures are the polarizer/analyzer combination, small-angle phase gratings, and integrated-optic devices such as directional coupler and Mach-Zehnder modulators [1,2]. These configurations have a relationship between transmitted ( $I_t$ ) and incident ( $I_i$ ) light intensity given by:

$$I_t = I_i \sin^2(\Theta) \quad (5.3)$$

Typically these structures are used as linear devices, in that the transmitted intensity is linearly related to the incident intensity by a term that is a function of  $\Theta$  which is independent of the incident or transmitted light. However, these optical structures are nonlinear functions of  $\Theta$  as given by equations (5.2) and

(5.3). The nonlinear relations between incident and transmitted intensities occur when  $\Theta$  is controlled by the optical intensity of the input light or output light, and thus the full nonlinear character of equations (2) and (3) is invoked. Another example of a nonlinear optical structure is the cut-off modulator [17], but this device does not have a periodic behavior as given in equations (5.2) and (5.3).

A nonlinear optical structure can be used with either linear or nonlinear optical materials. As an example consider the application of the Fabry-Perot interferometer to form a bistable-optical-device (BOD) with linear or nonlinear optical materials within the Fabry-Perot resonator. The operation of a BOD requires of  $\Theta$  as a function of light intensity. The device is intrinsic if  $\Theta$  is controlled only with light using nonlinear optical materials [1], while the use of an electronic drive to generate optical nonlinearities [74,75], or an external electronic feedback circuit that is controlled by input or output light intensity, constitutes a hybrid device [2]. Although hybrid devices typically exhibit longer switching times than intrinsic BODs, they can also be made with much lower and flexible optical switching intensities.

Nonlinear optical materials employed with a Fabry-Perot interferometer have been used to develop or propose bistable operation from nonlinear absorption, dispersion, and intensity effects [1,2,18-21,74,75]. Intrinsic nonlinear optical materials [1,2,18-21] and electronically driven optical nonlinearities as found in diode laser amplifiers [74,75] have been explored. In these cases, the nonlinear optical material is placed within a Fabry-Perot and controls the transmission properties of the interferometer by varying the index of refraction within the Fabry-Perot structure, and thus changes  $\Theta$ . In particular, a bistable optical device may function as an optical switch, a limiter, a pulse shaper, or an optical memory. Such devices can constitute the basic components for digital optical computing applications [22-24].

Hybrid optical/electronic (HO/E) devices using Fabry-Perot interferometers are based essentially on the structure shown in Figure 5.1, and have been built from bulk components or integrated-optic channel waveguides [1, 25-28]. An electro-optic phase modulator is placed within the resonant cavity, and a fraction of the transmitted beam intensity is monitored by a detector. The detector signal, which is proportional to the output light intensity, is amplified and fed back to drive the modulator. This simulates a nonlinear effect, since the electro-optically controlled index of refraction is now a function of the light intensity. A typical input-output characteristic for such a device [2] is similar to that shown in Figure 5.4. The output signal exhibits hysteresis, that is, the output intensity of the device for a given input intensity depends on the past history of the device. The speed of such a hybrid device is limited by the response time of the detector circuit. However, this type of nonlinearity can be much greater than an intrinsic device (since it is limited only by the sensitivity of the detector), and it is much more flexible and controllable because the feedback electronics can be electronically tuned. The device characteristics may be adjusted by varying an applied bias voltage to the electro-optic crystal, and the device is easier to fabricate since it depends only on the well-established linear phase modulator.

Other nonlinear optical device structures that are electronically controllable have been employed to develop hybrid nonlinear optical systems. Nonlinear optical configurations employing polarizer/analyzer combinations [29-37], integrated-optic directional couplers [38,39], integrated optic Mach-Zehnder interferometers [40,41], and cut-off modulators [42] have been explored.

#### 5.1.3 NONLINEAR ELECTRONIC FEEDBACK:

Most bistable optical devices use optical nonlinearities or linear electronic feedback. Relatively little work has been done with nonlinear electronic feedback [43,44], except to enhance an existing optical nonlinearity [45]. The essence

FIGURE 5.1

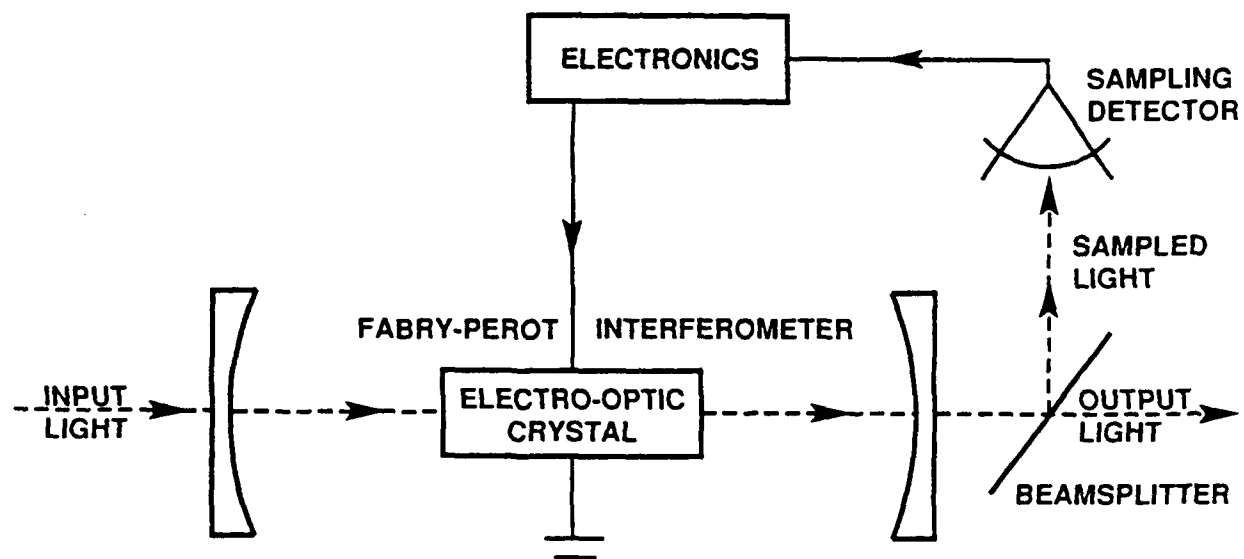


Figure 5.1. Schematic of optical bistable Fabry-Perot hybrid device.

of the bistable hybrid optical-electronic nonlinear optical device based on nonlinear electronic feedback that controls linear optical modulators is illustrated in Figure 5.2. Light enters a linear optical modulation system. Part of the light is sampled and directed to a detector that provides an electronic signal that varies a nonlinear electronic circuit. This nonlinear-electronic circuit then provides a signal that controls the linear optical modulation system. The linear modulation system responds to the nonlinear electronic control to modify the light, so that the exiting light has a nonlinear behavior as a response to the incident light.

As an alternative to the use of nonlinear-optical materials and structures, nonlinear electronic feedback to control linear optical modulators provides a means of developing new nonlinear optical devices. Such devices can be flexible, compact, and electronically and optically tuneable, and can provide nonlinear optical characteristics which are difficult or impossible to obtain by other means. New bistable optical devices are proposed based on a linear optical deflector, in which the electronic feedback circuit supplies all of the necessary nonlinearity. The nonlinear electronic circuit can be as simple as a single electronic thresholding element in order to simulate bistability and hysteresis effects. More complex electronics can provide multiple levels of bistability and hysteresis, or vary the nonlinear response over a range of nonlinear characteristics. The use of electronic nonlinearity frees a design from the constraints of high optical intensities as needed in intrinsic devices, and the need to drive a nonlinear optical structure over the complete range of its nonlinearity. Thus, the hybrid optical/electronic approach using linear optics and nonlinear electronics is an attractive approach to bistable optical devices.

The following sections describe an experimental implementation of a bistable optical device based on a bulk acousto-optic light modulator with nonlinear

FIGURE 5.2

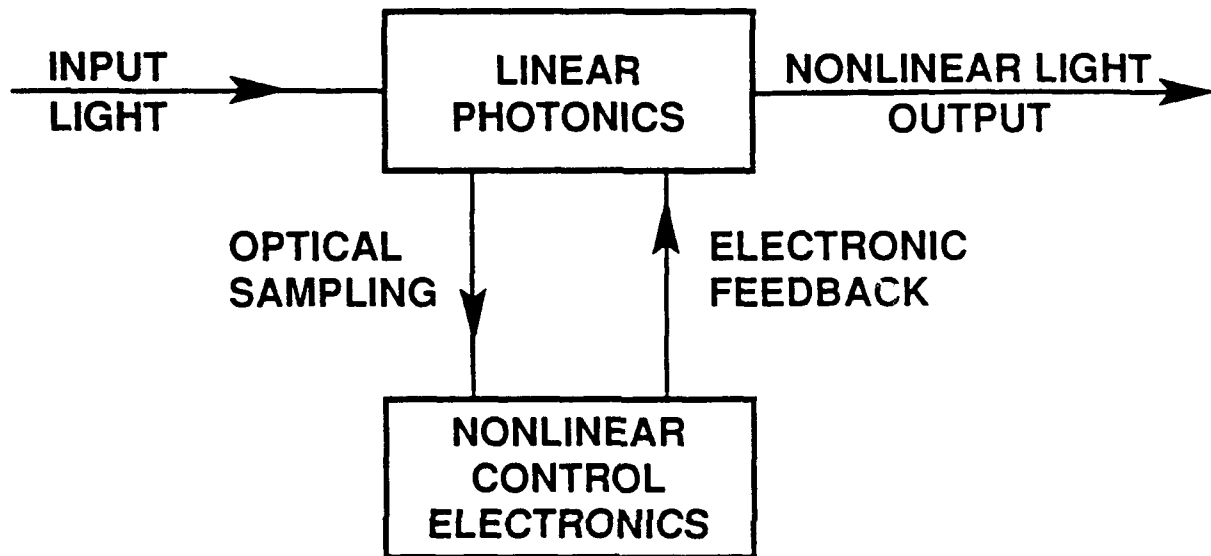


Figure 5.2. Concept diagram of a hybrid optical/electronic nonlinear optical device with nonlinear electronic feedback.



electronic feedback. Experimental results are given, and a conceptual device using electro-optic light modulators is discussed.

## 5.2 ACOUSTO-OPTIC BISTABLE OPTICAL EXPERIMENT

The basic theory of the acousto-optic bistable optical experiment is illustrated in Figure 5.3. A linear acousto-optic (AO) deflector, driven by a modulated microwave signal, is used to generate a diffracted beam. Light intensity (incident or output from the AO deflector) is monitored by a photodetector, whose output voltage is connected to a nonlinear feedback circuit as shown. When the diffracted light signal exceeds the threshold set by the electronic thresholding device in the feedback loop, the nonlinear electronics modulate the microwave signal. The microwave signal in turn controls the diffraction efficiency of the acousto-optic cell, and thus the degree of light modulation. Use of the acousto-optic modulator is partially predicated on the simplicity of the sampling scheme. The acousto-optic cell generates two light beams either of which can be sampled or used as the signal light. This eliminates additional optics that split the light for sampling or signal purposes as required by other modulator techniques [28-37]. In general, a phase-grating type modulator, either acousto-optic or electro-optic, provides the secondary beams without the additional beam-splitting optics.

Consider operation of the system with the first order diffracted light (Figure 5.3) of the acousto-optic modulator acting to control the nonlinear electronics. The electronics realize a simple thresholding nonlinearity that is an abrupt "low" to "high". For a range of diffracted light intensity, the signal from the photodetector remains below the threshold level for triggering the nonlinearity. Since the feedback is inoperative, the output light intensity from the AO cell increases linearly with the incident intensity to point (1) in Figure 5.4. When the diffracted light intensity exceeds threshold and feedback begins to occur, the magnitude of the acousto-optic driving signal increases abruptly; this causes

**FIGURE 5.3**

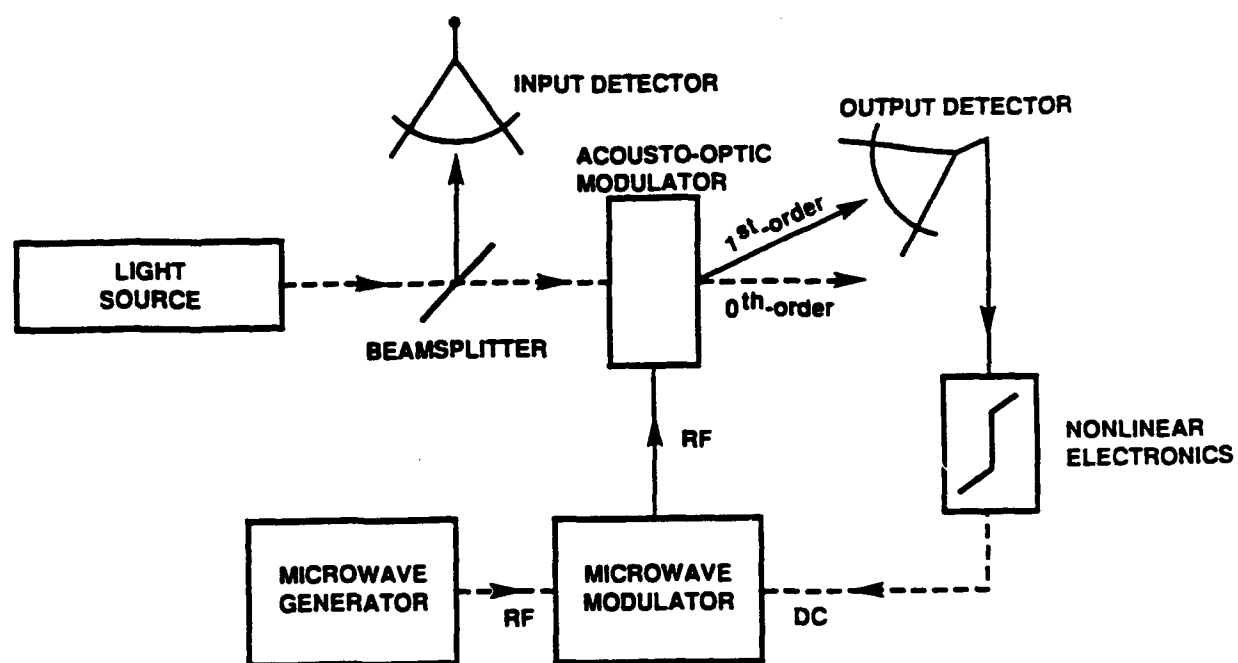


**Figure 5.3. Schematic of acousto-optic deflector implementation of hybrid optical/electronic binary optical device.**

a corresponding sudden increase in the diffracted light amplitude from point (1) to point (2) of Figure 5.4. Beyond this point, the diffracted light intensity continues to increase linearly with incident light intensity, up to point (3); note that the slope will differ from its initial value below point (1) because of the additional contribution of the feedback loop to the acousto-optic signal. If the incident light intensity is then decreased, the diffracted intensity will also decrease linearly following the slope between points (2) and (3). However, this curve does not cross the threshold level until after the incident intensity has fallen below the level which caused the original "jump" from (1) to (2). As a result, the output intensity will continue to decrease linearly with decreasing input intensity until the output intensity falls below threshold; at this point, the feedback signal stops and the diffracted light intensity falls abruptly at point (4). A further decrease in incident intensity will cause the output intensity to decrease linearly along the lower portion of the curve, as shown in Figure 5.4. In this way, nonlinear electronic feedback of the diffracted light signal can be used to generate optical bistability and hysteresis characteristics using a linear acousto-optic device. It should be noted that the nonlinear threshold does not have to be controlled by the first order diffracted light. The incident light, and the 0<sup>th</sup>-order of the diffracted light, can also be used to control the nonlinear threshold producing different nonlinear optical output than shown in Figure 5.4.

Figure 5.5 is a schematic of the acousto-optic bistable optical experiment that demonstrates the hybrid optical/electronic nonlinear optical concept. There are basically three parts to the experimental configuration. These are the optical path, the acousto-optic deflector and its microwave system, and the nonlinear electronic feedback circuitry.

The optical path begins with a linearly polarized, 10 mW HeNe laser operating at the 632.8 nm wavelength. An NEC #GLG5261 laser was the light source

FIGURE 5.4

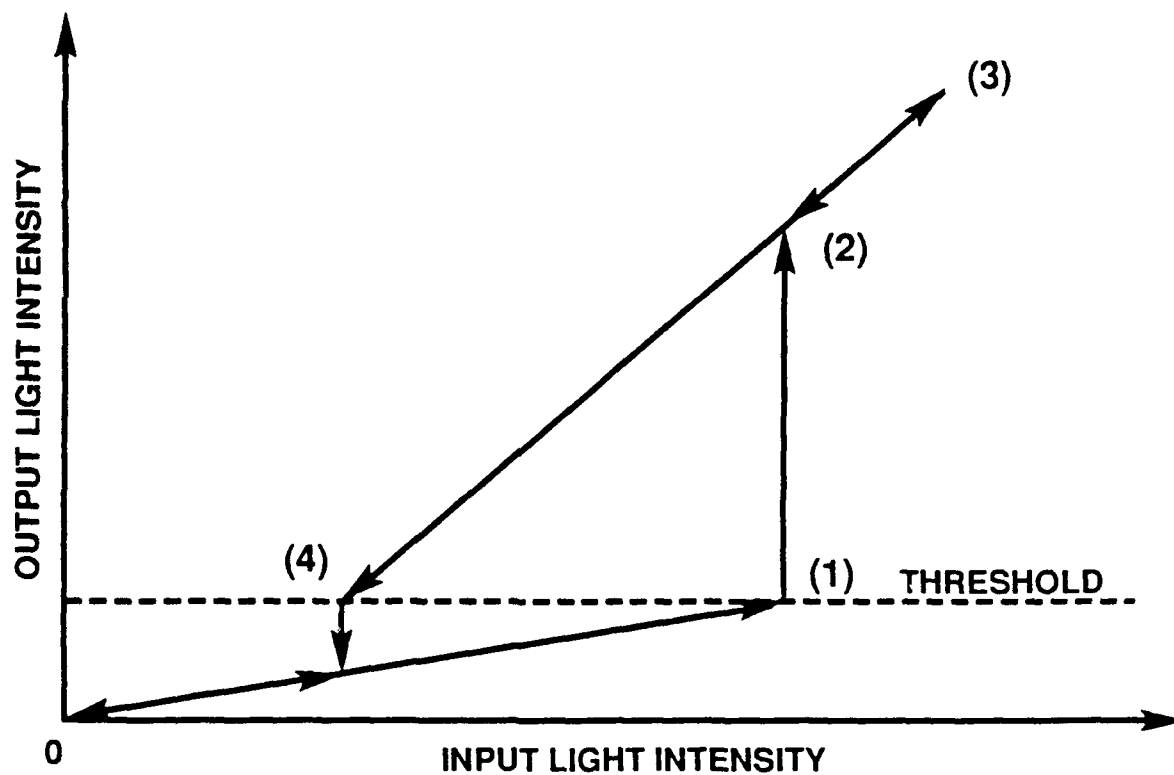


Figure 5.4. Theoretical behavior of acousto-optic deflector HO/E bistable optical device. Arrows indicate the direction of first increasing and then decreasing optical input power.

FIGURE 5.5

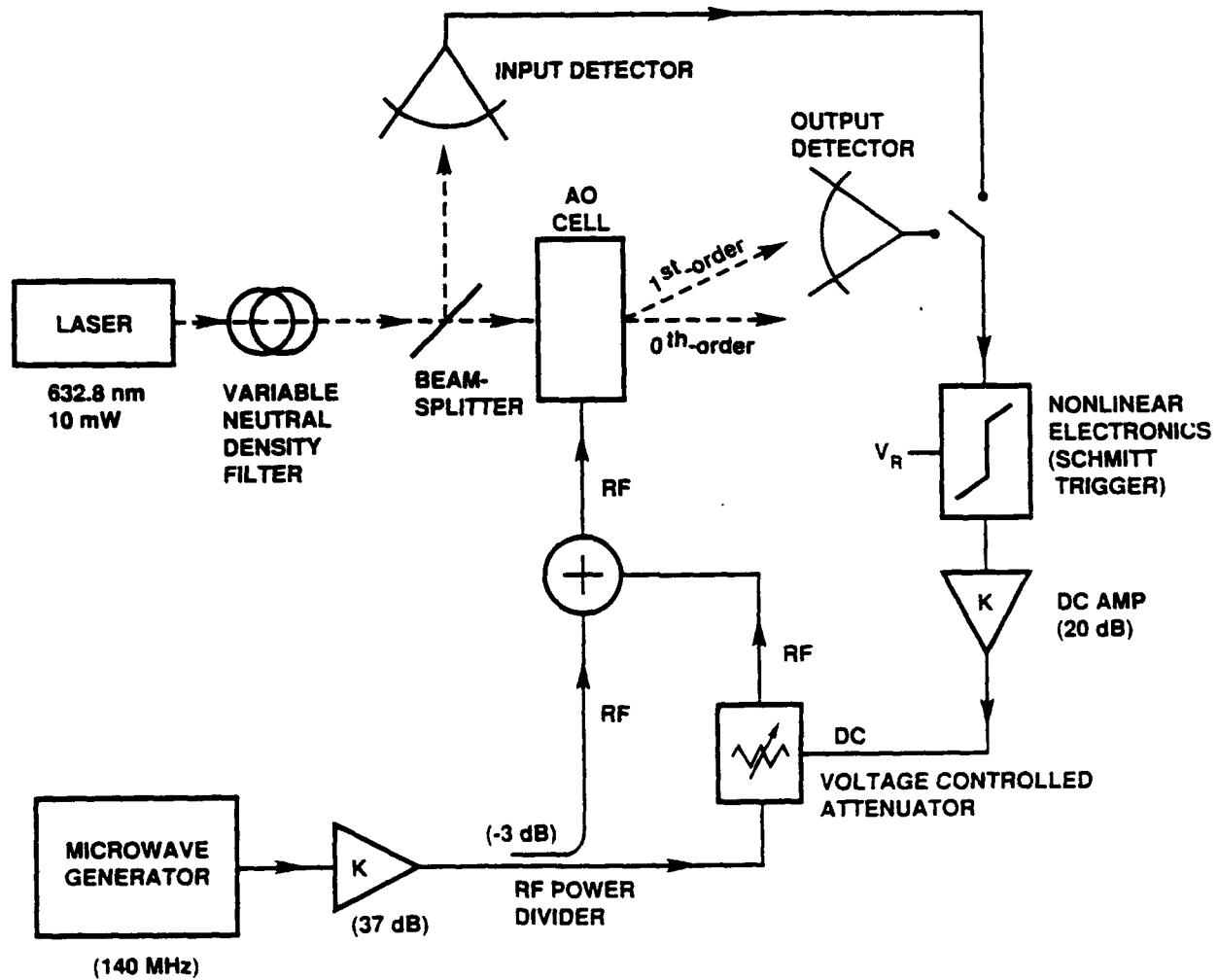


Figure 5.5. Schematic of experimental HO/E bistable optical device with linear acousto-optic modulation and nonlinear electronic feedback.

for this experiment. Light from this laser transversed a Polaroid variable neutral density filter that controlled the incident light intensity. Following the neutral density filter, a 90% transmissive optical beam splitter was used to direct part of the beam towards a photodiode detector to monitor the incident light. The main part of the beam was then focused and collimated by a lens system and was incident on an acousto-optic (AO) deflector operated in the Bragg regime. The 1<sup>st</sup>-order beam was detected by a photodiode detector. Though available, the 0<sup>th</sup>-order beam was not utilized in this experiment. The photodiode detectors employed were Hewlett Packard PIN photodiodes model 5082-4220.

The acousto-optic deflector for this experiment was an NEC bulk acousto-optic device fabricated from lead molybdate (NEC #OD8813A) with a center operating frequency of 140 MHz. The device was capable of generating over 80% diffraction efficiency in the Bragg regime. The AO device was driven from a Hewlett Packard VHF signal generator supplemented by an RF-power amplifier (ENI, Inc. #403L) with 37 dB gain. Microwave power emerging from the amplifier was split by a -3 dB power divider (Pomona Electronics). Half of the RF-power directly entered a summer (#MCL PSC 2-1) with the remainder entering a voltage-controlled attenuator (VCA). The portion of the signal that was sent directly to the summer provides the initial bias to drive the AO modulator with no feedback, while the remaining signal was modulated by the VCA to control the AO cell. The VCA attenuates an RF-signal by an amount proportional to an external DC control voltage. The voltage variable attenuator device chosen was a Mini-circuits voltage-controlled attenuator (PAS-2), designed to operate from 10 MHz to 1 GHz. This was a low power device, requiring only 100 mW operating RF-power and less than 1 V for DC control. The attenuator output vs. control voltage is shown in Figure 5.6, for a fixed RF-input of 3 V (peak-to-peak into 50 $\Omega$ ). The modulated RF-signal from the VCA was then combined at the

summer with the microwave signal taken directly from the power divider. The microwave signal from the summer thus controlled the diffraction efficiency of the acousto-optic cell. The modulation for the VCA was a "DC" signal from the nonlinear feedback electronics.

There are many possible realizations for the nonlinear electronics. In this experiment, a Schmitt trigger (regenerative comparator) followed by an operational-amplifier inverter was chosen for simplicity, availability, and cost. The Schmitt trigger is essentially an op-amp configured with a voltage divider feedback circuit and external bias voltage as shown in Figure 5.7(a). Details of this circuit are described in reference [46]. The Schmitt trigger employed is capable of nanosecond switching times, while requiring low drive power. The Schmitt trigger is also capable of producing its own electronic hysteresis as shown in a typical response curve of Figure 5.7(b). The amount of hysteresis may be controlled by varying the choice of resistors in Figure 5.7(a). In order to avoid interference with the bistable optical hysteresis, the Schmitt trigger hysteresis was set to 0.001 V. Further, the switching voltage (triggering level) of this Schmitt trigger can be varied electronically by adjusting the bias voltage  $V_R$ . The optical bistable device required a trigger to switch between "low" and "high" states, rather than the characteristic response of Figure 5.7(b). To realize this response, an op-amp inverter was inserted after the Schmitt trigger. A unity gain op-amp was also added after the inverter to isolate the thresholding device, and to act as a voltage follower. A schematic of the final thresholding circuit is shown in Figure 5.8. Because the VCA response to the DC control is linear between 0.45 and 0.9 V, the Schmitt trigger was engaged at a threshold of 0.6 V.

To begin the nonlinear electronic feedback, a signal from either the incident light monitoring detector, or the 1<sup>st</sup>-order diffracted light detector, entered and controlled the nonlinear electronics. Figure 5.5 shows control from the 1<sup>st</sup>-order

FIGURE 5.6

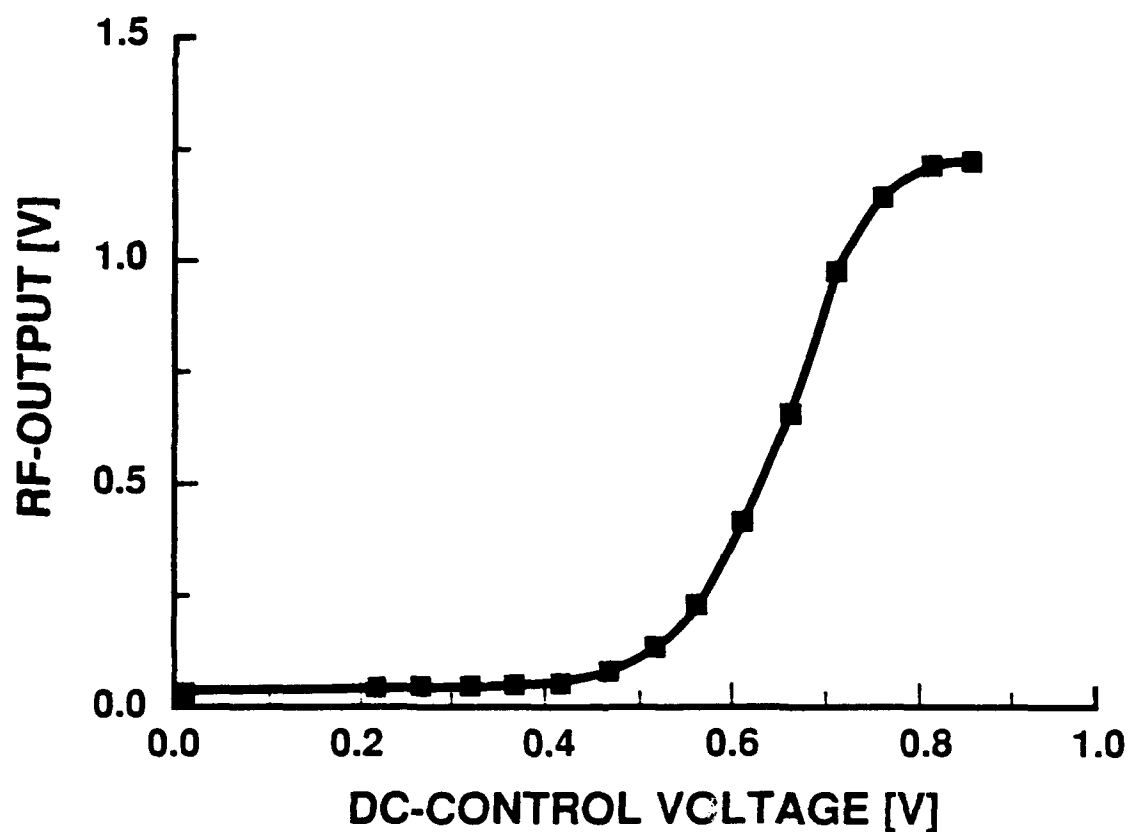


Figure 5.6. Measured voltage controlled attenuator characteristics. RF-output peak-to-peak voltage (into  $50\Omega$ ) versus applied DC-control voltage. Input RF-signal = 3V peak-to-peak (into  $50\Omega$ ).



FIGURE 5.7

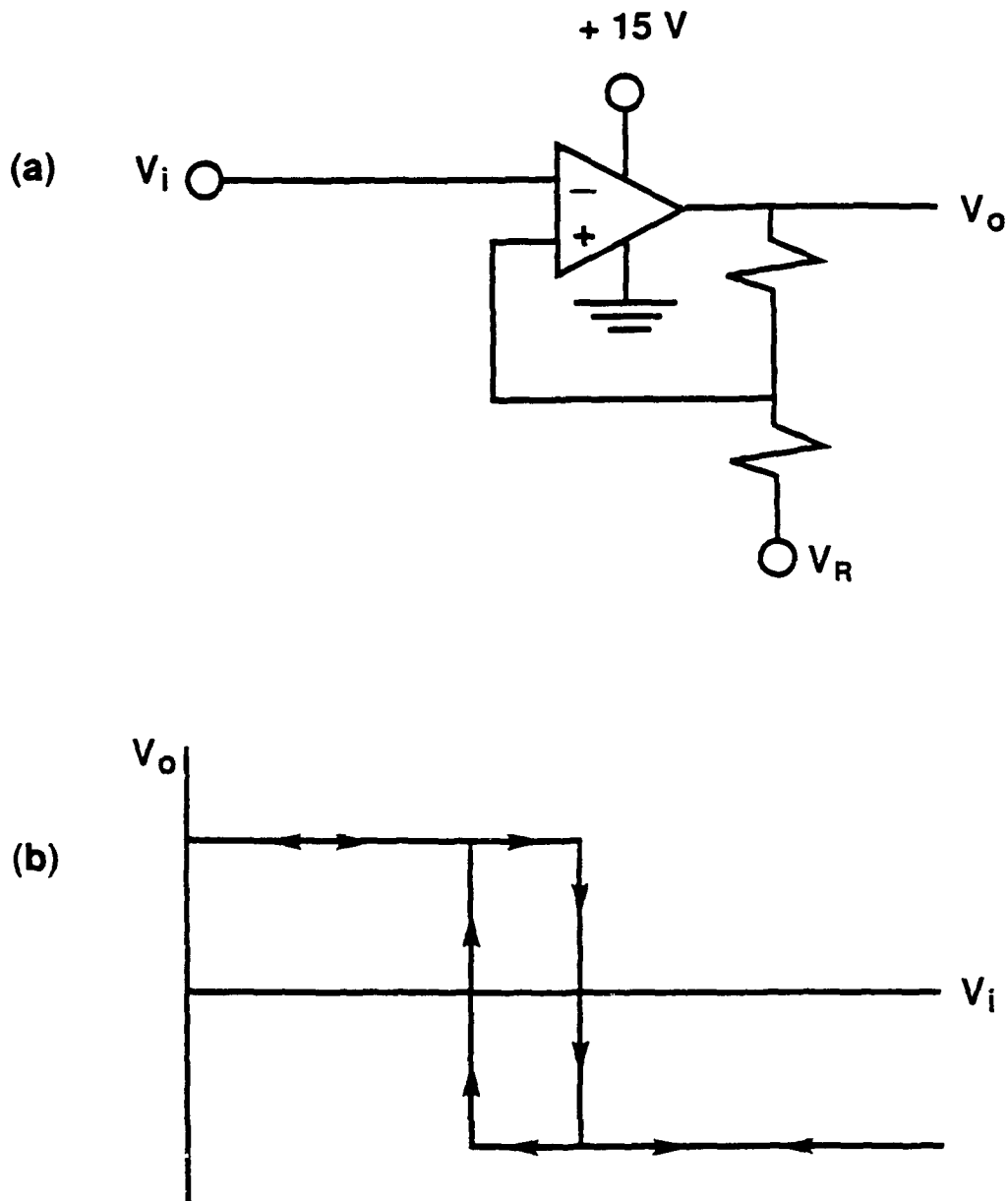


Figure 5.7. (a) Schmitt trigger circuit. (b) Theoretical voltage output ( $V_o$ ) versus input voltage ( $V_i$ ) response of a Schmitt trigger.  $V_R$ : threshold voltage.

FIGURE 5.8

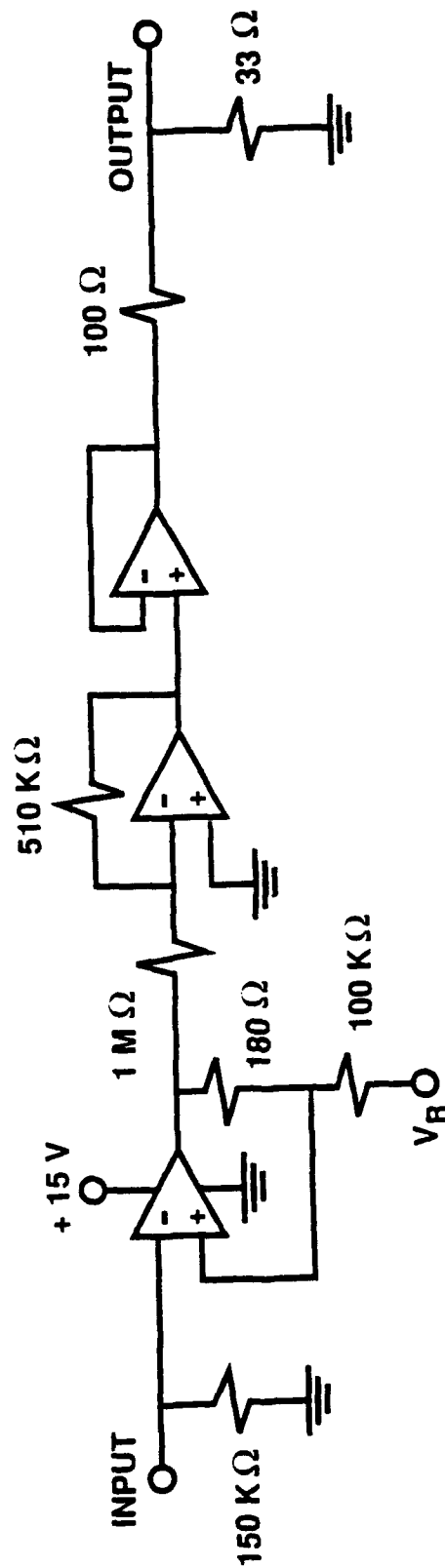


Figure 5.8. Nonlinear thresholding circuit for experimental nonlinear electronics (Figure 5.5). Input from differential amplifier following output detector. Output to VCA control terminal. Operational Amplifiers: LF356N8 (Schmitt trigger), LM318N (inverter), LM310N (unity gain follower).

diffracted light. Initially, the output detector signal is below the Schmitt trigger threshold. The control signal for the attenuator is therefore near zero, and the VCA blocks most of its RF-input to the AO device. Thus, below threshold the output light intensity varies linearly with the input light intensity following the characteristic of the AO device. When the output signal exceeds the Schmitt trigger threshold, the feedback loop is engaged and the control signal to the VCA increases abruptly. The VCA then begins to pass a portion of its input RF-signal to the AO modulator through the summing junction, as shown in Figure 5.5. This sudden increase in the AO drive voltage causes an increase in the diffracted light intensity. In this manner, the output light intensity increases abruptly when the input intensity reaches the necessary triggering level. After this switching has occurred, the Schmitt trigger remains on and the VCA control increases linearly with the output detector signal. As the control voltage increases, the attenuation decreases linearly, so that the drive signal to the AO device also increases linearly. The optical input-output characteristic is therefore linear above threshold, but with a different slope than below threshold because the signal to the AO device is now varying with the input light intensity. Similarly, the output light decreases linearly with decreasing input light until the output detector signal falls below threshold. The Schmitt trigger then turns off, disengaging the feedback loop, and the AO device once again operates with a fixed drive voltage.

### 5.3 EXPERIMENTAL RESULTS

Figures 5.9, 5.10, and 5.11 present the experimental results. The OUTPUT (vertical) axes of these figures represents the 1<sup>st</sup>-order diffracted light intensity measured as a DC voltage from the output photodetector (Figure 5.5). The INPUT (horizontal) axis is a measure of the incident light as monitored by the input detector (Figure 5.5). The units of the data and figures are in volts (V) as the DC electric potential measured directly from the photodetectors. Voltage

error measurement for the experiments was  $\pm 0.05\text{V}$ . Figures 5.9 and 5.10 are the results of experiments in which the nonlinear electronics were controlled from the detector sensing the 1<sup>st</sup>-order diffracted light exiting the AO modulator. This configuration for control of the nonlinear electronics was discussed in some detail in the previous section, and schematically illustrated in Figure 5.5. Figure 5.11 shows results from an experiment in which the signal to control the nonlinear electronics was obtained from the input light detector.

Figures 5.9 and 5.10 show the experimental system operating as a bistable optical device with hysteresis. Data was first taken in a forward direction of increasing the incident light to the AO cell, and then a reverse direction of decreasing the incident light, as presented by the figures. The arrows indicate the general direction of the forward and reverse data. The results shown in Figures 5.9 and 5.10 differ in that the biasing voltage of the Schmitt trigger,  $V_R$ , is 1.5 V for Figure 5.10 and 1.6 V for Figure 5.9. As can be seen from the two figures, the bistability and hysteresis are electronically controllable. Figure 5.9 has a higher optical threshold for the bistable effect to initiate and a lower range of hysteresis than Figure 5.10.

As discussed, the nonlinear electronics control for the data of Figure 5.11 was obtained from the incident light. Control from the incident light would theoretically yield a bistability without hysteresis because the input intensity crosses the bistability threshold at the same point whether it is increasing or decreasing. Figure 5.11 illustrates that this has been verified. The bias,  $V_R$ , on the Schmitt trigger was also changed to 1.7 V for this experiment. However, a direct comparison of the incident light bistability threshold of Figure 5.11 to that of Figures 5.9 and 5.10 would be erroneous since more incident light is needed to cause the diffracted light from the AO cell to reach the necessary intensity to trigger the nonlinear electronics threshold.

FIGURE 5.9

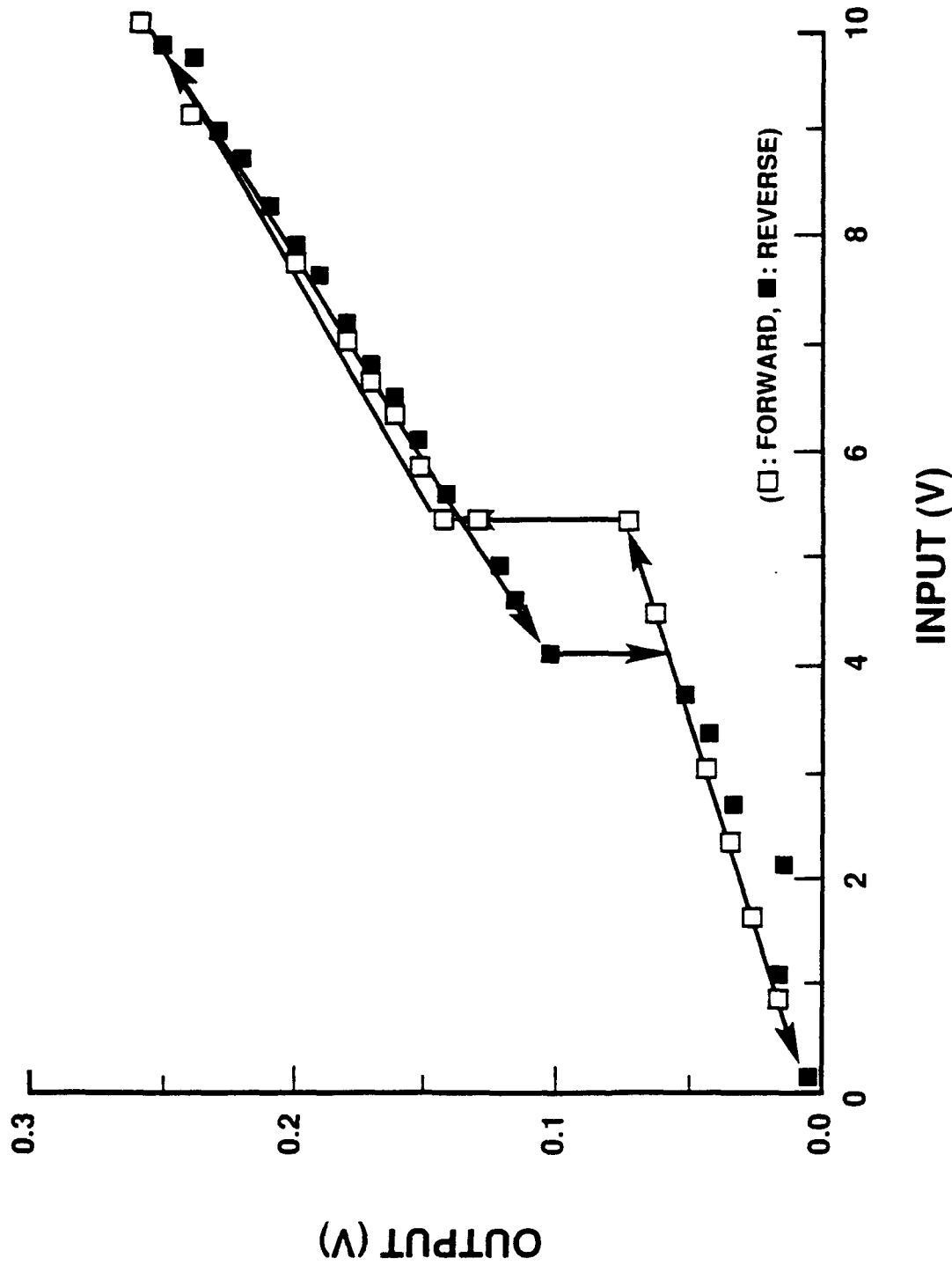


Figure 5.9. Bistability with hysteresis. Experimental results of acousto-optic HO/E bistable optical device with nonlinear electronic feedback. Photodetector voltage from 1<sup>st</sup>-order diffracted light (OUTPUT) versus photodetector voltage of input light monitor (INPUT). Nonlinear electronic feedback circuit triggered from output photodetector. Schmitt trigger threshold voltage,  $V_R = 1.6$  V.

FIGURE 5.10

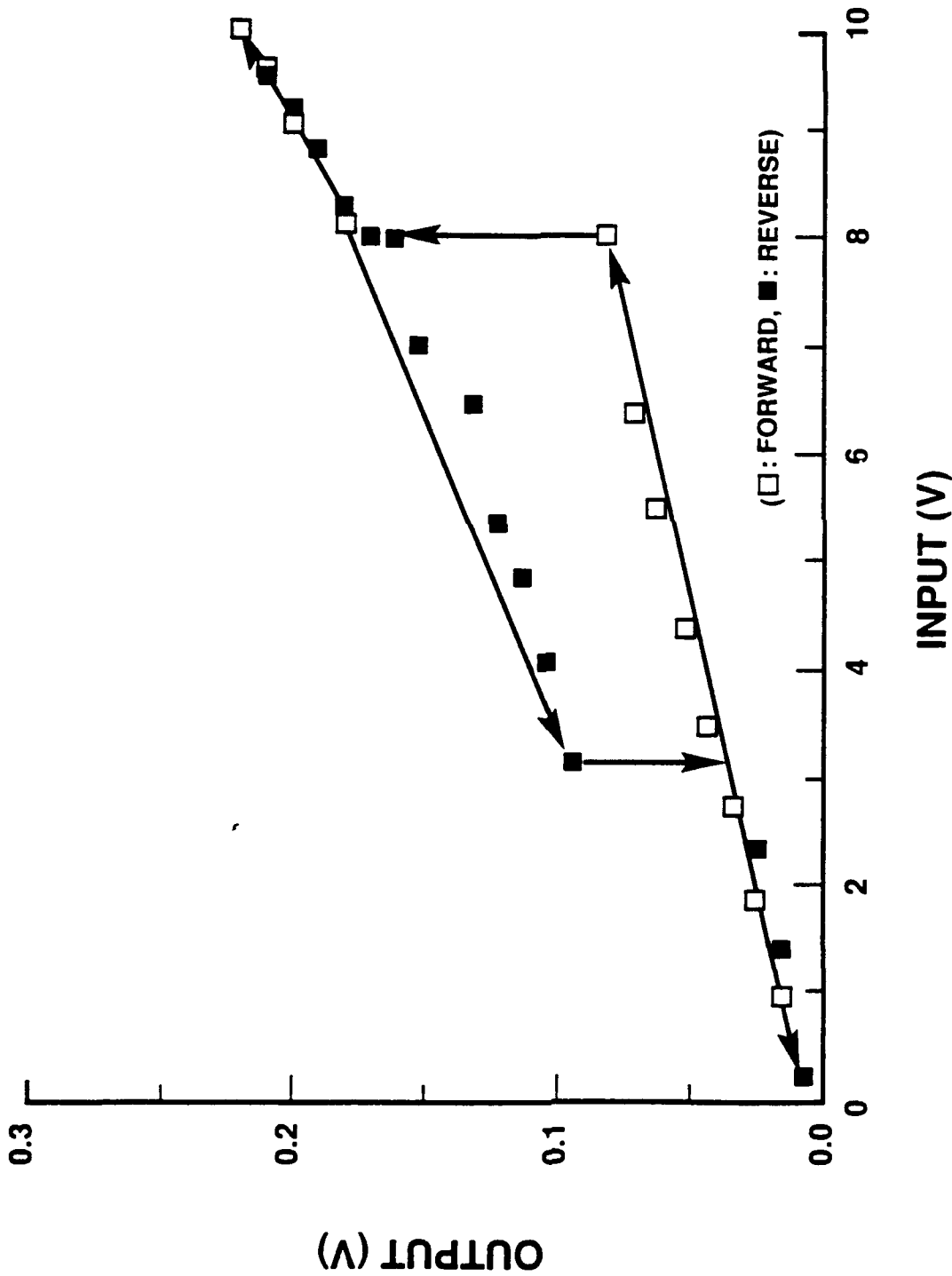


Figure 5.10. Bistability with hysteresis. Experimental results of acousto-optic HO/E bistable optical device with nonlinear electronic feedback. Photodetector voltage from 1<sup>st</sup>-order diffracted light (OUTPUT) versus photodetector voltage of input light monitor (INPUT). Nonlinear electronic feedback circuit triggered from output photodetector. Schmitt trigger threshold voltage,  $V_R = 1.5$  V.

FIGURE 5.11

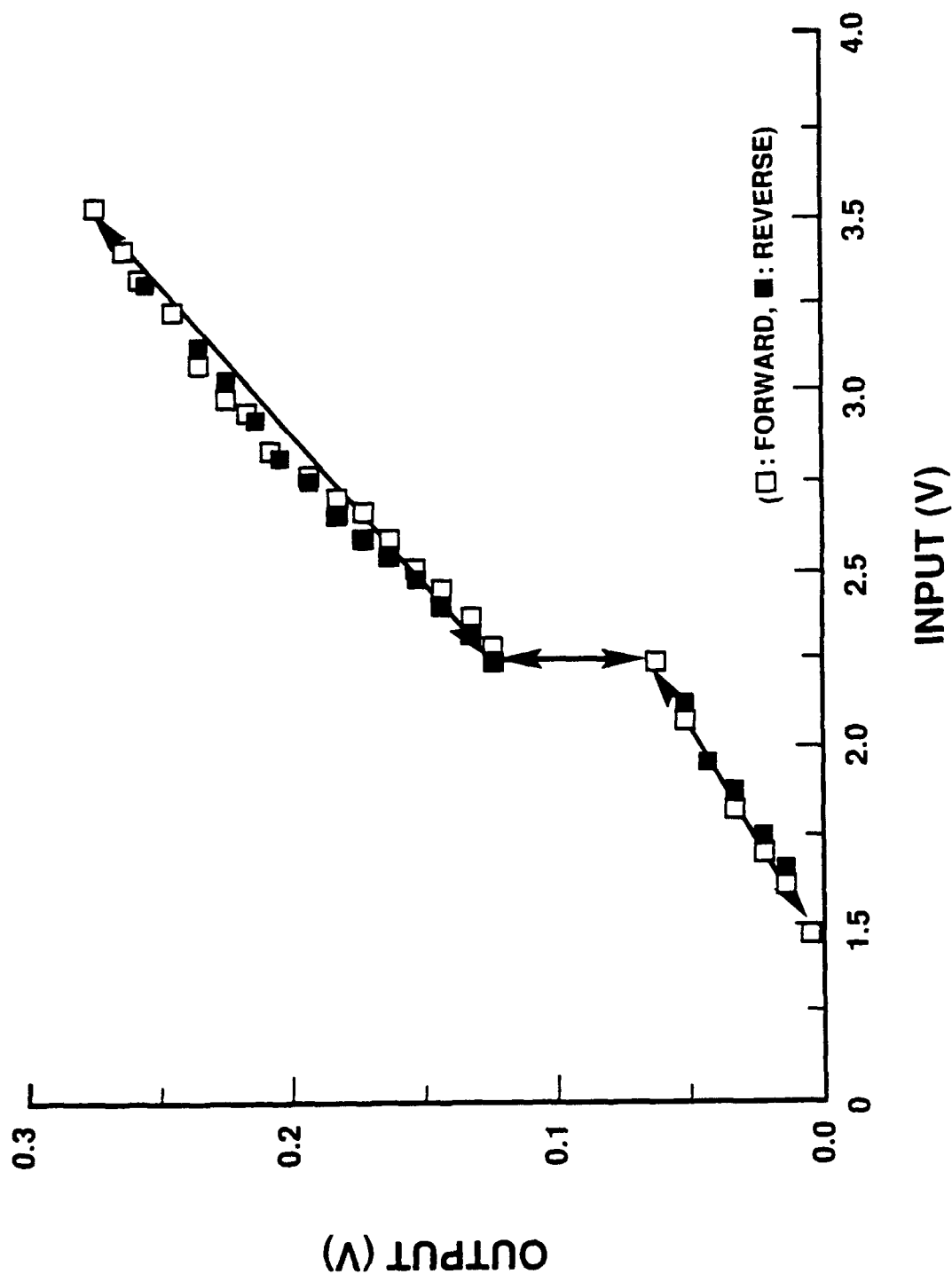


Figure 5.11. Bistability. Experimental results of acousto-optic HO/E bistable optical device with nonlinear electronic feedback. Detector voltage from 1<sup>st</sup>-order diffracted light (OUTPUT) versus detector voltage of input light monitor (INPUT). Nonlinear electronic feedback circuit triggered from input photodetector. Schmitt trigger threshold voltage,  $V_R = 1.7$  V.

An acousto-optic hybrid optical/electronic bistable optical system has been demonstrated. This hybrid system provides the ability to generate programmable optical switching and hysteresis effects using linear optical devices and nonlinear electronic feedback. This has been accomplished by taking advantage of the easily generated nonlinearities in conventional semiconductor electronics and readily available linear acousto-optic modulators. Since there are implementations other than the one reported here, issues such as the switching speed and power requirements of the hybrid system have not been addressed, and are areas for future research. Also in this configuration, a small inherent latency time associated with the response of the feedback loop exists, which should be minimized in future systems. With this experimental configuration and available equipment, the latency time was not measurable.

The acousto-optic binary optical device has potential applications in optical signal processing and computing systems. As a component of an optical signal processing system, the acousto-optic BOD can be cascaded, and since several optical beams can be switched by a single acousto-optic modulator, the hybrid device is applicable to parallel architectures. Another possibility involves operating the acousto-optic deflector in the Raman-Nath regime instead of the Bragg regime to produce several diffracted orders with a separate feedback signal derived from each order to produce versatile switching characteristics and multistable states. Finally, we note that this architecture could be modified so that the optical deflector is controlled by a separate light signal, which could be incoherent, that is not the light incident on the AO cell. The bias signal to the deflector would be obtained from the detected intensity of a second light beam, which would then govern the switching of the principle beam. In this manner, a weak light signal (on the order of  $\mu\text{W}$ ) could control the transmission of a much stronger signal (on the order of watts).



As configured, this experimental model of a BOD used a bulk acousto-optic modulator and component electronics, and has demonstrated a proof of concept. Although the device has potential application to optical signal processing systems, an integration of modulators and electronics would reduce size, decrease power, and permit the fabrication of arrays to be formed which have the potential to be used as spatial light modulators. Acousto-optic modulators can be built as wafer devices [2]; however, two drawbacks to AO cells are the need for a microwave signal to drive the deflection mechanism, and damping the acoustic wave to prevent acoustic interference from acoustic reflections, or stray RF-signals. These limitations necessitate exploration of other approaches to the development of integrated hybrid devices, which retain the advantages of the linear phase grating. Hence, an alternative approach is the use of electro-optic phase gratings as the modulator.

#### 5.4 CONCEPTUAL ELECTRO-OPTIC HYBRID OPTICAL/ELECTRONIC NONLINEAR OPTICAL DEVICE

Electro-optic phase-grating modulators have characteristics similar to acousto-optic cells. Electro-optic devices can be operated in either Bragg or Raman-Nath mode similar to acousto-optic modulators, but without a travelling-wave acoustic or electric field. Electro-optic modulators are electro-quasistatic (EQS) devices that are driven by modulating electric potentials, on the order of 5 to 20 Volts [2], which are compatible with microelectronic devices. To illustrate an integrated optical-electronic device, Figure 5.12 presents a schematic of a cross-section and perspective view of an electro-optic phase grating modulator and micro-optics integrated with electronics that form an electro-optic hybrid optical/electronic nonlinear optical device. The following discussion examines the structure, operation, materials, electro-optic phase-grating modulator, and micro-optics that compose this device.

FIGURE 5.12

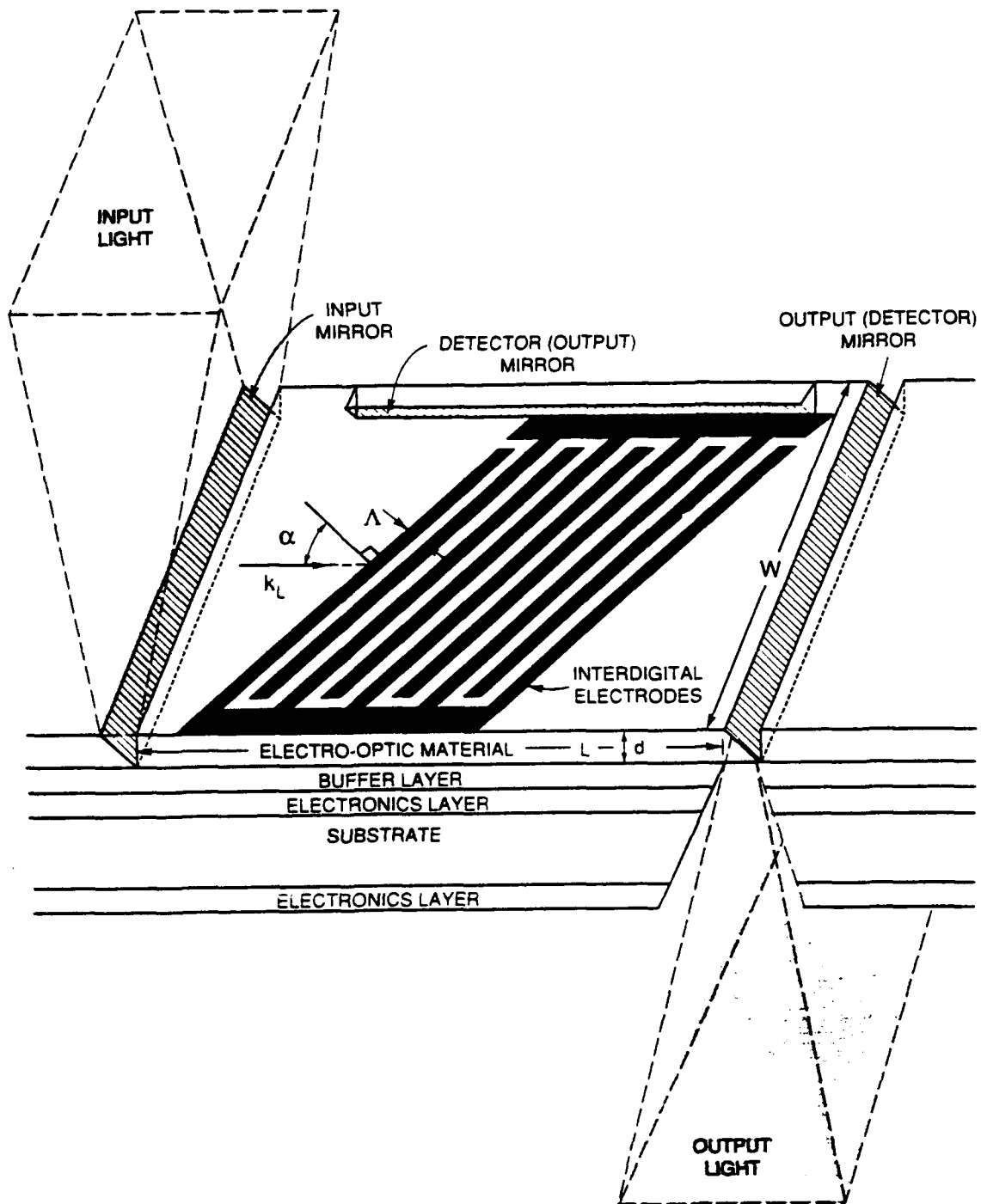


Figure 5.12. Integrated electro-optic hybrid optical electronic nonlinear optical device concept.

#### 5.4.1 DEVICE STRUCTURE and OPERATION:

Figure 5.12 shows a general structural scheme for integrating electronics and optics for hybrid devices. The basic configuration of the device is a semiconductor substrate with accompanying electronics, a buffer layer between the optical device and the electronics, a waveguide electro-optic modulator, and micro-optics. The semiconductor substrate is used as the base material for physical support of the device and to provide the electronics material. Both sides of the semiconductor substrate are available for fabricating microcircuits that form the illustrated electronics layers. These layers contain the electronics of the hybrid structure including detectors, nonlinear electronics, and control circuits. As shown in Figure 5.12, a buffer layer separating the electro-optic material from one of the electronics layers is presented, and on top of the buffer layer is the electro-optic material deposited as a thin-film planar optical waveguide. The buffer layer may be optional depending on the electronics configuration and electronics materials, and may be a single layer or multiple layer. This buffer layer can provide several functions. The buffer may act as an electrical or optical isolation to protect the electronics or electro-optical device. As an optical isolation, the buffer layer is transparent to the light, and has an index of refraction lower than that of the electro-optical waveguide. This lower index of refraction confines the light to the electro-optical waveguide. With sufficient thickness of the buffer layer, the light is prevented from interfering with the electronics layer by being absorbed in the materials that comprise the electronics. The buffer layer also prevents optical loss from the absorption within or scattering from the electronics. As an electrical isolation, the electric fields of the electro-optic device and electronics are physically separated from each other thus reducing interference between the respective devices. Alternatively, an electrical common plane may be placed within the buffer layer and sandwiched between two insulators.

One insulator is in contact the electronics layer and the other is in contact with the electro-optical waveguide. This common electrical metal plane terminates electric fields from the electronics and interdigital electrodes, and hence electrically isolates the two regions. Additionally, the buffer layer acts as a planarizing medium to compensate for the surface relief of the electronics layer, thereby reducing scattering from the electro-optic waveguide sidewall nearest the electronics. Surmounting the buffer layer is the electro-optic waveguide onto which a surface interdigital electrode structure is fabricated. The interdigital electrode provides the modulating electric field to create the electro-optic phase-grating. The electro-optic waveguide may be a single mode or multi-mode waveguide with a thickness,  $d$ , in the range of  $0.5\ \mu\text{m}$  to  $20\ \mu\text{m}$ . In order to launch incident light into the waveguide modulator, and remove modulated light, micro-optics are fabricated into the waveguide and substrate. Figure 5.12 shows micro-optic planar mirrors embedded in the electro-optic waveguide, and a window through the electronics substrate. If the electronics substrate is transparent to the light or does not perturb the light, such as changing polarization, then the window is not necessary. The basic hybrid structure of Figure 5.12 is designed to provide integrated operation of optics and electronics on a single substrate. With this architecture, the device offers flexible and diverse options as to the nonlinear optical characteristics.

Figure 5.12 illustrates a particular scheme of operation that shows the essential characteristics of the optical component hybrid nonlinear optical device. Incident light is directed into the electro-optic waveguide by a planar micro-optic mirror. The light travels in the waveguide until it encounters the modulator. The electro-optic modulator acts as a phase grating mirror to channel part of the light towards the detector micro-optic mirror. Light that is not diverted by the modulator continues to travel in its original direction toward the output mirror,

and is directed out of the waveguide by the output mirror and exits the device through the window. These micro-optic mirrors may be metallic or dielectric. The light deflected by the phase-grating modulator travels to a mirror (detector mirror) which directs this light to a detector in the electronics layer, and thus, the deflected light is the sampled light. This sampled light then controls the nonlinear electronics which in turn controls the modulator in the feedback loop. Consequently, the undeflected light that passes through the modulator and leaves the device is modified nonlinearly.

The previous paragraph presents only one mode of operation of the hybrid device shown in Figure 5.12. Also shown in the figure is a reversal of the roles of the deflected and undiverted light from the modulator. The detector mirror becomes the output mirror, and the deflected light is the output light. The undiverted light then becomes the detected (sampled) light. Another option for device operation is to sample the input light. If the input micro-optic mirror is a partially metallized or dielectric mirror, part of the incident light can proceed through the mirror to the electronics layer and be detected as the sampled light. Hence, the input or modulated light can be used as the sampled light to control the nonlinear electronics.

#### 5.4.2 MATERIALS and DEVICE FABRICATION:

In order to realize an integrated hybrid optical/electronic nonlinear optical device, materials and fabrication methods for the optical and electronic components must be compatible. The electronic components are limited to semiconductor materials whether single materials such as silicon and germanium, or compound semiconductors such as gallium arsenide. Electro-optical materials for the optical modulator can also be semiconductors primarily compounds (GaAs, InP, ZnSe, ZnTe), crystalline ceramics such as perovskites [2], and more recently developed electro-optic organic materials like the organic crystal 2-methyl

4-nitroaniline (MNA) [7,47,48], or guest-host and backbone pendant polymers [7,49-58]. This range of choices of materials is reduced due to fabrication requirements, and is principally limited by ability to integrate the electronic and electro-optic functions.

The most direct means of integrating the optical and electronic functions is to use a semiconductor material that is also an electro-optic material. Integrated optoelectronic devices, which combine electronics and electro-optic devices on a single substrate using GaAs and related AlGaAs, is an major area of research. Nonlinear electronics and detectors can be fabricated on one surface of a substrate. The optical components can be formed on the opposite surface. Metallic vias through the substrate can electrically connect the electronics to the interdigital electrodes. The approach of using an electro-optic semiconductor is attractive because of the use of a single material foundation. However, electro-optic semiconductors do not have the electro-optic strength [2] of the perovskite crystalline ceramics, or the more recently developed organic materials. Thus the semiconductor optical device must have a longer propagation path for the light, or larger electric field, to evoke the same modulating effects on the light.

Perovskite crystalline ceramics have been the most popular electro-optic materials due to the comparatively large electro-optic coefficients [2], and are at least one order of magnitude stronger than electro-optic semiconductors. The essential chemical structure of the perovskites is (metal)(metal)O<sub>3</sub>. Materials such as LiNbO<sub>3</sub>, LiIO<sub>3</sub>, LiTaO<sub>3</sub>, PZT, PLZT, KTN, and BaTiO<sub>3</sub> are examples of these electro-optic materials [2]. Though the electro-optic properties make these materials attractive for the optical modulator, these materials cannot presently be directly grown on semiconductor substrates. These materials are grown as single crystals from a melt with temperatures on the order of 1000°C, and these temperatures would damage the semiconductors. Further, epitaxial layers of

the perovskites do not lattice match to semiconductors thus inhibiting uniform single-crystal growth. The growth of the electro-optic perovskites does not presently appear to be a viable approach to the fabrication of the hybrid optical/electronic nonlinear device. However, an alternative method in which the semiconductor electronics is attached to the electro-optic material may be feasible because of the recent development of the epitaxial lift-off technique [59-60]. This technique permits fabrication of thin-film GaAs electronics which can be removed from the substrate on which the electronics are fabricated, and then directly attached to the electro-optic material. The GaAs electronics are then held in place by Van-der-Waals force. This method may permit an effective integration of crystalline ceramics and GaAs electronics as an integrated structure; however, this process requires the additional manufacturing steps of physical removal of the GaAs electronics and attachment to the optical material. As compared with monolithically fabricating the electronics with the optics, the possibility of damage to the thin-film or misalignment of the electronics is enhanced with the epitaxial lift-off process.

Alternatives to electro-optic semiconductors and crystalline ceramics are the recently developed electro-optic organic materials [7, 49-58]. The two principal types of organics are the electro-optic crystals and the poled polymers. These materials have electro-optic coefficients on the order of or larger than the crystalline ceramics. The crystalline organic MNA has an electro-optic coefficient ( $r_{ij}$ ) of 64 pm/V. The poled polymers have exhibited coefficients of 14 pm/V to 100 pm/V. Besides the relatively high electro-optic coefficients, these materials have the major advantages of low growth and processing temperatures, and smaller electro-quasistatic (EQS) dielectric constants. The low processing temperatures (22°C to 200°C) permit these materials to be directly integrated

with semiconductor electronics without thermally damaging the electronic devices. The EQS dielectric constants are those associated with the applied electric field of the interdigital electrodes and determine the capacitance of the interdigital electrodes. Whereas the perovskites have EQS dielectric constants from 40 ( $\text{LiNbO}_3$ ) to 1800 ( $\text{BaTiO}_3$ ), the optical organics have dielectric constants on the order of 4. Accordingly, the lower EQS dielectric constant of the optical organics permits faster switching speeds. Of the two main types of organic electro-optic materials, the poled polymers offer the greatest possibility of forming thin films for waveguide layers. Though bulk optical-quality single-crystals of MNA have been grown, thin films for useable waveguides have not been successfully formed. In contrast, thin film poled polymer materials have been deposited for low loss dielectric waveguides [55-57]. These materials are typically spun onto a substrate to form the waveguide layer, and are initially deposited as an amorphous film that does not have electro-optic properties. In order to induce electro-optic effects, the film is heated beyond its glass transition temperature (typically less than  $200^\circ\text{C}$ ) and a poling electric field is applied. The previously randomly oriented electro-optic dipoles of the material are then sufficiently mobile to align with the poling field thus forming in aggregate an electro-optic susceptibility [7,49-57]. With the poling field remaining in place, the material is then cooled to ambient temperatures. The poling field for the device of Figure 5.12 is generated from the interdigital electrodes. This technique has been successfully applied to form integrated optic type devices such as channel waveguides, Mach-Zehnder interferometers, and directional couplers [55-57]. A more complete review of the science and technology of electro-optical organic compounds can be found in reference 7, and 49 through 58. Besides the spin-deposit and electric field poling method of forming the electro-optic organic materials, vapor deposition,



and ionized-cluster-beam/partially-ionized-beam deposition techniques are being examined to deposit the electro-optic organics. This technique is also a low temperature method and has the additional advantage of inducing electro-optical dipole orientation concurrent with film growth.

The interdigital electrodes that generate the electric field for the electro-optic phase grating are based on the wavelength of light and electro-optic material that forms the waveguide. In its most efficient operation, the electrodes are designed to form a Bragg reflector for the mode of the waveguide that is selected for modulation. Assuming only single mode operation, an estimate of the periodicity,  $\Lambda$  (Figure 5.12), can be made by using the expression [2]:

$$\Lambda = \lambda / 2n \cos(\alpha) \quad (5.4)$$

where  $\lambda$  is the free space wavelength of the light,  $n$  the index of refraction of the material, and  $\alpha$  the reflection angle measured from the normal to the grating (Figure 5.12). With a wavelength on the order of  $1.0 \mu\text{m}$  and index of refraction of 2, and an  $\alpha$  of 45 degrees,  $\Lambda$  would be  $0.47 \mu\text{m}$ . Chirped gratings have been fabricated with periodicities of less than  $0.3 \mu\text{m}$  [2,61], which is well within the capability of electron beam lithography, whether by direct write or for mask fabrication, and also holographic lithography. Larger periodicity can be attained with a smaller  $\alpha$ , and 45 degrees is not a limitation. The length,  $L$ , of the device, taken to be the length of the modulator, is derived from Figure 2.12 as:

$$L = w + W \tan(\alpha) \quad (5.5)$$

where  $W$  is the width of the device, and  $w$  is dependent on the interaction length ( $\ell$ ) of the reflector (Figure 5.12), with

$$w = \ell / \cos(\alpha) \quad (5.6)$$

The interaction length,  $\ell$ , is based on the intended efficiency of the modulator which is the ratio of the deflected light ( $I_d$ ) intensity to the incident light ( $I_i$ ) intensity. An approximate relation between  $I_d$  and  $I_i$  [2] is given by:

$$\frac{I_d}{I_i} = \tanh^2\left(\frac{\pi n^3 r \ell E}{2\lambda}\right) \quad (5.7)$$

where  $n$  is the unperturbed index of refraction of the electro-optical material,  $r$  is the electro-optic coefficient,  $\ell$  is the interaction length of the reflector, and  $E$  the magnitude of the applied electric field. Consider a 50% ( $I_d/I_i = .5$ ) deflection efficiency. This places the initial operating point in the middle of the linear operating range of the deflector. With the material values of  $n = 2.28$ ,  $r = 30$  pm/V (LiNbO<sub>3</sub> parameters [2]), and an electric field ( $E$ ) of 1 MV/m, the interaction length ( $\ell$ ) is 1.6 mm. By raising the electric field to 10 MV/m,  $\ell$  is 160  $\mu$ m. These electric fields are easily compatible with electronic circuitry voltages of 5 V to 20 V and interdigital transducer spacing of 10  $\mu$ m to 0.2  $\mu$ m. If  $\alpha = 45^\circ$ , and  $W$  is taken to be equal to  $w$ , then a device area of 5 mm x 5 mm is an upper bound on miniaturization. Correspondingly smaller areas are attainable with larger applied electric fields or larger electro-optic coefficients. Thus the reflecting modulator is capable of being fabricated with current manufacturing technology, and has dimensions that permit miniaturization to form arrays.

In order to bring light into the waveguide structure and direct it out of the waveguide, various coupling techniques can be employed depending on the direction from which light is to enter the device [61]. End-coupling methods, such as fiber coupling and lens focusing, in which the light is initially parallel to the waveguide, is not applicable to light striking the device from an angle out of the plane of the waveguide. External prism coupling is a possibility for light that is not coplanar with the waveguide, but prism coupling does not permit light to be coupled that is striking perpendicular to the plane of the waveguide, nor

to direct light through the electronics substrate. Further, the prism is a bulky component that must be added to the device with the accompanying problem of aligning the prism with the waveguide. Alternatively, micro-optics presents a feasible technique to launch light into the waveguide from directions not coplanar with the waveguide, and integrated with the waveguide using the accuracy of microelectronics fabrication techniques. Two micro-optics techniques have been developed that are applicable to the hybrid device. One method uses gratings to direct light into the waveguide [2,61], and the other uses micro-optic mirrors. Gratings have been fabricated with electron-beam and holographic lithography, and with ion milling and directional gaseous etching such as reactive-ion-etching [61]. More experience has been obtained with gratings than mirrors. Comparatively, gratings are more spectrally limited than mirrors, and thus new grating designs would have to be implemented for different wavelengths. Additionally, for efficient coupling of light to the waveguide, the size of the gratings ( $\sim 1$  mm) would be larger than mirrors ( $\sim$  thickness of the waveguide,  $10\mu\text{m}$ ). Figure 5.12 illustrates micro-optic mirror coupling. Optical quality mirrors have been fabricated with ion assisted beam etching (IABE) [62-64], focused-ion-beam (FIB) milling [65-67], and mass-transport [67,68]. Mirrors have been fabricated in semiconductor materials [62-65, 67-69] and organic polymers [66]. Though shown as planar mirrors in Figure 5.12, curved mirrors can be fabricated with IABE and FIB milling. Curved mirrors can be used to improve single mode launching of light into waveguides that are multi-mode, and correct for focusing distortion of light that is directed onto the mirrors. Micro-optics for directing light into and out of the electro-optic waveguide, and that are integrated with the waveguide, can be accomplished with current fabrication methods. However, because of the small size of these elements only a small fraction of the light that would fall onto the overall device will enter the micro-optics, if left unaided. Thus an external

mechanism for directing light onto the micro-optics embedded in the waveguide is needed. This can be accomplished with standard optics; however, the bulk size of standard optics prevents the development of arrays, and external micro-optic methods must be considered. A discussion of external micro-optics is presented in the next section.

The hybrid optical/electronic nonlinear optical device is a conceptual device that can be fabricated with current fabrication microelectronic fabrication technology. The electronics aspect of the device are not pursued further since the optical part of the device is intended to be fabricated with available semiconductor devices. The hybrid device has been presently considered in a stand alone context; however, an advantage of the small structure discussed, and microelectronic manufacturing techniques, is the ability to integrate many of these single devices as elements of arrays and develop nonlinear systems.

## 5.5 HO/E NONLINEAR OPTICAL ARRAYS

A HO/E nonlinear-optical-array is essentially composed of an assembly of the nonlinear device shown in Figure 5.12, and a means of bringing light into and out of the nonlinear array. Figure 5.13 illustrates these two components of the system as a general scheme, and specifically as a spatial light modulator. An array of HO/E nonlinear optical devices, and a technique (micro-optic arrays) for inserting the incident light into the electro-optic waveguide and recollimating the output light, is shown. The discussion which follows separately presents each of these components, and then combines them as a spatial light modulator.

### 5.5.1 ARRAY:

The HO/E nonlinear-optical-array structure of Figure 5.13 shows a general geometry of the array of devices. Each element in Figure 5.13 forms a distinct pixel. These pixels can be optically and electronically isolated from each other,

FIGURE 5.13

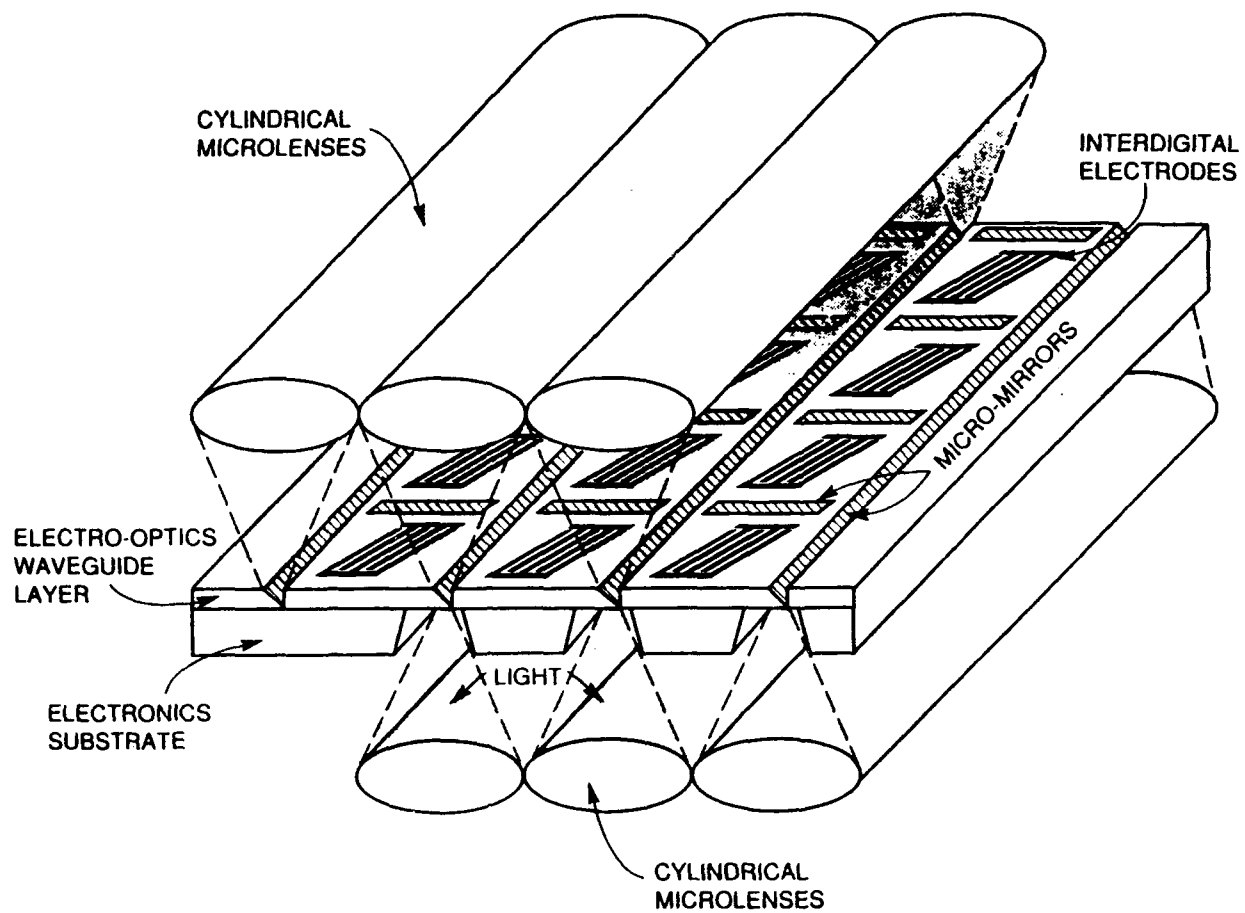


Figure 5.13. Monolithic array of integrated electro-optic HO/E nonlinear optical elements. Wavefront spatial light modulator geometry.

or connected. Micro-optic lenses, waveguides, gratings, and partially transmitting mirrors can be employed to optically connect elements. As an example, Figure 5.13 shows the output mirror of one element as the input mirror of its neighbor. If this mirror is partially transmitting then light from one cell can influence the behavior of its neighboring cell. Connecting the cells electronically is dependent on metallic interconnects in the electronic layers. By establishing optical and electronic paths between the elements, neighboring pixels can influence the behavior of each other thereby creating a connected network. This network can then act as a nonlinear network with possible application to optical neural networks.

#### 5.5.2 EXTERNAL MICRO-OPTIC ARRAYS:

In order to efficiently bring light that is out of the plane of the electro-optics waveguide into a nonlinear optical element, the light is collected and directed onto the micro-optics embedded in the electro-optic waveguide layer. Figure 5.12 shows micro-mirrors as the embedded micro-optics of the waveguide. To channel the light onto the micro-mirrors, a focusing element is needed. The focusing element in this example is a cylindrical microlens. A single cylindrical microlens can direct light onto a micro-optic mirror that serves as the optical input mechanism to a one-dimensional array of HO/E elements. An array of the microlenses can then insert light into a two-dimensional array as illustrated in Figure 5.13. To form a precise two-dimensional pattern that conforms to the nonlinear HO/E array, separate cylindrical lenses should be avoided. By taking advantage of accurate microelectronic fabrication methods, arrays of cylindrical or circular lenses can be manufactured. These microelectronic fabrication methods include mass-transport [70], ion milling, reactive-ion-etching, FIB-milling, photothermal [71], and ion-exchange techniques [72,73]. The microlens arrays would most likely be fabricated as independent structures, and then aligned and

attached as part of the package of the total system. However, with low deposition temperature materials, such as the parylenes, polyimides, and siloxanes, that can be deposited directly on the electro-optical materials, the possibility exists of integrating the "external" optics with the rest of the device as a monolithic structure.

### 5.5.3 SPATIAL LIGHT MODULATOR:

The total device shown in Figure 5.13 is illustrative of the geometry of a spatial light modulator (SLM). The SLM geometry presents a structure that performs the complex tasks of modulating the wavefront of a light beam with a planar optical device, and in a miniaturized package. Figure 5.13 shows how external optics can focus light onto a linear micro-optic mirror which injects the light into a set of one-dimensional HO/E nonlinear optical devices. The array separates the line of light into segments, and thus forms smaller pixels. Each one-dimensional HO/E array creates pixels, and thus, forms a two-dimensional spatial modulation pattern. The output micro-optic mirrors then redirects each pixel onto a second cylindrical array pattern to construct a nonlinearly modulated wavefront. Hence, from the design of a single planar element, an array can be envisioned that can be extended to the formulation of a nonlinear spatial light modulator.

## 5.6 CONCLUDING DISCUSSION

New hybrid optical/electronic nonlinear optical devices have been presented based on a linear optical modulator controlled with nonlinear electronic feedback. This architecture provides the potential for realizing nonlinear optical switching effects unobtainable by other means. Results of an experiment with a bulk acousto-optic modulator and a Schmitt trigger providing nonlinear and programmable control have been reported. This experiment demonstrated the

concept of linear modulation with nonlinear electronic control. Tuneable bistability and hysteresis were found by triggering from the diffracted light from the AO modulator. By triggering from the input light, bistability without hysteresis was obtained. The application of a deflector modulator did not require external optics for light sampling. This proof of principle established the basis for a conceptual device using an electro-optic deflector. A discussion of the design, fabrication, and operation of the electro-optic device was presented that indicates such a device is feasible with current materials and fabrication technology, and can be successfully implemented. From the single element electro-optic device, arrays can be developed for nonlinear network systems and spatial light modulators. Future research includes development of the electro-optic hybrid optical/electronic structure and extension to arrays, and examination of the stability criteria of the nonlinear feedback. As a final note, the integrated optical and electronic structure of the electro-optic device is also applicable to linear modulation with linear feedback electronic control.

## 5.7 ACKNOWLEDGEMENTS

It is a pleasure to thank Mr. Mark Noble of the Rensselaer Polytechnic Institute, and Capt. George Nowak of the United States Military Academy, West Point, for their assistance in implementing the experimental apparatus.



## Chapter V - REFERENCES

- [1] M. S. Schubert and B. Wilhelm, *Non-linear Optics and Quantum Electronics*, New York, NY: John Wiley and Sons, 1986.
- [2] A. Yariv and P. Yeh, *Optical Waves in Crystals*, New York, NY: John Wiley and Sons, 1984.
- [3] *Nonlinear Optical and Electroactive Polymers*, ed. by P. N. Prasad and D. R. Ulrich, New York, NY: Plenum Press, 1988.
- [4] *Organic Materials For Non-Linear Optics*, ed. by R. A. Hann and D. Bloor, London: Royal Society of Chemistry, Burlington House, 1989.
- [5] *Non-Linear Optical Properties of Organic and Polymeric Materials*, ed. by D. J. Williams, Washington, D. C.: American Chemical Society, 1985.
- [6] *Non-linear Optical Properties of Organic Molecules and Crystals*, ed. by D. S. Chemla and J. Zyss, New York, NY: Academic Press, 1987.
- [7] D. Williams, "Polymers in Non-linear Optics," in *Electronic and Photonic Application of Polymers*, ed. by M. J. Bowden and S. J. Turner, Washington D. C.: American Chemical Society, 1984, pp. 297-330.
- [8] "Nonlinear Optical Properties of Materials," ed. by C. M. Bowden and J. W. Haus in *J. Opt. Soc. Amer. B*, vol. 6, no. 4, pp. 778-823, 1989.
- [9] S.-K. Kwong, M. Cronin-Golomb, and A. Yariv, "Optical bistability and hysteresis with photorefractive self-pumped phase conjugate mirror", *Appl. Phys. Lett.*, vol. 45, no. 10, pp. 1016-1018, 1984.
- [10] S. W. Koch, H. E. Schmidt and H. Haug, "Optical bistability due to induced absorption: Propagation dynamics of excitation profiles," *Appl. Phys. Lett.*, vol. 45, no. 9, pp. 932-934, 1984.
- [11] M. S. Choi, J. H. Hur, and M. A. Gundersen, "Optoelectronic bistability in Gallium Phosphide," *Appl. Phys. Lett.*, vol. 52, no. 9, pp. 1563-1564, 1988.
- [12] M. Cronin-Golub and A. Yariv, "Optical limiters using photorefractive nonlinearities," *J. Appl. Phys.*, vol. 57, no. 11, pp. 4906-4910, 1985.
- [13] G. I. Stegeman and C. T. Seaton, "Nonlinear integrated optics," *J. Appl. Phys.*, vol. 58, no. 12, pp. R57-R78, 1985.
- [14] D. A. B. Miller, D. S. Chemla, T. C. Damen, A. C. Gossard, W. Weigmann, T. H. Wood, and C. A. Burrus, "Novel hybrid optically-bistable switch: The quantum well self-electro-optic effect device," *Appl. Phys. Lett.*, vol. 45, no. 1, pp. 12-15, 1984.
- [15] D. A. B. Miller, D. S. Chemla, T. C. Damen, T. H. Wood, C. A. Burrus, A. C. Gossard, and W. Weigmann, "The quantum well self-electro-optic effect device: Optoelectronic bistability and oscillation, and self linearized modulation," *IEEE J. Quantum Electron.*, vol. QE-21, no. 9, pp. 1462-1476, 1986.
- [16] A. L. Lentine, F. B. McCormick, R. A. Novotny, L. M. F. Chirovsky, L. A. D'Asaro, R. F. Kopf, J. M. Kuo, and G. D. Boyd, "A 2 kbit Array of Symmetric Self-Electrooptic Effect Devices," *IEEE Photon. Technol. Lett.*, vol. 2, no. 1, pp. 51-52, 1990.

- [17] A. Neyer and W. Sohler, "High speed cutoff modulation using a Ti-diffused  $\text{LiNbO}_3$  channel waveguide," *Appl. Phys. Lett.*, vol. 35, no. 3, pp. 256-258, 1979.
- [18] F. S. Felber and J. H. Malburger, "Theory of nonresonant multistable optical devices," *Appl. Phys. Lett.*, vol. 28, no. 1, pp. 731-733, 1976.
- [19] H. M. Gibbs, S. L. McCall, T. N. C. Venkatesan, A. C. Gossard, A. Passner, and W. Wiegmann, "Optical bistability in semiconductors," *Appl. Phys. Lett.*, vol. 35, no. 6, pp. 451-453, 1979.
- [20] T. N. C. Venkatesan and S. L. McCall, "Optical bistability and differential gain between 85 and 296°K in a Fabry-Perot containing ruby," *Appl. Phys. Lett.*, vol. 30, no. 6, pp. 282-284, 1977.
- [21] J. M. Gibbs, S. L. McCall, and T. N. C. Venkatesan, "Differential Gain and bistability using a sodium-filled Fabry-Perot interferometer," *Phys. Rev. Lett.*, vol. 36, no. 19, pp. 1135-1138, 1976.
- [22] A. M. Glass, "Materials for Optical Information Processing," *Science*, vol. 226, no. 4675, pp. 657-662, 1984.
- [23] S. D. Smith, "Lasers, non-linear optics and optical computers," *Nature*, vol. 316, no. 6026, pp. 319-324, 1985.
- [24] D. G. Feitelson, *Optical Computing*, Cambridge, MA: MIT Press, 1988.
- [25] P. W. Smith and E. H. Turner, "A bistable Fabry-Perot resonator," *Appl. Phys. Lett.*, vol. 30, no. 6, pp. 280-281, 1977.
- [26] P. W. Smith, I. P. Kaminow, P. J. Maloney, L. W. Stuly, "Integrated bistable optical devices," *Appl. Phys. Lett.*, vol. 33, no. 1, pp. 24-26, 1978.
- [27] P. W. Smith, E. H. Turner, and P. J. Maloney, "Electrooptic nonlinear fabry-perot devices," *IEEE J. Quantum Electron.*, vol. QE-14, no. 3, pp. 207-212, 1978.
- [28] M. Okada, K. Takizawa, "Instability of an electrooptic bistable device with a delayed feedback," *IEEE J. Quantum Electron.*, vol. QE-17, no. 10, p. 2135-2140, 1981.
- [29] E. Garmire, J. H. Marburger, and S. D. Allen, "Incoherent mirrorless bistable optical devices," *Appl. Phys. Lett.*, vol. 32, no. 5, pp. 320-321, 1978.
- [30] A. Feldman, "Ultralinear bistable electro-optic polarization modulator," *Appl. Phys. Lett.*, vol. 33, no. 3, pp. 243-245, 1978.
- [31] M. Okada and K. Takizawa, "Electrooptic Nonlinear Devices with Two Feed Signals," *IEEE J. Quantum Electron.*, vol. QE-15, no. 10 pp. 1170-1175, 1979.
- [32] M. Okada and K. Takizawa, "Optical Multistability in the Mirrorless Electrooptic Device with Feedback," *IEEE J. Quantum Electron.*, vol. QE-15, no. 2, pp. 82-85, 1979.
- [33] M. Okada and K. Takizawa, "Optical Regenerative Oscillation and Nonstable Pulse Generation in Electrooptic Bistable Devices," *IEEE J. Quantum. Electron.*, vol. QE-16, no. 7, pp. 770-776, 1980.
- [34] M. Okada, "REDUCTION OF THE SWITCHING ENERGY IN ELECTROOPTIC BISTABLE DEVICES," *Opt. Comm.*, vol. 35, no. 1, pp. 31-36,

1980.

- [35] M. Okada, "OPTICAL REGENERATIVE OSCILLATION AND MONOSTABLE PULSE GENERATION IN HYBRID BISTABLE OPTICAL DEVICES," *Opt. Comm.* vol. 34, no. 2, pp. 153-158, 1980.
- [36] M. Okada and K. Takizawa, "Instability and Transient Responses of an Electrooptic Bistable Device," *IEEE J. Quantum Electron.*, vol. QE-17, no. 4, pp. 517-524, 1981.
- [37] H. M. Gibbs, F. A. Hopf, D. L. Kaplan, and R. L. Shoemaker, "Observation of chaos in optical bistability," *Phys. Rev. Lett.*, vol. 46, no. 7, pp. 474-477, 1981.
- [38] P. S. Cross, R. V. Schmidt, R. L. Thornton, and P. W. Smith, "Optically controlled two channel integrated-optical switch," *IEEE J. Quantum Electron.*, vol. QE-14, no. 8, pp. 577-580, 1978.
- [39] H. Ito, Y. Ogawa, K. Makita, and H. Inaba, "Integrated bistable optical multivibrator using electro-optically controlled directional coupler switches," *Electron. Lett.*, vol. 15, no. 24, pp. 791-793, 1987.
- [40] H. Ito, Y. Ogawa and H. Inaba, "Integrated bistable optical device using Mach-Zehnder interferometric optical waveguide", *Electron. Lett.*, vol. 15, no. 10, pp. 283-285, 1974.
- [41] A. Schnapper, M. Papuchon, and C. Puech, "OPTICAL BISTABILITY USING AN INTEGRATED TWO ARM INTERFEROMETER," *Opt. Commun.*, vol. 29, no. 3, pp. 364-368, 1979.
- [42] W. Sohler, "Optical bistable device as electro-optic multivibrator," *Appl. Phys. Lett.*, vol. 36, no. 5, pp. 351-353, 1980.
- [43] T.-C. Poon, S. K. Cheung, "Acousto-Optic nonlinear device," Nov. 4, 1988 presented Optical Society of America 1988 Annual Meeting, Oct. 30 - Nov. 4, 1988, Santa Clara, CA.
- [44] N. P. Vlannes, C. M. DeCusatis, P. K. Das, "Optical-electronic nonlinear optical device using acousto-optic deflectors with nonlinear feedback," presented Optical Society of America 1989 Annual Meeting, Oct. 16-20, 1989 Orlando, FL.
- [45] M. M. Ibrahim, "The gain-bandwidth product of hybrid optical transistors," *IEEE J. Quantum Electron.*, vol. 24, no. 11, pp. 2227-2230, 1988.
- [46] P. M. Chirlian, *Analysis and Design of Integrated Electronic Circuits*, 2nd ed. , pp. 664-667, New York, NY: Harper and Row Inc., 1987.
- [47] B. F. Levine, C. G. Bethea, C. D. Thurmand, R. T. Lynch, and J. L. Bernstein, "An organic crystal with an exceptionally large optical second harmonic coefficient: 2-methyl-4-nitroaniline," *J. Appl. Phys.*, vol. 50, no. 4, pp. 2523-2527, 1979.
- [48] G. F. Lipscomb, A. F. Garito, and R. S. Narang, "An exceptionally large linear electro-optic effect in the organic solid MNA," *J. Chem. Phys.*, vol. 75, no. 3, pp. 1509-1516, 1981.
- [49] K. D. Singer, J. E. Sohn, and S. J. Lalama, "Second harmonic generation in poled polymer films," *Appl. Phys. Lett.*, vol. 49, no. 5, pp. 248-250, 1986.

- [50] K. D. Singer, S. L. Lalama, J. E. Sohn, and R. D. Small, "Electro-Optic Organic Materials," in *Optical Nonlinear Properties of Organic Molecules and Crystals*, vol. 1, ed. by D. S. Chemla and J. Zyss, New York, NY: Academic Press, 1988, pp. 437-468.
- [51] C. S. Willand, S. E. Feth, M. Scozzafava, D. J. Williams, G. D. Green, J. I. Weinschenk, III, H. K. Hall, Jr., and J. E. Mulvaney, "Electric-Field Poling of Nonlinear Optical Polymers," in *Nonlinear Optical and Electroactive Polymers*, ed. by P. N. Prasad and D. R. Ulrich, New York, NY: Plenum Press, 1988, pp. 107-120.
- [52] R. N. Demartino, E. W. Choe, G. Khamarian, D. Hass, T. Leslie, G. Nelson, J. Stamatoff, D. Stuetz, C. C. Tang, and H. Yoon, "Development of Polymeric Non-linear Optical Materials", in *Non-linear Optical and Electroactive Polymers*, ed. by P. N. Prasad and D. A. Ulrich, New York: Plenum Press, 1988, pp. 169-188.
- [53] K. D. Singer, M. G. Kuzuk, and J. S. Sohn, "Orientationally Ordered Electro-Optical Materials," in *Non-linear Optical and Electroactive Polymers*, ed. by P. N. Prasad and D. R. Ulrich, New York: Plenum Press, 1988, pp. 189-204.
- [54] D. R. Ulrich, "Overview: Non-linear Optical Organics and Devices," in *Organic Materials for Non-linear Optics*, ed. by R. A. Hann and D. Bloor, Burlington House, London: Royal Chemical Society, 1989, pp. 241-263.
- [55] R. Lytel, G. F. Lipscomb, J. Thackara, J. Altman, P. Elizordo, Stiller and B. Sullivan, "Non-linear and Electro-Optic Devices," in *Non-linear Optical and Electroactive Polymers*, ed. by P. N. Prasad and D. R. Ulrich, New York: Plenum Press, 1988, pp. 241-263.
- [56] J. I. Thackara, G. F. Lipscomb, R. S. Lytel, and J. Ticknor, "Advances in Organic Electro-Optic Devices", *Non-linear Optical Properties of Polymers*, ed. by A. J. Heeger, J. Orenstein, and D. R. Ulrich, Boston, MA: Materials Research Society, 1987, pp. 10-27.
- [57] J. I. Thackara, G. F. Lipscomb, M. A. Stilley, A. J. Ticknor, and R. S. Lytel, "Poled electro-optic waveguide formation in thin-film organic media," *Appl. Phys. Lett.*, vol. 49, no. 52, pp. 1031-1033, 1986.
- [58] J. F. McDonald, N. P. Vlannes, G. E. Wnek, and T.-M. Lu, "DIELECTRIC, CONDUCTING, AND PHOTONIC POLYMERS FOR DEVICES IN MULTICHIP PACKAGING," in *Electronic Packaging Materials, IV, Materials Research Society Symposium Proceedings, Vol. 154*, ed. by E. Lillie, Boston, MA: Materials Research Society, 1989, pp. 387-398.
- [59] E. Yablonovitch, T. Gmitter, J. P. Harbison, and R. Bhat, "Extreme selectivity in the lift-off of epitaxial GaAs films," *Appl. Phys. Lett.*, vol. 51, no. 26, pp. 2222-2224, 1987.
- [60] E. Yablonovitch, E. Kapon, T. J. Gmitter, C. P. Yun, R. Bhat, "Double heterostructure GaAs/AlGaAs thin film diode lasers on glass substrates," *IEEE Photon. Technol. Lett.*, vol. 1, no. 2, pp. 41-42, 1989.
- [61] H. Nishihara, M. Haruna, and T. Suhara, *Optical Integrated Circuits*, New York: McGraw-Hill, 1989.
- [62] T. H. Windham and W. D. Goodhue, "Monolithic GaAs/AlGaAs diode laser/deflector devices for light emission normal to the surface," *Appl. Phys.*

*Lett.*, vol. 48, no. 24, pp. 1675-1677, 1986.

- [63] J. P. Donnelley, W. D. Goodhue, T. H. Windham, R. J. Bailey, and S. A. Lambert, "Monolithic two-dimensional surface-emitting arrays of GaAs/AlGaAs diode lasers," *Appl. Phys. Lett.*, vol. 51, no. 11, pp. 1138-1140, 1987.
- [64] J. P. Donnelley, R. J. Bailey, C. A. Wand, G. A. Simpson, and K. Rauschenbach, "Hybrid approach to two-dimensional surface emitting diode laser arrays," *Appl. Phys. Lett.*, vol. 53, no. 11, pp. 938-940, 1988.
- [65] L. R. Harriott, R. E. Scotti, K. D. Cummings, and A. F. Ambrose, "Micro-machining of integrated optical structures," *Appl. Phys. Lett.*, vol. 48, no. 25, pp. 1704-1706, 1986.
- [66] R. Selvaraj, H. T. Lin, and J. F. McDonald, "Integrated Optical Waveguides in Polyimide for Wafer Scale Integration," *J. Lightwave Technol.*, vol. LT-6, no. 6, pp. 1034-1044, 1988.
- [67] R. A. Elliot, R. K. DeFreez, J. Pureta, J. Orloff, H. Nambra, E. Omura, and H. Namizaki, "Performance and Lifetests of Focused Ion Beam Micromachined Diode Lasers," *LEOS'88 Conference Proceedings*, Nov. 2-4, 1988, Santa Clara, California, IEEE Catalog Number: 88CH2683-1, pp. 34-36, 1988.
- [68] Z. L. Liao and J. N. Walpole, "Surface-emitting GaInAsP/InP laser with low threshold current and high efficiency," *Appl. Phys. Lett.*, vol. 46, no. 2, pp. 115-117, 1985.
- [69] Z. L. Liao, J. N. Walpole, and D. Z. Tsang, "Fabrication, Characterization, and Analysis of Mass-Transported GaInAsP/InP buried Heterostructure Lasers," *IEEE J. Quantum Electron.*, vol. QE-20, no. 8, pp. 855-865, 1984.
- [70] Z. L. Liao, V. Diadiuk, J. N. Walpole, and D. E. Mull, "Large-numerical-aperture InP lenslets by mass-transport," *Appl. Phys. Lett.*, vol. 52, no. 22, pp. 1859-1861, 1988.
- [71] D. Baranowski, L. G. Mann, R. H. Bellman, and N. F. Borelli, "Photothermal technique generates lens arrays," *Laser Focus World*, vol. 25, no. 11, pp. 139-143, 1989.
- [72] M. M. Abouelleil, A. J. Cantor, R. H. Hobbs, "Ion-Exchange Microlens Arrays in Glass," presented at American Ceramics Society Fall Meeting, Nov. 6-9, 1988, paper number 5-G-88F.
- [73] A. J. Cantor, M. M. Abouelleil, R. H. Hobbs, "Ion-Exchange Microlens Arrays," *1989 LEOS Annual Meeting Conference Proceedings*, Oct. 16-20, 1989, Orlando, FL, IEEE Catalog Number: 89CH2641-9, pp. 183-184, 1989.

## CHAPTER VI

# High Resolution Image Reconvery From Image Plane Arrays Using Convex Projections

Henry Stark and Peyma Oskoui

### 6.1 INTRODUCTION

In remote sensing and astronomy, images are often reconstructed from data obtained by fixed or scanning detector arrays superimposed on the image field [1]. Since detectors are typically much larger than the blur spot of the imaging optics, a naive reconstruction of the image from the detector data would produce an image of lower resolution than that furnished by the imaging optics. The reduction of detector size to match the blur spot of the imaging optics may not be technically feasible, and even if it were, the associated signal-to-noise ratio of the detector output might be too low to be useful [2].

In [3] Frieden and Aumann argued that by allowing intentional overlap of successive scans and rescans of the same area from different directions, there might be enough information in the acquired data to allow for a higher resolution reconstruction i.e., one more commensurate with the imaging optics. They illustrate such increased resolution reconstructions using a least-squares algorithm they call *filtered localized projection*.

In this paper we also attempt to reconstruct high-resolution images from coarse detector data but we use an algorithm that enables the incorporation of prior data. The algorithm, which is a realization of the method of convex projections, alternatively known as the method of projections onto convex sets (POCS), is a two-dimensional extension of a one-dimensional algorithm earlier used in computerized-tomography [4]. The method of POCS is often used to recover "missing" information in limited-data situations [5-9]. In [4], however, it was used explicitly to reconstruct an image from a set of line-integrals called

raysums. In this paper the image is reconstructed from a set of area integrals in a fashion that parallels the approach in [4]. Moreover, in addition to allowing the use of prior knowledge, the method of POCS does not require any particular detector or scanning geometries; detectors can be of any size, the scanning can be in any direction, and the angular scan increments need not be uniform.

## 6.2 THE METHOD of CONVEX PROJECTIONS

Consider an unknown signal  $s(x)$  that is known to enjoy properties  $\pi_1, \pi_2, \dots, \pi_m$ . With each property  $\pi_i$  there is associated a set  $C_i$  which is the set of all signals enjoying property  $\pi_i$ . Often these sets are closed (they contain their limit points) as well as convex meaning that if  $s_1(x)$  and  $s_2(x)$  belong to  $C_i$  then the weighted sum  $\mu s_1(x) + (1 - \mu)s_2(x)$  belong to  $C_i$  for any  $0 \leq \mu \leq 1$ . Of importance is the observation that  $s(x)$  must belong to the solution set  $C_s \triangleq \bigcap_{i=1}^m C_i$  assuming that this intersection is not empty. The central theorem of the method of POCS is the following: the recursion

$$f^{(k+1)} = P_m P_{m-1} \dots P_2 P_1 f^{(k)}, \quad f^{(0)} \triangleq f_0$$

where  $f_0$  is an arbitrary starting point, converges weakly [10] to a feasible solution that lies in  $C_s$ . The projection operator or *projector*  $P_i$  projects an arbitrary signal  $f$  onto the closed, convex sets,  $C_i, i = 1, \dots, m$ . By *projection* we mean the function (point)  $g \in C_i$  nearest to the original arbitrary signal  $f$ .

The central problem in POCS is to synthesize the projectors  $P_i, i = 1, \dots, m$ . While this may not be a trivial task, it is in general, much easier to do than to find  $P_s$ , i.e., the projector that projects onto the solution set  $C_s$  in one step.

## 6.3 THE METHOD of POCS APPLIED to the PROBLEM at HAND

### A. DATA CONSTRAINTS:

Consider a detector with response function  $\sigma(x, y)$  when centered at the origin and aligned with some convenient orthogonal coordinate system  $(x, y)$ , for

example, the rectangularly shaped detector of length  $a$  and width  $b$  in Figure 6.1(a). Now assume that the detector is superimposed on the image  $f(x, y)$  and let its response function when it is in position  $j$  be  $\sigma_j(x, y)$ . Then the detector output  $d_j$  is given by:

$$d_j = \int \int_{-\infty}^{\infty} f(x, y) \sigma_j(x, y) dx dy. \quad (6.1)$$

The geometry is shown in Figure 6.1(b). The rectangular detector in Figure 6.1 would, for example, have response:

$$\sigma_j(x, y) = \text{rect}\left[\frac{(x - x_j) \cos \theta_j + (y - y_j) \sin \theta_j}{a}\right] \cdot \text{rect}\left[\frac{(y - y_j) \cos \theta_j - (x - x_j) \sin \theta_j}{b}\right] \quad (6.2)$$

when shifted to  $x_j, y_j$  and rotated, as shown, by an amount  $\theta_j$ .

We recognize equation ((6.1) to be an inner product. Thus we write  $d_j = (f, \sigma_j)$  using the well-known inner product notation. The problem then becomes: given readings  $d_i, i = 1, \dots, K$  and prior constraints or properties  $\pi_{K+1+j}, j = 0, \dots, N - K - 1$ , how do we reconstruct an image whose resolution is higher than that which would result from a naive reconstruction from the detectors alone?  $N$  here is the total number of measurements and prior constraints.

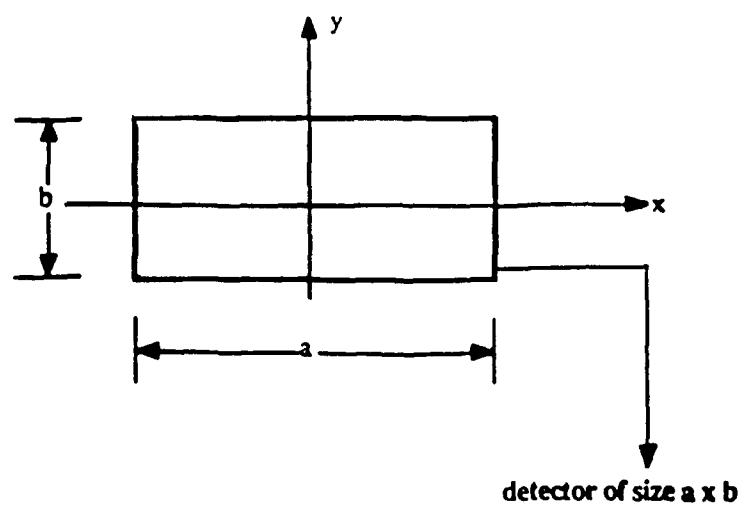
In real-world situations, the processing is often done by computer. In this case the finite size of the pixels must be accounted for. One way to do this is to include in the detector response the fractional pixel areas included within the detector footprint. The detector output at the  $j$ 'th reading can be written as

$$d_j = \sum_l \sum_k f(l, k) \sigma_j(l, k), \quad (6.3)$$

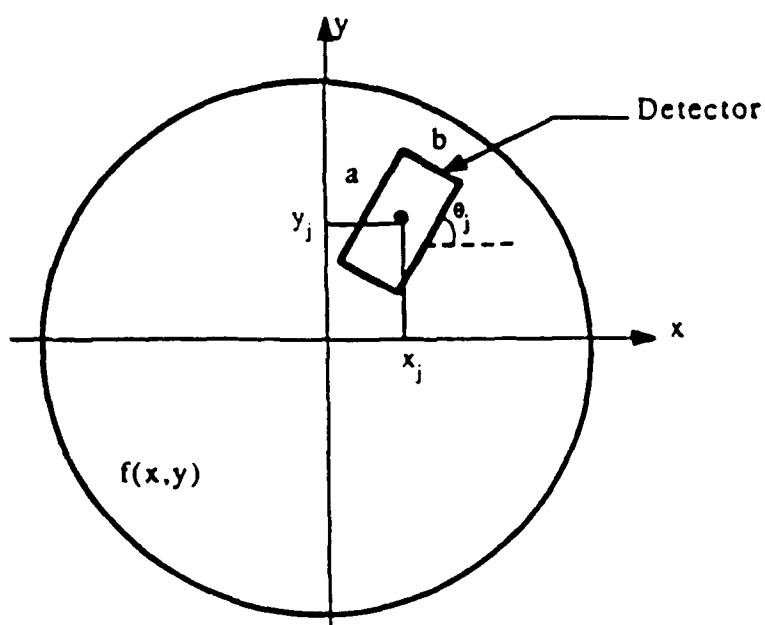
where  $f(l, k)$  is the brightness of the pixel centered at  $(l, k)$  and  $\sigma_j(l, k)$  is the detector response at position  $(l, k)$  and includes the fractional area of the pixel at  $(l, k)$  within the detector footprint when it is in the  $j$ 'th position. For example



FIGURE 6.1



(a)



(b)

Figure 6.1. (a) rectangular detector of size  $ab$ . (b) detector over image  $f(x,y)$ , displaced by  $x_j$  and  $y_j$  and rotated through an angle  $\theta_j$ .

suppose that the detector has a uniform, say unity, response over its footprint; then,

$$\sigma_j(l, k) = \begin{cases} 0, & \text{when pixel centered at } (l, k) \text{ lies wholly outside} \\ & \text{detector footprint;} \\ 1, & \text{when pixel centered at } (l, k) \text{ lies wholly within} \\ & \text{the detector footprint;} \\ r_j, & (0 < r_j < 1) \text{ when the pixel centered at } (l, k) \text{ lies partially} \\ & \text{within the detector footprint.} \end{cases} \quad (6.4)$$

In equation (6.4)  $r_j$  is the fractional area of that portion of the  $(l, k)$ 'th pixel that lies within the detector footprint. Equation (3) is recognized to be a discrete two-dimensional inner product. It too, therefore, can be written as  $d_j = (f, \sigma_j)$ .

We now define the sets  $C_j, j = 1, \dots, K$  as:

$$C_j = \{f(x, y) : (f, \sigma_j) = d_j\}. \quad (6.5)$$

In words,  $C_j$  is the set of all image functions whose inner product with the detector function  $\sigma_j$  is  $d_j$ . We note that the  $K$  sets described in equation (6.5) are in effect  $K$  constraints on the image. Since  $f$  occurs linearly in the expression  $(f, \sigma_j) = d_j$  it is possible, in principle, to obtain enough equations - even with detectors larger than a pixel - so that a formal solution can be obtained by matrix inversion. For example if the image has  $P^2$  pixels and  $K = P^2$  is the number of independent equations  $(f, \sigma_j) = d_j$  then by matrix inversion of the  $P^2$  linear equations,  $f(x, y)$  can be found [11]. However, since  $P$  is typically 525 to 1000 or more the matrix inversion process is ill-conditioned and practically not feasible.

Returning to equation (6.5) we show in Appendix A that  $C_j$  is: a) convex; b) closed; and c) has projection  $g(x, y)$  given by:

$$g = P_j h = \begin{cases} h(x, y), & \text{if } (h, \sigma_j) = d_j \\ h(x, y) + \frac{d_j - (h, \sigma_j)}{(\sigma_j, \sigma_j)} \sigma_j(x, y), & \text{otherwise.} \end{cases} \quad (6.6)$$

In equation (6.6),  $h(x, y)$  is an arbitrary function in the  $L_2$  space of square-integrable functions;  $(h, \sigma_j)$  is an inner product;  $g(x, y)$  is the projection of  $h(x, y)$

onto  $C_j$ ;  $P_j$  is the projector; and  $d_j$  is the measurement constraint and is assumed given. In POCS equation (6.6) is used recursively. Thus, if  $f_n(x, y)$  represents the  $n$ 'th estimate of the correct but unknown image  $f(x, y)$ , the improved estimate  $f_{n+1}(x, y)$  would be obtained at the next step, from

$$f_{n+1}(x, y) = \begin{cases} f_n(x, y), & \text{if } (f_n, \sigma_j) = d_j \\ f_n(x, y) + \frac{d_j - (f_n, \sigma_j)}{(\sigma_j, \sigma_j)}, & \text{otherwise.} \end{cases} \quad (6.7)$$

We note in equation (6.6) that  $(\sigma_j, \sigma_j)$  is not merely the area of the detector; it includes terms involving  $r_j^2$  and therefore depends on the position of the detector array relative to the image plane coordinates.

#### B. PRIOR KNOWLEDGE:

In addition to the constraints imposed by the data, these are additional constraints that can be imposed from prior knowledge (all functions in this discussion are assumed to belong to  $L_2$ ; the usual  $L_2$  norm and inner product are used throughout). The only prior knowledge constraint sets used in this paper are:

1. The amplitude constraint set  $C_A$ :

$$C_A = \{g(x, y) : \alpha \leq g(x, y) \leq \beta, \beta > \alpha\} \quad (6.8a)$$

The projection of an arbitrary function  $h(x, y)$  onto  $C_A$  is:

$$g = P_A h = \begin{cases} \alpha & \text{if } h(x, y) < \alpha; \\ h(x, y), & \text{if } \alpha \leq h(x, y) \leq \beta; \\ \beta, & \text{if } h(x, y) > \beta. \end{cases} \quad (6.8b)$$

2. The energy constraint set  $C_E$ :

$$C_E = \{g(x, y) : \|g\|^2 \leq E\}, \quad (6.9a)$$

where  $E$  is the maximum allowable energy in the reconstructed image. The projection of the function  $h(x, y)$  onto  $C_E$  is:

$$g = P_E h = \begin{cases} h(x, y), & \text{if } \|h\|^2 \leq E \\ (E/E_h)^{1/2} h(x, y), & \text{if } \|h\|^2 > E \end{cases} \quad (6.9b)$$

In equation (6.9b),  $E_h \triangleq \|h\|^2$ .

### 3. The reference-image constraint set $C_R$ :

$$C_R = \{g(x, y) : \|g - f_R\| \leq \epsilon_R\}. \quad (6.10a)$$

In equation (6.10a),  $f_R$  is a prior-known reference function and  $\epsilon_R$  is the allowed rms deviation from the reference and is known *a priori*.  $C_R$  is sometimes called the “sphere constraint” because the set includes all  $L_2$  functions that lie within a sphere of radius  $\epsilon_R$  and centered at  $f_R$ . The projection onto  $C_R$  is:

$$g = P_R h = \begin{cases} h, & \text{if } \|h - f_R\| \leq \epsilon_R \\ \frac{h - f_R}{\|h - f_R\|} & \text{if } \|h - f_R\| > \epsilon_R. \end{cases} \quad (6.10b)$$

Note that  $C_R$  is a generalization of  $C_E$ . By setting  $f_R = 0$ ,  $\epsilon_R = (E)^{1/2}$  and  $E_h = \|h\|^2$ , we obtain equation (6.9b).

### 4. The bounded support-constraint set $C_s$ :

$$C_s = \{g(x, y) : g(x, y) = 0 \text{ for } (x, y) \in A\}. \quad (6.11a)$$

In equation (6.11a)  $A$  is some finite region in  $R \times R$ . The projection operator onto  $C_s$  is:

$$g = P_s h = \begin{cases} h(x, y) & \text{if } (x, y) \in A \\ 0, & \text{otherwise.} \end{cases} \quad (6.11b)$$

The derivation of all these projectors are given in other places, e.g., [5],[12].

We omit repeating them here.

## 6.4 EXPERIMENTAL RESULTS

### A. RECONSTRUCTION from DETECTOR READINGS:

We attempt to reconstruct images from low-resolution data gathered in two different ways: 1) a fixed detector array is superimposed on the image field but controlled, sequenced, rotation between the image field and the detector array

is permissible (Figure 6.2); and 2) an array is scanned across the image and data is collected for different positions during the scan (Figure 6.3).

In the example shown in Figure 6.2, each detector has dimensions 4 (horizontal)  $\times$  2 (vertical) (all dimensions are in pixels) while the number of pixels in the image is 64. Hence a minimum of 8 angular displacement are required to yield enough equations to solve for the 64 unknown brightness levels. In the example shown in Figure 6.3, a single vertical pass is enough to yield the 64 required equations. Readings are obtained every time the detector array is wholly superimposed over a fresh row. Except for the comparison with the method proposed in [1], which requires the configuration of Figure 6.3, all of our experiments are done using the fixed array in which rotation between array and image is used to get additional equations.

The image to be reconstructed is a  $64 \times 64$  version of the widely-used Shepp-Logan phantom [13] shown in Figure 6.4(a). Superimposed on the image is a rectangular detector array consisting of 8 detectors along the horizontal and 16 detectors along the vertical. Each detector has dimension 8 along the horizontal and 4 in the vertical. As there are  $64 \times 64 = 4096$  unknown brightness a full data set would require a minimum of 32 angular displacements ( $128 \times 32 = 4096$ ). Note that for each angular displacement we obtain approximately 128 equations.

The first experiment shows the feasibility of using POCS as an alternative to matrix inversion for reconstructing the image. Figure 4 shows the reconstruction of the Shepp-Logan phantom using POCS and only the data constraints given in equation (6.5) for  $j = 1, \dots, 4096$ ; no prior knowledge about the image was assumed. In Figure 6.4(b) is shown the reconstruction after 10 iterations; in Figure 6.4(c) after 50; and in Figure 4(d) after 100. The fine structure in the Shepp-Logan phantom becomes evident after 50 iterations and, except for some noise, is exactly reproduced after 100 iterations. We note that the mean-square

FIGURE 6.2

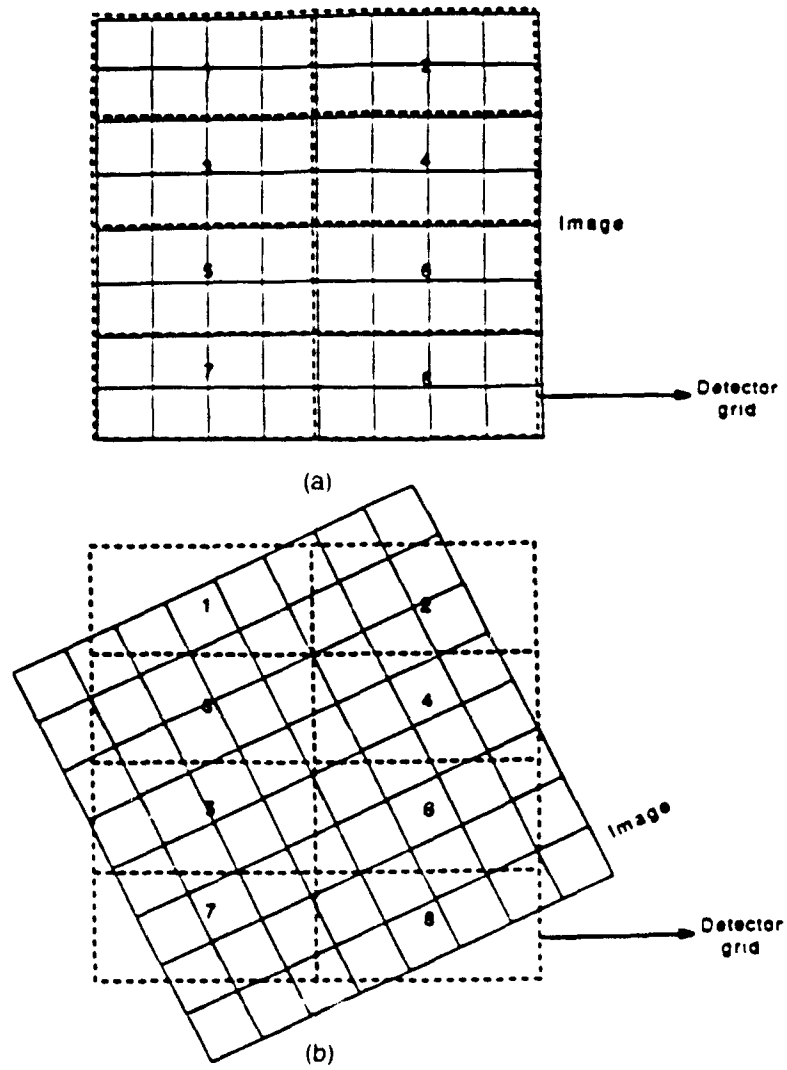
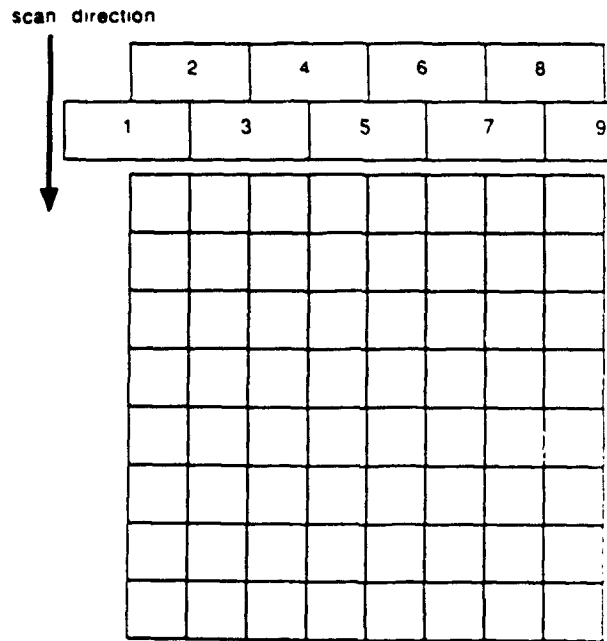


Figure 6.2. Rotation between detector array and image field to get additional information.

**FIGURE 6.3**



**Figure 6.3. Scanning configuration of detectors. Information is obtained as detectors scan the image field in a vertical direction.**

FIGURE 6.4

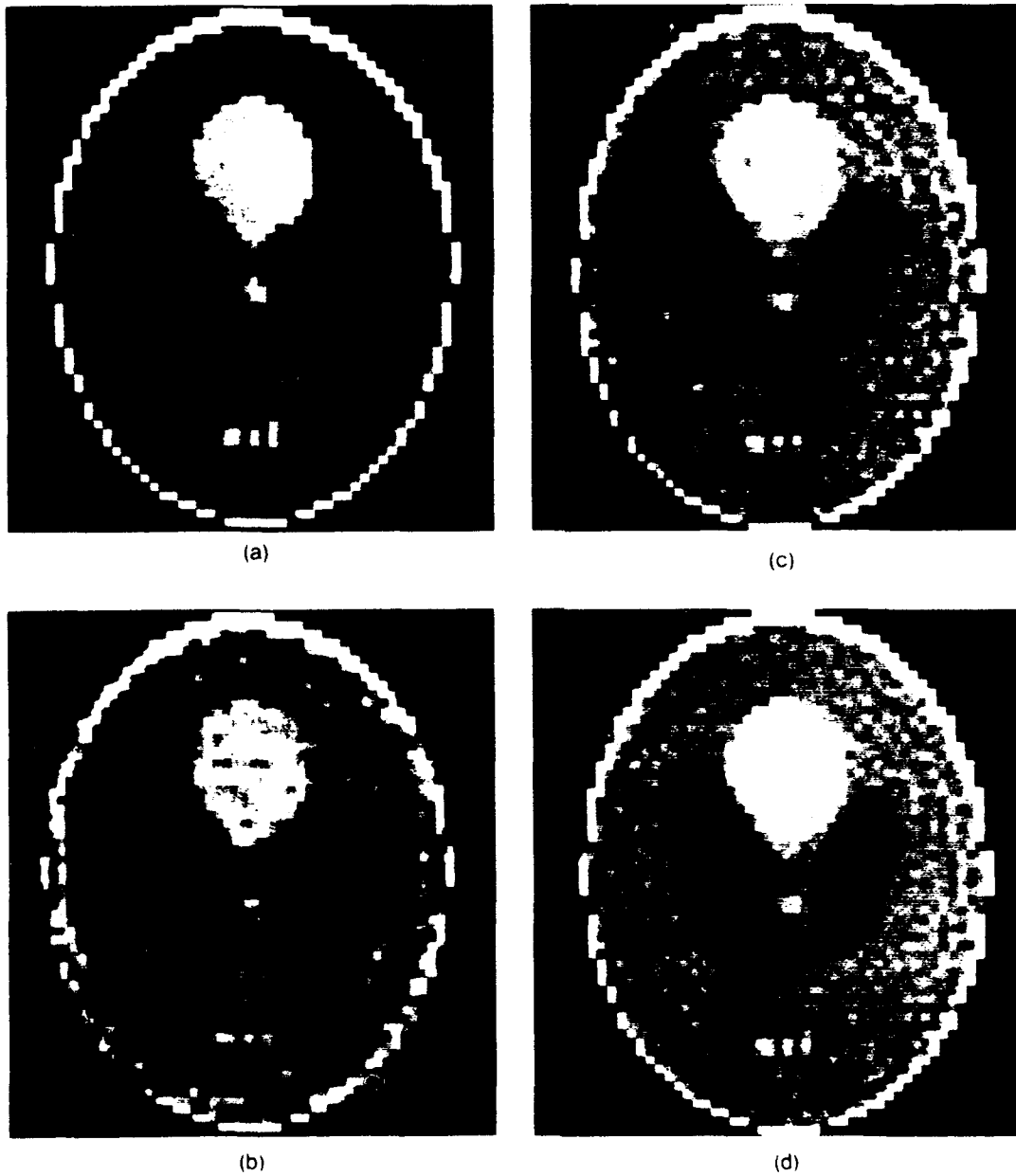


Figure 6.4. Reconstruction of high-resolution images from full data sets using convex projections without reference image constraint. Initial image is zero image. 128 detectors of size  $8 \times 4$  were used in 32 views. (a) original image; (b) reconstruction after 10 iterations; (c) after 50 iterations; (d) after 100 iterations.



error due to the noise is still decreasing at 100 iterations but at a very slow pace; the rms error at this point is 6.8 percent. The algorithm used to get these results is given by:

$$f_{n+1}(x,y) = P_K \dots P_1 f_n, \quad n = 0, 1, \dots \quad (6.12)$$

where  $P_k, k = 1, 2, \dots, K$  is implicitly defined in equation (6.7). The starting point for the recursion in equation (6.12) is the uniform ellipse shown in Figure 6.5. The visual influence on the reconstruction of the starting point  $f_0$  decreases with increasing number of iterations. In Figure 6.6, the recursion of equation (6.12) is used for: a)  $f_0$  as in Figure 6.5; and b)  $f_0 = 0$ . Both are clearly converging to the correct solution but the algorithm using the more propitious  $f_0$  is smoother than the reconstruction initialized by  $f_0 = 0$ . The rms error history for the two reconstructions starting with different initializations is shown in Figure 6.7.

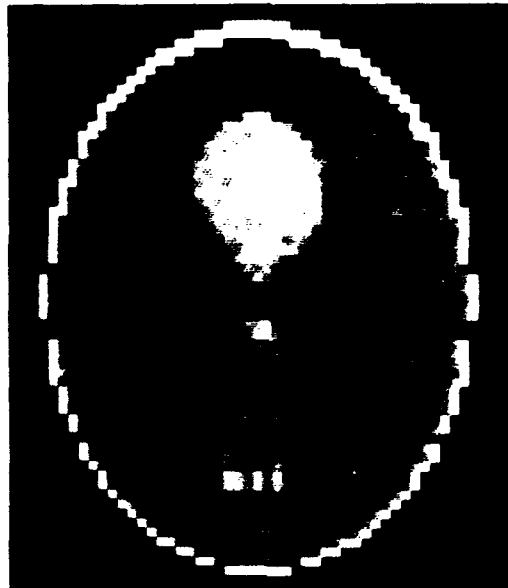
Figure 6.8 explores the effect of limited-view reconstruction by POCS. Out of a full angular range of  $180^\circ$  (divided into 32 view angles) we *do not* collect data in regions of angular diameter at extent 20, 40, 60 and 90 degrees, respectively. Hence the numbers of available detector readings and the number of equations available for reconstruction are reduced from the full data set of 4096 to  $(8 \times 16) \times 29 = 3712$ ,  $(8 \times 16) \times 25 = 3200$ ,  $(8 \times 16) \times 21 = 2688$  and  $(8 \times 16) \times 15 = 1920$  respectively. To ameliorate the effect of insufficient data we use prior knowledge associated with the sets  $C_A$  and  $C_R$ , - the amplitude and reference image constraint sets respectively. In  $C_A$ , we let  $\alpha = 0, \beta = 1$  and in  $C_R$  we let  $f_R$  be the image of Figure 6.5 which we also pick as  $f_0$ ; the parameter  $\epsilon_R$  was set to  $\epsilon_R = \|f_R - f_T\|$  where  $f_R$  is the true image shown in Figure 6.4(a). The results are given in Figure 6.8. As expected, the visibility decreases with increasing loss of data but even with 40 degrees of missing view data the fine structure in the Shepp-Logan reconstruction is still visible in Figure 6.8(b). The results should be contrasted

FIGURE 6.5

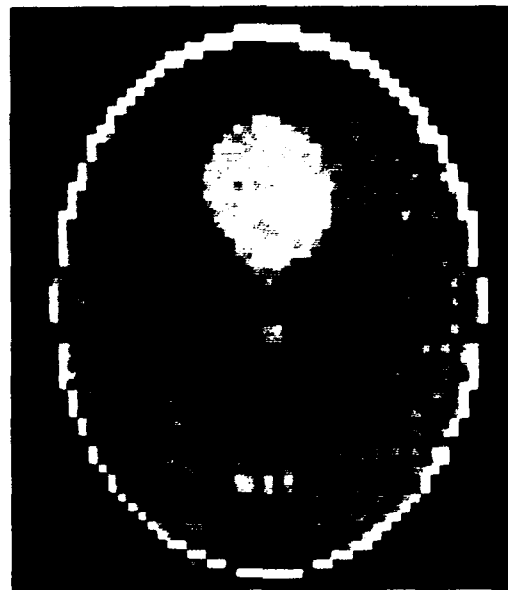


Figure 6.5. The image sometimes used as the initial image and/or the reference image. It consists of a uniform ellipse.

FIGURE 6.6



(a)



(b)

Figure 6.6. Reconstruction using convex projections after 100 iterations; (a) initial image is that of Figure 6.5; (b) initial image is zero image. Reference image constraint not in use.

FIGURE 6.7

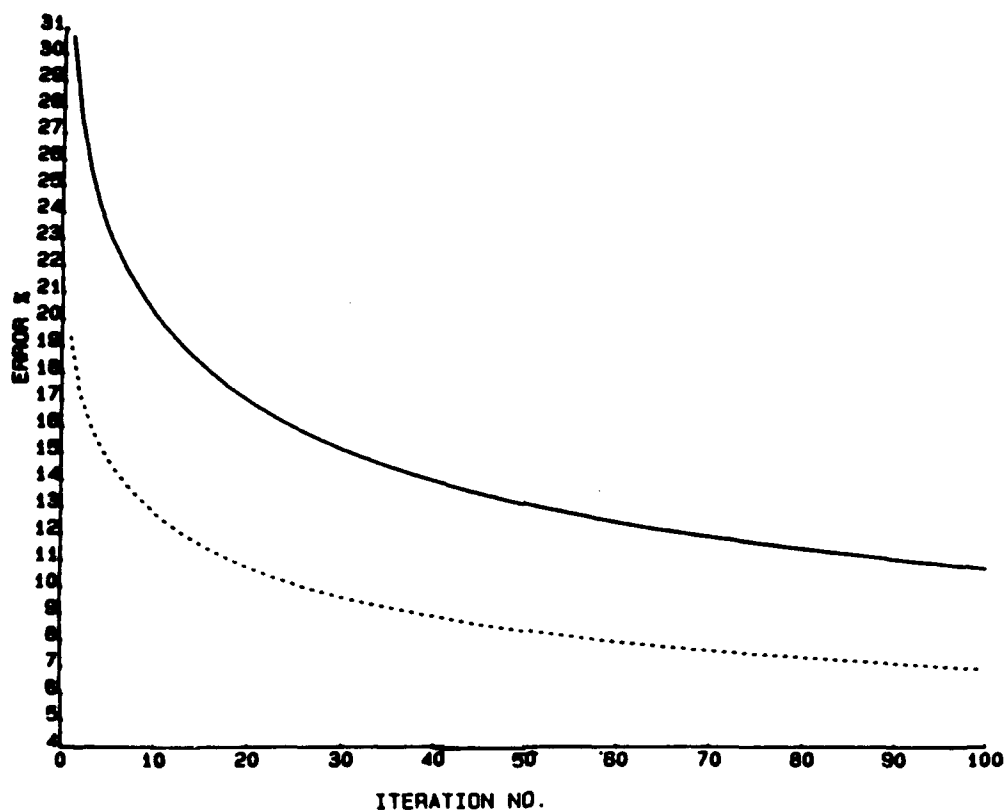


Figure 6.7. Error history of reconstructions by convex projections: Solid line shows the reconstruction error when  $f_0 = 0$ ; dotted line has  $f_0$  in Figure 6.5.

FIGURE 6.8

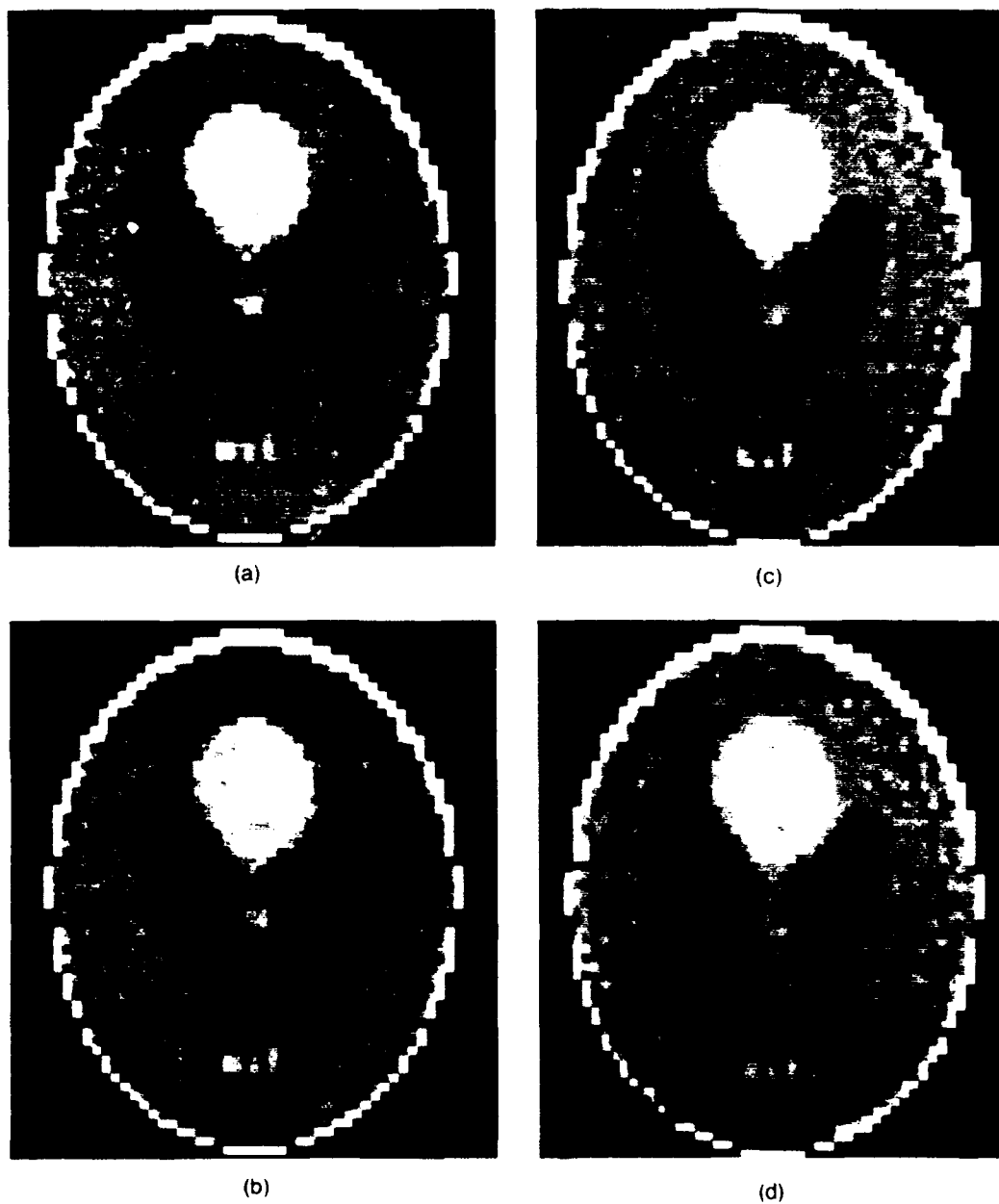


Figure 6.8. Limited-view reconstructions using POCS after 100 iterations. Initial image  $f_0$  is that of Figure 6.5. (a) 20 degrees of missing data; (b) 40 degrees of missing data; (c) 60 degrees of missing data; (d) 90 degrees of missing data.

FIGURE 6.9

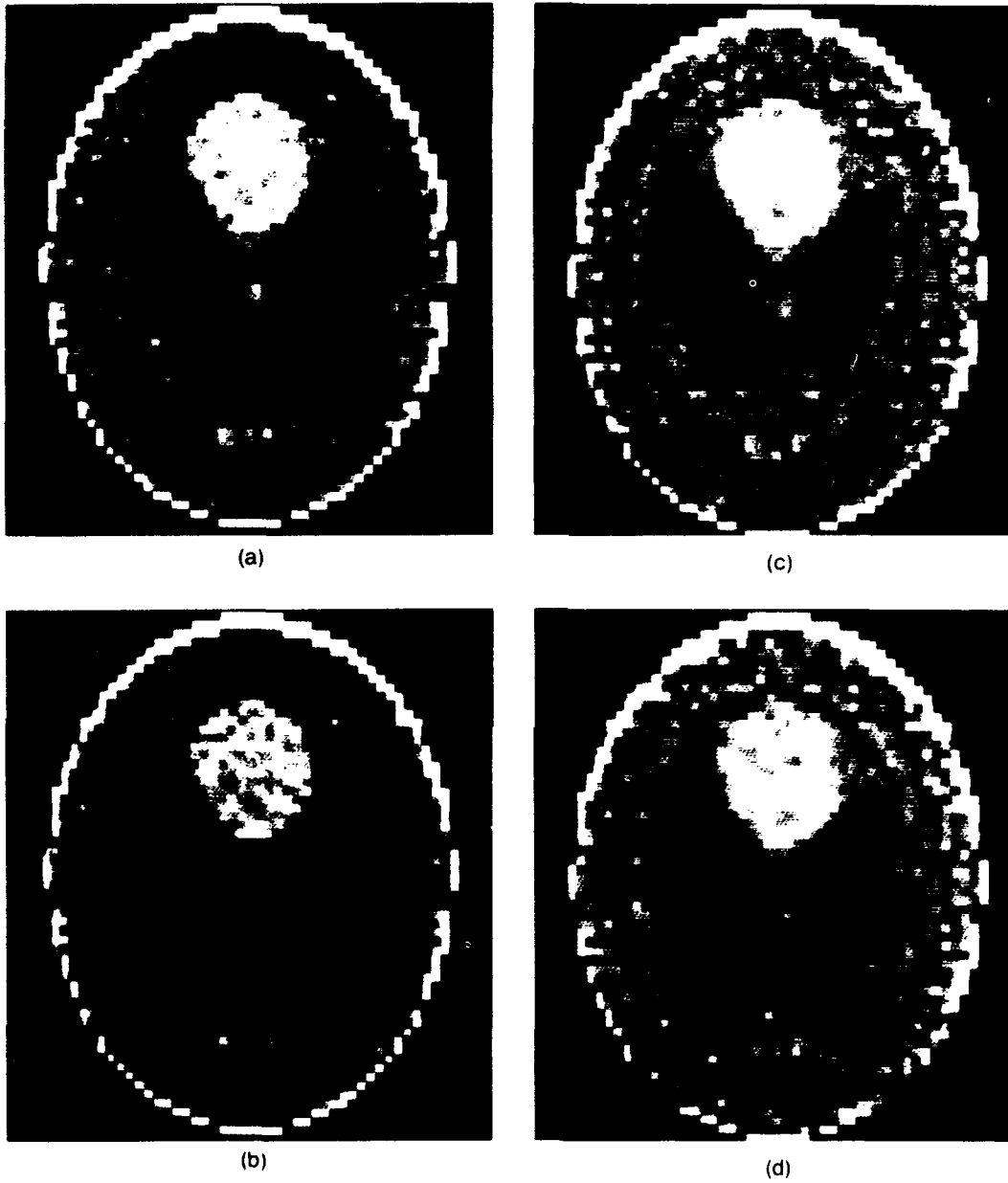


Figure 6.9. Same as Figure 6.8 but reference image constraint and amplitude level constraint omitted. Also initial image is  $f_0 = 0$ . This image is reconstructed from data only while that of Figure 6.8 uses prior knowledge.

with Figure 6.9 where the reconstructions were attempted without using prior knowledge.

#### B. THE EFFECT of NOISE:

To investigate the effect of noise on the image recovery procedure we made the following assumptions: the average intensity,  $I$ , across any detector is constant both in time and in displacement across the detector; the number of photons striking the detector is a Poisson process; and the noise in each detector is independent of the noise in any other detector. The average light energy sensed by the detector in a given time interval  $\Delta t$ , is given by  $A_D \Delta t I$ , where  $A_D$  is the detector area, and in this discussion,  $\Delta t$  is the integration time of the detector. It is assumed that the quantum efficiency of the detector is one. The amount of energy per unit photon is given as  $h\nu$ , where  $h$  is Plank's constant and  $\nu$  is the frequency of the radiation. Hence the average number of photons in an integration time of the detector,  $\mu$ , is given as:

$$\mu = \frac{A_D \Delta t I}{h\nu} = \alpha I \quad (6.13)$$

$$\alpha = \frac{A_D \Delta t}{h\nu}. \quad (6.14)$$

Since this is a Poisson process, the variance,  $\sigma^2$ , is equal to the mean,  $\mu$ :

$$\sigma^2 = \alpha I, \quad (6.15)$$

To generate a given signal-to-noise (SNR) ratio, we adjust  $\alpha$  to have the value:

$$\log \alpha = 0.1[SNR - 10 \log I]. \quad (6.16)$$

The parameter  $\alpha$  is computed this way for each detector reading. Thus equation (6.16) is more properly written as:

$$\log \alpha_n = 0.1[SNR - 10 \log I_n], \quad n = 1, \dots, K \quad (6.17)$$

where  $K$  is the total number of readings. This procedure is one way of defining a signal-to-noise ratio for the whole image; no doubt there are others.

The actual procedure for generating noisy data then consisted of the following steps. Because we were interested only in high signal-to-noise we used the Gaussian approximation to the Poisson law to generate random samples with the correct variance. Thus, say that at the  $n$ 'th reading we measure a *noiseless* intensity  $I_n$ . Then the correct photon variance, from equation (6.15), is  $\alpha_n I_n$  where  $\alpha_n$  is computed from equation (6.17) for any specified SNR. The next step is to use a random number generator to generate a photon-noise term from a Gaussian pdf with mean 0 and variance  $\alpha_n I_n$ . This sample is converted to intensity noise by dividing by  $\alpha_n$ . The total measured intensity is then the sum of  $I_n$  and the noise component obtained as described above. This procedure is repeated for every detector reading in the image plane array.

The results for SNR's of 30 dB and 50 dB as shown in Figure 6.10 for 100 iterations. The 30 dB SNR reconstruction is noisy enough to obliterate the details of the image. Results are much better for 50 dB SNR but there is still considerable noise present. We found that the smoothing induced by the  $C_R$  constraint had little effect for this image. Finding effective noise-suppressant schemes for reconstruction from noisy data is left for future research.

### C. COMPARISON with TWO-STEP LEAST-SQUARES:

In a recent paper [3], Frieden and Aumann proposed a two-step least-squares scheme for reconstructing high-resolution images from data obtained from scanning arrays. There too, the blur spot of the imaging optics was significantly smaller than the size of the array detector elements. The authors called their algorithm *filtered localized projection* (FLP). The essential ingredients of the algorithm are the following. The detector data vector  $I$  is related to the original



FIGURE 6.10

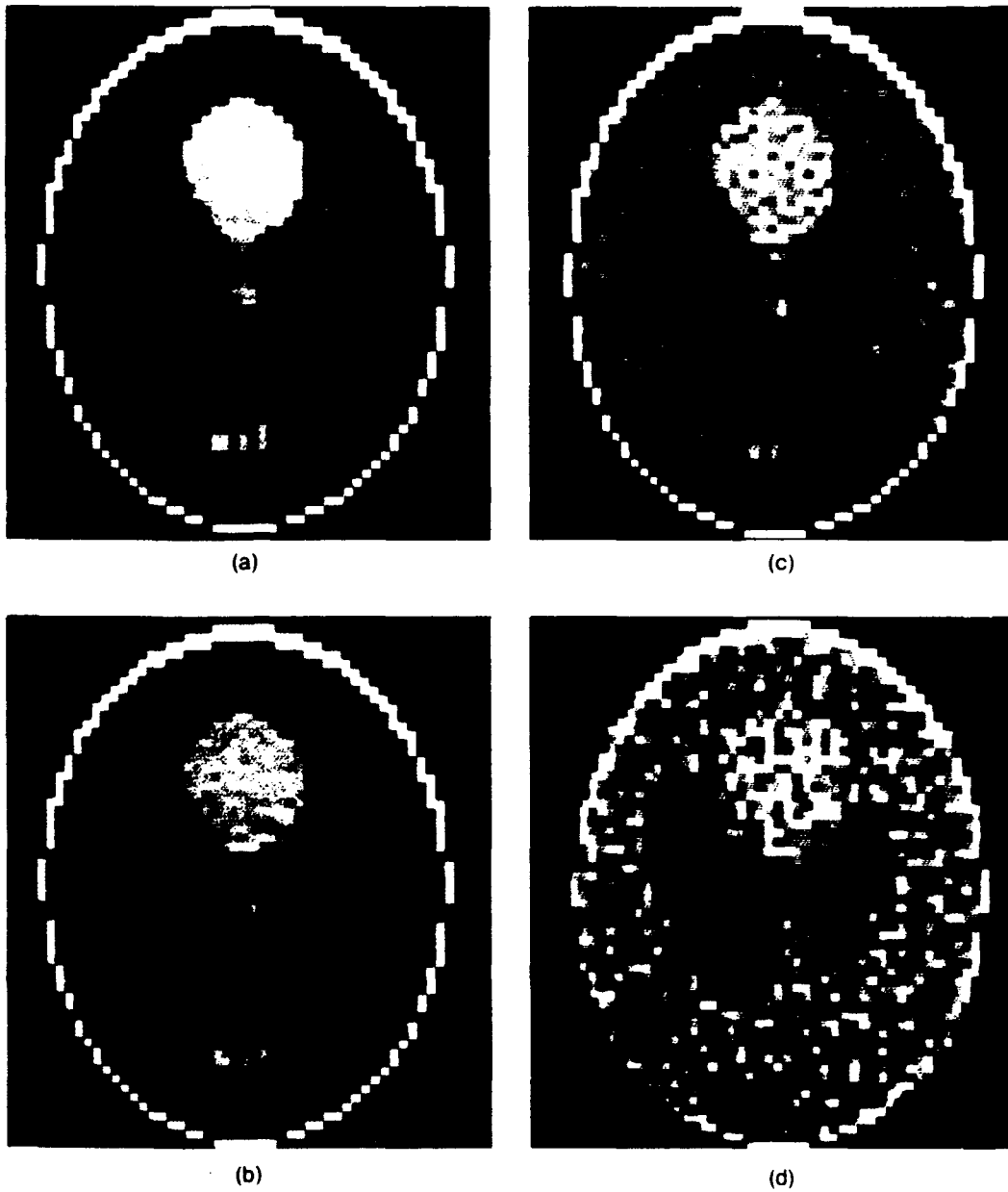


Figure 6.10. Effect of noise on POCS reconstructions after 100 iterations. (a) original image; (b) reconstruction from noiseless data; (c) reconstruction from 50 dB SNR data; (d) reconstruction from 30 dB SNR data.

(unblurred) image vector  $O$  by:

$$I = HO,$$

where  $H$  is the array blur matrix. In the first step a preliminary estimate of  $O$ ,  $O_p$  is obtained from:

$$O_p = H^T I = H^T HO.$$

This is what Frieden and Aumann called the localized projection (LP) image of  $O$ . In the second step, an inverse filter  $H^+$  is applied to  $O_p$  to produce a final estimate  $\hat{O}$ . In particular, if  $[H^T H]^{-1}$  exists and

$$H^+ \triangleq [H^T H]^{-1},$$

then

$$\hat{O} = [H^T H]^{-1} H^T O_p \triangleq \hat{O}_{LS}.$$

Of course, if there is no noise and the equations are consistent, the original image is reconstructed. Thus the FLP method realizes the least-squares estimator  $\hat{O}_{LS}$  in two steps.

Another way to inverse filter  $O_p$  is to recognize that  $H^T H$  is Toeplitz and therefore is associated with a well-defined point-spread function connecting the LP reconstruction and true object. Hence the LP image can be inverse filtered in the frequency plane by a fast Fourier transform to yield  $\hat{O}$ .

In our research we compared the FLP method using frequency-plane inverse filtering with the POCS approach. While both techniques furnished good results each had certain advantages compared with the other. The results are discussed below.

In the first experiment of this series, we used a scanning arrangement similar to that shown in Figure 6.3; each detector was one pixel high and two pixels wide. We call this a two-point horizontal blur (2-PHB). The test image is shown in

Figure 6.4(a), i.e.,  $64 \times 64$  Shepp-Logan phantom. All the detectors were assumed to have unity response. The point-spread function in this case is the sequence  $\dots, 0, 0, 1, 2, 1, 0, 0, \dots$ . For the POCS reconstructions,  $f_0$  was taken as the zero image,  $f_R$  was the uniform ellipse of Figure 6.5, and the region  $A$ , enclosing the ellipse and representing our knowledge of the finite support of the object, was a rectangle of dimension  $50 \times 60$ . Figure 6.11(a) shows the results for the 2-PHB. Figure 6.11(a) is the unprocessed detector image - the 2-PHB effect is evident. In Figure 6.11(b), the LP image  $0_p = H^T I$ . The FLP image is shown in Figure 6.11(c) and should be compared to the POCS reconstruction after 30 iterations in Figure 6.11(d). Both approaches, POCS and FLP, yield comparable results and represent significant improvements over the unprocessed detector image of Figure 6.11(a).

Figure 6.12 shows a much more severe blurring is introduced by using  $4 \times 1$  detectors which introduce a four-point horizontal blur (4-PHB). The unprocessed detector image (Figure 6.12(a)) as well as the LP image (Figure 6.12(b)) are so badly blurred that the finer details in the Shepp-Logan object are obliterated. The FLP image (Figure 6.12(c)) is quite good except for a mottled background. The same kind of mottling appears after 30 iterations in the POCS image which, in other respects, is quite good. When the POCS image is reconstructed after 100 iterations (Figure 6.12(d)), an excellent noise-free image is reconstructed which is superior to FLP image (Figure 6.12(c) or 6.11(c)). On the other hand, it may be possible to improve the FLP image by techniques other than simple inverse filtering which is known to be noisy.

It appears that both FLP and POCS can recover high-resolution images from badly blurred detector images. While the FLP technique is much faster than POCS, the latter seems to yield better results when the blurring is severe.

FIGURE 6.11

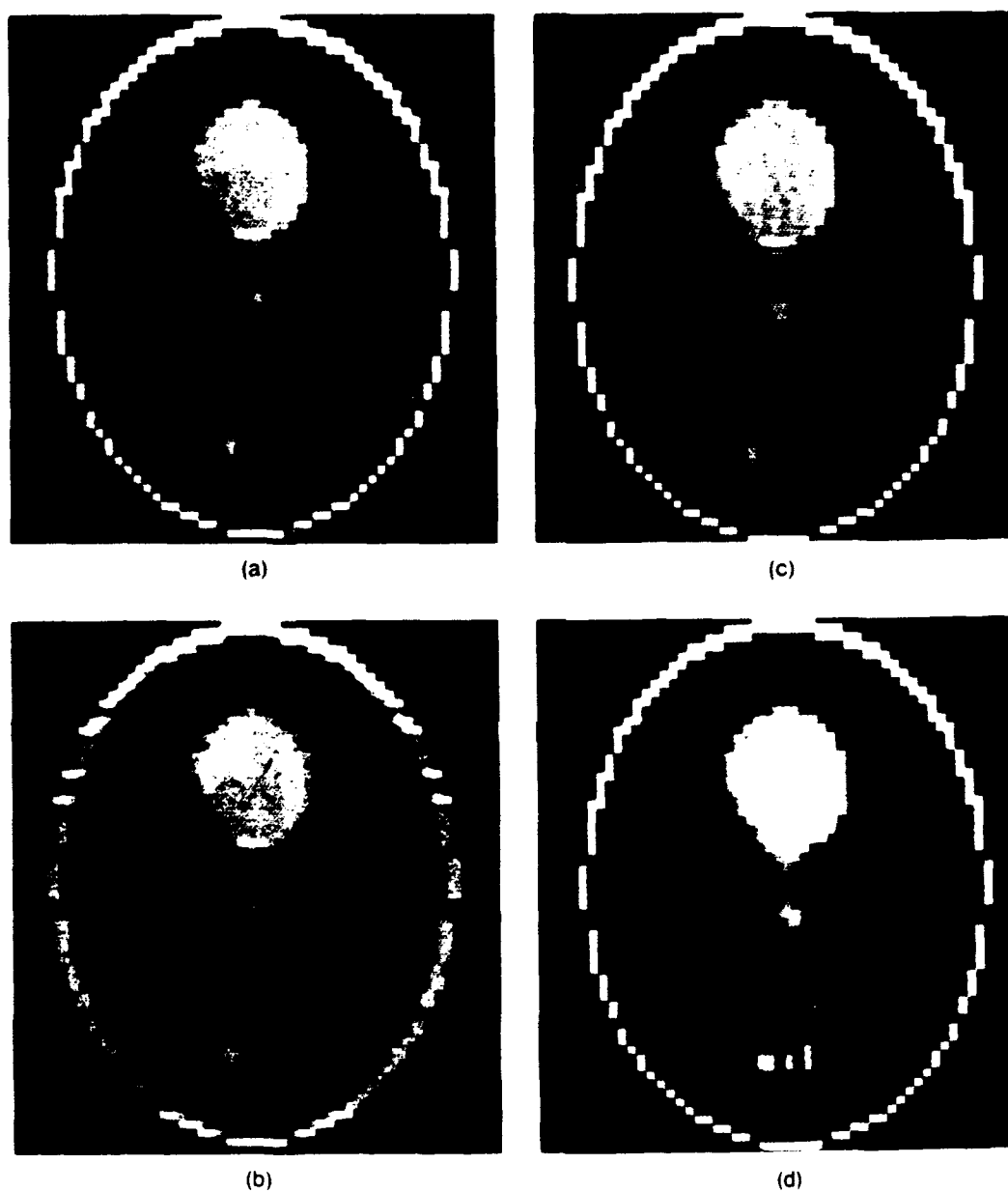


Figure 6.11. Comparison of POCS and FLP reconstruction algorithms for the two-point blur. (a) unprocessed detector image; (b) LP image; (c) FLP image; (d) POCS images after 100 iterations with  $f_0 = 0$  and all constraints in effect.

FIGURE 6.12

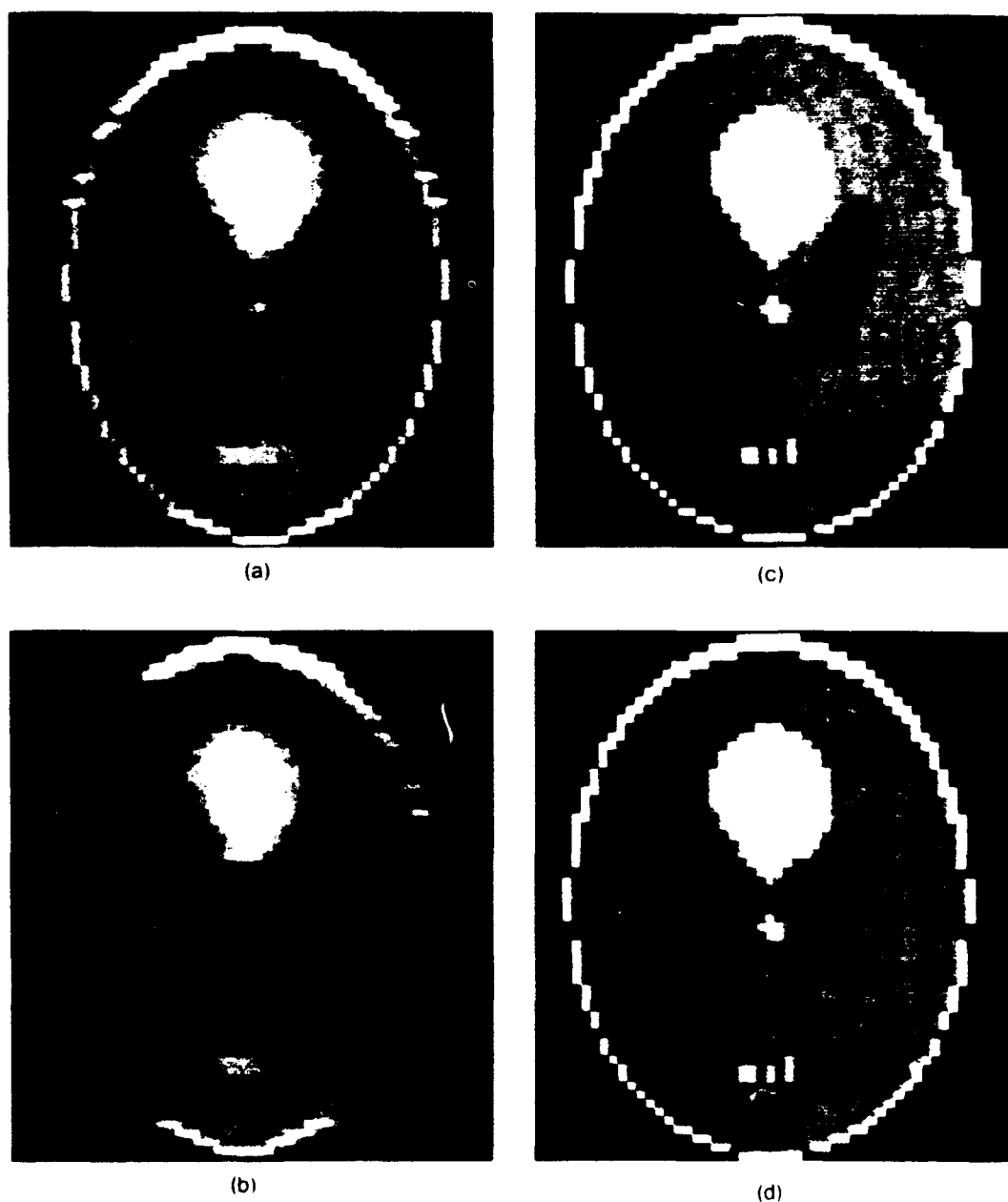


Figure 6.12. Same as Figure 6.11 except for more severe four-point blur; (a) unprocessed detector image; (b) LP image; (c) FLP image; (d) POCS image after 100 iterations.

In the final experiment in this series compared POCS and FLP when the obtained data is incomplete, i.e., when some of the detectors are not working. In [3] it is pointed out that data obtained from the Infrared Astronomical Satellite (IRAS) suffers from missing scan tracks due to dead detectors. We were interested to see which technique was more susceptible to the propagating interference resulting from dead detectors. To this end we returned to the 2-PHB case and set the response of four central detectors equal to zero. More specifically, if the scanning configuration shown in Figure 6.3 is adopted for a  $64 \times 64$  image, and the detectors are numbered from  $-32$  to  $+32$  (the  $-32$ nd detector playing the role of detector no. 1 in Figure 6.3 and the  $+32$ nd detector playing the role of detector No. 9) then detectors zero to three were set to zero.

The results are shown in Figure 6.13. In Figure 6.13(a) is shown the unprocessed detector image. Both the blurring and the effect of the dead detectors are evident. Figure 6.13(b) shows the LP image. The FLP image is shown in Figure 6.13(c); note the artifacts introduced by high-pass filtering. These artifacts are not visible in the POCS image which is shown in Figure 6.13(d) after 30 iterations. Thus it appears that the POCS method is less likely to propagate the effects of dead detectors into the rest of the image than the FLP method. How to recover the missing picture data when detectors go bad is another matter and is left for future research.

FIGURE 6.13

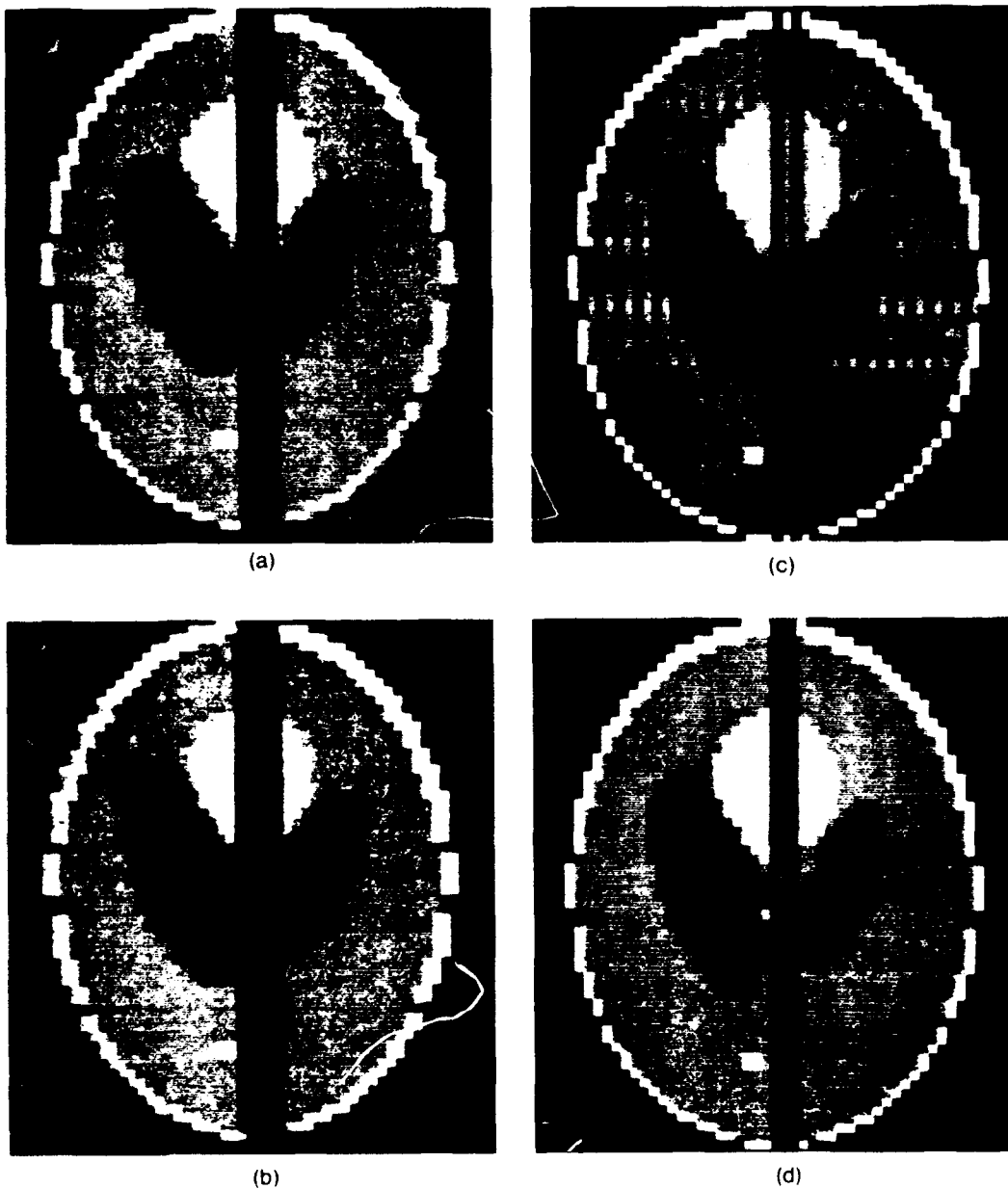


Figure 6.13. Effect of dead detectors on POCS and FLP reconstruction algorithms. Two-point horizontal blur is in effect. (a) unprocessed detector image; (b) LP image; (c) FLP image using correct inverse filter known *a priori*; (d) POCS image after 30 iterations.

## Chapter VI - REFERENCES

- [1] J.A. Richards, *Remote Sensing Digital Image Analysis*, New York, NY: Springer-Verlag, 1986.
- [2] A detector of area  $A$ , with quantum efficiency  $\mu$ , exposed to uniform light intensity  $I$  at frequency  $\nu$  will have a signal-to-noise ratio  $\text{SNR} = \mu I A \Delta t / h \nu$  if the integration time is  $\Delta t$  and a Poisson process is assumed.
- [3] B.R. Frieden and H.H.G. Aumann, "Image reconstruction from multiple 1-D scans using filtered localized projections," *App. Opt.* vol. 26, pp. 3615-3621, 1987.
- [4] P. Oskoui-Fard and H. Stark, "Tomographic image reconstruction using the theory of convex projections," *IEEE Trans. Med. Imaging*, vol. MI-3, pp. 45-58, 1988.
- [5] M.I. Sezan and H. Stark, "Tomographic image reconstruction from incomplete data by convex projections and direct Fourier method," *IEEE Trans. Med. Imaging*, vol. MI-3, pp. 91-98, 1984.
- [6] A. Lent and H. Tuy, "An Iterative method for the extrapolation of band-limited functions," *J. Math. Anal. Appl.*, vol. 83, pp. 554-565, 1981.
- [7] A. Papoulis, "A new algorithm in spectral analysis and band-limited extrapolation," *IEEE Trans. Circuits Sys.*, vol. CAS-22, pp. 735-742, 1975.
- [8] R.W. Gerchberg, "Super resolution through error energy reduction," *Opt. Acta*, vol. 21, pp. 709-720, 1974.
- [9] B.P. Medoff, W.R. Broady, M. Nassi, and A. Macovski, "Iterative convolution backprojection algorithms for image reconstruction from limited data," *J. Opt. Soc. Am.*, vol. 72, pp. 1493-1500, 1983.
- [10] Weak convergence, also known as inner product convergence is identical to the more familiar strong convergence, i.e.,  $\|f - f_k\| \rightarrow 0$ , in the finite-dimensional case.
- [11] One should make a distinction between the original function that generated the measurements and is assumed to lie in the set of functions that are square integrable over some domain, and the set of reconstructed images composed of square pixels, or of linear combinations of some other basis functions. From a finite set of measurements, one will obtain a reconstructed image  $f(x, y)$  that is an element of the finite dimension set of possible reconstructed images. This reconstructed image is taken to be an approximation of the function that generated the measurements. The original function can be recovered exactly only if it happens to lie in the set of possible reconstructed images.
- [12] D.C. Youla and H. Webb, "Image restoration by the method of convex projections: Part 1-Theory," *IEEE Trans. Med. Imagi. g*, vol. MI-1, pp. 81-94, 1982.
- [13] L.A. Shepp and B.F. Logan, "The Fourier reconstruction of a head section," *IEEE Trans. Nucl. Sci.*, vol. NS-21, pp. 21-43, 1974.



## APPENDIX A

### A. CONVEXITY of $C_j$ of EQUATION (6.5):

Let  $h_1, h_2 \in C_j$ . Then

$$(\mu h_1 + (1 - \mu)h_2, \sigma_j) = \mu(h_1, \sigma_j) + (1 - \mu)(h_2, \sigma_j) = \mu d_j + (1 - \mu)d_j = d_j$$

for any  $\mu$  including  $0 \leq \mu \leq 1$ .

### B. CLOSENESS of $C_j$ :

Let a sequence  $\{h_n\} \subset C_j$  have limit  $h$ . Then from the Cauchy-Schwartz inequality:

$$|(h_n - h, \sigma_j)| \leq \|h_n - h\| \|\sigma_j\| \rightarrow 0 \quad (A-1)$$

since  $h$  is the limit of the sequence  $\{h_n\}$ . Hence

$$(h_n - h, \sigma_j) \rightarrow 0 \quad (A-2)$$

or

$$(h_n, \sigma_j) \rightarrow (h, \sigma_j) = d_j. \quad (A-3)$$

### C. PROJECTION onto $C_j$ :

To find the projection  $g = P_j h$  where  $h$  is an arbitrary real function, we solve:

$$\min_{g \in C_j} \int_{-\infty}^{\infty} (h - g)^2 dx dy \quad (A-4)$$

for the continuous case, or

$$\min_{g \in C-j} \sum_{l,k} (h(l,k) - g(l,k))^2 \quad (A-5)$$

for the discrete case. Thus, to be specific, consider the continuous case. Equation (A-4) is equivalent to:

$$\min \int_{-\infty}^{\infty} (h - g)^2 dx dy \quad (A-6)$$

subject to  $(g, \sigma_j) = d_j$ . Using the method of Lagrange multipliers, we get:

$$\min \int_{-\infty}^{\infty} (h - g)^2 dx dy + \lambda [(g, \sigma_j) - d_j] \quad (A-7)$$

where  $\lambda$  is the Lagrange multiplier. Differentiating equation (A-7) and solving for  $g(x, y)$  gives:

$$g(x, y) = h(x, y) - \frac{\lambda}{2} \sigma_j. \quad (A-8)$$

If equation (A-8) is used in  $(g, \sigma_j) = d_j$  we get:

$$\frac{\lambda}{2} = \frac{(h, \sigma_j) - d_j}{(\sigma_j, \sigma_j)}. \quad (A-9)$$

Using this result in equation (A-8) gives the final result:

$$g(x, y) = h(x, y) + \frac{d_j - (d_j, \sigma_j)}{(\sigma_j, \sigma_j)} \sigma_j(x, y) \quad (A-10)$$

which is equation (6.6).

## APPENDIX B

### Papers and Presentations

#### Papers:

1. P. Das, C. DeCusatis, and D. M. Litynski, "Use of Spread Spectrum Techniques in Optical Transform Domain Processing," *Proc. MILCOM* (classified), pp. 203-213, 1988.
2. C. DeCusatis and P. Das, "Spread Spectrum Techniques in Optical Communication Using Transform Domain Processing," to be published in *IEEE Journal on Selected Areas in Communications*.
3. C. DeCusatis and P. Das, "Optical Controller for Adaptive Phased Array Antennas Using Neural Network Architecture," *SPIE Proc. 1217, OE/LASE*, Los Angeles, CA, to be published.
4. H. Stark and P. Oskoui, "High Resolution Image Recovery from Image Plane Arrays Using Convex Projections," *J. Opt. Soc. Amer. A*, vol. 6, no. 13, pp. 1715-1726, 1989.
5. N. P. Vlannes, C. M. DeCusatis, and P. K. Das, "Hybrid Optical/Electronic Nonlinear Optical Devices," submitted.
6. J. F. McDonald, N. P. Vlannes, T.-M. Lu, G. E. Wnek, T. C. Nason, and L. You, "Photonic Multichip packaging (PMP) using Electro-Optic Organic Materials and Devices," *SPIE International Symposium on Advances in Interconnects and Packaging, 1390-13*, to be published.

#### Presentations:

1. P. Das, C. DeCusatis and D. M. Litynski, "Use of Spread Spectrum Techniques in Optical Transform Domain Processing," presented at the Military Communications Conference, San Diego, Oct 23-26, 1988.
2. C. DeCusatis and P. Das, "Spread Spectrum Techniques in Optical Communication Using Transform Domain Processing," presented 6th IEEE International Workshop on Microelectronics and Photonics in Communications," Cape Cod, MA, June 7-9, 1989.
3. H. Stark and P. Oskoui, "High Resolution Image Recovery from Image Plane Arrays Using Convex Projections," presented at Signal Recovery and Synthesis Meeting at Sea Crest Resort, Cape Cod, MA, June 14-16, 1989. Meeting sponsored by AFOSR and Optical Society of America.
4. N. Vlannes, C. DeCusatis, and P. Das, "Hybrid Optical/Electronic Nonlinear Optical Device Using Acousto-Optic Deflectors with Nonlinear Feedback," presented at OPTICS'89, Optical Society of America Annual Meeting, Orlando, FL, Oct. 16-20, 1989.
5. C. DeCusatis and P. Das, "Optical Controller for Adaptive Phased Array Antennas Using Neural Network Architecture," presented at the SPIE, OE/LASE meeting, Los Angeles, CA, Jan. 14-19, 1990.

6. K. Nelson and N. Vlannes, "Analysis of Electro-Optic Waveguides with Embedded Electrode Structures," presented at OPTCON'90, IEEE Lasers and Electro-Optics Society Annual Meeting, Boston, MA, Nov. 5-9, 1990.
7. J. F. McDonald, N. P. Vlannes, T.-M. Lu, G. E. Wnek, T. C. Nason, and L. You, "Photonic Multichip Packaging (PMP) using Electro-Optic Organic Materials and Devices," presented at SPIE OE/BOSTON'90, International Symposium on Advances in Interconnects and Packaging, Boston, MA, Nov. 5-9, 1990.